TESI DI PERFEZIONAMENTO IN FISICA

SCUOLA
NORMALE
SUPERIORE

# X-Rays during the Cosmic Dawn

*Author:*
Harman Deep Kaur

*Supervisor:*
Andrei Mesinger

*Academic year: 2017/18 – 2019/20*

# Declaration of Authorship

I, Harman Deep Kaur, declare that this Thesis titled, "X-Rays during the Cosmic Dawn" is my own original work and is based on the following papers:

- Kaur, H.D. ; Gillet, N. ; Mesinger, A., *Minimum size of 21-cm simulations*, Mon. Not. Roy. Astron. Soc., Volume 495, Issue 2, June 2020, Pages 2354–2362
- Kaur, H.D. ; Qin, Y. ; Mesinger, A. ; Pallottini A. ; Fragos, T. ; Basu-Zych, A., *The 21-cm signal from the cosmic dawn: metallicity dependence of high-mass X-ray binaries* , Mon. Not. Roy. Astron. Soc., Volume 513, Issue 4, July 2022, Pages 5097–5108
- Qin, Y. ; Mesinger, A. ; Kaur, H.D. ; Pallottini A. ; Fragos, T. ; Basu-Zych, A., *Inferring the properties of the first X-ray binaries from the 21cm signal during the Cosmic Dawn* (in prep.)

# *Abstract*

**X-Rays during the Cosmic Dawn**

The first billion years of the Universe, from the recombination era to the epoch of reionization still largely remain an enigma. How did the structures form and evolve in the Universe? When did the first stars begin to appear? What were their properties? What was the nature of the objects which heated and reionized the surrounding intergalactic medium?

With advances in observational astronomy, it has been established that the tiny initial perturbations of the order $\sim 10^{-5}$ in the cosmic microwave background (CMB) radiation grew under gravitational instability and evolved to the structures that we see today. However, the period from the Dark Ages till the epoch of reionization (EoR) remains unobserved by direct observations. Ongoing powerful telescopes such as James Webb Space Telescope, Atacama Large Millimeter/submillimeter Array, etc. aim to observe the galaxies at high redshifts. However, besides being unable to capture the faintest galaxies, they might not probe the first sources of heating and reionization.

In this Thesis, we exploit the potential of the redshifted 21-cm neutral hydrogen line as an indirect yet significant complementary probe of early sources of heating of the intergalactic medium (IGM). The signal is sensitive to the thermal state of the IGM. Studies suggest that X-rays from High Mass X-ray Binaries (HMXBs) drive temperature fluctuations in the IGM, during the so-called epoch of heating (EoH). The corresponding cosmic 21-cm signal should be detectable at high signal-to-noise by the upcoming radio-interferometers such as the Hydrogen Epoch of Reionization (HERA) and Square Kilometer Array (SKA). Its timing and amplitude of fluctuations during the EoH can give reveal valuable information on the nature of early sources of heating.

We predict the 21-cm signal by performing cosmological simulations using a semi-numerical simulation code, `21cmFAST`. Since the early galaxies were rare and biased, with their abundances modulated by long-wavelength modes of the underlying density field, the limited size of the cosmological simulations can underestimate the amount of structure in the signal. This effect is significant, especially during the early EoH. We quantify the minimum box size needed for simulating the power spectrum of the 21-cm signal from the Cosmic Dawn up to the EoR.

Current theoretical models of the EoH are based on empirical scaling relations between the population-averaged X-ray luminosity ($L_X$) to star-formation rates (SFRs) of local galaxies. However, both theoretical models of HMXB evolution and recent observations suggest that this $L_X$/SFR relation should have a strong dependence on metallicity. We model the impact of an evolving metallicity dependence of HMXBs on the 21-cm signal from the EoH. Motivated by the current uncertainties, we present forecasts for various mass-metallicity relations as well as $L_X$/SFR relations. The Thesis is organized as follows.

1- Chapter 1 covers the cosmological and astrophysical framework which underlies the thesis. The topics range from the standard cosmological model to various aspects of galaxy formation and evolution.

2- Chapter 2 provides an overview of the properties of the IGM such as ionization and thermal evolution. It provides a detailed discussion on the heating of the IGM by X-rays by various X-ray sources, especially HMXBs, and their global scaling relations. The Chapter ends with a brief section on several observational probes of the IGM.

3- Chapter 3 provides details on the physics of the 21-cm signal, its role in probing the IGM, the relevant theoretical framework, observation of the signal, and the challenges it entails.

4- In Chapter 4, we work out what is the minimum size of the simulation box to simulate the 21-cm signal, without losing the structure due to missing wave modes. We quantify the bias and cosmic scatter by running simulations of different sizes and comparing the corresponding 21-cm power spectra with respect to a large simulation box, in terms of telescope noise.

5- In Chapter 5, we explore the metallicity dependence of HMXBs and its effect on the corresponding 21-cm signal. We develop a methodology to relate $L_X$/SFR with gas-phase metallicity. We work out how well the metallicity-independent $L_X$/SFR models can produce similar effects on the 21-cm signal as the metallicity-dependent ones.

6- In Chapter 6, we constrain the properties of the early HMXBs during the EoH. Following up the previous work of Chapter 5, we quantify how our metallicity-dependent $L_X$/SFR and mass-metallicity relations can be recovered from upcoming 21-cm observations

7- The Thesis ends with a discussion of conclusions and future aspects in the last chapter.

# *Acknowledgements*

I dedicate this Thesis to my mother who has played an instrumental role in my education.

I would like to express my deepest gratitude to my supervisor, Andrei Mesinger, whose guidance and advice carried me through all stages of my Ph.D. I am deeply indebted to all my collaborators, especially Nicolas Gillet, Yuxiang Qin, and Andrea Pallottini for their constant support and constructive criticism. I thank Jaehong Park and Caroline Heneka for their valuable suggestions.

I am grateful to my colleagues and friends for their support and motivation. Special thanks to Mahsa Kohandel, Kirill Zatrimaylov, Valentina Morotti, Sarina Pampana, and Angad Yuvraj for always being there for me. I am extremely grateful to Mariagrazia Trapanese who always supported and nurtured me like a sister. Thanks to Harry Mann and Roni Madhvani for their emotional support.

# Contents

# Chapter 1

# Introduction

In this chapter, I begin with an overview of the standard cosmological model in §1.1. Subsequently, in §1.2, I describe the widely-accepted theory of how the structures formed and evolved in the Universe.

## 1.1 The standard Cosmology

The current standard cosmological model utilizes two fundamental theories of physics – the Standard Model of particle physics and the theory of general relativity to describe the evolution of the observable Universe from the Big Bang to its present state. It is based on the cosmological principle which states that the Universe is homogeneous and isotropic on sufficiently large scales ($\sim$ 100 megaparsecs). According to the Big Bang model, the Universe began in the form of hot and dense plasma, around 13.8 billion years ago. Shortly after the Big Bang, the Universe went through a phase of rapid accelerated expansion known as "inflation" (Guth 1981). During this phase, the quantum fluctuations in the field driving inflation seeded tiny density fluctuations in the primordial plasma (see Baumann (2009) review). Eventually, these fluctuations, under the influence of gravity, grew into the structures we see today.

An important event in the history of the early Universe is the formation of dark matter and baryons. At temperature above $\sim$ 1 eV, the Universe consisted of a plasma of free electrons and nuclei. Photons were tightly coupled to electrons via Thomson scattering. When the temperature became sufficiently low, the electrons and nuclei combined to form primarily neutral hydrogen. This process is known as "recombination" and it occurred at redshift $\sim$ 1320. As the number of free electrons decreased, the photons started decoupling from the matter at redshift $\sim$ 1100, thus forming the CMB we see today. The period just after recombination and till the advent of the first astrophysical object is referred to as the "Dark Ages". During this period, the cold dark matter (CDM) started collapsing due to gravity in the

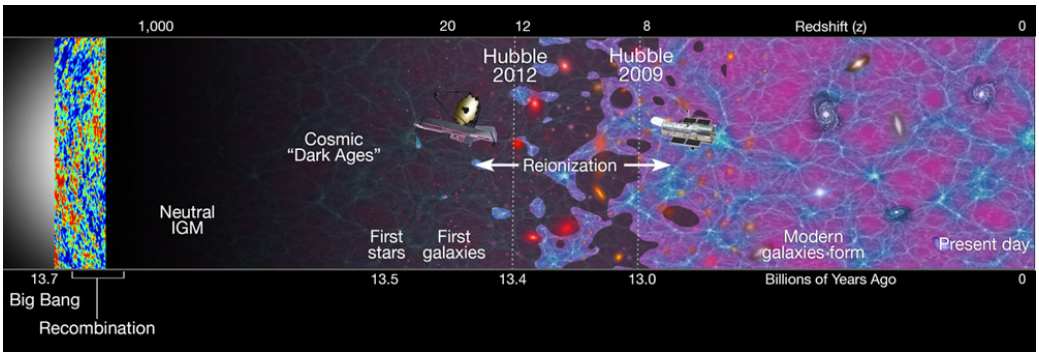


**Figure 1.1:** Schematic illustration of the timeline of the Universe. Different stages of the evolution of the Universe have been shown, from Big Bang, the recombination of plasma to form the first neutral atoms, the Dark Ages followed by the advent of the harbingers of Cosmic Dawn – the first stars and galaxies, whose radiations affect their surroundings, till the present Universe. Image credit: NASA/ESA.

dark matter halos. As the baryons cooled down and settled in these halos, the first stars, galaxies, and black holes came into existence. This epoch of their arrival is known as "Cosmic Dawn". These first sources emitted radiations which modified the thermal and ionization state of the IGM. Their X-rays heated the IGM during the epoch of heating. The last phase transition occurred with the reionization of the neutral hydrogen by UV radiation, during the epoch of reionization. A schematic timeline of the Universe illustrating different epochs is shown in Fig. 1.1.

Now, I will describe the fundamentals of standard cosmology and the basic terms associated with it.

### 1.1.1 Lambda-CDM model

Even though the predictions for the existence of dark matter and dark energy, which constitutes the major part of our Universe, were made in the twentieth century, it was only at the beginning of the twenty-first century that the Lambda-CDM (or $\Lambda$ CDM) model was established as the most widely accepted model of cosmology. It is a parametrization of the Big Bang model and is composed of four components: ordinary matter, cold dark matter, radiation, and a cosmological constant, $\Lambda$, which signifies dark energy that accounts for the cosmological expansion.

The model provides a good fit with a range of observations. Its statistical predictions of the CMB are in excellent agreement with observations carried out by various observational efforts such as Cosmic Background Explorer (COBE; e.g. Smoot et al. 1992), Wilkinson Microwave Anisotropy Probe (WMAP; e.g. Page et al. 2003; Komatsu et al. 2009) and the Planck Collaboration et al. (2016a). The existence of dark

energy is validated by the observations of Type-Ia Supernovae (e.g. Riess et al. 1998; Perlmutter et al. 1999).

Another major success of the $\Lambda$ CDM model is in its explanation of the large-scale assembly of structures in the Universe, and the detection of baryonic acoustic oscillation feature (BAO) in the CMB power spectrum confirmed by Sloan Digital Sky Survey (SDSS; Tegmark et al. 2004; Eisenstein et al. 2005).

In the following subsections, I introduce the basic terminology of the model.

### 1.1.2 Redshift and scale factor

Redshift parameter $z$ is defined as the fractional shift in wavelength ($\lambda_{\rm emit}$) of a photon emitted by a distant galaxy observed at a wavelength $\lambda_{\rm obs}$:

$$z = \frac{\lambda_{\rm obs} - \lambda_{\rm emit}}{\lambda_{\rm emit}} \, . \tag{1.1}$$

Scale factor is a dimensionless quantity used to determine the relative expansion of the Universe. Proper coordinate ( $\mathbf{r}_{\rm p}$) at time $t$ is related to comoving coordinate $\mathbf{r}$ through scale factor $a$ as:

$$\mathbf{r}_{\rm p}(t) = a(t)\mathbf{r} \, . \tag{1.2}$$

### 1.1.3 Hubble's law

Hubble's law states that the rate at which the extra-galactic objects recede from each other is proportional to the proper distance between them:

$$\dot{\mathbf{r}_{\rm p}} = H_0 \mathbf{r}_{\rm p} \, , \tag{1.3}$$

$H_0$ denotes the value of the Hubble parameter i.e. at $z = 0$.

### 1.1.4 FRW metric

For a homogeneous and isotropic Universe, the relation between space and time is provided by the Friedmann-Robertson-Walker (FRW) metric which can be written in spatial coordinates $(r, \theta, \phi)$ as:

$$-\,{\rm d}s^2 = -c{\rm d}t^2 + a^2(t)\left[\frac{{\rm d}r^2}{1 - Kr^2} + S_{\rm k}^2(r)({\rm d}\theta^2 + sin^2\theta {\rm d}\phi^2)\right] \, . \tag{1.4}$$

Here d$s$ is the line element of the space-time, $c$ is speed of light, $K$ is a constant which defines the geometry of the Universe and $S_{\rm k}(r)$ is given by:

$$S_{\rm k}(r) = \begin{cases} = \sin(\sqrt{K}r)/\sqrt{K}\,, & \text{for } K > 0 \\ = r\,, & \text{for } K = 0 \\ = \sinh(\sqrt{K}r)/\sqrt{-K}\,, & \text{for } K < 0\,. \end{cases} \tag{1.5}$$

### 1.1.5 Friedmann equations and equation of state

For an ideal liquid with a given density $\rho$ and pressure $P$, the Friedmann equations can be written for the FRW metric using Einstein's field equations as follows:

$$H^2 = \left(\frac{\dot{a}}{a}\right)^2 = \frac{8\pi G}{3}\rho - \frac{K}{a^2}\,, \tag{1.6}$$

$$\frac{\ddot{a}}{a} = -\frac{4\pi G}{3}\left(\rho + 3P\right). \tag{1.7}$$

Here, $G$ is the Newtonian Gravitational constant. The pressure of the fluid is related to the mass density $\rho$ through equation of state: $P = \omega\rho$. For non-relativistic matter, $\omega = 0$, for radiation, $\omega = 1/3$ and for cosmological constant, $\omega = -1$. For matter-dominated Universe, $\rho \propto a^{-3}$. Inserting this value of $\rho$ into eq. 1.6 and putting $K = 0$ for a flat Universe, $a \propto t^{2/3}$. Similarly, for a radiation-dominated Universe, $\rho \propto a^{-3}$ which gives $a \propto t^{1/2}$.

### 1.1.6 Density parameter

The critical density is defined for a spatially flat Universe using the Friedmann equations (i.e. putting $K = 0$ in eq. 1.6) as:

$$\rho_{\rm crit} = \frac{3H^2}{8\pi G}\,. \tag{1.8}$$

Density parameter ($\Omega$) is the ratio of actual density and critical density:

$$\Omega_i = \frac{\rho_i}{\rho_{\rm crit}}\,, \tag{1.9}$$

where $i$ denotes the component of the Universe, i.e. radiation ($\Omega_{\rm r}$), matter ($\Omega_{\rm m}$), curvature ($\Omega_{\rm k0}$) and cosmological constant ($\Omega_\lambda$).

Therefore, we can write the Hubble parameter in terms of cosmological quantities as:

$$\begin{aligned} H(z) &= H_0\sqrt{\Omega_{\rm r}(z) + \Omega_{\rm m}(z) + \Omega_\lambda(z)} \\ &= H_0\sqrt{\Omega_{\rm r0}(1+z)^4 + \Omega_{\rm m0}(1+z)^3 + \Omega_{\rm k0}(1+z)^2 + \Omega_{\lambda 0}}\,. \end{aligned} \tag{1.10}$$

## 1.2 Structure formation

As mentioned in the section above, the early Universe is assumed to be almost smooth containing tiny primordial density fluctuations ( $\sim 10^{-5}$) with respect to the global cosmic background density. According to inflationary models, these primordial fluctuations were seeded by tiny quantum fluctuations during the inflationary period of the Universe. With time, these fluctuations grew larger and larger due to gravitational instability and eventually collapsed to form various cosmic objects.

The early stages of structure formation and evolution are well explained by the linear theory of evolution of perturbations which employs Newtonian dynamics and Friedmann equations. The linear framework works well for scales down to 10 $h^{-1}$Mpc. However, below this scale, perturbations start evolving in a non-linear fashion.

The plan for this section is as follows. First, I discuss the linear theory of perturbations. Subsequently, I describe the popular model of the non-linear evolution of density fluctuations, followed by their statistical modelling. The section ends with a discussion of a different approach to studying the evolution of perturbations, the Lagrangian perturbation theory.

### 1.2.1 Linear evolution of density perturbations

A density fluctuation at a comoving coordinate $\mathbf{x}$ and cosmic time $t$ with respect to the mean background density $\bar{\rho}(t)$ of a uniform FRW Universe can be written as:

$$\delta(\mathbf{x}, t) = \frac{\rho(\mathbf{x}, t) - \bar{\rho}(t)}{\bar{\rho}(t)} \,. \tag{1.11}$$

For a density perturbation in the linear regime, i.e. $\delta << 1$, we can employ linear perturbation theory to study its evolution. We use the three hydrodynamic equations for a non-relativistic fluid with pressure $P$ and mass density $\rho$ in a matter-dominated Universe, as most of the structure formation relevant for this Thesis takes place in the matter-dominated era.

The continuity equation is based on the energy conservation principle and can be written in physical coordinates (denoted by subscript p) as:

$$\frac{\partial \rho}{\partial t} + \nabla_{\rm p}.(\rho + P)\mathbf{v}_{\rm p}) = 0 \,. \tag{1.12}$$

The Euler equation specifies the acceleration of the fluid element under the gravitational potential $\Phi$, and force due to pressure:

$$\frac{\partial \mathbf{v}_\mathrm{p}}{\partial t} + (\mathbf{v}_\mathrm{p}.\nabla_\mathrm{p})\mathbf{v}_\mathrm{p} = -\frac{1}{\rho}\nabla_\mathrm{p} P - \nabla_\mathrm{p}\Phi \,. \tag{1.13}$$

Lastly, we write the Poisson equation for the gravitational potential sourced by $\rho$ as:

$$\nabla^2_\mathrm{p}\Phi = 4\pi G\rho \,. \tag{1.14}$$

For dark matter perturbations, we can put $P = 0$, assuming a pressure-less collapse, in the continuity and Euler equations and obtain the following equations:

$$\frac{\partial \rho}{\partial t} + \nabla_\mathrm{p}.(\rho \mathbf{v}_\mathrm{p}) = 0 \,, \tag{1.15}$$

$$\frac{\partial \mathbf{v}_\mathrm{p}}{\partial t} + (\mathbf{v}_\mathrm{p}.\nabla_\mathrm{p})\mathbf{v}_\mathrm{p} = -\nabla_\mathrm{p}\Phi \,. \tag{1.16}$$

We can further write $\rho$ in terms of scale factor $a$ as: $\rho = \bar{\rho}_0(1+\delta) = \bar{\rho}a^{-3}(1+\delta)$, where $\rho_0$ is the value of mean density at $z = 0$. To introduce the cosmic expansion, we transform the system from physical coordinates to comoving coordinates using the following relations:

$$\mathbf{r}_\mathrm{p} = a\mathbf{x}, \;\; \mathbf{v}_\mathrm{p} = \dot{\mathbf{r}_\mathrm{p}} = a\dot{\mathbf{x}} + \mathbf{v}_\mathrm{pec} \,, \tag{1.17}$$

where $\mathbf{v}_\mathrm{pec}$ is the peculiar velocity and gradient $\nabla = a\nabla_\mathrm{p}$.

To develop more physical insight we move the Eulerian system to Lagrangian in which our reference frame travels along the fluid element. The Eulerian derivative ($\frac{\partial}{\partial t}$) can be converted to Lagrangian derivative ($\frac{d}{\mathrm{d}t}$) as:

$$\frac{\partial}{\partial t} = \frac{d}{\mathrm{d}t} - a^{-1}\dot{a}\mathbf{x}\cdot\nabla \,. \tag{1.18}$$

Inserting the above results into eq. 1.16, we obtain:

$$\dot{\delta} + a^{-1}\nabla\cdot[(1+\delta)\mathbf{v}_\mathrm{pec}] = 0 \,. \tag{1.19}$$

Using the above results into eqs. 1.16 and 1.14 and keeping only first-order perturbations and perturbed part of the gravitational potential, the three equations can be reduced to the following equation:

$$\ddot{\delta} + 2\frac{\dot{a}}{a}\dot{\delta} - 4\pi G\bar{\rho}_0 a^{-3}\delta = 0 \,. \tag{1.20}$$

The second term on the left-hand side is called "Hubble drag" as it shows how the

cosmic expansion suppresses the growth of density perturbations. The third term shows how gravity promotes the growth of perturbations. The solution to this equation is given by:

$$\delta = \frac{3}{5}t^{2/3} + \frac{2}{5}t^{-1}, \tag{1.21}$$

where the first term on the right-hand side is called the "growing mode" and the second term is called the "decaying mode" of the density fluctuation. Since in case of matter-dominated Universe, scale-factor $a \propto t^{2/3}$, this implies the density fluctuation grows as $\delta \propto a$.

### 1.2.2 Non-linear evolution: spherical collapse model

Having discussed the linear perturbation theory, we now move to the non-linear regime to study how the virialized dark matter halos formed out of the cosmological density field.

If the density perturbation, $\delta \gtrsim 1$, the density modes no longer grow independently but start coupling each other. The simplest analytical model used for describing this non-linear evolution of density fluctuations is the spherical collapse model. The spherical collapse model assumes that initially, the Universe is homogeneous except for a spherical perturbation. The Universe contains collision-less dark matter only [1]. The model assumes de-Sitter cosmology (i.e. spatially flat and matter-dominated). A spherical perturbation can be visualized as consisting of many concentric mass shells with a small thickness which are able to cross each other. The total mass $M$ within a spherical shell of physical radius $R$ can be written in terms of mean background density $\rho$ at time $t$ as:

$$M(< R) = \frac{4}{3}\pi R^3(t)\bar{\rho}(t)(1 + \delta(t)) \,. \tag{1.22}$$

The evolution of the overdensity can be expressed in form of the equation of motion as follows:

$$\frac{\mathrm{d}^2 R}{\mathrm{d}t^2} = -\frac{GM}{R^2} \,. \tag{1.23}$$

Integrating the above equation, we obtain the equation of energy conservation per unit mass for the shell:

$$\frac{1}{2}\left(\frac{\mathrm{d}R}{\mathrm{d}t}\right)^2 - \frac{GM}{R} = E \,, \tag{1.24}$$

[1] In reality, baryons also play a role in the evolution of structures but we neglect their role in this simple model.

where $E$ is the energy of the shell. For an initial perturbation, $\delta_i$ at radius $r_i$, the first and second terms on the left hand-side, i.e. kinetic energy (KE) and potential Energy (PE) can be further expanded using $\dot{r}_i = H_i r_i$ and $\Omega_i = \bar{\rho}_i(8\pi G)(3H_i^2)$ as follows:

$$KE = \frac{H_i^2 r_i^2}{2},\ PE = -\frac{GM}{r_i}\ . \tag{1.25}$$

Therefore,

$$E = \frac{H_i^2 r_i^2}{2}\left[1 - \Omega_i(1+\delta_i)\right]\ . \tag{1.26}$$

For a perturbation to collapse, $E < 0$ or $1 + \delta_i > \Omega_i^{-1}$. The parametric solution to eq. 1.24 is given by:

$$\begin{aligned} R &= A(1 - cos\theta), \\ t &= B(\theta - sin\theta)\ , \end{aligned} \tag{1.27}$$

where $A = \frac{GM}{2|E|}$, $B = \frac{GM}{(2|E|)^{3/2}}$ and $\theta \in (0, 2\pi)$. Therefore, we can write:

$$1 + \delta(t) = \frac{9}{2}\frac{(\theta - sin\theta)^2}{(1 - cos\theta)^3}\ . \tag{1.28}$$

The redshift at which the system collapses ($z_{\rm coll}$) can be calculated as:

$$1 + z_{\rm coll} = \frac{\delta_0}{1.686}\ , \tag{1.29}$$

where $\delta_0$ is the overdensity at $z = 0$. Therefore, we can say that the structures collapse when their linearly extrapolated overdensity reaches a "critical density", $\delta_{\rm c}$. Its value is 1.686 for $z = 0$ and can be extrapolated to higher redshifts as:

$$\delta_{\rm c} = \frac{1.686}{D(z)}\ , \tag{1.30}$$

where $D(z)$ is called linear growth function which describes the linear growth of density perturbations and is calculated as:

$$D(z) = \frac{5\Omega_{\rm m0}}{2}\frac{H(z)}{H_0}\int_z^\infty {\rm d}z \frac{1+z}{(H(z)/H_0)^3}\ . \tag{1.31}$$

From eq. 1.27, we can see the shell first expands, reaches a maximum radius ($R_{\rm turn}$), and then collapses back to $R = 0$. To find the turnaround radius $R_{\rm turn}$, we put $K.E. = 0$ in eq. 1.24 and obtain:

$$R_{\rm turn} \approx \frac{r_i}{\delta_i}\ . \tag{1.32}$$

In reality, the shells oscillate and acquire gravitational equilibrium. This state of equilibrium is called virialization. The virialized radius $r_{\rm vir}$ can be calculated by

using equation of conservation of energy and the virial theorem as follows:

$$KE_{\rm vir} + PE_{\rm vir} = E \,,$$
$$\frac{PE_{\rm vir}}{2} = -\frac{GM}{r_{\rm turn}} \,.$$

Solving the above equations, we obtain the virial radius:

$$r_{\rm vir} = \frac{r_{\rm turn}}{2} \,. \tag{1.33}$$

The overdensity, $\delta_{\rm vir}$ of the virialised system is given by the following expression:

$$1 + \delta_{\rm vir} \approx 18\pi^2 \approx 180 \,. \tag{1.34}$$

This system is called a dark matter halo.

### 1.2.3 Statistics of density perturbations

The previous sections focused on tracing the evolution of a single density perturbation. This subsection will provide a statistical description of the evolution of multiple density perturbations.

As per the paradigm of inflation the primordial density fluctuations are believed to be described by a Gaussian random field, which has been confirmed by Gaussianity measurements of CMB anisotropies observations (e.g. Komatsu et al. 2003). Therefore, a density fluctuation at a position $\mathbf{x}$ at a given time can be thought of as a sum of plane waves in Fourier space with modes independent of each other, i.e. $\delta(\mathbf{x}) = \sum \delta_{\mathbf{k}} e^{i\mathbf{k}.\mathbf{x}}$, with the amplitude of the plane wave given by the following expression :

$$\delta_{\mathbf{k}} = \frac{1}{V} \int \mathrm{d}^3\mathbf{x}\, \delta(\mathbf{x})\, e^{-i\mathbf{k}.\mathbf{x}} \,, \tag{1.35}$$

where $V$ is the representative volume of the Universe. The probability distribution of a Gaussian random field $\delta(\mathbf{x})$ over positions $\mathbf{x_1}, \mathbf{x_2}, ..., \mathbf{x_N}$ can be written as:

$$\mathcal{P}(\delta_1, \delta_2, \delta_3, ..., \delta_N) = \frac{\exp^{-Q}}{\sqrt{(2\pi^N)\det(C)}} \,, \tag{1.36}$$

where $\delta_1 = \delta(\mathbf{x_1}), \delta_2 = \delta(\mathbf{x_2})$, etc., $Q = \frac{1}{2}\sum_{i,j} \delta_i (C)^{-1}_{i,j} \delta_{i,j}$, and $C_{i,j} = \langle \delta_i \delta_j \rangle$ is the two-point correlation function, $\xi(r) = \langle \delta(\mathbf{x})\delta(\mathbf{x}+\mathbf{r}) \rangle$ calculated for two spatial positions separated by scalar distance $r$.

Thus, the statistics of density fluctuations can be fully described by two-point correlation function or its Fourier transform known as the power spectrum:

$$P(k) = \int \mathrm{d}^3 r \xi(r) e^{-i\mathbf{k}.\mathbf{r}} \,. \tag{1.37}$$

The joint probability distribution of density fluctuations with amplitudes $|\delta_{\mathbf{k_i}}|$ and phases $\phi_i$ is given by as $\mathcal{P}(\delta_{\mathbf{k_1}}, \delta_{\mathbf{k_2}}, \delta_{\mathbf{k_3}}, .., \delta_{\mathbf{k_N}})\mathrm{d}|\delta_{\mathbf{k_1}}|\mathrm{d}|\delta_{\mathbf{k_2}}|..\mathrm{d}|\delta_{\mathbf{k_N}}|\mathrm{d}\phi_1\mathrm{d}\phi_2..\mathrm{d}\phi_N$. Since they follow a Gaussian distribution, their joint probability distribution can be written as follows :

$$\mathcal{P}(\delta_{\mathbf{k_1}}, \delta_{\mathbf{k_2}}, \delta_{\mathbf{k_3}}, .., \delta_{\mathbf{k_N}})\mathrm{d}|\delta_{\mathbf{k_1}}|\mathrm{d}|\delta_{\mathbf{k_2}}|..\mathrm{d}|\delta_{\mathbf{k_N}}|\mathrm{d}\phi_1\mathrm{d}\phi_2..\mathrm{d}\phi_N = \Pi_{i=1}^{N}\mathcal{P}(\delta_{\mathbf{k_i}})\mathrm{d}|\delta_{\mathbf{k_i}}|\mathrm{d}\phi_i \,, \tag{1.38}$$

as the k-modes are independent of each other and $\phi$ is uniformly distributed over range of 0 to $2\pi$.

Therefore the probability distribution can be written as :

$$\mathcal{P}(\delta_{\mathbf{k}})\mathrm{d}|\delta_{\mathbf{k}}|\mathrm{d}\phi_{\mathbf{k}} = \exp^{\frac{-|\delta_{\mathbf{k}}|^2}{2\langle|\delta_{\mathbf{k}}|^2\rangle}} \frac{|\delta_{\mathbf{k}}|\mathrm{d}|\delta_{\mathbf{k}}|}{\langle|\delta_{\mathbf{k}}|^2\rangle} \frac{\mathrm{d}\phi_{\mathbf{k}}}{2\pi} \,, \tag{1.39}$$

with variance at scale $k$, i.e. $\sigma_k^2 = \langle|\delta_{\mathbf{k}}|^2\rangle$. Since variance $\sigma^2 = \xi(0)$, using eq. 1.37 we can relate $\sigma_k^2$ with $P(k)$ as:

$$\sigma_k^2 = \frac{1}{2\pi^3} \int P(k)\mathrm{d}^3 k \,. \tag{1.40}$$

It is customary to define a dimensionless power spectrum or power per logarithmic wavenumber bin as follows:

$$\Delta_{\mathrm{k}}^2 = \frac{k^3}{2\pi^2} P(k) \,. \tag{1.41}$$

Using the above expression of the power spectrum, eq. 1.40 can be written as:

$$\sigma_k^2 = \int \Delta^2(k) \frac{\mathrm{d}k}{k} \,. \tag{1.42}$$

The variance on a specific length-scale or equivalent mass-scale can be quantified by smoothing the density field with a window function. For a sphere centered at $\mathbf{x}$ and radius $R$, the smoothed density fluctuation can be written as :

$$\delta(\mathbf{x}, R) = \int \delta(\mathbf{x}) W(\mathbf{x} - \mathbf{x}', R)\mathrm{d}^3\mathbf{x} \,, \tag{1.43}$$

where $W(\mathbf{x})$ is a window function such that $\int W(\mathbf{x} - \mathbf{x}, R)\mathrm{d}^3\mathbf{x} = 1$. A popular choice of window function is the spherical top-hat window function defined as follows:

$$W(\mathbf{r}) = \begin{cases} \sim 1, & \text{for } |r| \leq R \\ \sim 0, & \text{for } |r| > R \,. \end{cases} \tag{1.44}$$

It can be written in k-space as :

$$W(\mathbf{k}) = 4\pi R^3 \left[ \frac{\sin(kR)}{(kR)^3} - \frac{\cos(kR)}{(kR)^2} \right] . \tag{1.45}$$

The corresponding Fourier transform of the smoothed density fluctuation is given by the following expression:

$$\delta(\mathbf{k}, R) = \delta(\mathbf{k})\tilde{W}(kR) , \tag{1.46}$$

where $\tilde{W}(kR)$ is the Fourier transform of the window function. Thus the variance of the smoothed density field on scale $R$ can be written in terms of the power spectrum as follows:

$$\sigma^2(R) = \frac{1}{2\pi} \int P(k)\tilde{W}(kR)k^2 \mathrm{d}k \tag{1.47}$$

In order to quantify the number of structures formed on a given mass scale $M$, we need to define mass variance $\sigma^2(M)$ of mass fluctuations $\delta_M = \delta(\mathbf{x}, M)$ as follows:

$$\sigma^2(M) = \langle (\delta_M)^2 \rangle = \left\langle \left( \frac{M(\mathbf{x}, R) - \bar{M}(R)}{\bar{M}(R)} \right)^2 \right\rangle , \tag{1.48}$$

where $M(\mathbf{x}, R) = V_W \int \rho(\mathbf{x}')W(\mathbf{x} - \mathbf{x}')\mathrm{d}^3\mathbf{x}$, average mass $\bar{M}(R) = V_W\bar{\rho}$, $V_W = 4\pi R^3/3$ being the volume of the window function. Inserting these values of terms into the equation above, we obtain:

$$\sigma^2(M) = \sigma^2(R) = \langle \delta_M^2 \rangle = \int_0^\infty \Delta_k^2 W_k^2 \frac{\mathrm{d}k}{k} . \tag{1.49}$$

The mass variance as a function of mass scale is shown in Fig. 1.3. The matter power spectrum $\sigma_k^2$ is a fundamental quantity in cosmology and is commonly expressed as:

$$\sigma_k^2 = Ak^n T^2(k) D^2(z) . \tag{1.50}$$

Here, $Ak^n$ is the initial power spectrum predicted by various inflationary models (Guth 1981; Guth and Pi 1982). The most common choice of $n$ is 1, a scale-invariant power spectrum proposed by Harrison and Zeldovich (Harrison 1970; Zeldovich 1972). $T(k)$ is transfer function that modifies the initial power spectrum by encapsulating the effects of all physical processes occurring at small scales during matter-radiation equality and recombination (Bardeen et al. 1986; Eisenstein and Hu 1999). The transfer function for adiabatic CDM cosmology provided in Eisenstein and Hu (1999) is plotted in Fig. 1.2. $D(z)$ is the linear growth function defined in eq. 1.30. It is conventionally normalized to unity at $z = 0$. A is the normalization constant

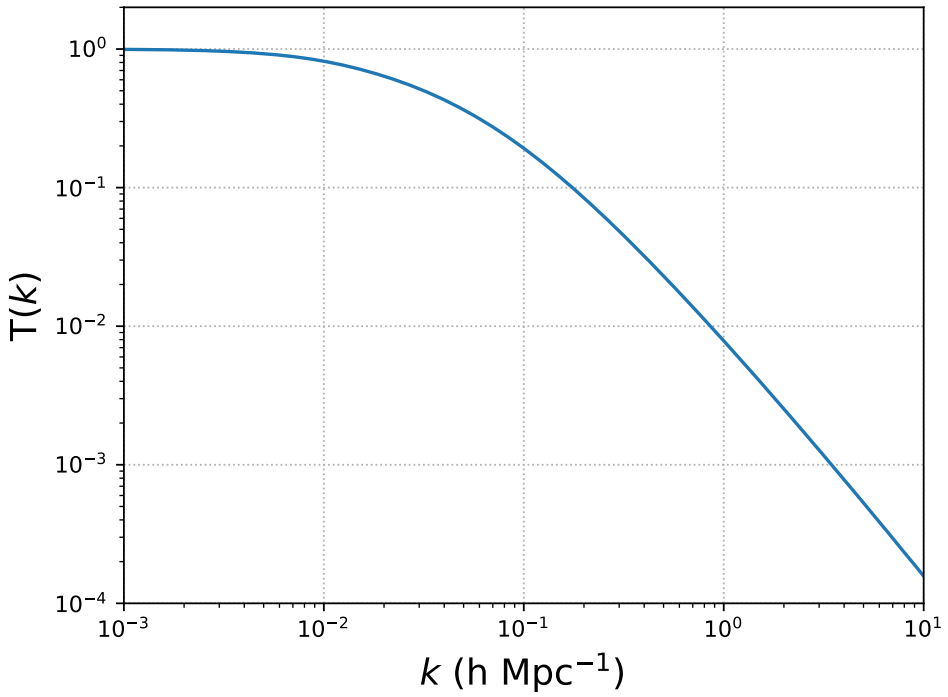


**Figure 1.2:** Transfer function as a function of $k$–scale computed using the fitting formula for adiabatic CDM provided in Eisenstein and Hu (1999).

corresponding to the amplitude of density fluctuations on scales of 8 $h^{-1}$ Mpc at $z = 0$ using a spherical top-hat window function. The currently observed value of $\sigma_M$ $(z = 0, R = 8\,h^{-1}\,\text{Mpc})$ is 0.82, as suggested by Planck Collaboration et al. (2016a).

### 1.2.4 Halo mass function

An important component of the theory of structure formation is to predict the how many halos are formed in a given mass range at a given redshift. This subsection will describe the statistics of halo mass function (HMF).

HMF quantifies the number of dark matter halos per unit halo mass per unit comoving volume of the Universe at a given redshift. In 1974, Press and Schechter (1974) provided an analytical calculation of HMF assuming a Gaussian distribution of density fluctuations and with the help of the spherical collapse model. To explain their formalism, we consider a density field $\delta_M$ smoothed on a mass scale $M$. Since $\delta_M$ follows a Gaussian distribution with variance $\sigma_M$, its probability distribution is given by:

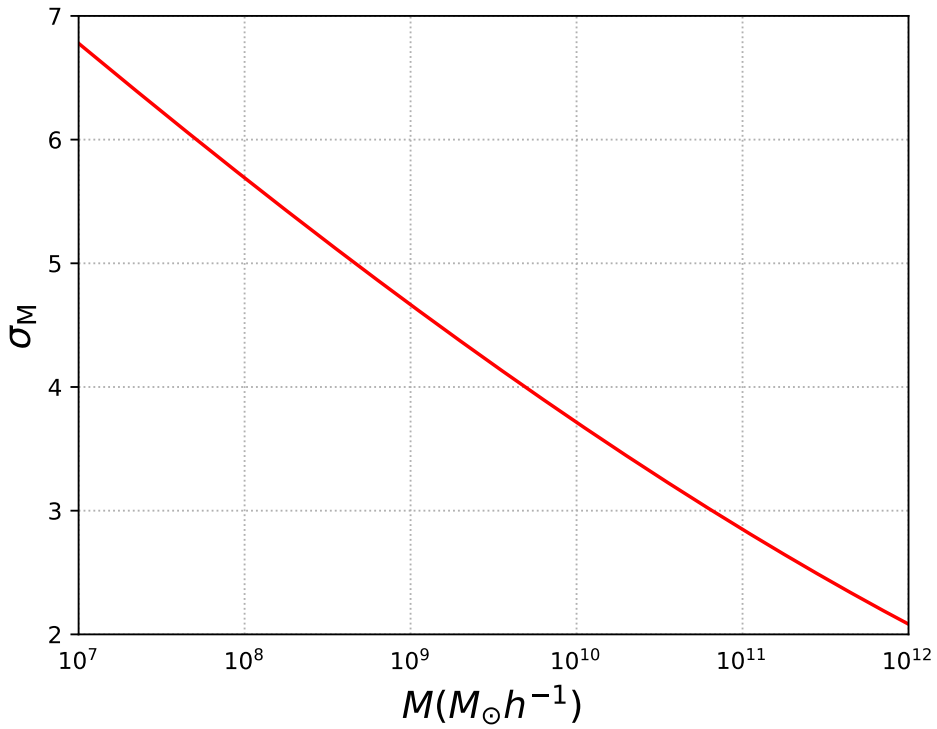


**Figure 1.3:** Mass variance as a function of scale of mass $M$ (eq. 1.3) at $z = 0$ calculated using spherical top-hat window function and transfer function shown in Fig. 1.2.

$$\mathcal{P}(\delta_M)\mathrm{d}\delta_M = \frac{1}{\sqrt{2\pi}\sigma_\mathrm{M}(M,z)}\exp^{\left(-\frac{\delta_M^2}{2\sigma_M^2(M,z)}\right)}\mathrm{d}\delta_M\,. \tag{1.51}$$

The fraction of matter in the Universe contained in halos with overdensity, $\delta_\mathrm{M}$ greater than the critical density $\delta_\mathrm{c}$ at redshift $z$ can be written as :

$$F_\mathrm{col}(>M_\mathrm{h},z) = 2\times\int_{\delta_\mathrm{c}}^{\infty}\frac{1}{\sqrt{2\pi}\sigma_\mathrm{M}(M,z)}\exp^{\left(-\frac{\delta_M^2}{2\sigma_M^2(M,z)}\right)}\mathrm{d}\delta_M\,. \tag{1.52}$$

The factor of 2 is used to consider the possibility that the overdensity $\delta_M$ on mass scale $M$ which could not surpass the critical density $\delta_\mathrm{c}$ might be a part of a more massive region $M'$ in which $\delta_{M'}$ is greater than $\delta_\mathrm{c}$ at the same redshift. This factor was derived by Bond et al. (1991). The number density of halos of mass between $M$ and $M + \mathrm{d}M$ can therefore be written as:

$$\frac{\mathrm{d}n(>M)}{\mathrm{d}M} = \frac{\bar{\rho}_0}{M}\frac{\mathrm{d}F_\mathrm{col}(>M_\mathrm{h},z)}{\mathrm{d}M} = -\sqrt{\frac{2}{\pi}}\frac{\bar{\rho}_0}{M}\frac{\mathrm{d}\ln M}{\mathrm{d}M}\frac{\delta_\mathrm{c}}{\sigma_M(M)}\exp^{\left(-\frac{\delta_M^2}{2\sigma_M^2(M,z)}\right)}\,. \tag{1.53}$$

The above expression is called Press-Schechter HMF. It is common to express the HMF in terms of logarithmic halo mass, i.e. $\mathrm{d}n/\mathrm{dln}M$. This is shown in Fig. 1.4 over a range of redshifts, computed using the transfer function from Eisenstein and

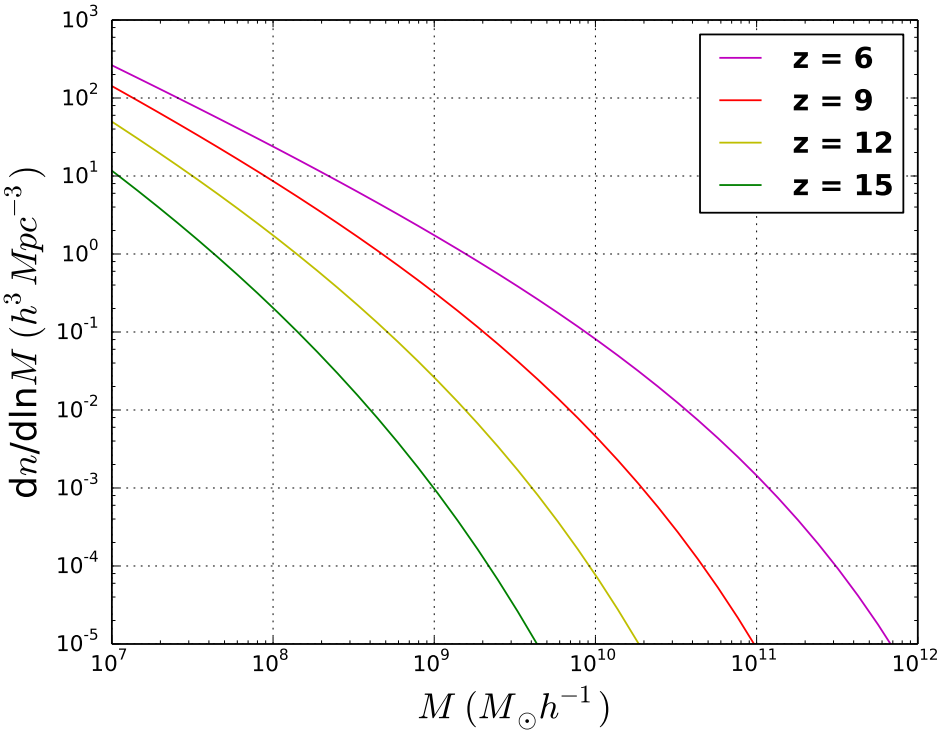


**Figure 1.4:** Halo mass function at various redshifts computed with Press-Schechter Formalism (Press and Schechter (1974)).

Hu (1999) and a spherical top-hat window function. It can be noticed that the halo mass function does not have a monotonic dependence on redshift. The abundance of low-mass halos increases with decreasing redshift.

The connection between two spatial points can be made analytically with the help of conditional mass function (e.g. Bond et al. 1991). It computes the collapse fraction of halos with mass greater than $M$ provided that the region which contains them has a linear overdensity $\delta_{\rm bias}$ on scale $M_{\rm bias}$:

$$F_{\rm col}(>M, z|M_{\rm bias,\ \delta_{\rm bias}}) = {\rm erfc}\left[\frac{\delta_{\rm c}(z)-\delta_{\rm bias}}{\sqrt{2(\sigma_{\rm M}^2-\sigma_{M_{\rm bias}}^2)}}\right]. \tag{1.54}$$

Although this function agrees relatively well with the results from N-body simulations (e.g. Jenkins et al. 2001; Warren et al. 2006; Cohn and White 2008; Tinker et al. 2008), it underestimates the number of high mass halos and overestimates the number of low mass halos (Efstathiou and Rees 1988; Cole et al. 2005, etc). Guided by more precise simulations, Sheth and Tormen (1999) modified the Press-Schechter HMF by using a more realistic ellipsoidal collapse model. The Sheth-Tormen HMF

is given by the following equation:

$$\frac{\mathrm{d}n_{\mathrm{ST}}}{\mathrm{dln}M} = \sqrt{\frac{2a}{\pi}}\frac{\bar{\rho}_0}{M}\left|\frac{\mathrm{dln}\sigma}{\mathrm{dln}M}\right|\left[1+\left(\frac{\nu^2}{a}\right)^p\right]\nu e^{-\frac{a\nu^2}{2}}\,, \tag{1.55}$$

where $\nu = \frac{\delta_c}{\sigma(M)}$, and the values of constants $A$, $a$ and $p$ can be determined by fitting to a numerical simulation. We can see that eq. 1.55 can be reduced to eq. 1.53 by putting $A = 0.5$, $a = 1$ and $p = 0$.

### 1.2.5 Lagrangian Perturbation theory

In a linear or quasi-linear regime, there is a more accurate model for describing the structure formation: Lagrangian Perturbation Theory. This theory was proposed by Zel'dovich, hence also known as *the Zel'dovich approximation* (Zel'Dovich (1970)). In this model, we follow the perturbations in the displacement of a fluid or particle instead of following its density perturbations in a fixed frame. The evolved position ($\mathbf{x}$) of the particle at time $t$ in terms of initial Lagrangian position $\mathbf{q}$ can be written as:

$$\mathbf{x}(\mathbf{q},t) = \mathbf{q} + \psi(\mathbf{q},t)\,, \tag{1.56}$$

where $\psi$ is the displacement vector. Using first-order approximation, we can write:

$$\dot{\delta} \approx -a^{-1}\nabla\cdot\mathbf{v}_{\mathrm{pec}} = -\nabla\cdot\dot{\mathbf{x}}\,. \tag{1.57}$$

Inserting the expression of $\mathbf{x}$ from eq. 1.56 into the above equation and integrating it over time, we arrive at the following expression:

$$\delta(\mathbf{q},t) \approx -\nabla\cdot\psi(\mathbf{q},t)\,. \tag{1.58}$$

Writing $\psi(\mathbf{q},t)$ as a product of two separable functions of time and space, i.e. $\psi(\mathbf{q},t) = a(t)\psi(\mathbf{q})$, we obtain:

$$\delta(a,t) \approx -a(t)\nabla\cdot\psi(\mathbf{q})\,. \tag{1.59}$$

The spatial component $\psi(\mathbf{q})$ depends only on density and is easy to evaluate in k-space. The temporal component $a(t)$ is similar to linear growth rate of density fluctuations, since in linear theory $\delta \propto D(t)$). Therefore, we can write:

$$\psi(\mathbf{q},t) = D(t)\psi(\mathbf{q})\,, \tag{1.60}$$

$$\mathbf{v} = \dot{D}(t)\psi(\mathbf{q})\,. \tag{1.61}$$

The Lagrangian perturbation theory gives relatively accurate results on quasi-linear scales and is often used for setting up the initial conditions in N-body simulations.

### 1.2.6 Galaxy formation

Having discussed the collapse and virialization of dark matter halos, I now focus on the baryons hosted by these halos.

In the case of baryons, an additional force related to pressure gradient due to spatial gradient in density is also considered. The pressure force per unit volume associated with the gas with pressure $P$ and density $\rho$ can be written as:

$$\mathbf{F} = -a^{-1}\frac{\partial P}{\partial \rho}\nabla\rho \tag{1.62}$$

$$= -a^{-1}c_s^2\bar{\rho}\nabla\delta\,, \tag{1.63}$$

where $\partial P/\partial\rho = c_s^2$ and $\rho = \bar{\rho}(1+\delta)$. Similarly, simplifying the Euler equation 1.16, we get:

$$\dot{v}_{\rm pec} + \frac{\dot{a}}{a}v_{\rm pec} = -a^{-1}\nabla\phi_{DM+b} - a^{-1}c_s^2\nabla\delta\,. \tag{1.64}$$

The gravitational potential term in Poisson equation contains both dark matter and baryon terms:

$$\nabla^2\phi_{\rm DM+b} = 4\pi G\bar{\rho}_0 a^{-1}\delta_{\rm DM+b}\,. \tag{1.65}$$

Solving the above equations and keeping the first-order terms only, we obtain:

$$\ddot{\delta} + 2\frac{\dot{a}}{a}\dot{\delta} = 4\pi G\bar{\rho}_0 a^{-3}\delta_{\rm DM+b} + a^{-2}c_s^2\nabla^2\delta\,. \tag{1.66}$$

On comparing the above equation with eq. 1.20 we can see the second term on the left-hand side shows how the cosmic expansion suppresses the growth of density perturbations. The first term on the right-hand side shows how gravity promotes the growth of perturbations while the second term shows how pressure gradients due to spatial gradients in density affect the growth of perturbations.

#### Jeans mass

An important scale in the study of galaxy formation is the scale on which the force associated with pressure balances out gravitational force. This scale is known as the Jeans scale and can be estimated as follows. For a static expansion, i.e., $\dot{a} = 0$ and approximating $\delta_{\rm DM+b}$ to the baryonic density fluctuation $\delta$ on large scales (e.g. Naoz

and Barkana (2005)) in eq. 1.66, we obtain:

$$0 = 4\pi G\bar{\rho}_0 a^{-3}\delta_{\rm DM+b} + a^{-2}c_{\rm s}^2\nabla^2\delta \,. \tag{1.67}$$

Transforming the above equation to Fourier space and using $\nabla^2 \rightarrow |\mathbf{k}|^2$, we obtain the following equation:

$$0 = (4\pi G\bar{\rho}_0 a^{-3} - a^{-2}c_{\rm s}^2|\mathbf{k}|^2)\delta_k \,. \tag{1.68}$$

The characteristic mode $k_{\rm j}$ defines the Jeans scale as follows:

$$k_{\rm j} = \left(\sqrt{\frac{4\pi G\bar{\rho}_0}{c_{\rm s}^2 a}}\right) \,. \tag{1.69}$$

The equivalent (comoving) Jeans wavelength can be written as:

$$\lambda_{\rm j} = \frac{2\pi}{k_{\rm j}} = \left(\sqrt{\frac{\pi c_{\rm s}^2}{G\bar{\rho}_0 a^{-1}}}\right) \,. \tag{1.70}$$

Therefore, we can say that the density perturbations with wavelengths greater than $\lambda_{\rm j}$ will start to collapse under gravity while the perturbations with wavelengths smaller than $\lambda_{\rm j}$ will be supported against gravity by the pressure force. We can similarly define Jeans mass ($M_{\rm j}$) as the mass enclosed within a sphere of radius $\lambda_{\rm j}/2$:

$$M_{\rm J} = \frac{4\pi}{3}\left(\frac{\lambda_{\rm j}}{2}\right)^3 \bar{\rho}_0 \tag{1.71}$$

$$= \frac{\pi^{5/2}}{6G^{3/2}}\bar{\rho}_0^{-1/2}(c_{\rm s}^2 a)^{3/2} \,. \tag{1.72}$$

As clear from the above equation, $M_{\rm J} \propto a^{3/2}$, therefore its value changes with redshift.

The Jeans mass thus provides an estimate of the scale above which a density perturbation begins to collapse under gravity. Since it is computed using the perturbation theory, it can only provide an estimate of the collapse scale in the initial phase of collapse and is not a sufficient condition for collapse. In the subsequent subsections, we will learn about another mass scale relevant to the collapse of baryonic structures, the cooling mass.

#### Virial Temperature

As the baryonic gas falls into the gravitational potential well of a dark matter halo, it gets shock-heated. For a halo massive enough to host the first galaxies, the gas must reach a characteristic temperature during its virialization known as the virial

temperature of the halo (Barkana and Loeb 2001). The virial temperature ($T_{\rm vir}$) can be calculated using the virial theorem, i.e. putting the absolute magnitude of gravitational potential energy equal to twice the magnitude of kinetic energy:

$$T_{\rm vir} \approx 10^4 {\rm K} \left(\frac{\mu}{0.6}\right) \left(\frac{M_{\rm h}}{10^8 {\rm M}_\odot}\right)^{2/3} \left(\frac{1+z}{10}\right) \left[\frac{\Omega_{\rm m0}}{0.3} \frac{1}{\Omega_{\rm m}(z)} \frac{\Delta_{\rm c}}{18\pi^2}\right] , \tag{1.73}$$

where $\mu$ is the average molecular weight of gas contained in the halo of mass $M_{\rm h}$, $z$ is the redshift at which the halo collapses, and $\Delta_{\rm c} = 18\pi^2$ is the overdensity of halo related to the critical density at its collapse redshift.

**Gas cooling**

Once the baryonic gas has virialized inside the dark matter halo, it must lose heat in order to support further collapse and ignite star formation. The most abundant elements in these interstellar clouds are hydrogen and helium, which act as potential coolants for the hot gas. The very first objects known as Pop III stars or minihalos are believed to have cooled down primarily through molecular hydrogen. When gas molecules collide with each other, they lose some of their thermal energy which goes into the excitation of vibrational and rotational states of molecular hydrogen (e.g. Abel, Bryan, and Norman 2002; Bromm, Coppi, and Larson 2002). The dominant process of $H_2$ formation in the pristine gas is:

$$\mathrm{H} + \mathrm{e}^{-1} \rightarrow \mathrm{H}^{-1} + h\nu \tag{1.74}$$

$$\mathrm{H}^{-1} + \mathrm{H} \rightarrow \mathrm{H}^2 + \mathrm{e}^{-1} . \tag{1.75}$$

The fraction of primordial hydrogen is around $10^{-7}$ for $z > 400$ via $H_2^+$ formation channel (e.g. Tegmark et al. 1997). However, its amount can increase as redshifts go below 100.

The fragile molecular hydrogen can be easily dissociated by photons with energies between 11.26–13.6 eV. Once the early stars form, even a small flux of their UV radiation is enough to photo-dissociate $H_2$ and therefore inhibit further star formation (e.g. Glover and Brand 2001). Subsequently, star formation can take place only through atomic hydrogen cooling, which requires $T_{\rm vir} \gtrsim 10^4$ K (e.g. Haiman, Abel, and Rees 2000; Ciardi and Ferrara 2005).

The minimum mass a gas cloud must have in order to fragment into stars is called cooling mass(Tegmark et al. 1997). Fig. 1.5 taken from Barkana and Loeb (2001) illustrates the cooling rates for molecular hydrogen and helium (solid curve)

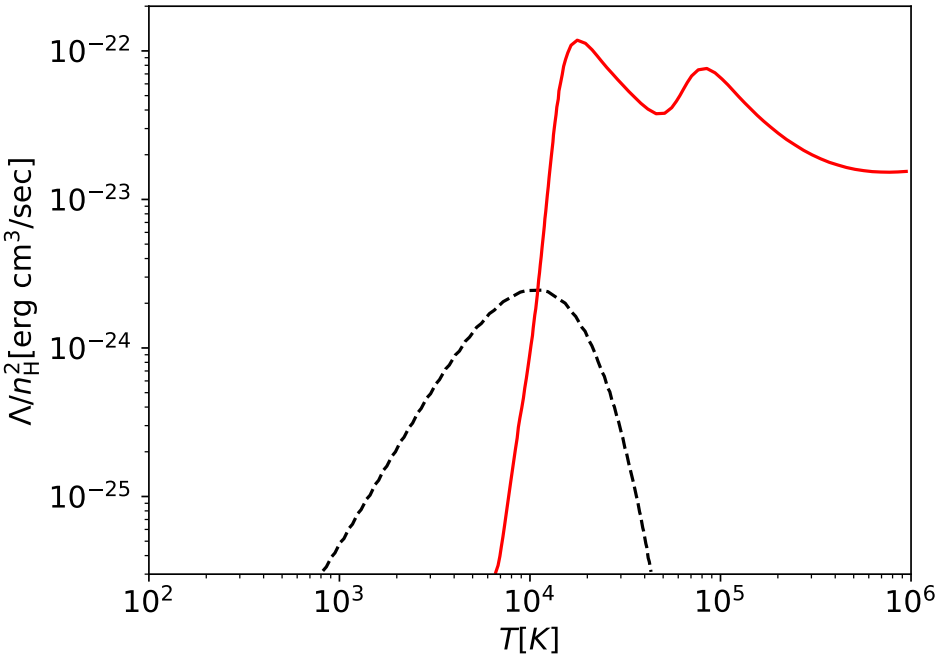


**Figure 1.5:** Cooling rate as a function of temperature. The red curve indicates cooling through atomic hydrogen and helium and the dotted black curve shows molecular hydrogen cooling. Figure taken from Barkana and Loeb (2001).

and for atomic hydrogen (dotted curve). It can be observed that atomic cooling becomes ineffective at temperatures below $\sim 10^4$ K. From eq. 1.73, this corresponds to halo mass threshold of $10^8$ $M_\odot$. Therefore, the main coolant for the very first objects is molecular hydrogen as it corresponds to a mass threshold of $\sim 10^6$ $M_\odot$.

# Chapter 2

# Inter-Galactic Medium (IGM)

Most of the matter in the Universe lies in the space between the galaxies, in form of a diffuse gas known as the IGM. The study of the IGM is a crucial part of cosmology as well as galaxy formation and evolution. It not only traces the dark matter on large scales but is also witness to various astrophysical phenomena caused by stellar radiation such as heating and reionization, metal enrichment through galactic winds, etc., making it an integral part of observational studies.

The outline of this chapter is as follows. I describe the models of the ionization and thermal state of the IGM in §2.1 and §2.2 respectively. §2.1 concludes with a brief discussion on the current probes of IGM, making way for the next chapter on the 21-cm signal as a probe for the IGM. In §2.3, I provide an overview of X-ray heating and its sources, covering a detailed discussion on X-ray binaries and their global-scaling relations. These scaling relations will be revisited in Chapter 5.

## 2.1 Ionization

In 1965, Gunn and Peterson (1965) predicted an absorption trough due to neutral hydrogen in the spectra of distant quasars blue-wards of the Ly-$\alpha$ emission line. The Ly-$\alpha$ trough was finally detected in the spectra of quasars at $z \approx 6.26$ with SDSS (Becker et al. 2001) but was not found in the spectra of the quasar at $z = 5.82,\ 5.99$. This discovery provided the first evidence that neutral hydrogen in the IGM must have gone through a phase of reionization, which culminated by $z \sim 6$ (Fan et al. 2006; McGreer, Mesinger, and D'Odorico 2015a).

As we learned in §1.1 of Chapter 1, the epoch of reionization is the last phase change of IGM which is marked by the ionization of neutral hydrogen. The transition occurred over an extended period of time as the UV radiation from the star-forming regions with their mean short paths first ionized the regions around their sources, and then with time, these ionized regions grew merged into one another, ultimately turning the entire neutral hydrogen into an ionized state.

In this section, we will learn how to model the ionization of the IGM, concluding with a brief discussion on the current observations and probes of the EoR.

### 2.1.1 Modelling the ionization process

In this subsection, we derive the redshift evolution of the ionized state of the IGM. To quantify the ionization at a given time or redshift, we use a quantity, the volume-averaged ionized fraction of neutral hydrogen ($x_{\rm HI}$). We follow the analytic framework in which the growth of ionized regions depends on the interplay between a source term, ionization by stars, and a sink term, recombination inside the HII regions (for more details, see *Understanding the Epoch of Cosmic Reionization* (2016)). We assume the reionization is a bimodal process i.e. a region is either fully ionized or fully neutral.

For a star-forming galaxy inside the neutral IGM, the rate of ionization of neutral hydrogen regions can be expressed as:

$$\langle n_{\rm H}\rangle \frac{{\rm d}V_{\rm HI}}{{\rm d}t} = \frac{{\rm d}N_\gamma}{{\rm d}t} - \alpha_{\rm AB}\langle n_{\rm H}^2\rangle V_{\rm HI} a^{-3}\,, \tag{2.1}$$

where $n_{\rm H}$ is the number density of neutral hydrogen in a comoving volume $V_{\rm HI}$, $N_\gamma$ is the number of photons per hydrogen atom which escape into the IGM and $\alpha_{\rm AB}$ is a recombination coefficient. The first term on the RHS indicates the rate of ionizing photons and the second term accounts for the recombination inside the ionized regions. $N_\gamma$ depends on a couple of factors:

$$N_\gamma = f_{\rm esc} N_{\gamma/{\rm b}} f_* N_{\rm b}^{\rm halo}\,, \tag{2.2}$$

where $N_{\rm b}^{\rm halo}$ is the total number of baryons inside the host halo, $f_{\rm esc}$ is the fraction of baryons inside the stars, $N_{\gamma/{\rm b}}$ is the number of photons per stellar baryon, and $f_{\rm esc}$ is the fraction of photons that escaped into the surrounding IGM. For the recombination term, we define a clumping factor $C = \langle n_{\rm H}^2\rangle / \langle n_{\rm H}\rangle^2$.

We can rearrange the eq. 2.1 to write down the evolution of the volume containing the HII region as below:

$$\frac{{\rm d}V_{\rm HI}}{{\rm d}t} = \frac{1}{\langle n_{\rm H}\rangle}\frac{{\rm d}[f_{\rm esc} N_{\gamma/{\rm b}} f_* N_{\rm b}^{\rm halo}]}{{\rm d}t} - \alpha_{\rm AB}\langle n_{\rm H}\rangle C V_{\rm HI} a^{-3}\,. \tag{2.3}$$

Now, we define the evolution of all ionized regions, using a volume filling factor $Q_{\rm HI} = V_{\rm tot}^{-1}\Sigma_i V_{\rm HI}^i$. Here $\Sigma_i V_{\rm HI}^i$ is the volume of all ionized regions out of total volume $V_{\rm tot}$. Therefore, the ensemble average over all ionized regions inside galaxies hosted

by halos at redshift $z$ is given by:

$$Q_{\rm HI} = f_{\rm esc} N_{\gamma/{\rm b}} f_* \int_{\infty}^{z(t)} \frac{{\rm d}F_{\rm col}(> M_{\rm min})}{{\rm d}t'} {\rm d}t' - \int_{\infty}^{z(t)} \frac{{\rm d}n_{\rm rec}}{{\rm d}t'} {\rm d}t' \tag{2.4}$$

$$= f_{\rm esc} N_{\gamma/{\rm b}} f_{\rm coll}(> M_{\rm min},\, z) - n_{\rm rec}(z)\,, \tag{2.5}$$

where $F_{\rm col}$ is the collapse fraction of halos defined in eq. 1.52, $M_{\rm min}$ is the halo mass threshold for cooling of gas inside halos, and $n_{\rm rec}$ is the total number density of recombinations per baryon during the EoR. The factors $f_{\rm esc}$, $N_{\gamma/{\rm b}}$ and $f_*$ are assumed to be redshift-independent and are therefore taken out of the integral. To first order, we can write:

$$Q_{\rm HI} \approx f_{\rm esc} N_{\gamma/{\rm b}} F_{\rm col}(> M_{\rm min},\, z) - \overline{n}_{\rm rec} Q_{\rm HI}(z) \tag{2.6}$$

$$\approx \frac{f_{\rm esc} N_{\gamma/{\rm b}}}{1 + \overline{n}_{\rm rec}} F_{\rm col}(> M_{\rm min},\, z)\,. \tag{2.7}$$

We can rewrite the above equation as:

$$Q_{\rm HI} = \eta f_{\rm coll}\,, \tag{2.8}$$

where $\eta$ is the "ionizing efficiency" defined as below:

$$\eta = 20 \left(\frac{f_{\rm esc}}{0.1}\right) \left(\frac{f_*}{0.03}\right) \left(\frac{N_{\gamma/{\rm b}}}{5000}\right) \left(\frac{1.5}{1 + \overline{n}_{\rm rec}}\right)\,. \tag{2.9}$$

The astrophysical parameters contained in eq. 2.8 are highly uncertain at high redshifts. $N_{\gamma/{\rm b}}$ depends on the Initial Mass Function (IMF) of stars, which itself doesn't have a robust measurement at high $z$. For Pop II stars, this number is $\sim 5000$ while for Pop III, it can go a magnitude higher (e.g. Tumlinson and Shull 2000). As studied in Chapter 1, the cooling threshold $M_{\rm min} \sim 10^6\ {\rm M}_\odot$ for molecular hydrogen-cooled halos and $\sim 10^8\ {\rm M}_\odot$ for atomic hydrogen-cooled halos. In Chapter 4 we will employ a physically-motivated parametrization to model the astrophysical parameters.

### 2.1.2 Current probes of the EoR

An important probe of reionization is the Ly-$\alpha$ forest observed in the spectra of bright, high-redshift galaxies and quasi-stellar objects (QSOs) or quasars. The photons emitted by these sources are absorbed by the intervening neutral hydrogen clouds at different redshifts, which imprint themselves as a series of absorption lines in the corresponding spectra. The rest-frame wavelength of this Ly-$\alpha$ absorption is

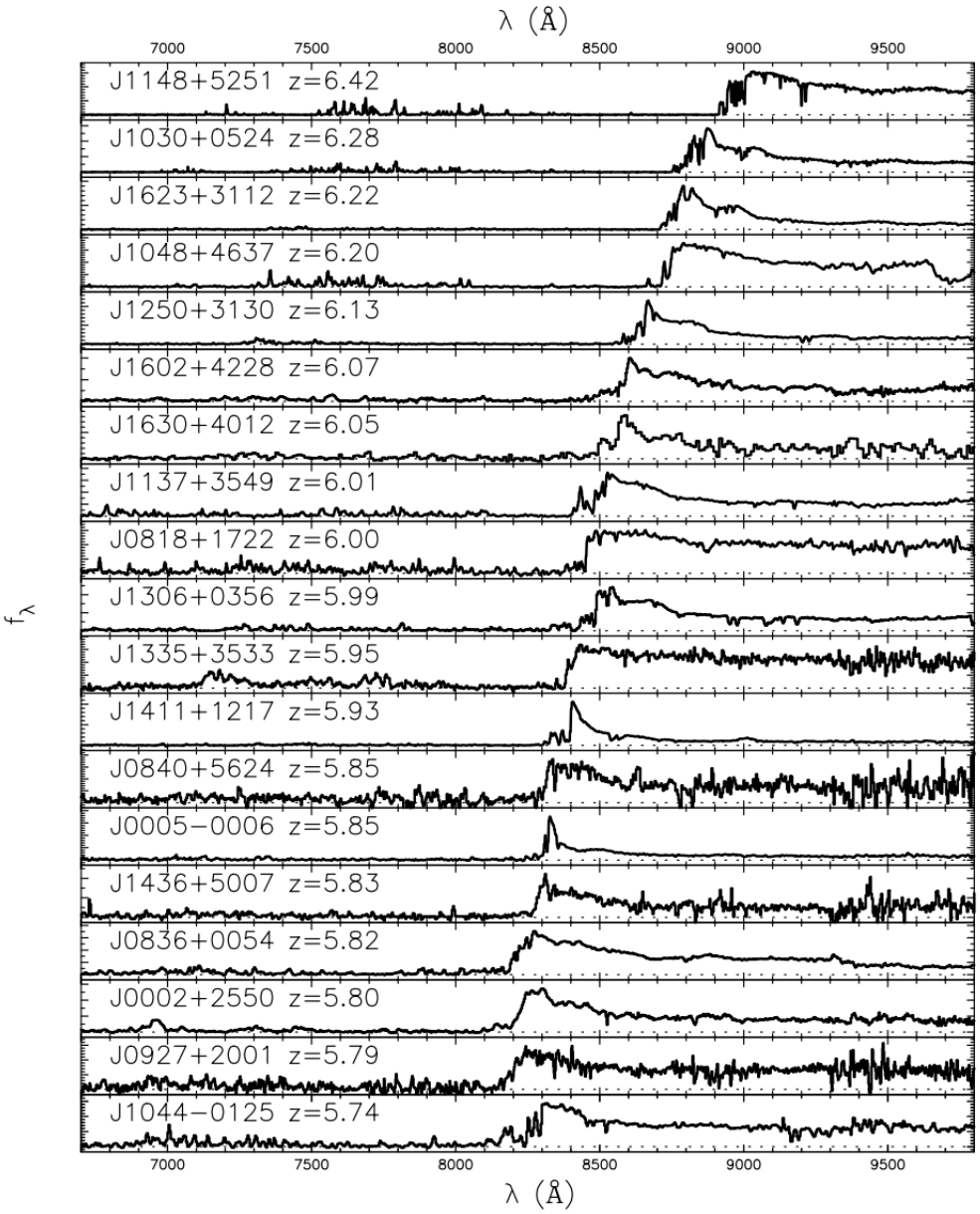


**Figure 2.1:** The Ly-$\alpha$ absorption lines observed in the spectra of 19 quasars observed with SDSS by Fan et al. (2006). The Ly-$\alpha$ forest lies blue-wards of the observed Ly-$\alpha$ emission lines of the quasars. The Gunn-Peterson absorption troughs can be seen in the spectra of QSOs at $z > 6$

. It can also be seen that the redshift evolution of Ly-$\alpha$ forest is not smooth, which can imply an inhomogeneous or patchy reionization.

1215.67 Å. If the column density of neutral hydrogen is sufficiently high, the absorption lines form a damping wing. Fig. 2.1 shows the spectra of 19 quasars at redshifts ranging from $z = 5.74 - 6.42$ observed with SDSS (Fan et al. 2006). It can be observed that long Gunn-Peterson troughs in the QSO spectra are absent at redshifts below $\sim$ 5–6, suggesting the end of reionization of the Universe.

Since Ly-$\alpha$ forest is sensitive to the column density of neutral hydrogen, it can probe the neutral hydrogen fraction as a function of redshift along the line of sight. For example, the optical depth of Ly-$\alpha$ photons can be used to put constraints on the ionized fraction of hydrogen (e.g. Rauch 1998). Another observational tool is to employ Ly-$\alpha$ emitting galaxies (Lyman-alpha emitters or LAEs), color or narrow-band selected galaxies having a detectable Ly-$\alpha$ emission. Various observational works have reported a drop in the Ly-$\alpha$ emission at $z > 6$ (e.g. Stark et al. 2010; Schenker et al. 2014). The drop in the Ly-$\alpha$ fraction can be utilized to probe the redshift evolution of neutral hydrogen around redshifts 6-7 (e.g. McQuinn et al. 2007; Mesinger and Furlanetto 2008). Moreover, the clustering measurements of the observed LAEs can also provide information on reionization. For example, the Ly-$\alpha$ lines of galaxies that lie inside ionized regions will correspond to a strong clustering signal (Furlanetto, Peng Oh, and Briggs 2006; Ouchi et al. 2010). Besides these observations, the patchy kinetic-Sunyaev signal (kSZ) also provides useful constraints on the EoR. The kSZ is a secondary CMB anisotropy caused by inverse-Compton scattering of CMB photons off free electrons in bulk motion (e.g. George et al. 2015)).

The CMB photons from the last scattering surface can provide constraints on the global reionization history of the IGM. The Thomson scattering of the CMB photons off the free electrons released by reionization suppresses the power spectrum of the CMB at sub-horizon angular scales, besides introducing a large-scale polarisation signal (Komatsu et al. 2011; Planck Collaboration et al. 2016a). The Thomson scattering optical depth of electrons to the CMB photons ($\tau_e$) can be computed as:

$$\tau_e = \int_0^{z_{dec}} \sigma_T n_e \frac{c H_0^{-1} dz}{(1+z)\sqrt{\Omega_m (1+z)^3 + \Omega_\Lambda}}, \tag{2.10}$$

where $z_{dec}$ is the redshift at which the CMB photons decoupled from the free electrons. It is noteworthy that the optical depth provides an integral constraint on the EoR, therefore, it can not be used to deduce the morphology or timing of reionization. In order to calculate the redshift evolution of the reionization process, one has to use a functional form for $n_e(z)$, making the optical depth a model-dependent

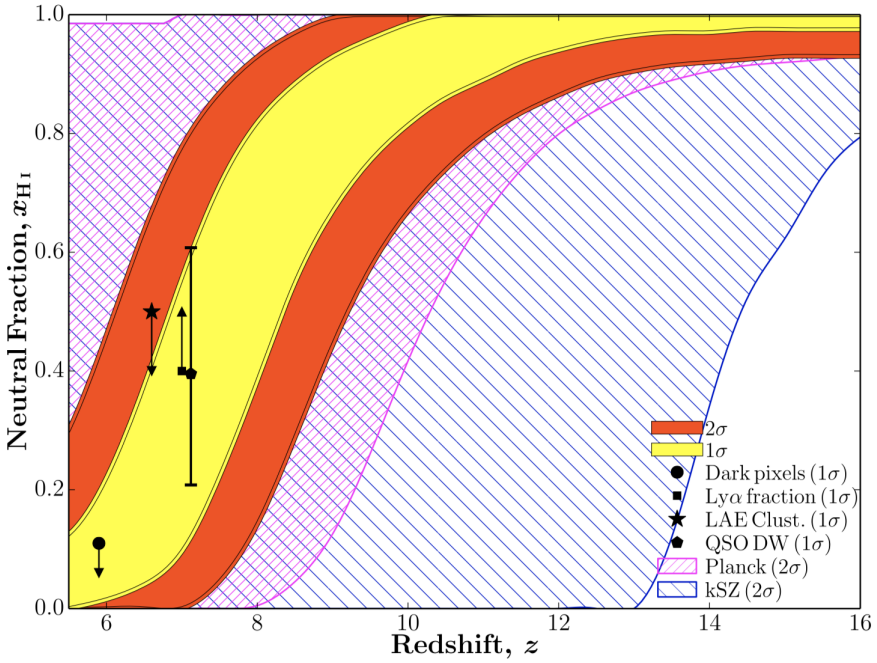


**Figure 2.2:** Current constraints on the redshift evolution of the neutral hydrogen fraction from samples of EoR models, using various EoR observational probes - optical depth of CMB photons (Planck Collaboration et al. 2016a), the dark fraction (McGreer, Mesinger, and D'Odorico 2015a), the evolution of neutral hydrogen in Ly-$\alpha$ fraction of LAE galaxies (Mesinger et al. 2015), LAE clustering (Ouchi et al. 2010), Ly-$\alpha$ damping wing (Greig et al. 2017a), patchy kinetic-Sunyaev signal (George et al. 2015). Figure taken from Greig and Mesinger (2017b).

probe of reionization.

Fig.2.2 shows $1\sigma$ (yellow region) and $2\sigma$ (red region) constraints from various EoR probes on the redshift evolution of neutral hydrogen, obtained by sampling the EoR models of Greig et al. (2017b) based on the analytic framework provided in §2.1.1. The reionization constraints at $z = 6.6$ are taken from the study of LAE clustering by Ouchi et al. (2010), constraints from the redshift evolution of Ly-$\alpha$ fraction from Mesinger et al. (2015) and the kSZ constraints are from secondary CMB anisotropy measurements of George et al. (2015). The constraints from dark fraction of QSO spectra i.e. zero-flux pixels of Ly-$\alpha$ or Lyman-$\beta$ forests observed in the spectra of high-redshift QSOs are taken from McGreer, Mesinger, and D'Odorico (2015b). The constraints from the damping wing of $z = 7.1$ QSO spectrum are from Greig et al. (2017a). Using the value of $\tau_e$ detected by Planck Collaboration et al. (2016a), Greig et al. (2017b) predicted that the EoR ended at $z \approx 7.64$. It can be noticed that although none of the probes provide tight constraints on reionization, together can provide decent information on the timing of reionization.

## 2.2 Thermal evolution

Considering that the IGM behaves as an ideal gas in local thermal equilibrium, we can write its temperature as follows:

$$T = \frac{2U_{\rm tot}}{3k_{\rm B}n_{\rm tot}}\,, \tag{2.11}$$

where $U_{\rm tot}$ is the total internal energy of the gas per unit volume, and $n_{\rm tot}$ is the total number density of the gas which contains mainly hydrogen and helium and can be approximated as $\approx n_{\rm b}(1+x_i)$, where $n_{\rm b}$ is the baryonic density and $x_i$ is the neutral fraction (with $i$ denoting the species: HI, HeI or HeII). The evolution of the gas temperature can then be written as:

$$\frac{{\rm d}T}{{\rm d}t} = \frac{2}{3k_{\rm B}}\left[\frac{1}{n_{\rm tot}}\frac{{\rm d}U_{\rm tot}}{{\rm d}t} - \frac{U_{\rm tot}}{n_{\rm tot}^2}\frac{{\rm d}n_{\rm tot}}{{\rm d}t}\right] \tag{2.12}$$

$$= \frac{2}{3k_{\rm B}n_{\rm b}(1+x_i)}\frac{{\rm d}U_{\rm tot}}{{\rm d}t} - \frac{T}{n_{\rm b}}\frac{{\rm d}n_{\rm b}}{{\rm d}t} - \frac{T}{(1+x_i)}\frac{{\rm d}x_i}{{\rm d}t}\,. \tag{2.13}$$

The total heating rate has two contributing terms:

$$\frac{{\rm d}U_{\rm tot}}{{\rm d}t} = \frac{{\rm d}Q}{{\rm d}t} + \frac{{\rm d}U_{\rm ad}}{{\rm d}t}\,. \tag{2.14}$$

Here, ${\rm d}Q/{\rm d}t$ is the total non-adiabatic heating rate per volume. ${\rm d}U_{\rm ad}/{\rm d}t$ is the adiabatic heating rate per volume and can be further expanded using the equation of state $\gamma = 5/3$ for a mono-atomic ideal gas as follows:

$$U_{\rm ad} = \frac{5}{2}(1+x_i)k_{\rm B}T\frac{{\rm d}n_b}{{\rm d}t}\,. \tag{2.15}$$

Finally, the equation of evolution of the gas temperature can be rewritten as:

$$\frac{{\rm d}T}{{\rm d}t} = \frac{2}{3k_{\rm B}n_{\rm b}(1+x_i)}\frac{{\rm d}Q}{{\rm d}t} + \frac{2T}{3n_{\rm b}}\frac{{\rm d}n_{\rm b}}{{\rm d}t} - \frac{T}{(1+x_i)}\frac{{\rm d}x_i}{{\rm d}t} \tag{2.16}$$

$$= -2TH + \frac{2T}{3\Delta}\frac{{\rm d}\Delta}{{\rm d}t} - \frac{T}{(1+x_i)}\frac{{\rm d}x_i}{{\rm d}t} + \frac{2}{k_{\rm B}n_{\rm b}(1+x_i)}\frac{{\rm d}Q}{{\rm d}t}\,. \tag{2.17}$$

Here, the first term on the RHS is the adiabatic cooling due to the expansion of the Universe, the second term represents the adiabatic cooling (heating) due to the evolution of overdensities (underdensities), the third term is energy contribution from change in the number of species and the last term is the non-adiabatic heating. The non-adiabatic heating rate depends on different terms as shown below:

$$\frac{{\rm d}Q}{{\rm d}t} = \frac{{\rm d}Q_{\rm comp}}{{\rm d}t} + \Sigma_i\frac{{\rm d}Q_{{\rm photo},i}}{{\rm d}t} + \Sigma_p\Sigma_i R_{p,i}n_e n_i\,, \tag{2.18}$$

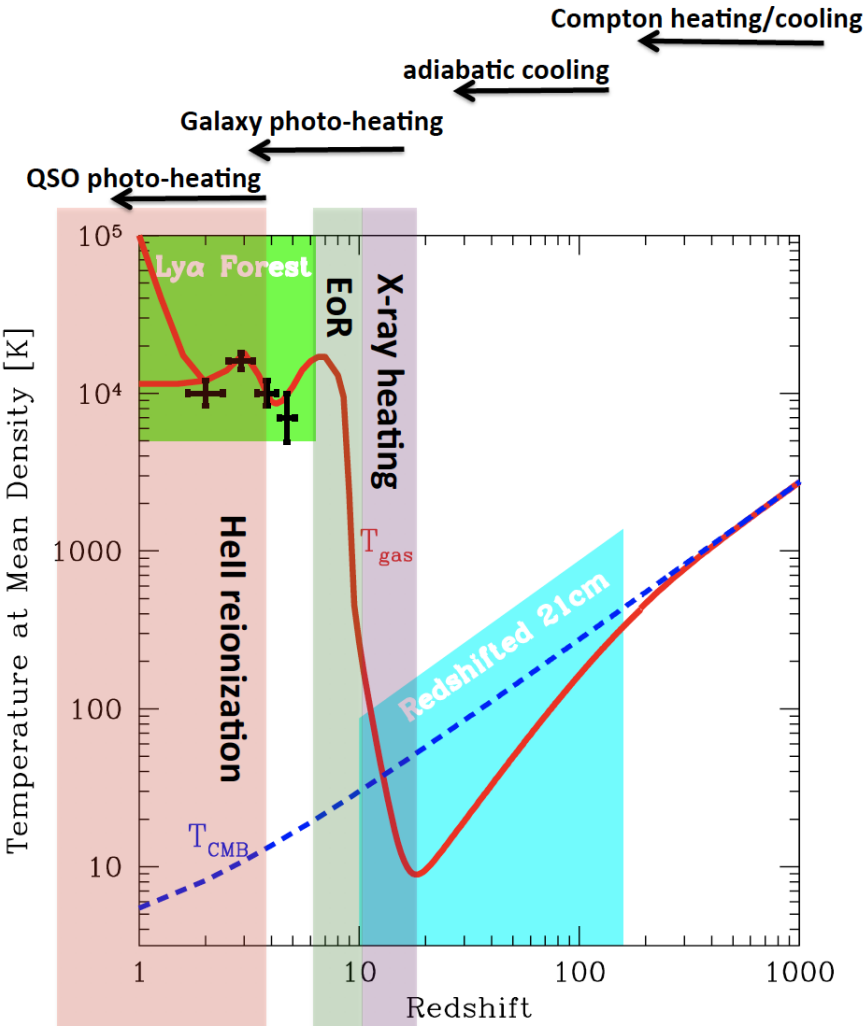


**Figure 2.3:** Evolution of temperature of gas ($T_{\rm gas}$) at mean density. The CMB temperature is shown in blue dashed line. Figure taken from the book "Structure formation in the early Universe" by Andrei Mesinger (in prep.), adapted from McQuinn (2016).

where $\mathrm{d}Q_{\rm comp}/\mathrm{d}t$ is the Compton heating/cooling due to electrons scattering off CMB photons and $\mathrm{d}Q_{{\rm photo},i}/\mathrm{d}t$ is the photo-heating rate of species $i$, and $R_{p,i}$ is the cooling rate coefficient for species $i$ for cooling process $p$. Compton heating rate can be calculated as follows:

$$\frac{2}{3k_{\rm B}n_{\rm b}(1+x_i)}\frac{\mathrm{d}Q_{\rm comp}}{\mathrm{d}t} = \frac{x_i}{1+f_{\rm He}+x_i}\frac{8\sigma_{\rm T}u_\gamma}{3m_e c}(T_\gamma - T)\,, \tag{2.19}$$

where $u_\gamma$ is the energy density of CMB, and $\sigma_{\rm T}$ is the Thomson scattering cross-section. The evolution of the gas temperature (denoted by $T_{\rm gas}$) is shown in Fig. 2.3. For comparison, the CMB temperature is shown as a dashed line. At $200 \lesssim z \lesssim 1100$, Compton scattering is effective as the leftover electrons from recombination scatter off the CMB photons. This sets $T_{\rm gas}$ equal to the CMB temperature. As the Universe becomes less dense with expansion, Compton heating becomes less effective and the gas decouples from the CMB at $20 \lesssim z \lesssim 200$. Adiabatic cooling sets $T_{\rm gas} \approx (1+z)^2$. With the advent of first luminous objects in the Universe, the gas is heated through different mechanisms such as heating by X-rays (e.g. Oh 2001; Ricotti and Ostriker 2004), resonant scattering off Ly-$\alpha$ photons (e.g. Madau, Meiksin, and Rees 1997; Furlanetto, Peng Oh, and Briggs 2006), and even shock heating (e.g. Furlanetto and Loeb 2004). X-rays are believed to be the primary source of heating of the IGM for $10 \lesssim z \lesssim 20$ (e.g. Furlanetto, Peng Oh, and Briggs 2006; McQuinn 2012; Fragos et al. 2013b; Pacucci et al. 2014). The following section discusses the heating of the IGM by X-rays in detail.

## 2.3 X-ray heating and its sources

X-ray photons first photo-ionize HI and HeI atoms in the IGM. Subsequently, the resulting electrons can cause collisional ionization, collisional excitation of HI and HeI, or can further collide with other free electrons, heating the medium (Furlanetto, Peng Oh, and Briggs 2006). With mean free paths of the orders of Mpcs, the X-rays are able to penetrate deep into the intergalactic medium (IGM), at a time when reionization was still in its infancy (Furlanetto, Peng Oh, and Briggs 2006; Pritchard and Furlanetto 2007; Mesinger, Furlanetto, and Cen 2011; McQuinn 2012, etc.). As a result, X-rays drive large-scale IGM temperature fluctuations, during the EoH (e.g. Pritchard and Furlanetto 2007; Santos et al. 2010; Mesinger, Furlanetto, and Cen 2011; Visbal et al. 2012; Pacucci et al. 2014; Munoz et al. 2022).

The main sources of X-ray heating are X-ray binaries (XRBs), Active Galactic Nuclei (AGNs), and the hot interstellar medium (ISM) (e.g. Field 1958; Fragos et al. 2013b; Madau, Meiksin, and Rees 1997; Chen and Miralda-Escudé 2004; Furlanetto, Peng Oh, and Briggs 2006; Pritchard and Furlanetto 2007; Pacucci et al. 2014; Madau and Haardt 2015; Mitra, Choudhury, and Ferrara 2018, etc.). I summarize these sources in the following subsections.

### 2.3.1 AGN

An important source of X-rays is AGNs. The black holes at the centers of massive galaxies, in their AGN phase, are believed to have significant effects on their host galaxies (e.g. review by Ferrarese and Ford (2005)). The accretion disk around these massive black holes (with mass $\sim 10^6 - 10^9$ $M_\odot$ ) are bright sources of X-ray radiation. Observational works such as Lehmer et al. (2012) studied various types of X-ray sources in distant star-forming galaxies, with a deep X-ray survey, Chandra Deep Field South (CDF-S). In their work, they found out that the AGNs dominate the X-ray number counts at bright fluxes. Basu-Zych et al. (2012) also studied the high redshift sample ($z \sim 1 - 8$) from CDF-S, in which they deduced that the X-ray luminosity density from AGNs is at least an order of magnitude higher than that corresponding to XRBs at $z \sim 0 - 3$.

### 2.3.2 ISM

Another important source of X-ray heating in normal galaxies is the diffuse hot interstellar medium (ISM) (e.g. Fabbiano 1989; Grimes et al. 2005; McQuinn 2012). Stellar winds and supernovae from massive stars can heat up the surrounding ISM, to temperatures of the order $\sim 10^6$–$10^7$ K (or sub-keV), culminating in a diffuse X-ray emission (e.g. Chevalier and Clegg 1985). The emission can occur either via thermal bremsstrahlung or metal-line cooling. The hot gas can provide significant contribution to the X-ray budget at lower energies ($\lesssim 1.5$ keV) (e.g. Mineo, Gilfanov, and Sunyaev 2012; Pacucci et al. 2014; Lehmer et al. 2016).

### 2.3.3 X-ray binaries (XRBs)

X-ray binaries are stellar systems that contain a compact object (neutron star or black hole) and a companion star. The two main classes of XRBS are low-mass X-ray binaries (LMXBs) and high-mass X-ray binaries (HMXBs). In HMXBs, the mass of

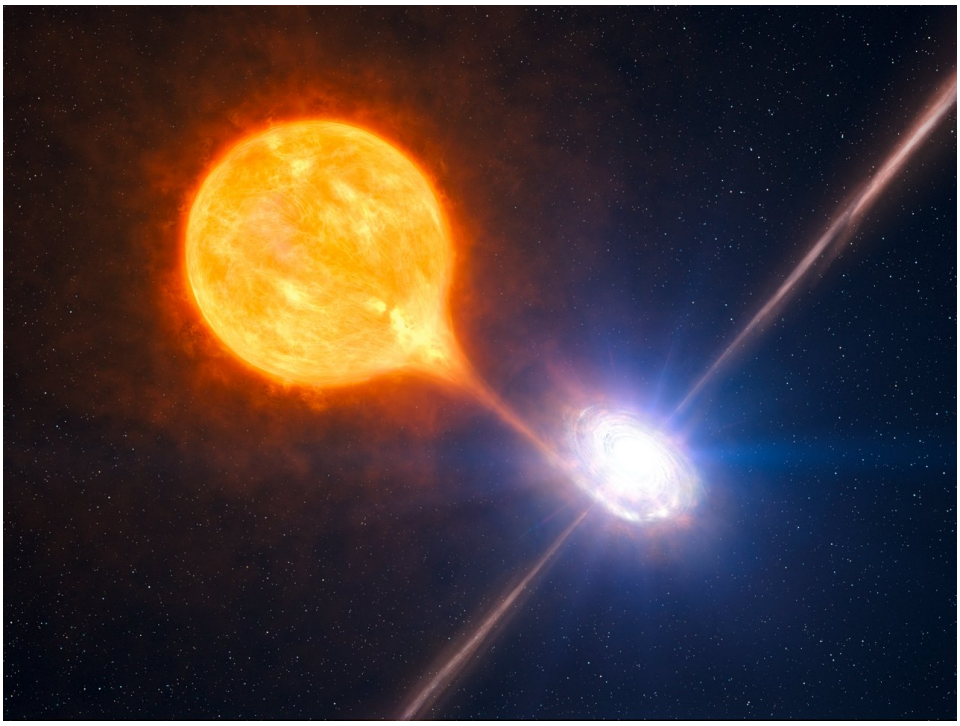

**Figure 2.4:** An artist's impression of an X-ray binary system containing a stellar black hole. Credit: ESO//L. Calçada/M.Kornmesser.

the companion star is typically $\gtrsim$ 10 $M_\odot$, while the LMXBs contain a less massive companion star, typically of mass $\lesssim$ 1 $M_\odot$.

As shown in Fig. 2.4, the matter from the donor star falls into an accretion disk around the compact star. The infalling gas gets gravitationally heated to extremely high temperatures, which results in the emission of X-ray photons from the accretion disk (e.g. Shakura and Sunyaev 1973).

The two main modes of accretion in XRBs are Roche lobe overflow and stellar winds (2.5). In the case of binaries containing massive donor stars, mass transfer can occur due to strong stellar winds. The donor star can eject mass as high as $\sim 10^{-5}$ $M_\odot$ of its mass, a portion of which gets captured by the gravitational potential of the compact star, thus emitting X-rays.

A star can also exceed its Roche lobe, resulting in mass transfer through the inner Lagrangian point of the binary system ($L_1$ in the top panel of Fig. 2.5), to the Roche lobe of the compact star. Since the angular momentum of the infalling matter is very high, an accretion disk is formed. This phenomenon is common in LMXBs, in which the stellar winds are not strong enough to cause mass transfer.

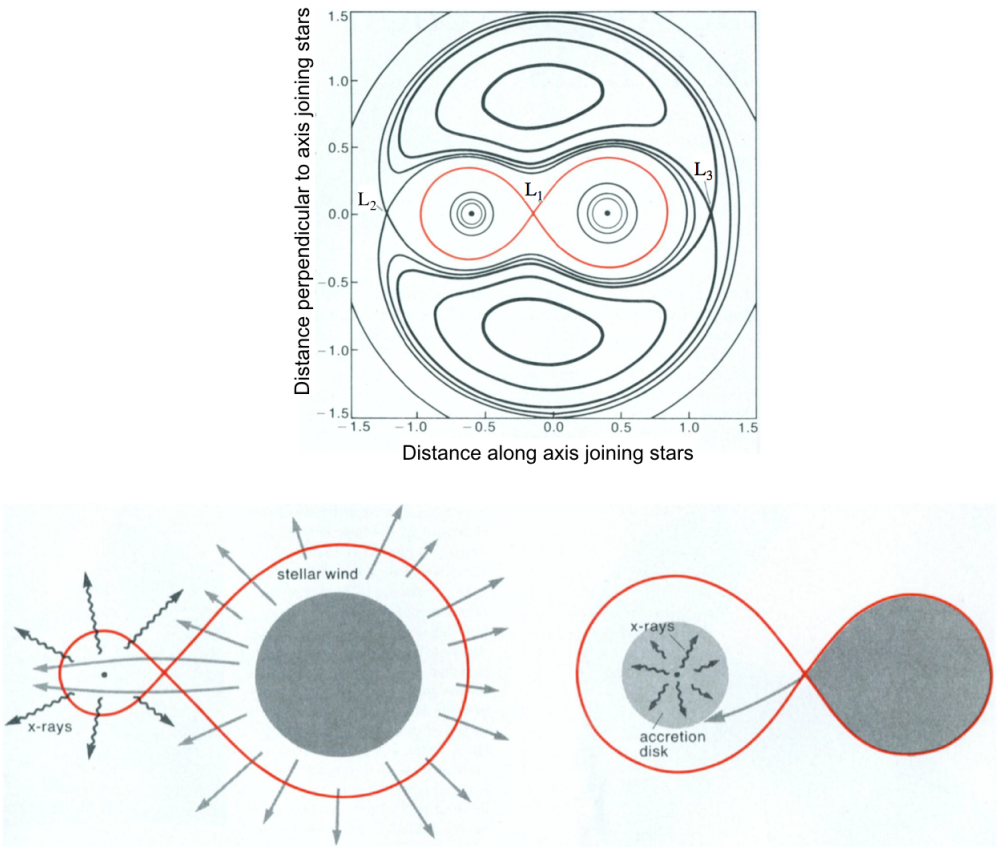


**Figure 2.5:** *Top panel*: The Roche potentials of an X-ray binary system shown in the orbit plane. Roche lobes of the two stars are shown in red. The effective gravity vanishes at the Lagrangian points- $L_1, L_2$ and $L_3$. If a star exceeds its Roche lobe, it can transfer the matter to the compact star through the innermost Lagrangian point, $L_1$. *Bottom panel*: Mass transfer from the donor star to the compact star due to stellar winds (*left*) and via Roche lobe overflow (*right*), resulting in X-ray emission. Illustration taken from Taam and Fryxell (1989).

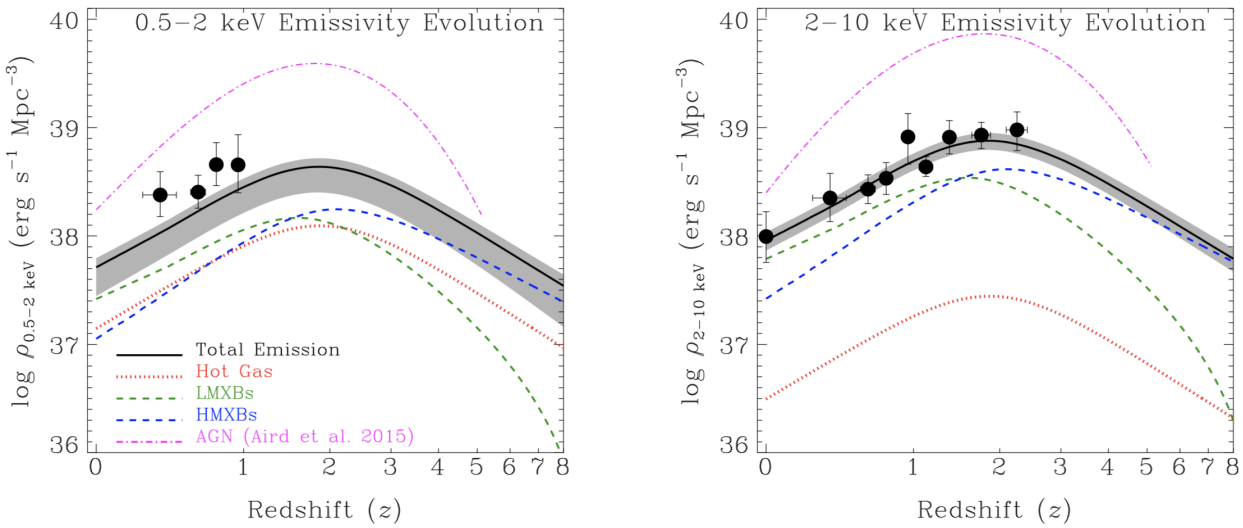


**Figure 2.6:** The estimated evolution of X-ray emissivity density of X-ray sources in normal galaxies as observed by CDF-S, in 0.5-2 keV (*left panel*) and 2-10 keV (*right*) bands, taken from Lehmer et al. (2016). The total emissivity density is shown as solid black curves. The filled circles are data points with error bars corresponding to best-fit parameters in agreement with analytical values of stellar mass and SFR density from Madau and Dickinson (2014). The solid black curves represent the total emissivity and the shaded gray regions include the uncertainties in the measurements of SFR, stellar-mass densities, and absorption of X-rays by the ISM. The emissivities from HMXBs (blue-dashed curve) and LMXBs (dashed green curve) are best-fit models of Fragos et al. (2013b). The hot gas emissivity (red dotted curve) is based on the X-ray luminosity-SFR scaling relation from Mineo, Gilfanov, and Sunyaev (2012). For comparison, AGN evolution from Aird et al. (2015) is also shown in magenta dot-dashed curves. In both energy bands, HMXBs are the dominant sources of X-rays at high redshifts ($z \gtrsim 6$).

### 2.3.4 Why are XRBs so important?

Fragos et al. (2013b) and Fragos et al. (2013a) (hereafter F+13a and F+13b, respectively) studied the X-ray emission from XRBs with *StarTrack* population synthesis code (Belczynski et al. 2008) and *Millenium-II* cosmological simulation (Guo et al. 2011), in light of optical and X-ray observations of the local galaxies taken by various surveys such as, Chandra, Spitzer, GALEX, etc. (e.g. Boroson, Kim, and Fabbiano 2011; Lehmer et al. 2007; Tzanavaris and Georgantopoulos 2008; Lehmer et al. 2008; Lehmer et al. 2010; Mineo, Gilfanov, and Sunyaev 2012). From their simulations, they inferred that X-ray emission from XRBs dominates over AGNs at $z \gtrsim 6-8$. Lehmer et al. (2016) further studied the evolution of X-ray emission with redshift, using X-ray data of normal galaxies from the CDF-S survey. Fig. 2.6 from their study shows the evolution of X-ray emissivity densities of different X-ray sources mentioned above, in the soft(0.5-2 keV) as well as the hard-band range (2-10 keV). The solid curve denotes the collective emissivity density of all sources, with the colored curves representing emission from HMXBs (blue-dashed) and LMXBs (green-dashed) taken from the maximum-likelihood model of F+13a. For comparison, the emissivity densities corresponding to hot ISM gas (Mineo, Gilfanov, and Sunyaev (2012)) and AGNs (Aird et al. (2015)) are also shown in red and pink dashed curves, respectively. As apparent in both panels, HMXBs are the major source of X-rays at high redshifts ($z \gtrsim 6$). HMXBs are expected to be the most prominent source of heating in the early Universe, soon after the formation of the first galaxies (e.g. Furlanetto, Peng Oh, and Briggs 2006; McQuinn 2012; Fragos et al. 2013b; Pacucci et al. 2014). In the following subsection, we discuss the global scaling relations of XRBs.

### 2.3.5 Global scaling relations of XRBs

Several observational studies have suggested that the collective X-ray emission from XRBs of a galaxy is correlated with galaxy-wide properties such as SFR and stellar mass of the host galaxy (e.g. Ranalli, Comastri, and Setti 2003; Persic and Rephaeli 2007; Lehmer et al. 2008; Lehmer et al. 2010; Kaaret, Schmitt, and Gorski 2011; Mineo, Gilfanov, and Sunyaev 2012; Mineo, Gilfanov, and Sunyaev 2012; Basu-Zych et al. 2012; Lehmer et al. 2016). In this section, I discuss the collective X-ray luminosity of XRB populations in galaxies and their global scaling relations.

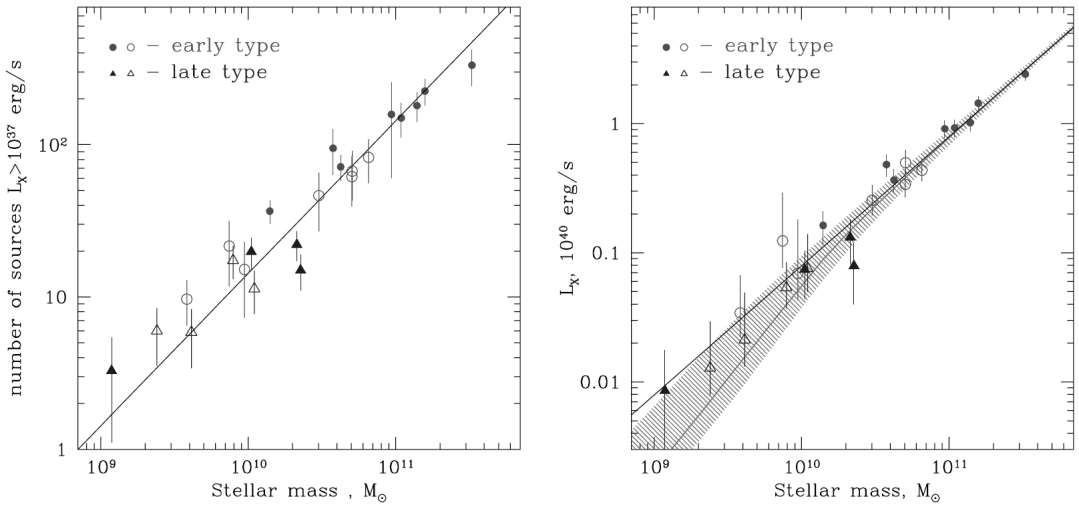


**Figure 2.7:** The number of sources with luminosities greater than $10^{37}$erg s$^{-1}$ (*left panel*) and their collective X-ray luminosity (*right panel*) as a function of stellar mass. The data contains old stellar populations observed with Chandra and contains galaxies of different morphologies, from Gilfanov (2004). The solid circles and triangles are early and late-type galaxies and the open circles and triangles are galaxies divided into smaller stellar masses. The solid line and the shaded area in the right panel represent the scaling between the most probable luminosity corresponding to their X-ray luminosity function and 67 percent uncertainty around it.

### X-ray luminosity – stellar mass of LMXBs

Due to their large evolutionary timescales ($\sim 10^8 - 10^9$ yr), the X-ray luminosity of LMXBs has a correlation with the total stellar mass of the host galaxy, which has been confirmed by various observations of nearby galaxies (e.g. Ghosh and White 2001; Grimm, Gilfanov, and Sunyaev 2002; Gilfanov, Grimm, and Sunyaev 2004a; Lehmer et al. 2010, etc.). Fig. 2.7 (from Gilfanov (2004)) shows the relation between the number of LMXBs in the old stellar populations probed by Chandra and their collective luminosity with the stellar mass of the host galaxy. The $L_X$–$M_*$ scaling is linear for $M_* \sim 10^9 - 10^{11.5}$ M$_\odot$.

### X-ray luminosity – SFR of HMXBs

HMXBs were first identified as transient objects fueled by gas supplied by a massive object when the initial observations of binary systems such as Cen X-3 and Cyg X-1 took place (e.g. Giacconi et al. 1971; Schreier et al. 1972). Since HMXBs are young stellar systems ($\sim$ 5–50 Myr) with such short evolutionary time scales ($\sim$ 1–10 Myr), it makes them potential tracers of recent star formation activity in their host galaxies (e.g. Sunyaev, Tinsley, and Meier 1978). Grimm, Gilfanov, and

Sunyaev (2003) studied the relation between the collective luminosity of HMXBs and the SFR of nearby star-forming galaxies, using the multiwavelength observations of Chandra, ASCA, RXTE-ASM, MIRKVANT/ TTM, etc., along with some data points at $z \sim 1.2$ observed with HDF-North and Lynx surveys. The corresponding collective X-ray luminosity vs SFR relation (hereafter, $L_X$/SFR) is shown in the left panel in Fig. 2.8. The best fit shown as dashed black line corresponds to $L_X/\mathrm{SFR} = 6.7 \times 10^{39}$ erg s$^{-1}$ M$_\odot^{-1}$ yr. The relation is linear at SFR $\gtrsim 4.5$ M$_\odot$ yr$^{-1}$. However, it becomes non-linear in the low-SFR part, which is due to the effects of statistics of small numbers of X-ray sources observed at those SFRs (also see Gilfanov, Grimm, and Sunyaev 2004a; Gilfanov, Grimm, and Sunyaev 2004b). Mineo, Gilfanov, and Sunyaev (2011) further studied the $L_X$/SFR relation of a relatively large sample of 38 nearby star-forming galaxies containing HMXBs, using multiwavelength data from different surveys such as Chandra, Spitzer, GALEX, and 2MASS. Their correlation is shown in the right panel of 2.8 with a linear fit of $L_X$ (erg s$^{-1}$) $= 3 \times 10^{39}$ SFR (M$_\odot$ yr$^{-1}$). The correlation contains a scatter of $\approx$ 0.4 dex. The $L_X$/SFR relation of HMXBs suffers a statistical scatter which is larger than expected, and has been attributed to other parameters such as variations in SFR history and metallicity. This was noticed in population synthesis models of XRBs, further supported by observations. For example, Kaaret, Schmitt, and Gorski (2011) and Brorby, Kaaret, and Prestwich (2014) studied the X-ray emission from the local, low-metallicity blue compact dwarf galaxies (BCDs) and found an elevation in their $L_X$/SFR scaling as compared to the local, near-metallicity galaxies of Mineo, Gilfanov, and Sunyaev (2012). The dependence of $L_X$/SFR on metallicity will be discussed in detail in Chapter 5.

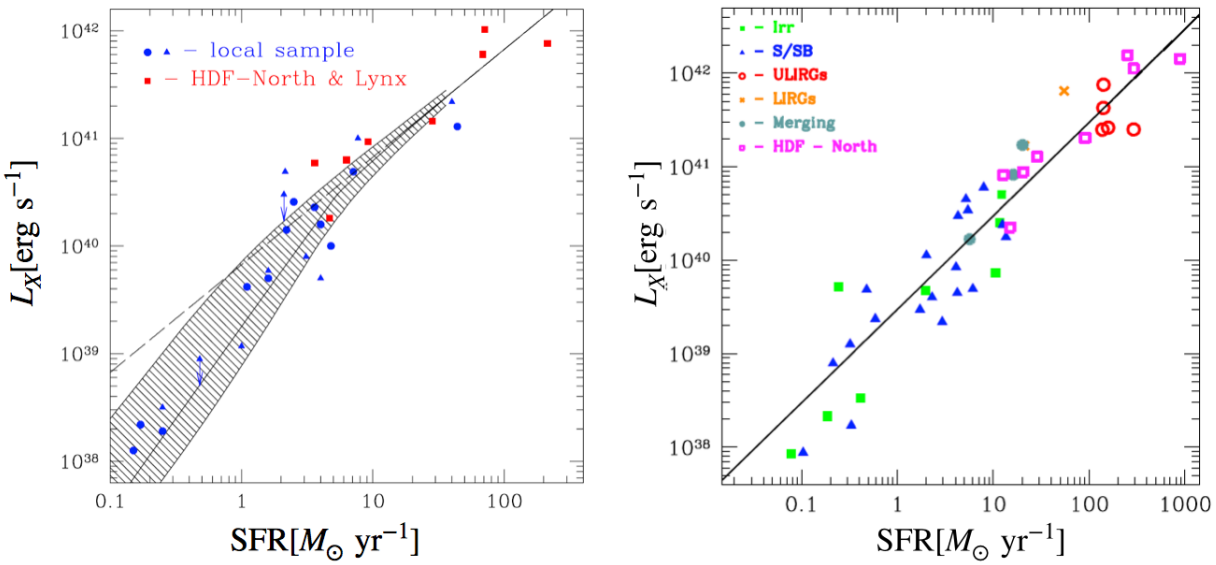


**Figure 2.8:** *Left panel*: Collective X-ray luminosity of HMXBs (in 2-10 keV band) vs star formation rate of the host galaxies from Grimm, Gilfanov, and Sunyaev (2003). The blue data points are local galaxy samples while red squares are $z \sim 1.2$ galaxy samples taken from Chandra HDF-North and Lynx surveys. The arrows display the upper limits on luminosities. The linear fit in dashed line is provided by $L_X$ (erg s$^{-1}$) $= 6.7 \times 10^{39}$ SFR ($M_\odot$ yr$^{-1}$). The thick solid line is the best fit from Gilfanov, Grimm, and Sunyaev (2004b). The non-linearity in the $L_X$/SFR relation at low SFR is due to discrete sources which constitute the X-ray luminosity. *Right panel*: X-ray luminosity of HMXBs (in 0.5-8 keV band) vs star formation rate of the host galaxies, from Mineo, Gilfanov, and Sunyaev (2011). The sample contains resolved as well as unresolved emission. The linear fit corresponds to $L_X$ (erg s$^{-1}$) $= 3 \times 10^{39}$ SFR ($M_\odot$ yr$^{-1}$).

# Chapter 3

# 21-cm signal as a probe of IGM

The 21-cm signal is an alternative probe of the first billion years of the Universe. It was first predicted by Jan Oort and Hendrick Van de Hurst in the 1940s and detected by Ewen and Purcell in 1951. In this chapter, we will learn in detail how the 21-cm signal traces the high-redshift Universe. I start with describing the underlying physics of the signal, how it is quantified, and its theoretical predictions in §3.1, §3.2 and §3.3 respectively. I consider different research works that explore the X-ray properties of the IGM with the 21-cm signal in §3.4. Then I proceed toward the observational aspects of the signal and the associated challenges in §3.5, which covers the basics of radio-interferometry, different types of foregrounds, and equations of sensitivity which will be used in the subsequent chapters. The section ends with a brief discussion of various interferometric efforts which aim to detect the 21-cm signal.

## 3.1 The underlying physics

The 21-cm line is produced by the spin-flip transition between the two hyperfine levels of the ground state of the neutral hydrogen atom. The 21-cm signal is measured in terms of brightness temperature. To define this temperature, we make use of the equation of radiative transfer, which describes the energy transfer of radiation passing through the IGM. For a radiation beam with spectral intensity $I_\nu$ at frequency $\nu$, the equation of radiative transfer ignoring scattering can be written as:

$$\frac{\mathrm{d}I_\nu}{\mathrm{d}s} = -k_\nu + j_\nu \,, \tag{3.1}$$

where $s$ is the path length along the light ray, $k_\nu$ is the absorption coefficient corrected for stimulated emission, and $j_\nu$ is the coefficient corresponding to spontaneous emission. The source function is defined as $S_\nu = j_\nu/k_\nu$. The optical depth is the integral of the absorption coefficient over path length i.e. $\tau = \int k_\nu \mathrm{d}s$. Inserting these expressions into eq. 3.1 and using initial conditions for $I_\nu$ : $I_\nu = I_\nu(0)$ at $\tau = 0$, we obtain

the following solution for $I_\nu$ :

$$I_\nu = I_\nu(0)e^{-\tau_\nu} + \int_0^{\tau_\nu} \mathrm{d}\tau' S_\nu(\tau'_\nu)e^{\tau'_\nu - \tau_\nu} \, . \tag{3.2}$$

If the emission and absorption coefficients are constant, $S_\nu$ can be pulled out of the integral. This reduces the above equation to:

$$I_\nu \approx I_\nu(0)e^{-\tau_\nu} + S_\nu(1 - e^{-\tau_\nu}) \, . \tag{3.3}$$

The above equation shows how the intensity of radiation changes as it passes through the IGM. For example, we can see that $S_\nu < 0$ corresponds to absorption and $S_\nu > 0$ corresponds to emission.

We can rewrite the above equation in terms of the brightness temperature of the 21-cm signal, $T_\mathrm{b}$. Since the frequencies of the photons related to the 21-cm signal are much smaller than the peak frequency of the CMB black body, we can take advantage of the Rayleigh-Jeans limit of Planck's law by putting $I_\nu = 2k_\mathrm{b}T_\mathrm{b}\nu^2/c^2$ and rewrite eq. 3.3 in terms of $T_\mathrm{b}$ as follows:

$$T_\mathrm{b}(\nu) = T_\mathrm{s}(1 - e^{-\tau_\nu}) + T_\mathrm{R}(\nu)e^{-\tau_\nu} \, , \tag{3.4}$$

where $T_\mathrm{R}$ is the brightness of the background radiation field taken to be the CMB temperature ($T_\gamma$). and spin temperature $T_\mathrm{s}$ is the excitation temperature for the 21-cm line. It quantifies the number density of atoms in two hyperfine levels of the ground state of hydrogen:

$$\frac{n_1}{n_0} = \frac{g_1}{g_0} e^{-E_0/k_\mathrm{B}T_\mathrm{s}} = 3e^{-E_0/k_\mathrm{B}T_\mathrm{s}} . \, , \tag{3.5}$$

where $i$ denotes the hyperfine levels (i.e. $i = 0$ for singlet state and $i = 1$ for triplet state), $g_i$ is the statistical weight corresponding to the hyperfine levels, $E_0 = 5.9 \times 10^{-5}$ eV is the energy splitting and $T_{21} = 0.068$ K is the equivalent temperature. The optical depth at the 21-cm frequency is given by the following equation (Furlanetto, Peng Oh, and Briggs 2006):

$$\tau_{\nu_{21}} \approx 0.0092(1+\delta)(1+z)^{1/2} \frac{x_\mathrm{HI}}{T_\mathrm{s}} \left( \frac{H(z)}{\mathrm{d}v_r/\mathrm{d}r} \right) \, , \tag{3.6}$$

where $\delta$ is the gas overdensity, and $\mathrm{d}v_r/\mathrm{d}r$ is the peculiar velocity gradient along the line-of-sight.

The 21-cm differential temperature is defined as the offset of the 21-cm brightness temperature ($T_\mathrm{b}$) with respect to the CMB temperature ($T_\gamma$) as follows :

$$\begin{aligned}\delta T_\mathrm{b}(\nu) = T_b - T_\gamma &= \frac{T_\mathrm{s} - T_\gamma}{1+z}(1 - e^{-\tau_\nu}) \\ &\approx 27 x_\mathrm{HI}(1+\delta)\left(\frac{H(z)}{\mathrm{d}v_r/\mathrm{d}r + H(z)}\right)\left(1 - \frac{T_\gamma}{T_\mathrm{s}}\right) \\ &\times \left(\frac{1+z}{10}\frac{0.15}{\Omega_\mathrm{m}h^2}\right)^{1/2}\left(\frac{\Omega_\mathrm{b}h^2}{0.023}\right)\ \mathrm{mK}\,. \end{aligned} \tag{3.7}$$

The second line assumes $\tau_{\nu_{21}} << 1$, a usually safe assumption for the IGM. The spin temperature is given by the equation below (Furlanetto, Peng Oh, and Briggs 2006):

$$T_\mathrm{s}^{-1} = \frac{T_\gamma^{-1} + x_\alpha T_\alpha^{-1} + x_\mathrm{c} T_\mathrm{k}^{-1}}{1 + x_\alpha + x_\mathrm{c}}\,, \tag{3.8}$$

where $x_\mathrm{c}$ is the coupling coefficient due to collisions, $x_\alpha$ is the coupling coefficient due to scattering of Ly-$\alpha$ photons, $T_\mathrm{k}$ is the kinetic temperature of the IGM, and $T_\mathrm{c}$ is the color temperature of the Ly-$\alpha$ radiation field. As clear from the equation above, $T_\mathrm{s}$ depends on various processes such as collisions, scattering by UV photons, and absorption by the CMB. Coupling collisions could be between hydrogen atoms, hydrogen atoms and electrons or between hydrogen atoms and helium, deuterium, ions, etc. The coupling coefficient $x_\mathrm{c}$ for a species $i$ is given by the following equation (Furlanetto, Peng Oh, and Briggs 2006):

$$x_\mathrm{c}^i = \frac{C_{10}}{A_{10}}\frac{T_*}{T_\gamma} = \frac{n_i k_{10}^i}{A_{10}}\frac{T_*}{T_\gamma}\,, \tag{3.9}$$

where $C_{10}$, $A_{10}$ are the de-excitaton rate per atom and spontaneous emission coefficient for 21-cm transition respectively, $k_{10}^i$ is the rate coefficient for de-excitation in collisions with species $i$ and $n_i$ is the number density of $i$. As obvious from its calculation, the collisional coupling is effective when the Universe is dense.

When the first sources of radiation turned on, their UV radiation caused decoupling of $T_\mathrm{s}$ from $T_\gamma$ through a mechanism known as Wouthuysen-Field (Wouthuysen 1952; Field 1958; WF) effect. This coupling occurs due to spin-flip transitions of the ground state neutral hydrogen atoms between its hyperfine levels upon absorption of Ly-$\alpha$ photons. Fig. 3.1 illustrates the hyperfine structure of 1S and 2P states of hydrogen. If a hydrogen atom in the singlet state absorbs a Ly-$\alpha$ photon, it can move to one of the 2P hyperfine states according to dipole selection rules. Then if the atom goes to the ground-level triplet state, a spin-flip occurs along with the emission of a Ly-$\alpha$ photon. In this way, resonant scattering of Ly-$\alpha$ photons by neutral hydrogen

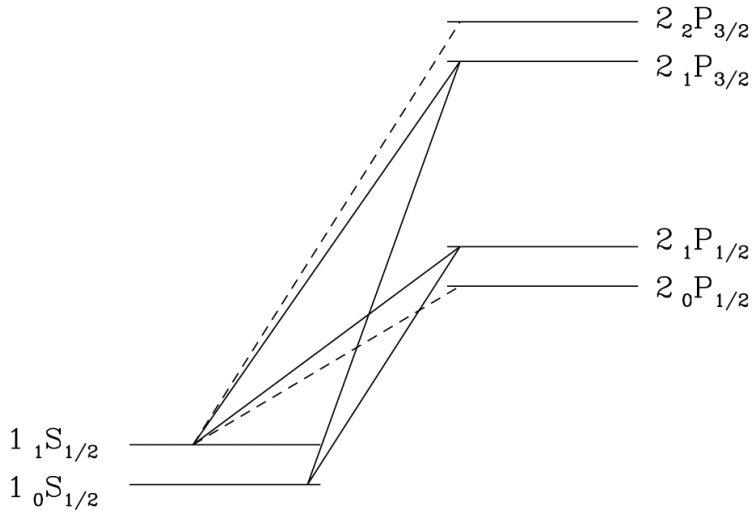


**Figure 3.1:** Level diagram showing the hyperfine splitting of the ground state neutral hydrogen atom. The solid (dashed) lines show the transitions which are allowed (prohibited) according to the electron dipole selection rules. The figure is taken from Furlanetto, Peng Oh, and Briggs (2006).

atoms can induce a spin-flip transition. As a result, the spin temperature is coupled to the color temperature ($T_c$) of the Ly-$\alpha$ radiation field and is determined by the shape of the photon spectrum at the Ly-$\alpha$ resonance. The corresponding coupling coefficient, $x_\alpha$ is given by (Furlanetto, Peng Oh, and Briggs 2006):

$$x_\alpha = \frac{4}{27}\frac{P_\alpha}{A_{10}}\frac{T_{21}}{T_\gamma} = 1.7 \times 10^{11}(1+z)^{-1} S_\alpha J_\alpha \,, \tag{3.10}$$

where $J_\alpha$ is the angle-averaged specific intensity of background radiation around Ly-$\alpha$ line, $S_\alpha$ is a correction factor that accounts for variations near the line center, and $P_\alpha$ is the scattering rate of Ly-$\alpha$ photons given by:

$$P_\alpha = 4\pi\chi \int d\nu J_\nu(\nu)\phi_\alpha(\nu) \,, \tag{3.11}$$

where $\chi \equiv \frac{\pi e^2}{m_e c} f_\alpha$ is the oscillation strength of the Ly-$\alpha$ transition, $J_\nu(\nu)$ is the angle-averaged specific intensity of the background radiation field, $\phi_\alpha(\nu)$ is the Ly-$\alpha$ absorption profile. Local absorption cross-section, $\sigma_\nu$ is given by: $\sigma_\nu \equiv \chi_\alpha \phi_\alpha(\nu)$. Since optical depth to Ly-$\alpha$ scattering is very large around the line center, a condition easily fulfilled at high redshifts, the large number of Ly-$\alpha$ scatterings sets $T_c \approx T_k$ (Field 1958), thus coupling the spin temperature to kinetic temperature.

The evolution of the 21-cm brightness temperature with redshift is shown in Fig. 3.2, taken from the book, *Understanding the Epoch of Cosmic Reionization* (2016). The

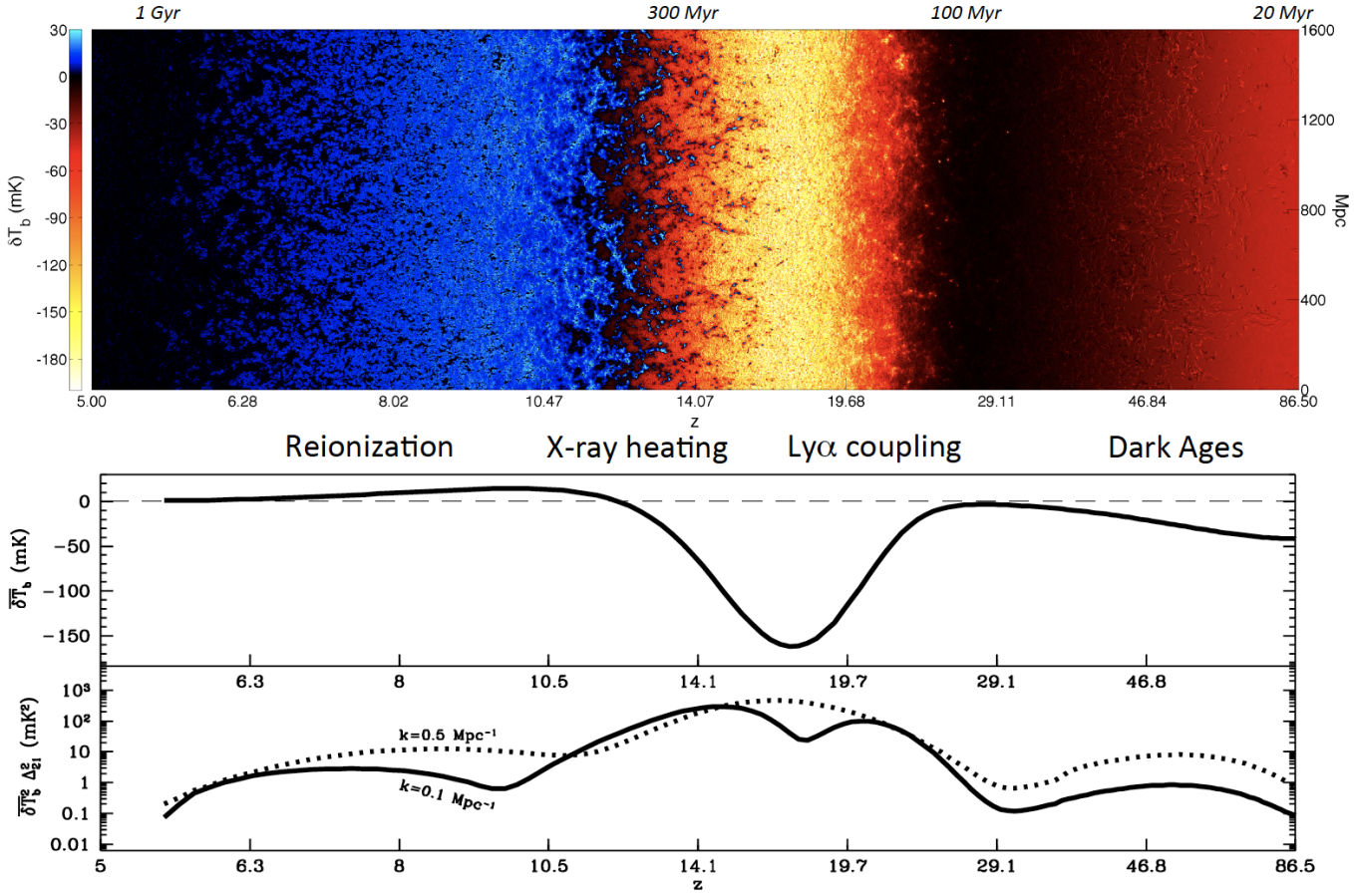


**Figure 3.2:** *Top panel*: Slice through the 21-cm brightness temperature field vs redshift. *Middle and bottom panels*: The redshift evolution of the corresponding global 21-cm signal and its power spectra at $k = 0.1$ Mpc$^{-1}$ (solid curve) and $k = 0.5$ Mpc$^{-1}$ (dotted curve) respectively. Figure taken from the book, *Understanding the Epoch of Cosmic Reionization* (2016).

second panel shows the global differential brightness temperature (3.7) evolves with redshift. At $z > 30$, the Universe is dense enough for $T_s$ to couple with $T_k$ via collisional coupling. Due to adiabatic expansion, $T_k$ evolves as $\propto (1+z)^2$. Therefore, the 21-cm signal is observed in absorption. However, after $z$ reaches $\sim 30$, $T_s$ decouples from $T_k$ as the Universe becomes less dense. Therefore, $\overline{\delta T}_b$ vanishes at $z \sim 30$. As the first sources begin to appear, their UV radiation initiates WF coupling, decoupling $T_s$ to $T_k$ and resulting in a strong absorption signal. Then, during the EoH ($10 \lesssim z \lesssim 20$), the IGM is heated primarily by X-rays prompting a 21-cm signal in emission. This is followed by the reionization phase, during which the neutral hydrogen fraction becomes so small that by $z \sim 6$, $\overline{\delta T}_b$ becomes zero again.

## 3.2 21-cm power spectrum

Another important observable for quantifying the 21-cm signal besides the globally-averaged signal is the 21-cm power spectrum, a quantity measured by radio interferometers. As explained in the previous section, the signal depends on various quantities such as the density field, neutral hydrogen fraction, radiation fields, etc. Therefore, spatial fluctuations in each of these quantities contribute to the fluctuations in the 21-cm signal.

To obtain the 21-cm power spectrum, I introduce a spatial perturbation to the 21-cm brightness temperature as follows:

$$\delta_{21}(\mathbf{x}) = (\delta T_b(\mathbf{x}) - \overline{\delta T}_b)/\overline{\delta T}_b \,, \tag{3.12}$$

where $\overline{\delta T}_b$ is a zero-mean quantity. In Fourier space, the 21-cm power spectrum $P_{21}(\mathbf{k})$ can be defined as the angle-averaged sum of the Fourier transform of the 21-cm brightness temperature fluctuation:

$$\langle \delta_{21}(\mathbf{k}_1)\delta^*_{21}(\mathbf{k}_2)\rangle = 2\pi^3\delta_D(\mathbf{k}_1 - \mathbf{k}_2)P_{21}(\mathbf{k}_1) \,, \tag{3.13}$$

where $\delta_{21}(\mathbf{k})$ is the Fourier transform of $\delta T_b(\mathbf{x})$ at comoving wavevector $\mathbf{k}$ , $\delta_D$ is the Dirac delta function, and angle brackets denote the spatial average. The 21-cm power spectrum in units of mK$^2$ can be written as:

$$\Delta^2_{21}(\mathbf{k}) = \bar{T}_b^2 \frac{k^3 P_{21}(\mathbf{k})}{2\pi^2} \,, \tag{3.14}$$

where $k^3P_{21}(\mathbf{k})/2\pi^2$ is the dimensionless power spectrum. The 21-cm brightness fluctuations can be written as a sum of different fluctuations to linear order, through

perturbative analysis (e.g. Barkana and Loeb 2005; Furlanetto, Peng Oh, and Briggs 2006; Santos, Cooray, and Knox 2005) as follows:

$$\delta_{21} = \beta_{\rm b}\delta_{\rm b} + \beta_x\delta_x + \beta_\alpha\delta_\alpha + \beta_T\delta_T - \delta_{\partial v} \,, \tag{3.15}$$

where $\delta_{\rm b}$ is the fluctuation in the underlying density field, $\delta_x$ is the fluctuation in the ionization fraction, $\delta_\alpha$ is the fluctuation in Ly-$\alpha$ coupling coefficient, $\delta_T$ is the fluctuation in gas temperature, and $\delta_{\partial v}$ is the fluctuation in the line-of-sight peculiar velocity gradient. Besides these terms, the cross-correlation terms also add to the 21-cm brightness temperature fluctuations. The power spectrum is shown in the bottom panel of Fig. 3.2 for two Fourier modes: $k = 0.1$ Mpc$^{-1}$ and 0.5 Mpc$^{-1}$. There are four important epochs in the evolution of the large scale (i.e. $k = 0.1$ Mpc$^{-1}$) 21-cm power spectrum. In early times before the stars appeared, the power spectrum traces the density field fluctuations. It reaches its peak at $z \sim 50$ and falls till $z \sim 30$. After $z \sim 30$ the radiation from the stars begins to propagate in the IGM, causing fluctuations in coupling and temperature. Therefore, the next peak in the power spectrum, at $z \sim 20$, is caused by the fluctuations in the Ly-$\alpha$ coupling coefficient. This is followed by temperature fluctuations during the EoH. The dip in the power spectrum between the Ly-$\alpha$ coupling peak and the heating peak is due to the cross-correlation terms between the density and ionization fields on large scales, which is not evident at medium scales such as $k = 0.5$ Mpc$^{-1}$. During the EoR the power spectrum traces the ionization fluctuations.

## 3.3 Beyond the power spectrum

As discussed before, the 21-cm power spectrum is an important observable used to measure the signal through observations. However, it has been shown in various works that the 21-cm signal is not entirely Gaussian during the EoR and EoH (e.g. Iliev et al. 2006; Mellema et al. 2006; Watkinson and Pritchard 2015; Majumdar et al. 2018; Ross et al. 2019). The spherically-averaged power spectrum is sufficient for measuring the signal on large scales in the early stages of reionization when the ionized bubbles are small in size. However in the later stages of reionization, as the bubbles grow in size, the PS does not completely capture the topology of reionization. Higher-order statistics can be useful for capturing the non-Gaussianity associated with the signal, among which a famous statistic is the bispectrum. It is the Fourier transform of the three-point correlation function and can be expressed

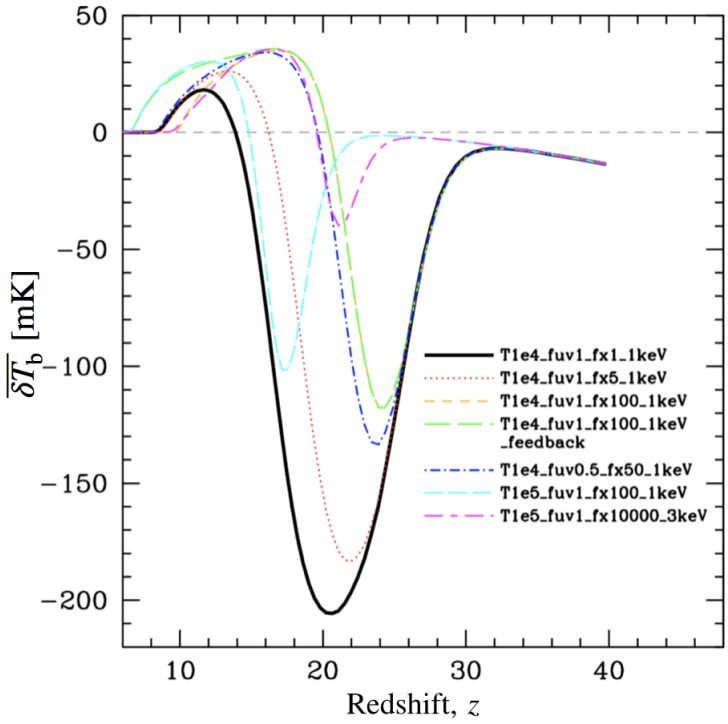


**Figure 3.3:** Redshift evolution of the global 21-cm brightness temperature for a range of parameters such as virial temperature (denoted by T), X-ray efficiency (fx), and UV efficiency (fuv), the mean energy of X-ray photons taken from the simulations of Mesinger, Ferrara, and Spiegel (2013). It is obvious how X-rays affect the timing and strength of heating. For example, a higher value of fx corresponds to a shallower and earlier absorption trough, keeping other parameters fixed.

as:

$$\langle \delta_{21}(\mathbf{k}_1)\delta_{21}(\mathbf{k}_2)\delta_{21}(\mathbf{k}_3)\rangle = 2\pi^3\delta_{\rm D}(\mathbf{k}_1-\mathbf{k}_2-\mathbf{k}_3)B_{21}(\mathbf{k}_1,\mathbf{k}_2,\mathbf{k}_3)\,. \tag{3.16}$$

The 21-cm bispectrum ($B_{21}$) thus measures the excess probability as a function of three spatial scales. As it involves three scales, it is common to simply its interpretation by using different configurations of scales (e.g. Lewis 2011; Watkinson et al. 2019). Even though the bispectrum carries additional information on the astrophysics of the 21-cm signal, it suffers from low signal-to-noise due to less number of k-modes, besides being difficult to visualize.

## 3.4 The 21-cm signal and IGM heating

As evident from eq. 3.7, the 21-cm signal is a significant probe of the thermal and ionization history of the Universe. It is sensitive to the properties of X-ray sources responsible for heating the IGM during the EoH (e.g. Pritchard and Furlanetto 2007; Mesinger, Ferrara, and Spiegel 2013; Pacucci et al. 2014; Fialkov, Barkana, and Visbal

2014). For example, Baek et al. (2010) performed fully radiative transfer simulations of the EoR and found out that the timing and duration of the transition of the 21-cm signal from absorption to emission depend on the types of sources of X-rays that heat the IGM. Mesinger, Ferrara, and Spiegel (2013) ran different large-box semi-numeric simulations of the 21-cm signal during the Dark Ages and up to reionization, by varying parameters such as the virial temperature of the hosting dark matter halos, X-ray efficiency and UV efficiency of stellar systems. The X-ray efficiency (fx) depends on the number of X-ray photons per stellar baryon and $f_*$, while UV efficiency (fuv) depends on the ionizing efficiency defined in eq. 2.9. As seen in Fig. 3.3, they found out that an increase in the X-ray efficiency corresponds to a shallower and earlier absorption trough, if other parameters such as UV-efficiency, virial temperature and mean X-ray photon energy are kept the same. Therefore, the timing and amplitude of the absorption trough of the 21-cm brightness temperature evolution can provide information on the X-ray sources. Fialkov et al. (2016) explored how the unresolved cosmic X-ray background along with the 21-cm signal constrain different types of high-redshift X-ray sources. Pacucci et al. (2014) studied the impact of X-ray SEDs on the 21-cm signal over a range of X-ray spectral index, $\alpha \approx 0.8$ – 0.3. Fig. 3.4 shows the slices through the 21-cm brightness temperature field for a hard (left panel) and a soft (right panel) X-ray SED, at $z \sim 16$, which corresponds to the redshift at which the large-scale (i.e. $k = 0.2$ Mpc$^{-1}$) 21-cm power spectrum peaks. Since the hard X-ray photons have longer mean free paths than the soft photons, they result in more uniform heating. Fig. 3.5 shows the corresponding redshift evolution of the large-scale 21-cm power spectrum (at $k = 0.2$ Mpc$^{-1}$). Keeping other parameters fixed, it can be observed that a soft SED corresponds to an amplitude of up to $\sim 3$ times larger than that corresponding to a hard SED. Ross et al. (2017) discovered in their large volume fully radiative transfer simulations that the hard, energetic X-ray photons correspond to an earlier and extended transition from absorption to emission of the signal. Therefore, the information on X-ray SED is imprinted in the signal, making it a robust probe of the properties of the early galaxies.

## 3.5 Observing the signal

The fundamental observable of a radio interferometer is the visibility function ($V$). An interferometer samples the visibility of a sky image in $u, v, w$ coordinates, which

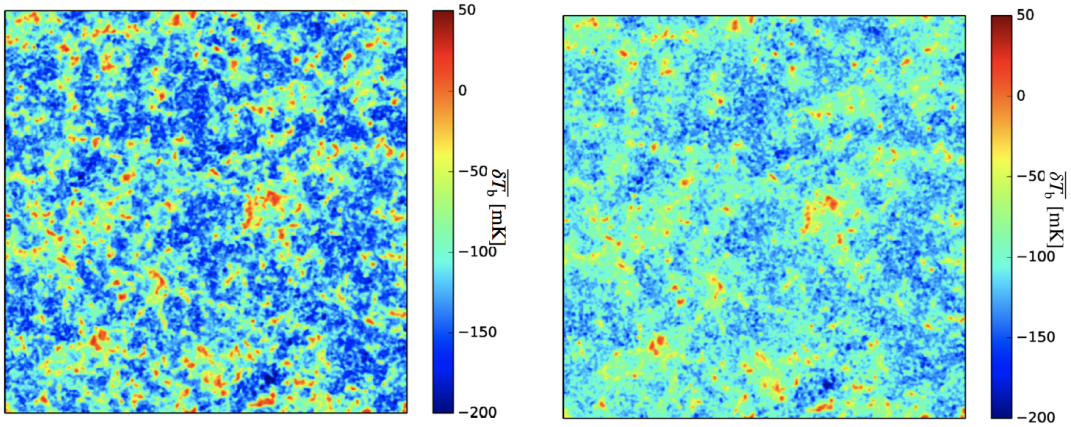


**Figure 3.4:** Slices through 21-cm brightness temperature field for soft X-ray SED (*left panel*) and hard X-ray SED (*right panel*) at $z \sim 16$ where large-scale ($k = 0.2$ Mpc$^{-1}$) power spectrum peaks, from the simulations of Pacucci et al. (2014). A soft X-ray SED results in more inhomogeneous heating as compared to a hard SED.

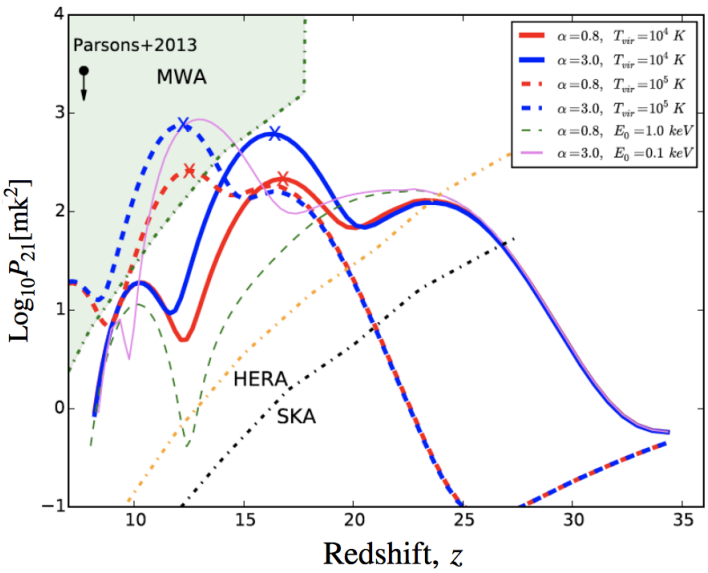


**Figure 3.5:** Redshift evolution of the large-scale ($k = 0.2$ Mpc$^{-1}$) 21-cm power spectrum computed with hard (red) and soft (blue) X-ray SEDs, taken from Pacucci et al. (2014). $T_{\rm vir}$ is the virial temperature of the host halo and $E_0$ is the minimum energy of X-ray photons that escape into the IGM. Green region marks the $2\sigma$ upper limits on the PS from PAPER (Parsons et al. 2014). A soft SED results in a larger PS amplitude as compared to a hard SED, if other parameters remain fixed.

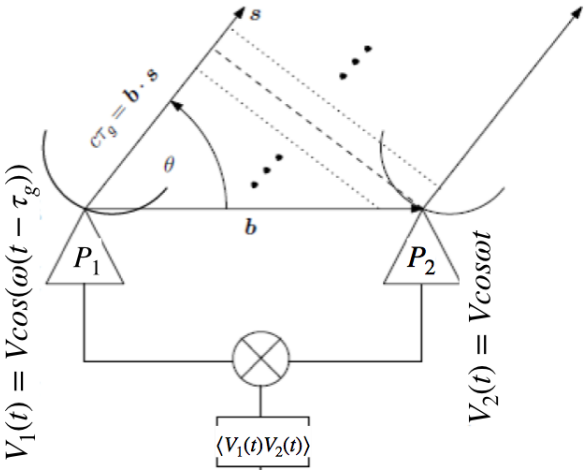


**Figure 3.6:** The geometry of a simple interferometer made of two antennae with baseline vector **b**. The correlator contains the response of the visibilities of two incident waves with a phase delay of $\tau_g$.

are the projections of the baseline vector (**b**). The visibility for a sky image source with specific intensity $I$ with angular coordinates $l$, $m$ is given by the following equation (Parsons et al. 2012):

$$V(u,v,w,\nu) = \int \frac{\mathrm{d}l\mathrm{d}m}{\sqrt{1-l^2-m^2}} A(l,m,\nu) I(l,m,\nu) e^{-2\pi i(ul+vm+w[\sqrt{1-l^2-m^2}-1])} , \tag{3.17}$$

where $\nu$ is the spectral frequency, $I = 2k_B T_b/\lambda^2$ is the specific intensity, $T_b$ is the brightness temperature, $\lambda$ is the mean wavelength, and $A(l,m,v)$ is a window function which describes the field-of-view and bandpass response of an interferometer pair. If an image is in a small area of the sky near the phase center, then using flat-sky approximation (Clark 1999) angular coordinates $l$ and $m$ can be approximated to zero. The Fourier transform of the visibility function can then be written as:

$$\tilde{V}(u,v,\eta) = \int \mathrm{d}l\mathrm{d}m\mathrm{d}\nu A(l,m,\nu) I(l,m,\nu) e^{-2\pi i(ul+vm+\eta\nu)} . \tag{3.18}$$

Following the formalism given in Parsons et al. (2012), using a top-hat window function, the 3D 21-cm power spectrum can be computed from visibility as follows:

$$P_{21}(\mathbf{k}) \approx \tilde{V}^2 \left(\frac{\lambda^2}{2k_B}\right)^2 \frac{X^2 Y}{\Omega B} , \tag{3.19}$$

where $B$ is the observing bandwidth, $X$, $Y$ are conversion factors used for converting angle and frequency into the comoving distance, and $\Omega$ is the solid angle of power primary beam squared divided by the square of the power primary beam. The vector

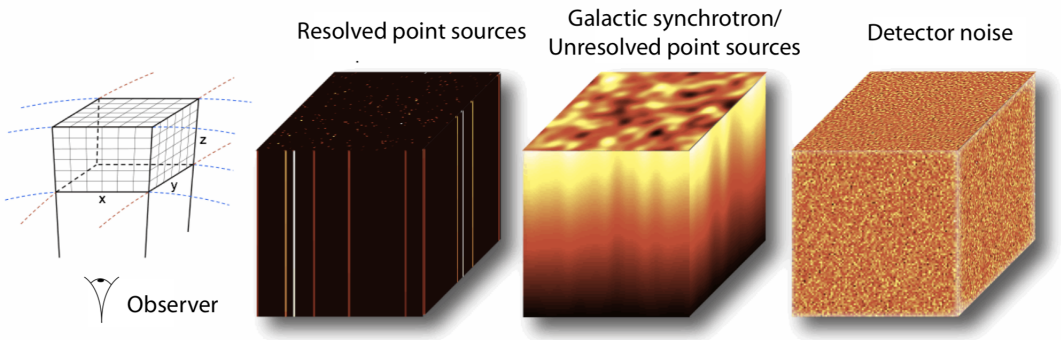


**Figure 3.7:** The 21-cm signal is contaminated by foregrounds as well as noise of the instrument used for observation. Illustration taken from Liu and Tegmark (2011).

**k** has a projection $k_\perp$ in the sky plane ($k_x$, $k_y$) and $k_{||}$ along the direction of line-of-sight (i.e. frequency axis). As shown in Fig. 3.7, the 21-cm signal is accompanied by foregrounds and detector noise. In the following subsections, I discuss various challenges faced while observing the signal and how to tackle them.

### 3.5.1 Foregrounds

The 21-cm signal is contaminated by various foregrounds at low frequencies ($\nu \sim 100 - 200$ MHz) (Shaver et al. 1999; Di Matteo et al. 2002; Oh and Mack 2003). The foreground sources can be broadly divided into resolved and unresolved point sources. Fig. 3.8 shows the angular power spectra of different foregrounds along with the 21-cm signal. The major contributor to foregrounds is the diffuse galactic synchrotron radiation (e.g. Shaver et al. 1999; Gnedin and Shaver 2004). This radiation is produced by the cosmic ray electrons propagating in the magnetic fields of the Milky Way (Ginzburg and Syrovatsk 1969). It dominates the sky at low frequencies with strength being $\sim$ 4 orders of magnitude above the 21-cm signal ($\sim$ 10 mK) at EoR ($\sim$ 150 MHz) Zaldarriaga, Furlanetto, and Hernquist 2004; Morales and Hewitt 2004. Other significant contaminants are extragalactic continuum sources, such as normal galaxies, AGNs and radio galaxies (Di Matteo et al. 2002; Santos, Cooray, and Knox 2005). The free-free emission from the sources of reionization can also contribute to foregrounds Oh and Mack 2003 at low frequencies. These extragalactic sources can create brightness temperature fluctuations larger than those associated with the 21-cm signal by one to two orders of magnitude.

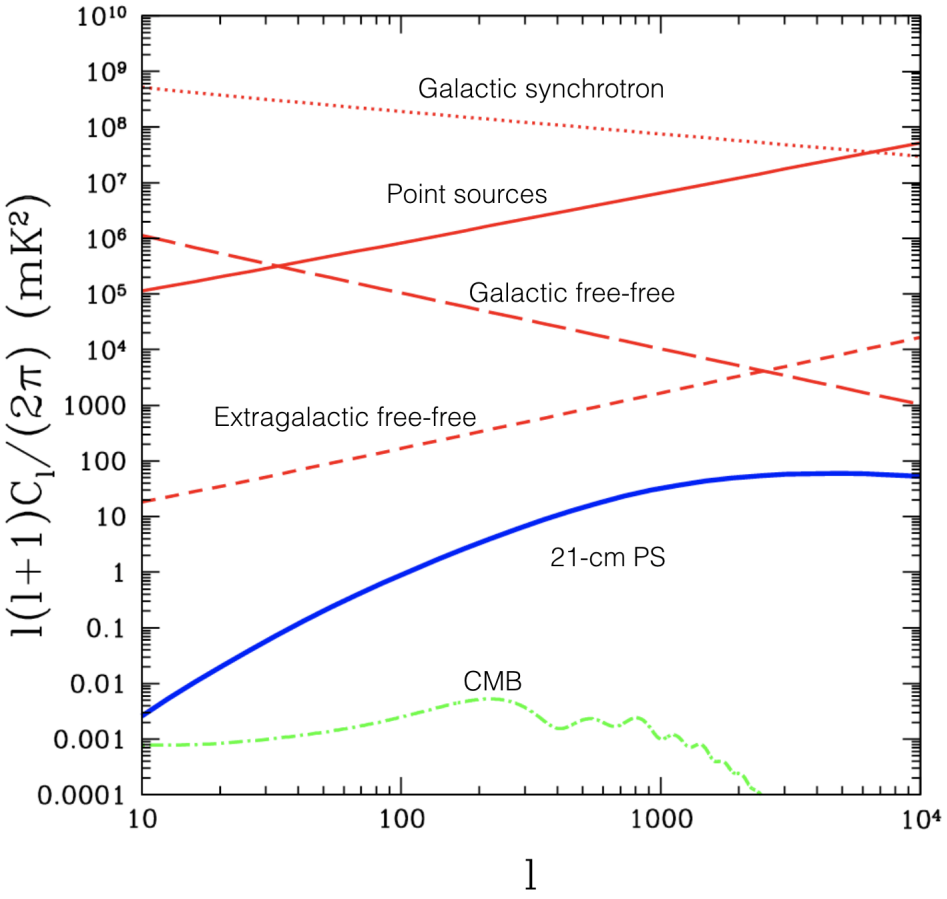


**Figure 3.8:** The 21-cm angular power spectrum at $z = 9.2$ ($\nu = 140$ MHz) shown as the thick blue line, along with various foregrounds labelled with their curves, taken from Santos, Cooray, and Knox (2005). The amplitude of fluctuations of foregrounds especially galactic synchrotron is much stronger than the 21-cm signal.

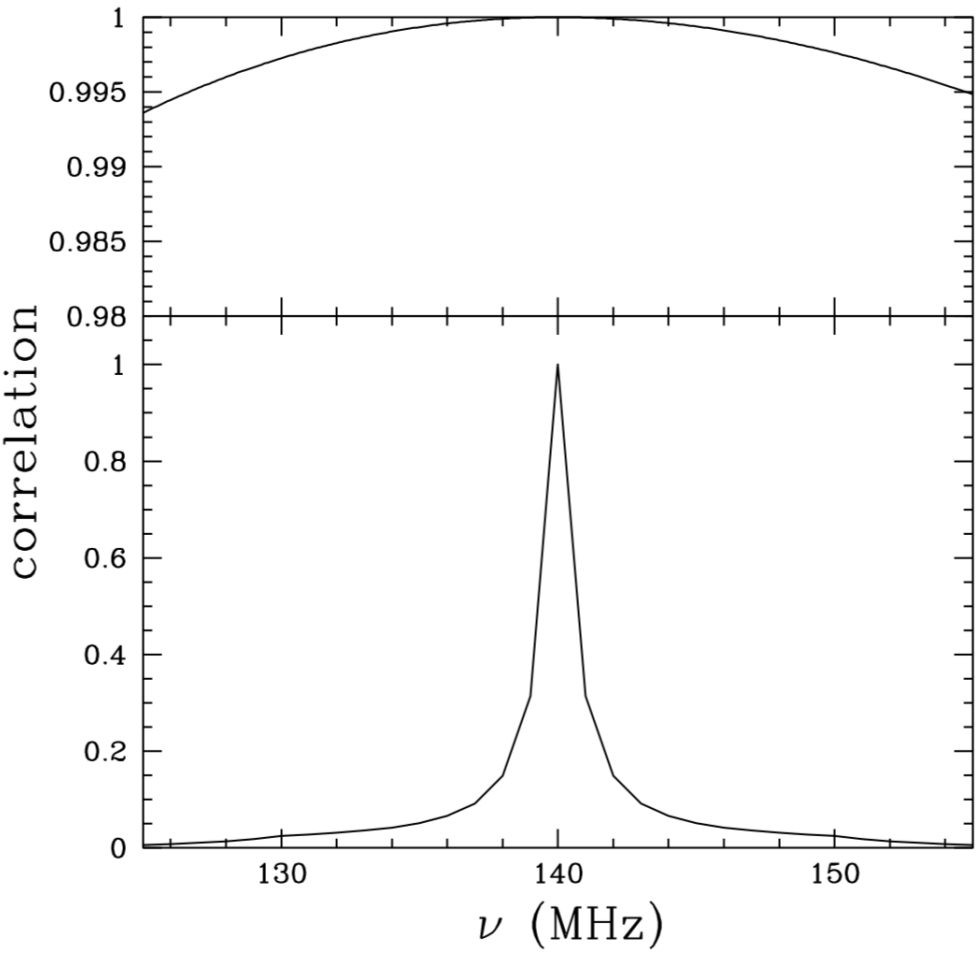


**Figure 3.9:** The frequency cross-correlation for the 21-cm signal and foregrounds at $l = 1000$ shown in bottom and top panels respectively, from Santos, Cooray, and Knox (2005). Using a multifrequency analysis, the foregrounds can be subtracted from the observed data.

**How to deal with foregrounds?**

For a robust measurement of the 21-cm signal, it is of utmost importance that the foregrounds are suppressed. There are two common ways in which foregrounds can be mitigated – foreground subtraction and foreground avoidance. The former technique relies on the spectral smoothness of foregrounds. Even though the exact form of all possible foregrounds is not known, the known foregrounds are nearly smooth over a wide range of frequencies. Various studies have found that these foregrounds have a nearly featureless power law with small variations in spectral index with direction and frequency (e.g. Rogers and Bowman 2008). This property can be utilized to separate out the foregrounds from the signal. For example, Santos, Cooray, and Knox (2005) employed a multi-frequency technique to study the frequency correlations of foregrounds. This is shown in Fig. 3.9. The top panel shows the frequency cross-correlation for foregrounds while the bottom panel shows the cross-correlation for the 21-cm signal, both at $l = 1000$ or $\Delta\nu = 1$ MHz. It is clear from the figure that the foregrounds have a much stronger correlation than the signal. Therefore, it is feasible to remove them from the 21-cm signal through multi-frequency analysis (also see Shaver et al. 1999; Di Matteo et al. 2002; Zaldarriaga, Furlanetto, and Hernquist 2004) by modelling the foregrounds and subtracting them off the observed data. Another method to get rid of foregrounds is foreground avoidance. As shown in eq. 3.19, the measured 21-cm power spectrum has both spatial ($k_\perp = \sqrt{k_x^2 + k_y^2}$) and frequency axes ($k_{||}$). Fig. 3.10 shows the power spectrum of data observed in four hours with PAPER (Pober et al. 2013a) as a function of cylindrical wavenumbers, $k_\perp$ and $k_{||}$. At the lowest $k_{||}$, the foregrounds are the strongest. However, with an increase in $k_\perp$, the foregrounds leak into even larger values of $k_{||}$. This is because of the intrinsic chromatic nature of interferometry. The fringe pattern obtained from interferometers depends on wavelength, coupling $k_\perp$ to $k_{||}$. This isolates the foregrounds to a ´wedge-like‘ region, making it possible to observe the 21-cm signal in the region outside the wedge where the foregrounds decrease by up to four orders of magnitude (also see Datta, Bowman, and Carilli 2010; Morales et al. 2012; Vedantham, Udaya Shankar, and Subrahmanyan 2012).

### 3.5.2 Detector noise

Besides foregrounds, an observation is also contaminated by the noise of the detector. The system temperature ($T_{\rm sys}$), therefore, contains detector noise besides the

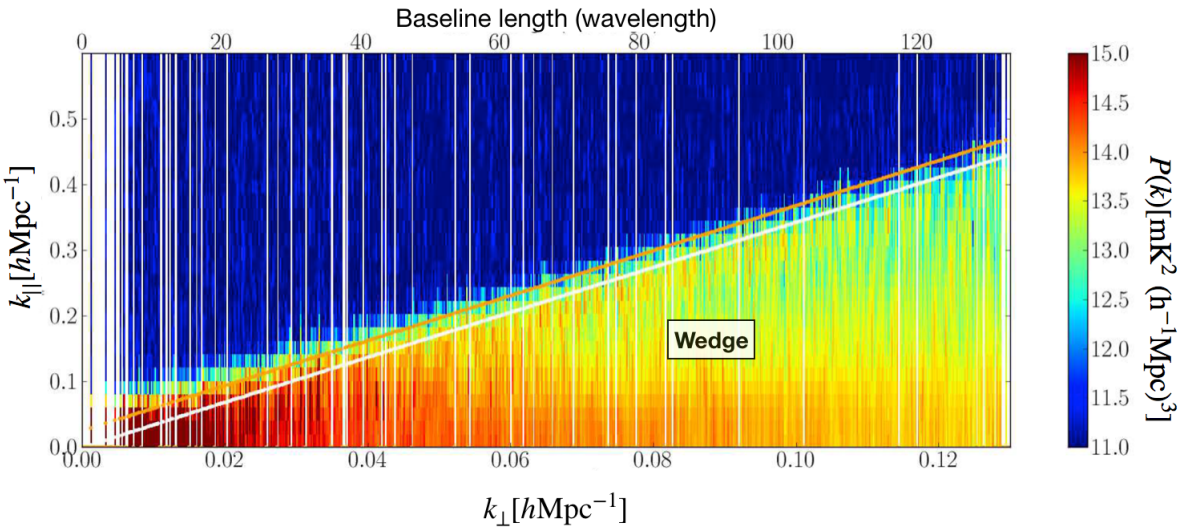


**Figure 3.10:** Logarithmic power spectrum of data observed with PAPER in 2-D space, taken from Pober et al. (2013a). The white line marks the horizon limit and the orange line is 50 ns beyond it. The foregrounds are limited to a wedge-shaped region.

cosmological signal, foregrounds, atmosphere, etc. This is caused by the thermal motion of electrons which can induce a power input into the detector. This white noise has a non-zero rms brightness temperature ($T_{\mathrm{N,\,rms}}$). The corresponding rms amplitude of visibility $V_N$ is provided by the following equation (Parsons et al. 2012):

$$\tilde{V}_{\mathrm{N}} = \frac{2k_{\mathrm{B}}T_{\mathrm{N,\,rms}}}{\lambda^2}\Omega B\ . \tag{3.20}$$

Inserting the above value of visibility into eq. 3.19, we can write the power spectrum of the thermal noise as:

$$P_{\mathrm{N}}(k) \approx X^2 Y \Omega B T^2_{\mathrm{N,\,rms}}(u,v,\eta)\ . \tag{3.21}$$

In integration time $t$, there is $2Bt$ number of independent measurements of noise for a particular k-mode. Therefore, if the thermal noise is considered to be Gaussian, then $T^2_{\mathrm{N,\,rms}} = T^2_{\mathrm{sys}}/Bt$. The eq. 3.21 can then be reduced to:

$$P_{\mathrm{N}}(k) \approx X^2 Y \frac{\Omega}{2t} T^2_{\mathrm{sys}}\ . \tag{3.22}$$

Similarly, the sensitivity to any k-mode of dimensionless power spectrum of noise can be expressed as:

$$\Delta^2_{\mathrm{N}}(k) \approx X^2 Y \frac{\Omega}{2t}\frac{k^3}{2\pi^2} T^2_{\mathrm{sys}}\ . \tag{3.23}$$


**Figure 3.11:** Several radio-interferometers set up to detect the 21-cm signal. Picture taken from Koopmans et al. (2019) review.

### 3.5.3 21-cm radio-interferometers

Various ground-based radio interferometers have been set up to capture the 21-cm signal. Efforts such as GMRT, MWA, LOFAR, HERA, SKA, etc. aim to observe the power spectrum whereas SARAS, EDGES, etc. aim to detect the sky-averaged signal.

*The Precision Array to Probe the Epoch of Reionization*[1], PAPER (Parsons et al. (2010) and Parsons et al. (2014)) was a first-generation interferometer set up in the Karoo desert of South Africa with the aim to observe the signal during the EoR. Even though it has been decommissioned, it did explore the associated foreground emission and paved the way for the foreground avoidance technique. *Murchison Widefield Array*[2] (MWA; Tingay et al. 2013) is another first-generation telescope with a large field of view, constructed in the Western Australian desert. It has provided some upper limits on the 21-cm power spectrum (Beardsley et al. (2016)) at $z \sim 6 - 9$. *The Hydrogen Epoch of Reionization Array*[3] (DeBoer et al. 2017) is a second-generation interferometer currently under construction in the Karoo desert of South Africa. It follows the same approach as PAPER but has improved sensitivity and uses foreground

[1] http://eor.berkeley.edu
[2] https://www.mwatelescope.org
[3] https://reionization.org

avoidance methodology. The first phase of HERA has recently published some results in which their team provided upper limits on the power spectrum at $z \sim 8$ and 10 ((HERA Collaboration et al., 2021a)). They also provided constraints on the X-ray $L_X$/SFR which I will discuss in Chapter 5 ((HERA Collaboration et al., 2021b)). *The Low-Frequency Array*[4] (LOFAR; van Haarlem et al. 2013) is an interferometer with a large field of view located in the Netherlands with the aim of detecting the 21-cm power spectrum from the EoR. It also works as a pathfinder to the *Square Kilometer Array*. It has provided upper limits on the power spectrum from the EoR at $z \sim 10$ (Patil et al. 2017) as well as the CD at $z \sim 25$ (Gehlot et al. 2019). *Experiment to Detect the Global EoR Signature*[5] or EDGES is a US-led experiment situated in Western Australia. The experiment aims to detect the signal from the CD up to the EoR. In 2018, the EDGES group reported the detection of the signal at $z \sim 17$, with the absorption trough being more than two orders of magnitude greater than the theoretical prediction (Bowman et al. 2018). This led to a series of research works on various theories such as the interaction between baryons and dark matter particles (Barkana 2018), the possibility of exotic astrophysics, etc. (Ewall-Wice et al. 2018). *Shaped Antennas to measure the background Radio Spectrum* [6] or SARAS is an experiment led by Raman Research Institute in India with the aim to detect the sky-averaged signal over the frequency range of 50–200 MHz. It has similar sensitivity as EDGES. In a recent paper, they cross-verified the EDGES signal but did not find any evidence of it, thereby refuting the reported claim of detection of the 21-cm absorption signal claimed by EDGES. (Singh et al. 2022).

The most promising among all state-of-the-art observational efforts is the SKA[7]. It is an intergovernmental effort being constructed in South Africa and Australia. With a large collecting area and sensitivity an order of magnitude larger than its precursors, it aims to detect the 21-cm signal over a wide frequency range of 50 MHz to 14 GHz in three phases (for a recent review see, e.g., Mesinger 2019).

After having covered various aspects of the 21-cm signal, I move towards the next chapters in which I will discuss how we model the 21-cm signal in our simulations with emphasis on the X-ray modeling during the Cosmic Dawn.

[4] http://www.lofar.org
[5] http://loco.lab.asu.edu/edges
[6] http://www.rri.res.in/DISTORTION/index.html
[7] https://www.skatelescope.org

# Chapter 4

# The optimum simulation box size for modelling the 21-cm signal

In this chapter, we quantify how large a simulation needs to be to capture the cosmic 21-cm signal. Using the public simulation code `21cmFAST` (e.g. Mesinger and Furlanetto 2007; Mesinger, Furlanetto, and Cen 2011), we perform a convergence study of the 21-cm power spectrum summary statistic. We begin the chapter with a discussion on the motivation behind this work. We explain what are the missing wavemodes with illustrations from previous works in this direction. In §4.2 and §4.3, we explain in detail our simulation tool and astrophysical model respectively. In §4.4, we explain how we model the telescope noise using a mock 1000h observation from the upcoming SKA-phase 1 telescope, in order to quantify the signal convergence. Then, in §4.5 we present our main results. §4.6 contains the conclusions of our work. Appendix A contains results for a different galaxy model, consistent with our fiducial results. We assume a standard ΛCDM cosmology with the following cosmological parameters: $h = 0.678$, $\Omega_{\rm m} = 0.308$, $\Omega_{\rm b} = 0.0484$, $\Omega_\Lambda = 0.692$, $\sigma_8 = 0.815, n_{\rm s} = 0.968$ based on result from Planck Collaboration et al. (2016a).

## 4.1 The missing wavemodes

As we studied in Chapter 3, the 21-cm signal is sensitive to the thermal and ionization states of the IGM. During the CD and EoR, the properties of the IGM gas were governed by radiation emitted by rare, newborn galaxies. These first sources of UV and X-ray photons were hosted by the extremely rare and biased halos that formed in the high sigma peaks of the initial density field. Therefore, the abundance of the galaxies hosted by such halos is modulated by long-wavelength modes of the density field. This so-called "peak-patch formalism" can be better understood with the help of the illustration shown in Fig. 4.1.

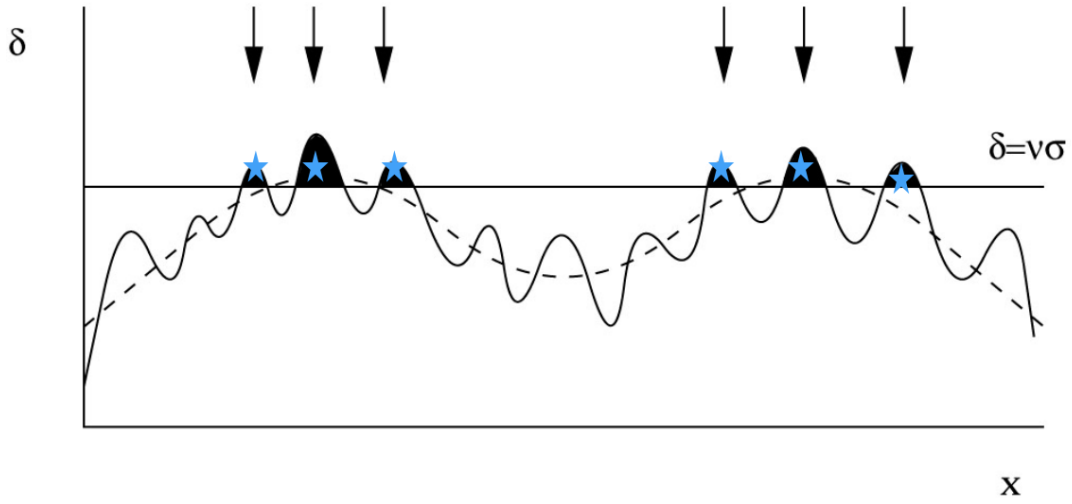


**Figure 4.1:** Peak-background split: a density fluctuation, $\delta$ made of two modes. The horizontal line shows the barrier for the collapse of halos with densities equal to or above a certain threshold forming in black regions. The abundance of the galaxies hosted by these halos is thus modulated by the long-wavelength modes. Figure adapted from Kaiser (1984).

In a linear regime, the density fluctuation $\delta(\mathbf{x})$ can be split into two components: a small-scale fluctuation, and a large-scale fluctuation. The regions which are overdense on large scales, get additional support from the large-wavelength modes in order to cross the overdensity barrier ($\delta = \nu\sigma$) required to form halos. This resulting modulation of galaxy formation is amplified at high redshifts due to the exponential cut-off in the abundance of massive halos toward high redshifts (see Fig. 4.2).

Using analytic, conditional halo mass functions Barkana and Loeb (2004) demonstrated how small-box simulations underestimate the amount of structure present in the Universe. In a cosmological simulation of size $R$ per side, the cosmic mean density and variance on scale $R$ are set to zero. This excludes the cosmic scatter in the number density of halos in different regions of the Universe. This underestimation of structure results in an EoR which occurs too rapidly, too homogeneously, and too late.

Barkana and Loeb (2004) further quantified this numerical bias and cosmic scatter in terms of "redshift bias". If a region at redshift $z$ has a mean overdensity $\delta_R$, its actual collapse fraction could be equal to the collapse fraction evaluated at another redshift $z + \Delta z$:

$$\frac{\Delta z}{z} = \frac{\bar{\delta}_R}{\delta_0} - (1+z)\left[1 - \sqrt{1 - \frac{\delta_R^2}{\delta_{R_{\rm min}}^2}}\right] . \tag{4.1}$$

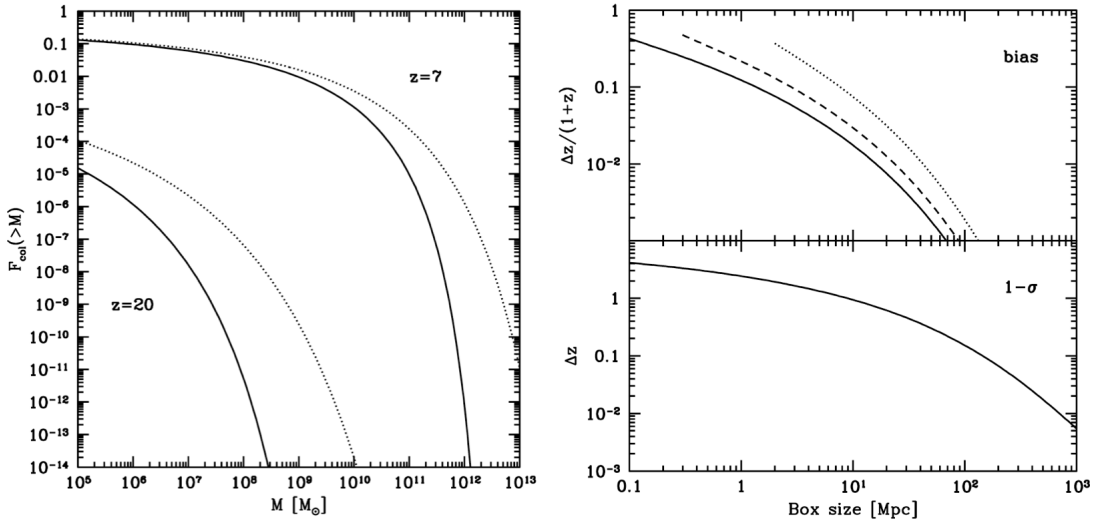


**Figure 4.2:** *Left*: Numerical bias in the collapse fraction of halos in simulation boxes of size 1 Mpc per side at $z = 20$ (*lower curves*) and 1 Mpc per side at $z = 20$ (*upper curves*). Dotted and solid curves represent the true and biased distribution respectively. *Right*: Numerical bias (top) for different halo masses (solid; $7 \times 10^5$ $M_\odot$, dashed; $10^8$ $M_\odot$ and dotted; $3 \times 10^{10}$ $M_\odot$) and cosmic scatter (bottom) expressed in form of shift in redshift vs simulation box size. The shift in 1-$\sigma$ scatter around the biased value of the mean collapse fraction is independent of the halo mass. Both figures are taken from Barkana and Loeb (2004).

This shift in redshift as a function of simulation box size is displayed in the right panel of Fig. 4.2. In the top panel, the numerical bias for three different halo masses is shown, along with 1-$\sigma$ scatter around the biased value of the mean collapse fraction in the bottom panel. As obvious, the redshift bias decreases with an increase in the size of the simulation box. Therefore, we can see how the long-wavelength modes can cause a scatter in the relevant redshifts during the EoR which the small-size simulations are not able to capture.

The effect of missing wavelength modes on reionization was further modelled by Iliev et al. (2014). They performed N-body + radiative-transfer (RT) simulations of the 21-cm signal for two simulation boxes of 100 $h^{-1}$ per side, having the same resolution but different initial conditions. They compared the results of these simulations with a large box (425 $h^{-1}$ Mpc per side). The dimensionless power spectra for the density field at $z = 6$ are shown in the left plot of Fig. 4.3. At the smallest scales, the two small simulation boxes yield more power than the large box due to higher resolution. However, at large scales (i.e. $k \lesssim 0.06\ h^{-1}$ Mpc$^{-1}$), the large box carries additional power, with the density fluctuations missing in the case of small boxes. Moreover, even though the smaller simulation boxes have the same resolution and

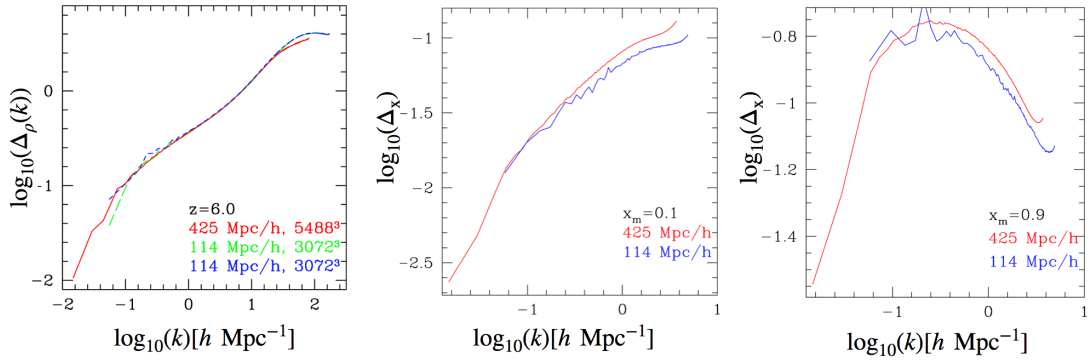


**Figure 4.3:** *Left*: Dimensionless power spectrum of density field for the boxes at z=6. *Middle* and *Right*: Ionization power spectra for the boxes at ionization fraction by mass, $x_{\rm m} = 0.1$ and $x_{\rm m} = 0.9$ respectively. Figure taken from RT simulations of Iliev et al. (2014).

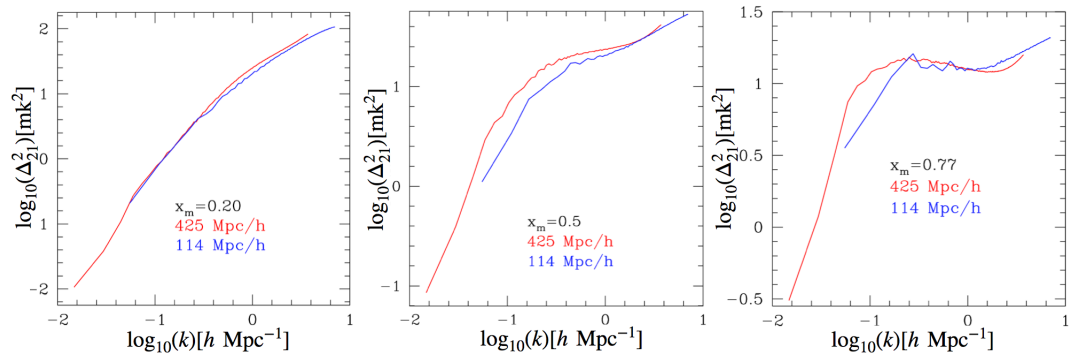


**Figure 4.4:** 21-cm power spectrum for ionization fraction by mass, $x_{\rm m} = 0.20, 0.5$ and $0.77$. Figure taken from Iliev et al. (2014).

size, they suffer from cosmic variance on large scales. The middle and plots of Fig. 4.3 show the ionization field power spectra at two different stages of reionization. As usual, the large simulation box carries more power than the small box.

Fig. 4.4 shows the corresponding 21-cm power spectra at three different stages of reionization. At the beginning of reionization, the power spectra from both simulations are similar to each other till the scales of overlap. However, as the reionization proceeds, the ionized bubbles grow much bigger in size in the large box as compared to the small ones. This increases the ionization fluctuations in the large box, as can be observed in the middle and right plots of the figure. They concluded that the simulations of box size $\gtrsim$ 200 Mpc per side are needed in order to find convergence in the 21-cm power spectrum during the EoR.

But what about the earlier stages of the Cosmic Dawn? These epochs are driven by soft UV and X-ray photons sourced by even more biased galaxies. Unlike ionizing photons, their long mean free path photons are capable of interacting with the IGM

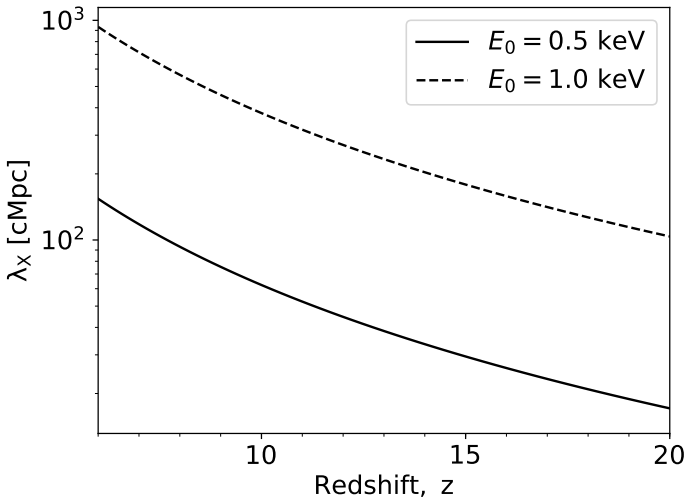


**Figure 4.5:** The mean free path of X-ray photons through a mean density, neutral IGM. Curves correspond to photons of energies 0.5 and 1.0 keV (c.f.4.2).

over a wide range of scales. For example, the mean free path of X-rays in the high-$z$ IGM is a strong function of the photon energy $E_X$ (e.g. McQuinn 2012):

$$\lambda_x \approx \bar{x}_{\rm HI}^{-1} \left(\frac{E_X}{300{\rm eV}}\right)^{2.6} \left(\frac{1+z}{10}\right)^{-2} {\rm cMpc}\,, \tag{4.2}$$

where $\bar{x}_{\rm HI}^{-1}$ is the average neutral fraction of the IGM. As seen in Fig. 4.5, $\lambda_X$ can be of the order of hundreds or thousands of Mpcs during CD, depending upon the energy threshold of X-ray photons escaping from the IGM. The corresponding large range of relevant scales, modulated by the highly biased first galaxies, results in large-scale ($k \lesssim 0.1$ Mpc$^{-1}$) fluctuations in the 21-cm power spectrum during the CD (e.g. Pritchard and Furlanetto 2007). This suggests that we might need even larger simulation boxes to model the CD.

After discussing the motivation for the work in this chapter, I proceed with a detailed discussion of the methodology of our simulations.

## 4.2 Simulation methodology

As we have noticed in the previous sections, the correct interpretation of the 21-cm signal requires a large range of scales and a large parameter space. For example, we need simulation boxes with lengths of the order of tens to hundreds of Mpcs for properly studying the IGM during the EoH and EoR, making it computationally very expensive to simulate the signal. Therefore, we use a semi-numeric code,

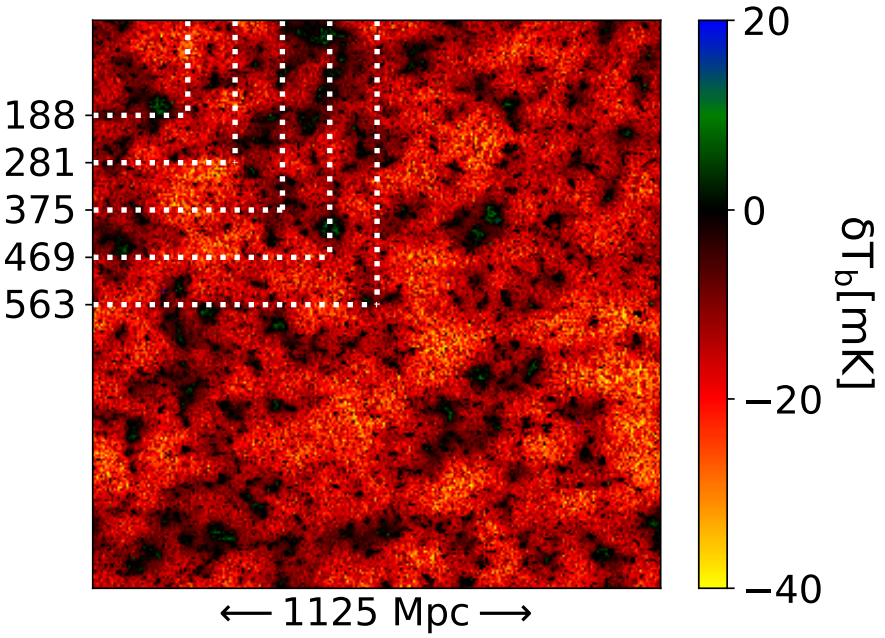


**Figure 4.6:** Slice-plot of 21-cm brightness temperature fluctuations for reference box at z=10.04 using `21cmFAST`. Figure taken from Kaur, Gillet, and Mesinger (2020).

`21cmFAST`, a public tool used for efficiently simulating the 21-cm signal. It implements certain analytical approximations for computing the properties of the IGM, which are discussed below.

### 4.2.1 Density, velocity and ionization fields

In `21cmFAST`, the initial conditions for density and velocity fields are generated in Lagrangian space from a high-resolution Gaussian field. The fields are smoothed onto a lower resolution grid and evolved according to the second-order Lagrangian perturbation theory (e.g. Scoccimarro 1998).

`21cmFAST` employs semi-numeric techniques to generate ionization fields. For identifying the ionized regions, it implements FFRT algorithm (Zahn et al. 2011) based on the excursion-set formalism from Furlanetto, Zaldarriaga, and Hernquist (2004), a method similar to calculating the Press-Schechter collapsed fraction (Lacey and Cole 1993). In this approach, the ionized regions are identified at different filtering scales, starting from a maximum scale and then going towards smaller scales till the scale equal to cell size ($R_{\rm cell}$) is achieved.

While reionizing the IGM, an ionizing photon can pass through sinks which are the HII regions with high column densities. These recombining systems can deplete the ionizing photons, thus impacting reionization (e.g. Miralda-Escudé, Haehnelt,

and Rees 2000; Ciardi et al. 2006; Kaurov and Gnedin 2014). The size of such self-shielded systems is 10 proper kpc (e.g. Schaye 2001), while the size of numerical simulations of EoR is of the order of hundreds of comoving Mpcs. Therefore, the inhomogenous recombinations can not be studied with numeric simulations of reionization due to the large dynamical range of scales required. These recombinations can be inhomogeneous as they are sensitive to the local density and radiation field.

`21cmFAST` makes use of a sub-grid model from Sobacchi and Mesinger (2014) to incorporate these recombinations. The model also includes reionization feedback from the star formation on sources and sinks. Each simulation cell at a location $\mathbf{x}$ and redshift $z$ computes the hydrogen recombination rate as follows:

$$\frac{\mathrm{d}n_{\rm rec}}{\mathrm{d}t}(\mathbf{x},z) = \bar{n}_{\rm H}\alpha_{\rm B}\Delta_{\rm cell}^{-1}\int_0^{180}[1-x_{\rm HI}]^2 P_{\rm V}\Delta^2\mathrm{d}\Delta\,, \tag{4.3}$$

where $\Delta_{\rm cell} = 1+\delta_{\rm nl}$ is the overdensity on the size of simulation cell, $\Delta = n/\bar{n}$ is the sub-grid overdensity, $P_{\rm V}(\Delta,\delta_{\rm cell},z)$ is the volume-averaged gas density distribution. It uses the functional form given by Miralda-Escudé, Haehnelt, and Rees (2000) and is adjusted for $\Delta_{\rm cell}$.$\alpha_{\rm B}$ is the case-B recombination coefficient at temperature of $10^4$ K, and $x_{\rm HI}(\Delta,\Gamma,z)$ is the neutral fraction at the overdensity $\Delta$ attenuated by the local , inhomogeneous ionizing background $\Gamma$. The attenuation is calculated analytically using Rahmati et al. (2013). The upper limit of the integral is motivated by the mean density of virialized halos in the spherical collapse model. Then the total number of recombinations per baryon, averaged over smoothing scale R is given by:

$$\bar{n}_{\rm rec}(\mathbf{x},z) = \left\langle \int_{z_{\rm ion}}^{z} \frac{\mathrm{d}n_{\rm rec}}{\mathrm{d}t}\frac{\mathrm{d}t}{\mathrm{d}z}\mathrm{d}z \right\rangle_R\,, \tag{4.4}$$

where $z_{\rm ion}$ is the redshift at which the cell was first ionized. `21cmFAST` thus marks a cell as "ionized" by comparing the number of photons in a region of scale $R$ with the number of baryons plus the average cumulative number of recombinations as follows:

$$\bar{n}_{\rm ion}(\mathbf{x},z) \gtrsim (1+\bar{n}_{\rm rec})(1-\bar{x}_{\rm e})\,, \tag{4.5}$$

where $\bar{x}_{\rm e} = 1-\bar{x}_{\rm HI}$ is the average ionization fraction.

### 4.2.2 X-ray background

The X-ray specific intensity (in units of erg s$^{-1}$ keV$^{-1}$ cm$^{-2}$ sr$^{-1}$) for photons with energy $E_{\rm X}$, as seen by a gas element at position $\mathbf{x}$ and redshift $z$ is given by:

$$J(\mathbf{x},z,E_{\rm X}) = \frac{(1+z)^3}{4\pi}\int_z^{\infty}\mathrm{d}z'\frac{c\mathrm{d}t}{\mathrm{d}z}\epsilon_{{\rm X},\nu}(z')e^{-\tau(z,z',E_{\rm X})}\,. \tag{4.6}$$

Here $\epsilon_{X,\nu}$ is the *specific* X-ray emissivity, evaluated in the rest frame $E_0 = E_X(1+z')/(1+z)$, and the term $\exp[-\tau(z,z',E_X)]$ accounts for attenuation by hydrogen and helium through a two-phased IGM between $z$ and $z'$ (see Mesinger, Furlanetto, and Cen (2011) for more details).

The comoving, soft-band X-ray emissivity (in erg s$^{-1}$ Mpc$^{-3}$) is computed as:

$$\epsilon_X(z) = \int_0^\infty \mathrm{d}M_\mathrm{h} \frac{\mathrm{d}n}{\mathrm{d}M_\mathrm{h}} f_\mathrm{duty} \dot{M}_* \frac{L_X}{\mathrm{SFR}} \,. \tag{4.7}$$

Here, a redshift-independent duty cycle, $f_\mathrm{duty} = \mathrm{e}^{-(M_\mathrm{turn}/M_\mathrm{h})}$ is used to account for lack or suppression in star-formation in halos of mass less than a turnover mass ($M_\mathrm{turn}$) (e.g. Hui and Gnedin 1997; Barkana and Loeb 2001; Springel and Hernquist 2003; Mesinger and Dijkstra 2008). $L_X/\mathrm{SFR}$ is the galaxy-integrated X-ray luminosity per star-formation rate, a term introduced in the discussion of HMXBs in 2. $L_X/\mathrm{SFR}$ is assumed that the X-ray spectral energy distribution (SED) follows a power law, i.e. $L_X \propto E_X^{-1}$, and a low energy cut-off of $E_0$ set by the typical opacity of the ISM of high redshift galaxies (e.g. Fragos et al. 2013b; Das et al. 2017). This X-ray emission is expected to come from either HMXBs or (less likely) the hot ISM. As both of these sources scale with the SFR of the galaxy, the X-ray SED can be normalized by the soft-band (i.e. $E_0 < E_X < 2$ keV) X-ray luminosity per star-formation rate as follows:

$$L_{X[E_0-2\text{ keV}]}/\mathrm{SFR} = \int_{E_0}^{2} \mathrm{d}E_X \; L_X/\mathrm{SFR} \,. \tag{4.8}$$

### 4.2.3 Heating and Ionization rates

The X-ray intensity drives the evolution of the ionized fraction ($x_\mathrm{e}$) and kinetic temperature ($T_\mathrm{k}$) of the IGM gas element according to the following set of equations:

$$\frac{\mathrm{d}x_\mathrm{e}(\mathbf{x},z)}{\mathrm{d}z} = \frac{\mathrm{d}t}{\mathrm{d}z}\left[\Gamma_X - \alpha_\mathrm{A} C x_\mathrm{e}^2 n_\mathrm{b} f_\mathrm{H}\right] \,, \tag{4.9}$$

$$\begin{aligned}\frac{\mathrm{d}T_\mathrm{k}(\mathbf{x},z)}{\mathrm{d}z} = {} & \frac{2}{3k_\mathrm{b}(1+x_\mathrm{e})}\frac{\mathrm{d}t}{\mathrm{d}z}\sum Q_\mathrm{p} \\ & + \frac{2T_\mathrm{k}}{3n_\mathrm{b}}\frac{\mathrm{d}n_\mathrm{b}}{\mathrm{d}z} - \frac{T_\mathrm{k}}{1+x_\mathrm{e}}\frac{\mathrm{d}x_\mathrm{e}}{\mathrm{d}z} \,,\end{aligned} \tag{4.10}$$

where $n_\mathrm{b}$ is the baryon number density, $\Gamma_X$ the ionization rate per baryon from X-rays, $\alpha_\mathrm{A}$ the case-A recombination coefficient, $C$ the clumping factor, $f_\mathrm{H}$ the hydrogen number fraction, $k_\mathrm{b}$ the Boltzmann constant, and the heating rate per baryon,

$Q_{\rm p}$, includes both Compton heating and X-ray heating. The X-ray heating and ionization rates are computed as:

$$Q_{\rm X}(\mathbf{x}, z) = \int d\nu \frac{4\pi J}{h\nu} \sum_i (h\nu - E_i^{\rm th}) f_{\rm heat} f_i x_i \sigma_i \,, \tag{4.11}$$

$$\Gamma_{\rm X}(\mathbf{x}, z) = \int d\nu \frac{4\pi J}{h\nu} \sum_i f_i x_i \sigma_i F_i \,, \tag{4.12}$$

where

$$F_i = (h\nu - E_i^{th}) \left( \frac{f_{\rm ion,HI}}{E_{\rm HI}^{\rm th}} + \frac{f_{\rm ion,HeI}}{E_{\rm HeI}^{\rm th}} + \frac{f_{\rm ion,HeII}}{E_{\rm HeII}^{\rm th}} \right) + 1 \,. \tag{4.13}$$

Here i stands for the atomic species: H, HeI and HeII, $E_i^{\rm th}$ is their corresponding ionization threshold, $f_i$ their number fraction, $x_i$ the ionization fraction, $\sigma_i$ the cross-section, $f_{\rm heat}$ is the fraction of the primary ionized electron's energy dissipating as heat and $f_{{\rm ion},j}$ is its energy contributing to secondary ionization of the species $j$, taken from Furlanetto and Stoever (2010). Following the ISM simulations in Das et al. (2017), we assume photons with energies below $E_0 = 0.5$ keV are absorbed by the host galaxies and unable to escape into the IGM.

### 4.2.4 Lyman-alpha background

For computing the spin temperature, we need to calculate the Ly-$\alpha$ background as well. There are two dominant sources of Ly-$\alpha$ photons: excitation of HI by X-rays, and direct stellar emission of photons between Ly-$\alpha$ and Lyman-limit. The total Ly-$\alpha$ background computed can therefore be written as:

$$J_{\alpha,{\rm X}}(\mathbf{x}, z) = J_{\alpha,{\rm X}}(\mathbf{x}, z) + J_{\alpha,*}(\mathbf{x}, z) \,. \tag{4.14}$$

For calculating the Ly-$\alpha$ background from X-rays:

$$J_{\alpha,{\rm X}}(\mathbf{x}, z) = \frac{c n_{\rm b}}{4\pi H(z)} \nu_\alpha \int_{z'}^{\infty} {\rm d}z'' \frac{{\rm d}\phi_{\rm X}/{\rm d}z''}{4\pi r_{\rm p}^2} \int_{{\rm Max}[\nu_0, \nu_\tau = 1]}^{\infty} {\rm d}\nu \Sigma_i (h\nu - E_i^{\rm th}) \frac{f_{{\rm Ly}\alpha}}{h\nu_\alpha} f_i x_i \sigma_i \,, \tag{4.15}$$

where $r_{\rm p}$ is the null-geodesic separation between $z'$ and $z''$ in proper units. and $(h\nu - E_i^{\rm th}) f_{{\rm Ly}\alpha}/h\nu_\alpha$ is the fraction of electron energy which goes into Ly-$\alpha$ photons.

The direct stellar emission can be quantified as (Barkana and Loeb 2005):

$$J_{\alpha,*}(\mathbf{x}, z) = \frac{f_* \bar{n}_{\rm b,0} c}{4\pi} \int_z^{\infty} {\rm d}z' (1+z')^3 (1 + \bar{\delta}_{\rm nl}^{\rm R''}) \frac{{\rm d}f_{\rm coll}}{{\rm d}z'} \sum_{n=2}^{n(z')} f_{\rm recycle}(n) \epsilon(\nu_n') \,. \tag{4.16}$$

Here, $\epsilon(\nu)$ is the number of photons produced per Hz per stellar baryon, calculated at the emitted frequency, $\nu_n' = \nu_n (1+z')(1+z)$, and $f_{\rm recycle}$ is the fraction of

cascades of Ly$n$ photons which result in Ly-$\alpha$ photons.

## 4.3 Astrophysical model

This section describes the astrophysical model used for modelling the 21-cm signal, taken from Park et al. (2019). It uses simple power-law scalings for relating galaxy properties to its halo mass. For example, the stellar mass, $M_*$ is related to the halo mass, $M_{\rm h}$ as shown below:

$$M_*(M_{\rm h}) = f_* \left(\frac{\Omega_{\rm b}}{\Omega_{\rm m}}\right) M_{\rm h} \,, \tag{4.17}$$

where

$$f_* = f_{*,10} \left(\frac{M_{\rm h}}{10^{10}\,{\rm M}_\odot}\right)^{\alpha_*} \,. \tag{4.18}$$

Here, $f_{*,10}$ is the fraction of galactic gas in stars normalized to the value in halos of mass $10^{10}$ M$_\odot$, and $\alpha_*$ is the corresponding power-law index for stellar fraction-halo mass relation. Similarly, the ionizing escape fraction, $f_{\rm esc}$ is taken to be a power law function of the halo mass, with normalization $f_{\rm esc,10}$ and power law index $\alpha_{\rm esc}$:

$$f_{\rm esc} = f_{\rm esc,10} \left(\frac{M_{\rm h}}{10^{10}\,{\rm M}_\odot}\right)^{\alpha_{\rm esc}} \,. \tag{4.19}$$

The star-formation rate of a galaxy in a halo of mass $M_{\rm h}$ can be computed as:

$$\mathrm{SFR} = \dot{M}_* = \frac{M_*}{t_* H(z)^{-1}} \,, \tag{4.20}$$

where $t_*$ is a typical star formation timescale as a fraction of the Hubble time, $H(z)^{-1}$.

Fig. 4.7 shows the UV LFs corresponding to the aforementioned scaling relations and parameters. The scaling relations are good at characterizing the population-averaged properties of high-$z$ galaxies. They are consistent with observed UV LFs at $z = 6$–$10$ and $M_{\rm uv} \geq -20$ (e.g. Bouwens et al. 2014; Bouwens et al. 2016a; McLeod, McLure, and Dunlop 2016; Finkelstein 2016; Livermore, Finkelstein, and Lotz 2017; Oesch et al. 2018; Gillet, Mesinger, and Park 2020; Atek et al. 2018; Ishigaki et al. 2018a; Bouwens et al. 2021). Moreover, various hydrodynamical simulations (e.g. Xu et al. 2016; Ma et al. 2020) and semi-analytic models (e.g. Sun and Furlanetto 2016; Mutch et al. 2016; Behroozi et al. 2019) imply power laws for the stellar-to-halo mass relation.

The fiducial values of the parameters are taken as: $f_{*,10} = 0.05$, $\alpha_* = 0.5$, $f_{\rm esc,10} = 0.1$, $\alpha_{\rm esc} = -0.5$, $M_{\rm turn} = 5 \times 10^8 {\rm M}_\odot$, $t_* = 0.5$, $L_{\rm X<2\,keV}/\mathrm{SFR} = 10^{40.5}$ erg s$^{-1}$M$_\odot^{-1}$ yr, and $E_0 = 0.5$ keV. These values correspond to the maximum a posteriori model

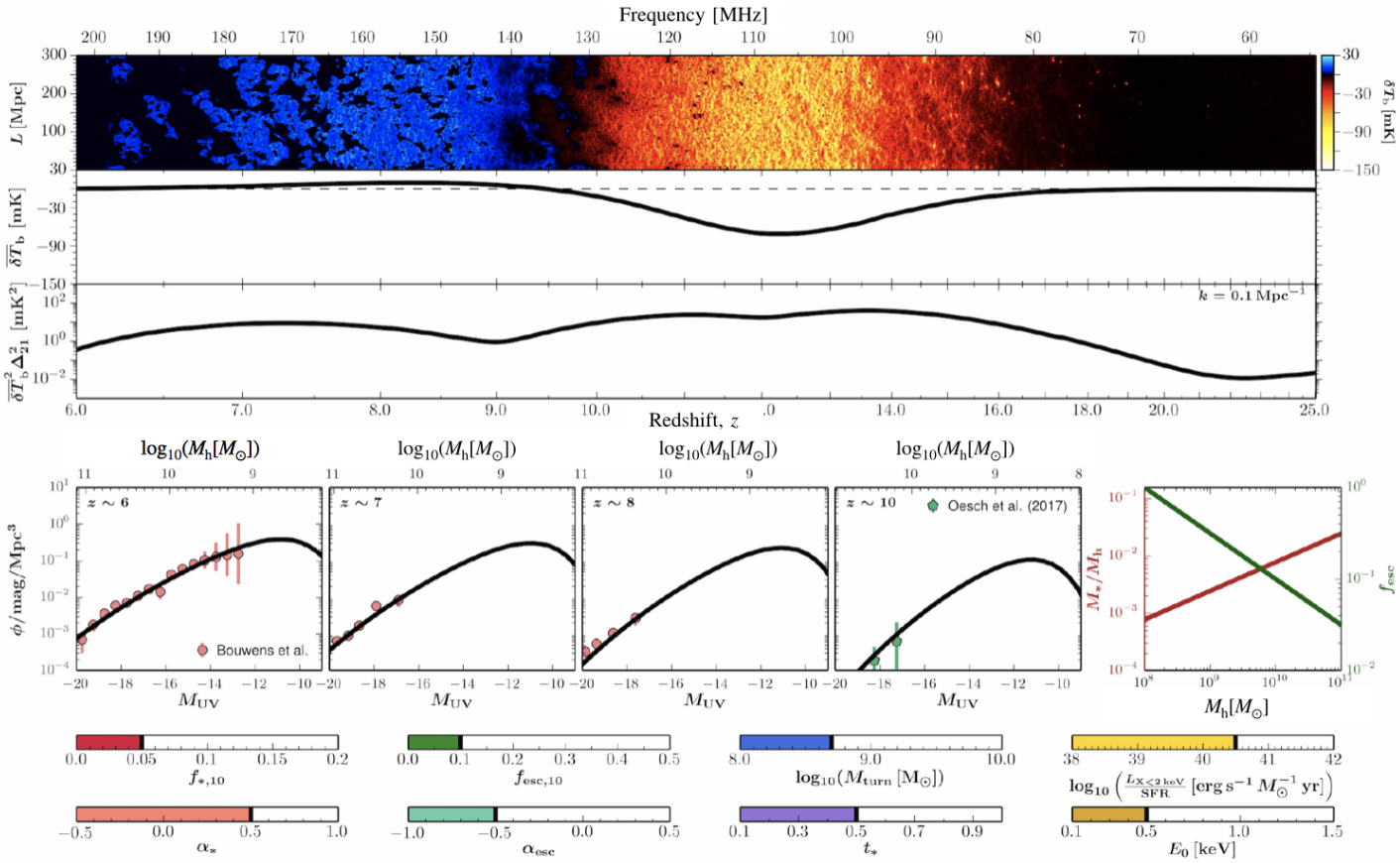


**Figure 4.7:** *Top panels*:The top three panels show a 1 Mpc slice through the 3D light-cone of 21-cm signal, the average brightness temperature offset and the power spectrum at $k = 0.1$ Mpc$^{-1}$ respectively, corresponding to the fiducial parameters from Park et al. (2019) *Bottom panels*: The four panels on the left show UV Luminosity functions (LFs) corresponding to the fiducial parameters, shown as thick solid curves at different redshifts. The colored points are the observed LFs from Bouwens et al. (2016a) at $z \sim 6$, Bouwens et al. (2014) at $z \sim 7-8$, Oesch et al. (2018) at $z \sim 10$. The right plot shows stellar mass per halo mass ($M_*/M_h$; maroon line) and escape fraction ($f_{esc}$; green line) as a function of halo mass. The toggles represent the values of fiducial parameters in Park et al. (2019).

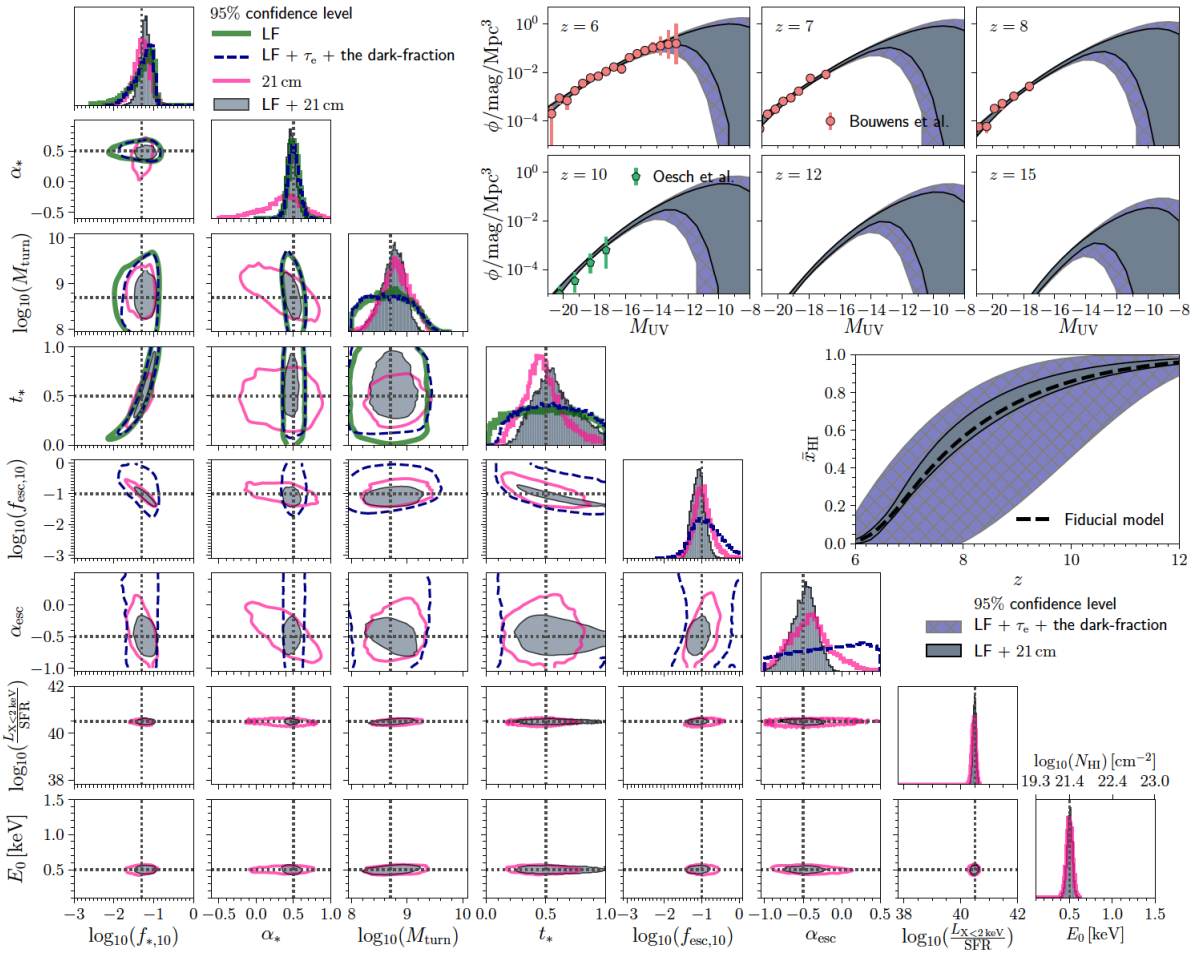


**Figure 4.8:** Corner plots showing constraints on parameters related to UV and X-ray properties of the early galaxies, from current data on galaxy luminosity function and reionization. Specifically, solid green curves, blue dashed curves, pink solid curves, and grey shaded regions represent constraints from data sets of LF only, LF+ $\tau_e$ + dark fraction, mock 21-cm PS, and LF+ PS, respectively, from Park et al. (2019). The top right panels show the corresponding 95 percent confidence levels of LFs computed using the posterior of their maximum likelihood model. The middle right plot shows the corresponding constraints on the evolution of the mean ionization fraction with redshift.

in Park et al. (2019), which used UV LFs, the electron scattering optical depth to CMB, and the QSO forest dark fraction in the likelihood, as shown in the corner plots of Fig. 4.8. The top and middle right panels contain the UV LFs and the redshift evolution of ionization, both obtained with the aforesaid parameters. It can be seen that the values of the UV parameters (i.e. $\alpha_*, f_{*,10}, \alpha_{\rm esc}, f_{\rm esc,10}, M_{\rm turn}, t_*$) are consistent with the observed UV luminosity functions (e.g. Bouwens et al. 2015; Bouwens et al. 2016b; Livermore 2016; Ishigaki et al. 2018b; Atek et al. 2018) and reionization constraints from the CMB (Planck Collaboration et al., 2016a) and high-$z$ QSOs (McGreer, Mesinger, and D'Odorico, 2015b), while the X-ray properties (i.e. $L_{\rm X<2\ keV}/{\rm SFR}, E_0$) are consistent with the observations of local, star-forming galaxies (e.g. Fragos et al. 2013b; Mineo, Gilfanov, and Sunyaev 2012).

## 4.4 Modeling the telescope noise

To calculate the expected sensitivities on the 21-cm signal, the python package `21cmSENSE` is used, which is based on the works of Pober et al. (2013b) and Pober et al. (2014). This section provides details on how telescope noise is computed using `21cmSENSE`.

The first step involves setting up an array configuration congruent with the SKA1-low Baseline Design [1], with compact antennae core having a maximal baseline length of 1.7 km. The telescope parameters follow the same design model. The system temperature is $T_{\rm sys} = 1.1 T_{\rm sky} + 40$ mK, giving a value of 351 K at 150 MHz. It consists of the receiver temperature, $T_{\rm rec} = 100$ K and the sky temperature, $T_{\rm sky} = 60\ {\rm K}(\lambda/1\ {\rm m})^{2.55}$. After setting up an array configuration, `21cmSENSE` makes the coverage of observation in $uv$ plane using the framework explained in §3.5. The power spectrum of the cosmological signal obtained from `21cmFAST` is taken as input and added to each $(u, v, \eta)$ voxel. The noise power spectrum for a given $k$-mode is calculated as explained in eq. 3.22 (Morales 2005; McQuinn et al. 2006):

$$P_{\rm N}(k,z) \approx X^2 Y \frac{k^3}{2\pi^2} \frac{\Omega'}{2t} T_{\rm sys}^2 \,. \tag{4.21}$$

Different independent modes are added in quadrature to obtain the total power spectrum of noise. Since this method of calculating sensitivities automatically tracks the number of independent modes, sample variance is also included while summing up the modes. Therefore, the total noise including both thermal noise and sample

[1] `https://www.skatelescope.org/wp-content/uploads/2012/07/SKA-TEL-SKO-DD-001-1_BaselineDesign1.pdf`

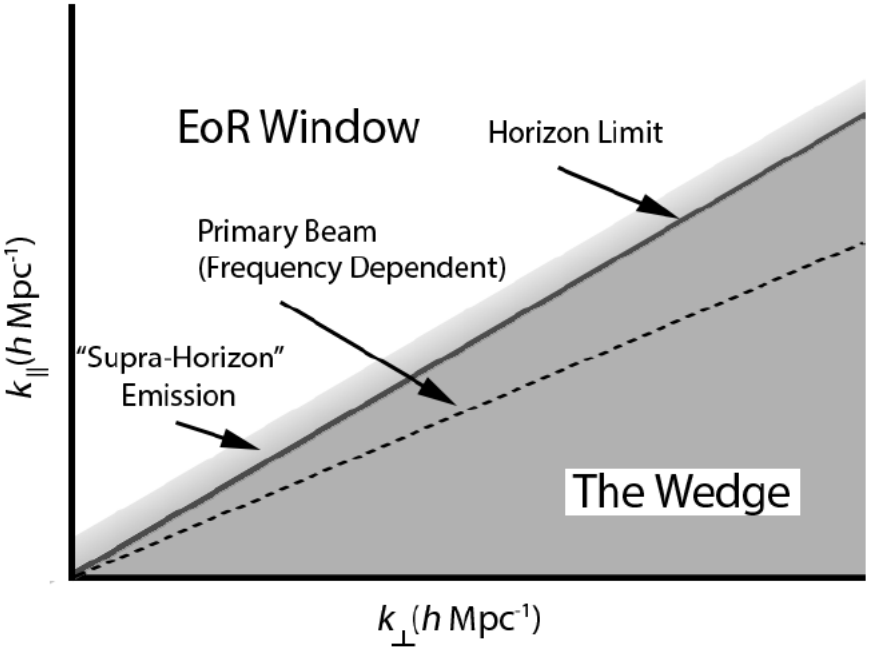


**Figure 4.9:** Different foreground models are described w.r.t. horizon limit (eq. 4.23) and Full-Width Half-Maximum of primary beam in Pober et al. (2014).

variance can be written as:

$$\delta P_{\mathrm{N+S}}(k,z) = \left(\sum_i \frac{1}{(P_{\mathrm{N},i} + P_{21})^2}\right)^{-\frac{1}{2}}, \tag{4.22}$$

where $P_{21}(k,z)$ is the 21-cm power spectrum as defined in Chapter 3 and the averaging is performed over modes $i$.

Note that it is assumed that the sample variance error follows Gaussian distribution. In reality, the 21-cm signal is non-Gaussian and this can affect the signal-to-noise ratio (S/N) of an experiment but this effect is prominent when S/N is sufficiently high (e.g., see the right panel of fig. 4.11, S/N is modest till reionization proceeds on large scales). This makes Gaussian noise a fairly reasonable approximation in the modest S/N regime relevant for most 21-cm observations ((Mondal et al., 2015)).

The foregrounds are expected to be limited to a wedge-like region as explained in §3.5.1. `21cmSENSE` provides three choices of foreground models, based on three different limits to foreground wedge. The wedge limit is set with respect to a "horizon limit" i.e. the $k_{||}$ mode on a given baseline which corresponds to the chromatic sine wave created by a flat-spectrum source located at the horizon, and is given by

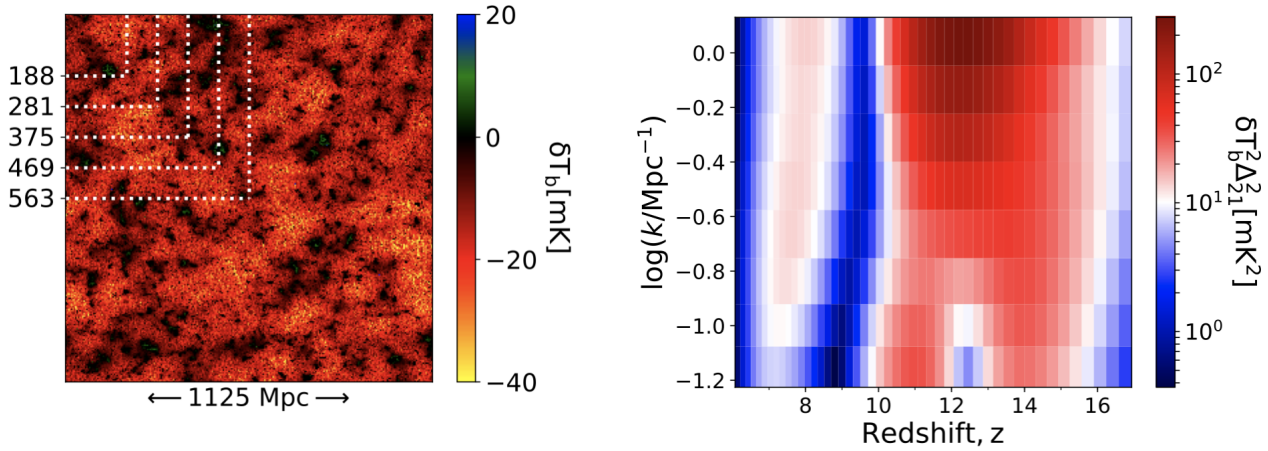


**Figure 4.10:** *Left panel*: Slice through the brightness temperature at $z = 10$ in a simulation box of length 1125 Mpc per side. The white dotted lines mark different simulation sizes. *Right panel*: The evolution of 3D 21-cm power spectrum with redshift, both plotted using `21cmFAST` and taken from Kaur, Gillet, and Mesinger (2020).

the following expression:

$$k_{||,\,\mathrm{hor}} = \frac{2\pi|\vec{b}|}{Yc} = \frac{1}{\nu}\frac{X}{Y}k_{\perp}\,. \tag{4.23}$$

The moderate foreground model uses a wedge limit of 0.1 $h$Mpc$^{-1}$ beyond the horizon limit (fig. 4.9), the optimistic model has the wedge up to the Full-Width Half-Maximum (FWHM) of the primary beam, and the pessimistic model has the wedge limit as the moderate model but only redundant baselines are added coherently. For this work, the optimistic foreground model is chosen since this choice would correspondingly translate to more stringent lower limits on the allowed box size, for a given target S/N.

## 4.5 Results

### 4.5.1 Reference simulation

In Figure 4.10, the results from the large- scale "reference" simulation are displayed. This simulation is 1125 Mpc on a side, computed on a $768^3$ grid. The resolution for initial conditions was taken to be $\sim 0.5$ Mpc, and the resolution for the evolved density, velocity, ionization fields, etc. was taken to be $\sim 1.5$ Mpc.

In the top left panel of Fig. 4.10, a slice through the brightness temperature box at $z = 10$ is shown, which corresponds to the late stages of the epoch of heating (EoH) for the chosen astrophysical parameters. For illustration purposes, different

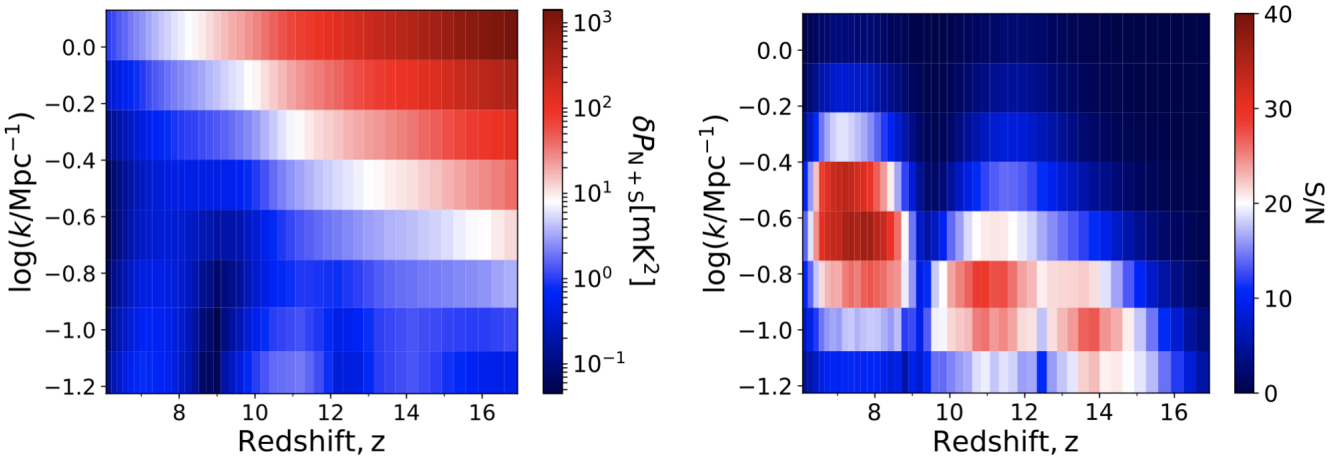


**Figure 4.11:** *Left*: The evolution of the noise power spectrum, including both thermal and sample variance, assuming a 1000h observation with SKA1-Low. *Right*: Signal-to-noise ratio (S/N), computed by dividing the power spectrum of the reference box (shown in the right plot of 4.10) by the noise shown in the left panel.

box sizes are also indicated using white lines. Large-scale fluctuations in the temperature are clearly visible. Even by eye, one can see notable structure in the 21-cm maps on scales comparable to the smallest box sizes. It can be pointed out that even the smallest box size, $L \sim 200$ Mpc encloses a volume that is a factor of $\gtrsim 10$ larger than what is currently accessible with state-of-the-art numerical simulations resolving atomically-cooled galaxies (e.g. Dixon et al. 2016; Doussot, Trac, and Cen 2019; Ocvirk et al. 2020; see also the review in Trac and Gnedin (2011)). The right panel of the figure 4.10 shows the redshift evolution of the 3D averaged power spectrum. Similar generic trends are recovered as suggested by previous works (e.g. Pritchard and Furlanetto 2007; Mesinger, Furlanetto, and Cen 2011, etc.). Namely, the large-scale power ( $k \lesssim 0.1$ Mpc$^{-1}$ has three peaks in the redshift evolution ($z \sim 14, 11, 7$ for the chosen set of astrophysical parameters). These correspond to the epochs of WF coupling, EoH, and EoR, when the large-scale PS is driven by spatial fluctuations in the WF coupling coefficient, kinetic temperature, and ionization fraction, respectively, as explained in detail in §3.1. The WF coupling and EoH peaks of the PS evolution merge on small scales, due to the stronger negative contribution of the cross-power terms of the power spectrum. The maximum amplitude of the power spectrum is seen for $z \sim 10 - 14$ on the largest length scales. The signal approaches zero as reionization is complete at $z \sim 6$.

The left panel of Fig. 4.11 shows the redshift evolution of the noise power spectrum, including both thermal and sample variance terms (c.f. eq. 4.22). As discussed

in the previous subsection, the thermal component was calculated for a 1000h integration with SKA1-low, assuming optimistic foregrounds. From the panel, the two trends in the noise evolution (c.f. Greig, Mesinger, and Koopmans (2020)) are evident: (i) on small scales, i.e. for $k \gtrsim 0.1$ Mpc$^{-1}$ the noise is dominated by thermal noise, and increases strongly with redshift independently of the cosmic signal. Therefore, noise increases with redshift. On large scales, i.e. $k \lesssim 0.1$ Mpc$^{-1}$ although the noise is generally still dominated by the smoothly-evolving thermal noise, the cosmic variance begins to have a non-negligible contribution. As a result, the noise structure can be seen to trace the structure in the cosmic signal, following the same trend as the power spectrum shown in the right panel of Fig. 4.10.

The right panel of Fig. 4.11 contains the corresponding S/N (i.e. the ratio of the power spectrum of the signal and noise discussed above). Although the signal is high on the largest scales, the S/N on such scales is very small due to high orders of thermal noise. Therefore, the large S/N ratio is observed on intermediate scales and low redshifts. From the figure it is clear that the highest S/N of order $\gtrsim 10$ occurs during the three large-scale peaks in the signal, corresponding to the reionization, heating, and WF coupling epochs.

### 4.5.2 Bias and scatter of the power spectrum

Keeping the astrophysical parameters the same, we perform simulations of smaller box sizes. To include cosmic variance, we also run simulations with different random realizations of the initial Gaussian-random field, corresponding to each box size. Table 4.1 carries whole information on the box sizes of the various simulations, including the number of independent realizations. The cell resolution is kept the same for all simulations ( 1.5 Mpc).

The impact of limited box sizes is further highlighted in Fig. 4.12. Here the gray curves show the redshift evolution of the large-scale power for all twenty realizations of the two small box sizes used in the study: 188 Mpc in the left panel and 375 Mpc in the right panel. The solid purple curves show the average over all of the realizations. The reference large-scale simulation is shown with a black curve in both panels. The Poisson uncertainty on the PS (i.e. the uncertainty on the mean amplitude from sampling a limited number of modes in Fourier space around $|\mathbf{k}| \approx 0.1$ Mpc$^{-1}$), is shown as green error bars for one of the realizations in each panel. It is apparent that the box-to-box scatter is larger than the Poisson uncertainty even for

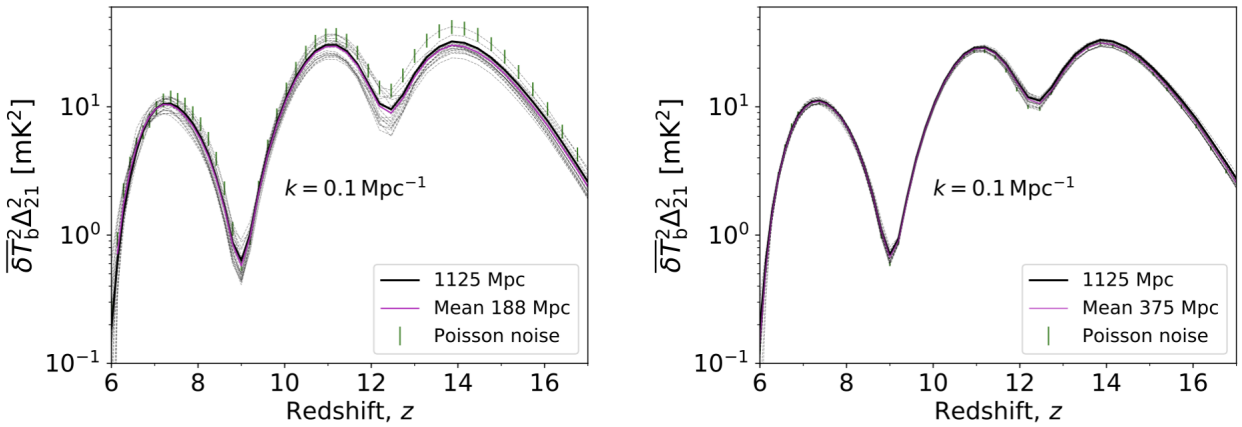


**Figure 4.12:** The redshift evolution of the cosmic 21-cm power spectrum at $k = 0.1$ Mpc$^{-1}$ for various realizations, using the same cosmological and astrophysical parameters. Gray dashed curves correspond to realizations of $L_{\rm box}$ = 188 Mpc (*left panel*) and 375 Mpc (*right panel*), while the corresponding average over all of the realizations is shown as a solid purple curve. The reference simulation of $L$ = 1125 Mpc is shown with a black solid curve. The green error bars on one of the simulations in each panel correspond to the Poisson uncertainty on the PS from a single small-box realization (from averaging over a discrete number of $k$-modes in Fourier space). The figure illustrates two expected trends: (i) a scatter in the measured 21-cm power from different realizations, which decreases with increasing box size; and (ii) a bias from the missing large-scale modes, with most of the small-box simulations having smaller large-scale power during the Cosmic Dawn.

**Table 4.1:** List of the smaller box simulations used in this work. Columns correspond to: (i) the side length of the simulation, $L$; (ii) the number of cells, $N_{\rm cell}$; (iii) the number of independent realizations, $N_{\rm real}$; (iv) the fractional bias in the 21-cm PS (c.f. eq. 4.24), averaged over all realizations, computed at the peak of the large-scale power, $(k = 0.1{\rm Mpc}^{-1}, z = 14)$; and (v) the mean of the S/N-weighted error, in units of the total noise (c.f. eq. 4.26; note that the median of this error is denoted with horizontal lines in Fig. 4.15).

| $L$(Mpc) | $N_{\rm cell}$ | $N_{\rm real}$ | $\langle \delta P \rangle$ (%) | $\Delta P_{\rm S/N,i}$ ($\sigma_{\rm tot}$) |
|---|---|---|---|---|
| 187.50 | $128^3$ | 20 | -6.6 $\pm$2.7($1\sigma$) | 0.90 $\pm$0.16($1\sigma$) |
| 281.25 | $192^3$ | 20 | -8.8 $\pm$1.6($1\sigma$) | 0.70 $\pm$0.14($1\sigma$) |
| 375.00 | $256^3$ | 20 | -5.6 $\pm$1.2($1\sigma$) | 0.48 $\pm$0.16($1\sigma$) |
| 468.75 | $320^3$ | 10 | -2.5 $\pm$1.2($1\sigma$) | 0.43 $\pm$0.08($1\sigma$) |
| 562.50 | $384^3$ | 10 | -1.4 $\pm$1.1($1\sigma$) | 0.30 $\pm$0.07($1\sigma$) |

a such relatively large-scale mode of $k \approx 0.1$ Mpc$^{-1}$ (corresponding to a comoving length of $\lambda = 2\pi/k \approx 60$ Mpc).

There are two points that can be noted down from Fig. 4.12, that confirm the expected trends (e.g. Barkana and Loeb 2004; Iliev et al. 2014): (i) the cosmic variance of the PS from different realizations decreases with increasing box size; and (ii) the PS constructed from smaller boxes *on average* underestimates the amount of 21-cm structure. As seen in the figure, the purple curves are below the black curves ( corresponding to the PS of the reference simulation).

We quantify the bias of (ii) for all of the simulations in this study by computing the fractional difference in power between the reference simulation and the smaller box simulations as follows:

$$\langle \delta P(L,k,z) \rangle \equiv \left\langle \frac{P_{\rm L,i} - P_{\rm ref}}{P_{\rm ref}} \right\rangle_{N_{\rm real}} . \tag{4.24}$$

Here, $P_{\rm ref}(k,z)$ corresponds to the PS of our reference, 1125 Mpc large-scale simulation, $P_{L,i}(k,z)$ to the PS of a given realization $i$ with box length $L$, and the averaging is performed over all $N_{\rm real}$ realizations of that box size.

The fourth column of Table 4.1 contains the corresponding values of $\langle \delta P(L) \rangle$ calculated at $z = 14$ when the $k = 0.1$ Mpc$^{-1}$ power peaks : during the Cosmic Dawn epoch when fluctuations in the Ly-$\alpha$ coupling dominate the signal (c.f. right panel of fig. 4.10 ). As seen in the table, box sizes lower than $L \lesssim 300$ underestimate the power at peak CD signal by up to $\sim$7–9%. This bias decreases to $\sim$ 1 % for the 563 Mpc simulations. This error is also much smaller during the EoR, falling to $\sim$ 1% even for $L \lesssim 300$ Mpc boxes. This is comprehensible since the ionization fluctuations during the EoR occur on smaller scales than the temperature and Ly$\alpha$

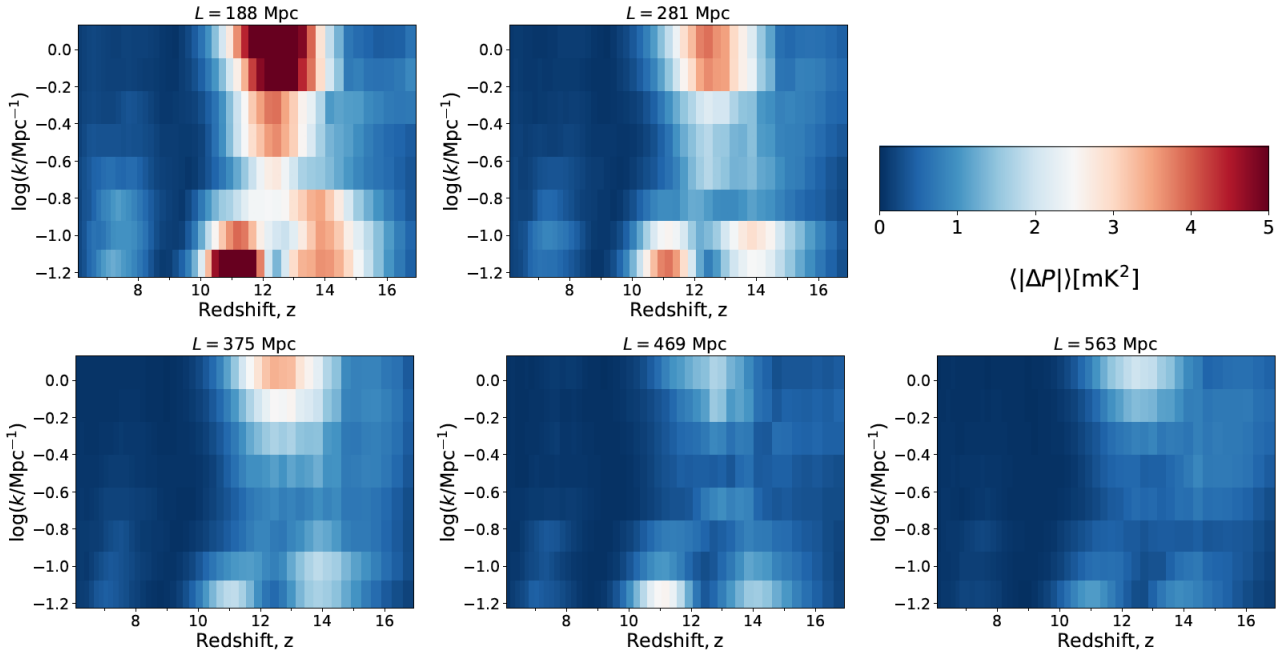


**Figure 4.13:** Absolute difference in the power spectra amplitudes of L = 188, 281, 375, 469, and 563 Mpc boxes with respect to the reference 1125 Mpc box, averaged over different realizations of the initial conditions.

coupling fluctuations during the Cosmic Dawn.

### 4.5.3 Convergence in the signal

In order to quantify the convergence of the small box simulations with respect to the reference, we quantify the average of absolute differences as follows:

$$\langle|\Delta P(L,k,z)|\rangle \equiv \langle|P_{\rm L,i} - P_{\rm ref}|\rangle_{N_{\rm real}} \,. \tag{4.25}$$

$\langle|\Delta P(L,k,z)|\rangle$ is a measure of the scatter in the PS amplitude at $(k,z)$, for a simulation of box length, $L$. These absolute differences in the power spectra are plotted in Fig. 4.13.

On large scales, the most significant differences in the PS occur during the three astrophysical epochs: (i) EoR at $z \sim 7$; (ii) EoH at $z \sim 11$; (iii) WF coupling at $z \sim 14$. These correspond to the three peaks of the large-scale power (c.f. right panel of Fig. 4.10). Of these, the EoH has the largest scatter. On small scales, the largest scatter occurs during the Cosmic Dawn, again tracing the amplitude of the power spectrum.

The PS differences in the smallest box simulations, $L = 188$ Mpc reach values of $\langle|\Delta P|\rangle \sim 7$ mK$^2$. As expected, there is a clear decrease in the scatter with the

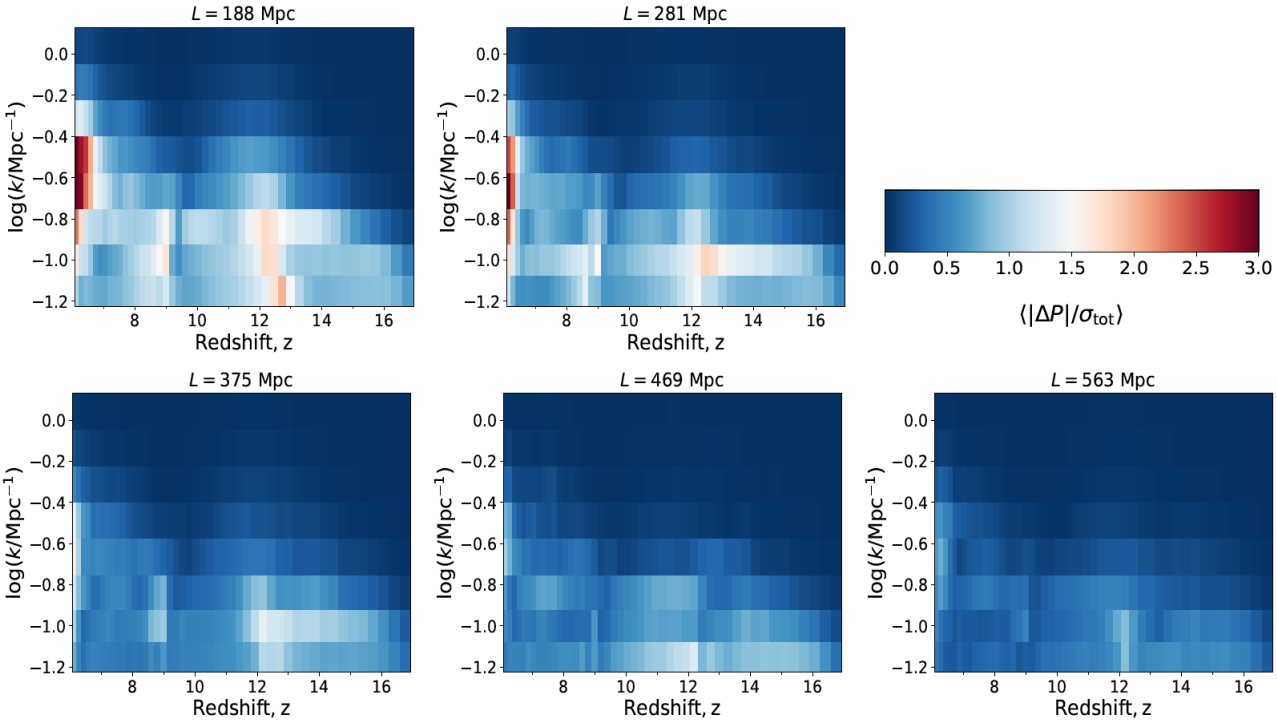


**Figure 4.14:** Same as Fig. 4.13, but dividing by the total noise (thermal and sample variance) in each (k; z) bin.

increasing simulation box size. For example, the maximum relative difference in the PS of boxes with size $\gtrsim 375$ Mpc is $\lesssim 3$ mK$^2$.

However, not all scales and redshifts are equally relevant from an observational perspective. For example, on small scales or at high redshifts, thermal noise can be quite high, making the 21-cm signal unobservable even with SKA1-low (c.f. Fig. 4.10). Since these modes are undetectable, they should be less important when estimating the convergence in the power spectra. Therefore, noise levels should also be put in perspective while analyzing Figure 4.13.

With this in mind, we re-plot the average PS differences of Fig. 4.13 in units of the total r.m.s. noise: $\langle|\Delta P|/\sigma_{\rm tot}\rangle$. Here $\sigma_{\rm tot}$ corresponds to the total noise, including thermal and sample variance of the reference simulation from eq. (4.22) with the Poisson sample variance of the small box realizations added in quadrature.

From Fig. 4.14 it can be seen that the small-scale differences in the thermal noise-dominated region of the $(k; z)$ space have diminished. The scatter in the PS differences expressed in terms of the total noise is largest on large scales where the thermal noise is the smallest. In particular, the late stages of the EoR and the CD show differences of up to $\sim 4\ \sigma_{\rm tot}$ for simulations of box sizes $L \sim 200 - 300$ Mpc. These differences decrease to below $1\ \sigma_{\rm tot}$ for the largest box sizes.

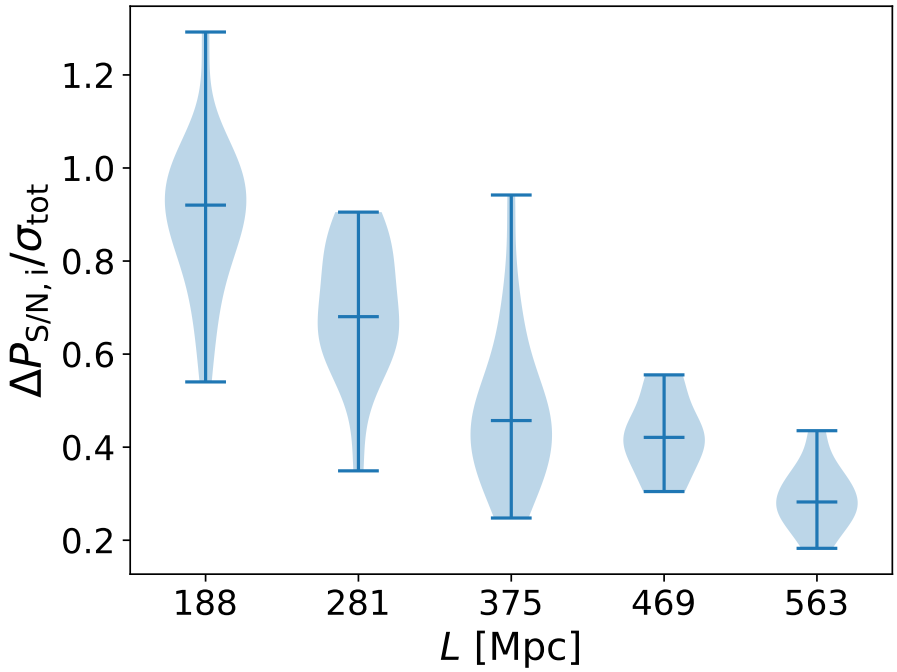


**Figure 4.15:** Violin plots of the S/N-weighted average over (k; z) of the absolute difference in PS amplitude, in units of the total noise (see equation). The middle horizontal lines denote the median of the distributions over realizations, $i$, while the bars enclose the full extent. Both the median and the spread of the S/N-weighted PS error decrease with increasing box size.

For defining the final summary statistic of the work, we marginalize the S/N-weighted power spectrum differences over $(k; z)$ space. The statistic is computed as follows:

$$\Delta P_{\mathrm{S/N,i}} = \frac{\int_z \int_k [\mathrm{S/N}] \frac{|P_{\mathrm{L,i}} - P_{\mathrm{ref}}|}{\sigma_{\mathrm{tot}}} dk\, dz}{\int_z \int_k [\mathrm{S/N}]\, dk\, dz} \,. \tag{4.26}$$

Here $\mathrm{S/N} = P_{\mathrm{ref}}/\sigma_{\mathrm{ref}}$ refers to the reference mock observation, shown in the bottom right panel of Fig. 4.11.

Equation (4.26) provides a single number for a given small-box realization, $i$, corresponding to the S/N-weighted average over $(k; z)$ of the absolute difference in PS amplitude, in units of the total noise. The corresponding distributions of $\Delta P_{\mathrm{S/N,i}}$ are plotted in Figure 4.15 for all box sizes. The distributions over realizations, $i$, are shown with violin plots. The median of the distributions is shown as the orange horizontal line and the bars mark the full range.

As expected, both the median and the spread of this S/N-weighted PS error decrease with increasing box size. For a box size of 188 Mpc, the median, S/N-weighted PS error is 0.9 $\sigma_{\mathrm{tot}}$, while the r.m.s. (1 $\sigma$) of the distribution is 0.16 $\sigma_{\mathrm{tot}}$. As

shown in the last column of table 4.1, the median for the boxes of size $\gtrsim 375$ Mpc reduces to $\lesssim 0.5\,\sigma$. For larger box sizes, none of our realizations have an S/N-weighted PS error greater than 1 $\sigma_{\rm tot}$.

## 4.6 Conclusions

Interferometric observations of the cosmic 21-cm signal are set to revolutionize our understanding of the epoch of reionization and Cosmic Dawn. However, interpreting these observations relies on our ability to accurately model the large-scale cosmological signal.

The first galaxies are likely very rare and biased, with their abundances modulated by long-wavelength modes of the density field (e.g. Bond and Myers 1996). Moreover, the radiation fields from these galaxies interact with the IGM over a large range of scales (e.g. Pritchard and Furlanetto 2007). Therefore, the limited volume of 21-cm simulations can underestimate the amount of structure in the cosmic 21-cm signal (e.g. Barkana and Loeb 2004; Iliev et al. 2014).

In this work, we quantify the minimum box size for simulating the power spectrum of the cosmic 21-cm signal. Using the public code `21cmFAST`, we perform multiple realizations of the cosmic 21-cm signal for a range of box sizes. We quantify convergence with respect to a mock observation of box length 1125 Mpc, with thermal noise computed for a 1000h observation with SKA1-low assuming the optimistic foreground scenario of Pober et al. (2014).

We find that simulations of box lengths $L \lesssim 200$ Mpc typically do not show a bias in the PS during the EoR; however, they do tend to underestimate the large-scale power during the earlier epoch of CD by $\sim 7\%$. There is also a notable scatter between different realizations. As expected, both the bias and scatter decrease with increasing box size.

We evaluate the absolute difference in the error between the power spectra from small-box realizations and the reference simulation. This error, averaged over multiple realizations, reaches values of up to $\sim 7$ mK$^2$ for the $L = 188$ Mpc simulation. We also compute this error in terms of the total noise, accounting for the fact that some modes are easier to detect than others. The error reaches values of $\sim 4\,\sigma_{\rm tot}$ for the smallest simulations.

Finally, we marginalize the error over all $(k; z)$ modes, weighted by the corresponding S/N. We conclude that box lengths of $L \gtrsim 250$ Mpc are needed to converge

at the level of $\lesssim 1\ \sigma$ of the total noise. This corresponds to simulation volumes $\gtrsim 10$ times larger than state-of-the-art radiative transfer simulations that resolve atomic cooling galaxies.

In Appendix A, we perform a similar exercise followed in this work for a different astrophysical model and obtain similar results.

# Chapter 5

# Metallicity dependence of high-mass X-ray binaries (HMXBs)

In Chapter 2, we learned how HMXBs are potentially the primary X-ray source of heating of the IGM during the EoH, and how their local galaxy-integrated X-ray luminosity correlated with the SFR of the host galaxy.

But what about the $L_X$/SFR relations of galaxies at higher redshifts i.e. the redshifts relevant to the EoH? Do the global $L_X$/SFR relations show evolution with redshift? This chapter will address these questions, focusing on the metallicity evolution of $L_X$/SFR relations of HMXBs with redshift.

The chapter begins with the motivation and a historical overview of research performed on the said topic in §5.1. Subsequently, I will present the work we carried out in Kaur et al. (2022). In §5.2, we present the steps for computing the X-ray emissivity during the Cosmic Dawn. In §5.3, we compute the associated thermal evolution of the IGM, followed by the evolution of the 21-cm signal. In §5.4, we quantify if simpler, constant $L_X$/SFR models can recover the same IGM evolution as predicted from the fiducial $L_X$/SFR–$Z$ relations. Finally we present our conclusions in §5.5.

We assume a standard $\Lambda$CDM cosmology with the following cosmological parameters: $h = 0.678$, $\Omega_m = 0.308$, $\Omega_b = 0.0484$, $\Omega_\Lambda = 0.692$, $\sigma_8 = 0.815$, $n_s = 0.968$ based on result from Planck Collaboration et al. (2016a).

## 5.1 Why metallicity dependence is important?

Several observational studies of high-redshift galaxies suggest that the normalization of $L_X$/SFR relation of HMXBs increases with redshift (Kaaret, Schmitt, and Gorski 2011; Prestwich et al. 2013; Basu-Zych et al. 2012; Brorby, Kaaret, and Prestwich 2014; Douna et al. 2015; Brorby et al. 2016; Lehmer et al. 2019a; Ponnada, Brorby, and Kaaret 2020; Fornasini et al. 2019; Fornasini, Civano, and Suh 2020; Lehmer et al. 2021). Basu-Zych et al. (2012) studied a large sample of HMXB-dominated

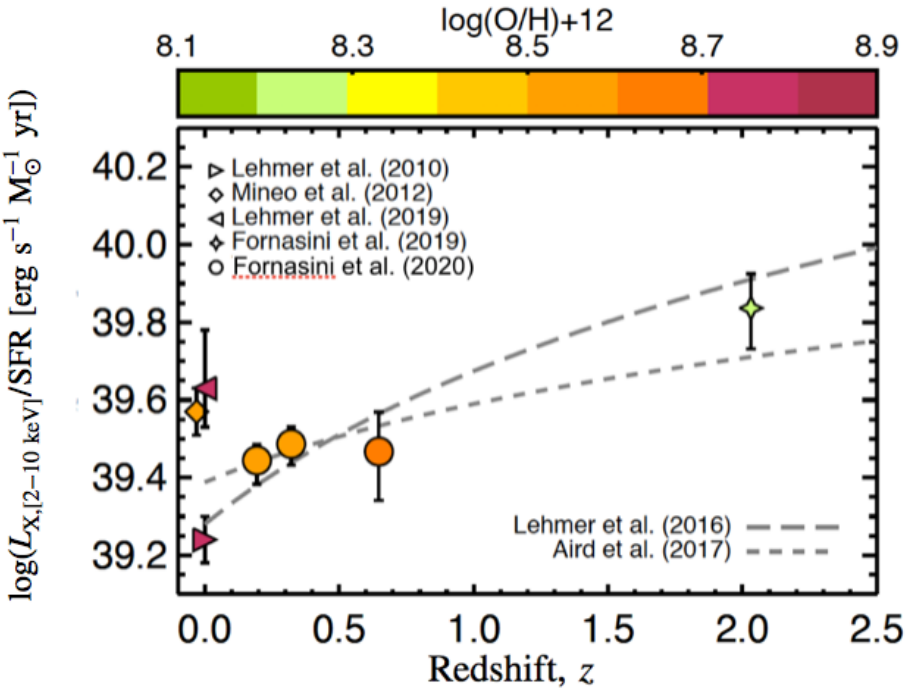


**Figure 5.1:** $L_X$/SFR in 2-10 keV range vs redshift plot of stacked galaxy samples of F+19; F+20 shown as circles and stars. The data points are color coded as per mean metallicities of galaxy samples. For comparison, local galaxy samples of M+12a are shown as triangles. The long dashed curve shows $L_X$/SFR relation of Lehmer et al. (2016) while the short dashed curve is taken from Aird, Coil, and Georgakakis (2017). Figure taken from F+20.

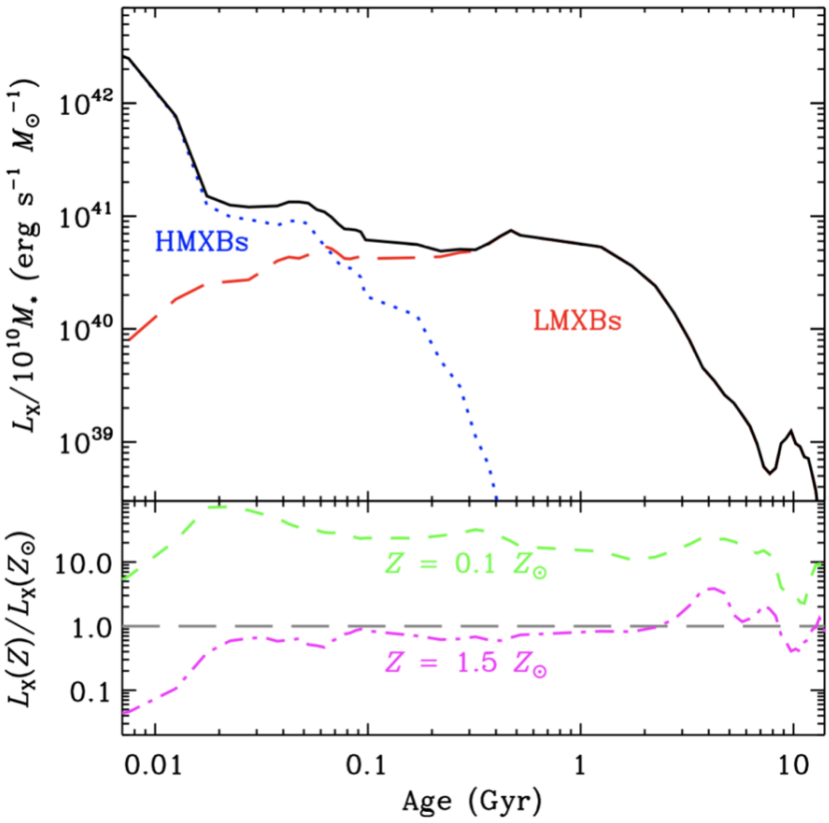


**Figure 5.2:** Evolution of an XRB population formed from a single starburst stellar population at solar metallicity, for one of the PS models of Fragos et al. (2013b) and Fragos et al. (2013a). Top panel shows the evolution of total bolometric X-ray luminosity per stellar mass with age of the population. The HMXBs (blue dotted curve) contribute more to the total X-ray luminosity for $\sim$ 100-300 Myr, as compared to LMXBs (red long-dashed curve). Bottom panel shows the luminosity evolution w.r.t. solar at two different metallicities. The luminosity at lower metallicity (i.e. $Z = 0.1\ Z_\odot$; green short-dashed) has a significant enhancement as compared to that at higher metallicity ($Z = 1.5\ Z_\odot$; magenta dot-dashed).

galaxies at redshifts between $z \approx 1-8$, using CDF-S. They reported an evolution in the $L_X$/SFR relation over a redshift range $z \approx 1-4$. Lehmer et al. (2016) studied the X-ray emission from galaxies at $z \approx 0-7$ using data from CDF-S survey and worked out a redshift dependence $L_X$/SFR for HMXBs as: $L_{X,[2-10\ \mathrm{keV}]}/\mathrm{SFR} \propto (1+z)$.

On the theoretical side, simulations of HMXBs suggest that the redshift evolution of $L_X$/SFR is due to the evolution of metallicity. Linden et al. (2010) studied the population synthesis models of young and bright HMXBs using StarTrack code (Belczynski, Kalogera, and Bulik 2002; Belczynski et al. 2008). They discovered that the number of HMXBs was significantly higher in low-metallicity environments (i.e. $Z \lesssim 0.2\ Z_\odot$). F+13a, F+13b explored various population synthesis models of XRBs generated with StarTrack code and using the observations of local galaxies as constraints. Fig. 5.2 demonstrates an interesting result of their study. In the top panel, the evolution of specific X-ray luminosity of a stellar population formed from a single star-burst vs the age of the population is shown. The bottom panel compares the evolution of X-ray luminosity per solar luminosity of a coeval XRB population at two quite different metallicities in units of solar metallicity. It can be seen that the X-ray luminosity has a significant enhancement at lower metallicity. This is in agreement with the theoretical expectations that weaker stellar winds resulting from lower metallicity environments would result in more X-ray luminous binaries, due to both a reduced expansion of the binary orbit and a reduced radial expansion of the companion which impacts when Roche-Lobe overflow occurs. This is also consistent with various observational works such as Mapelli et al. (2010), who studied the X-ray emission from Ultra-Luminous X-ray sources (ULXs) with X-ray luminosities $\gtrsim 10^{39}$ erg s$^{-1}$ and found out a possible anticorrelation between $L_X$/SFR and metallicity.

Brorby et al. (2016) (hereafter, B+16) provided the first observational work for the local $L_X$/SFR and metallicity relation for HMXB-dominated galaxies. They observed $L_X$/SFR of 10 Lyman break analogs (LBAs), which are local galaxies resembling high-redshift, star-forming galaxies observed with Chandra and lie in the metallicity range of 8.15 to 8.80 (shown as black hexagons in Fig. 5.5). Their corresponding SFRs were calculated using UV data from the GALEX archive, IR data from WISE All-Sky Survey, and gas-phase metallicites using SDSS data. The minimum cutoff for SFR-to-stellar mass ratio was set to $1 \times 10^{-10}$ yr$^{-1}$, to ensure that the galaxies were dominated by HMXBs. Their $L_X$/SFR enhancement for low-metallicity galaxies turned out to be higher, in line with the predictions from population synthesis

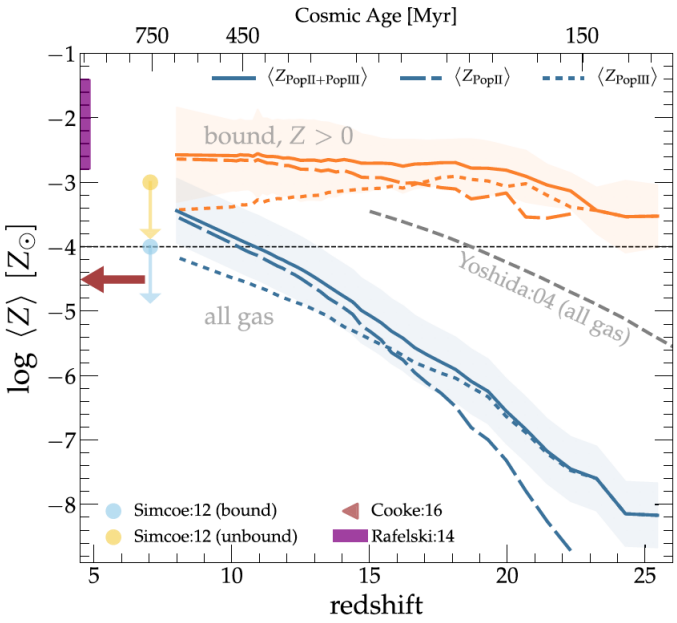


**Figure 5.3:** Evolution of mean metallicity of metal-enriched, bound systems (orange curves) and gas metallicity (blue curves) with redshift or cosmic age. The observational data contains damped Lyman $\alpha$ systems at $z = 7.04$ (blue/yellow points from Simcoe et al. (2012)) and $z > 4.7$ data from Rafelski et al. (2012) in purple. The figure is taken from Jaacks, Finkelstein, and Bromm (2019).

models. Fornasini et al. (2019) provided the first direct evidence that the evolution of $L_X$/SFR with redshift is attributed to metallicity evolution by studying the X-ray emission of $z \sim 2$ galaxies. They stacked a sample of 79 galaxies observed with various surveys such as Chandra AEGIS X-Deep, CDF-North, CDF-S, and CANDELS, using metallicity values from the MOSDEF survey. By binning the galaxies into different redshifts and metallicities, they found an enhancement of $\approx 0.4 - 0.8$ dex in $L_X$/SFR of $z \approx 2$ galaxies w.r.t. the local $L_X$/SFR relations. Fornasini, Civano, and Suh (2020) further examined the $L_X$/SFR relation for $z \approx 0.1 - 1.9$ and found no significant variation in $L_X$/SFR–$Z$ evolution with redshift. The redshift evolution of $L_X$/SFR of various observational works is shown in the right panel of Fig. 5.1 taken from Fornasini, Civano, and Suh (2020). The circular data points are stacked observations of Fornasini, Civano, and Suh (2020), the data point shown as green star is from Fornasini et al. (2019), and triangles are local observations of Mineo, Gilfanov, and Sunyaev 2012; Lehmer et al. 2010. The color indicates their gas-phase metallicities. The dark (light) grey dashed curve is from Lehmer et al. 2016; Aird, Coil, and Georgakakis 2017), normalized to the mean SFR of the galaxy samples of Fornasini, Civano, and Suh (2020). As obvious, the $L_X$/SFR relation shows an evolution with redshift, due to change in metallicity.

The metallicity dependence of $L_X$/SFR can be important for the EoH since the first galaxies are expected to form inside pristine gas with a rapidly-evolving metallicity (e.g. Wise et al. 2012; Xu, Wise, and Norman 2013; Pallottini et al. 2014; Jaacks, Finkelstein, and Bromm 2019; Ucci et al. 2021). Jaacks, Finkelstein, and Bromm (2019) studied the metal-enrichment of the pre-reionization Universe using simulation code, GIZMO, and sub-grid prescriptions for Pop III and Pop II systems (Jaacks et al. 2018). Fig. 5.3 shows the evolution of mean metallicity with redshift, along with some high-redshift observations of Pop-III only enriched damped Ly-$\alpha$ systems ($z \sim 7$; yellow and blue data points, $z > 4.7$; purple data). The orange curves represent the evolution of metal-enriched, bound systems or dark matter halos, while the blue ones represent the gas metallicity of the simulation volume. The solid lines show the total metallicity of Pop II and Pop III stars. Specifically, the total gas metallicity (i.e. PopII + PopIII) of the simulation volume shows a variation of $\langle Z/Z_\odot \rangle \approx$ -8 to -3.5, and the metallicity from star-forming regions varies from -2.5 to -3.5 over the redshift range of 8 – 25. The properties of the first generations of HMXBs can therefore be studied through the cosmic 21-cm signal at those redshifts (e.g. Madau and Fragos 2017; Qin et al. 2020). Indeed, the recent HERA phase-1 observations (HERA Collaboration et al., 2021a) have already put constraints on $L_X$/SFR of high-$z$ galaxies. Fig. 5.4 shows the marginalized PDFs of their $L_X$/SFR posteriors inferred from power spectrum measurements at $z \sim 8$ (HERA Collaboration et al. 2021a), along with other high-z observations such as UV LFs at $z \approx 6$–10, QSO dark fraction and optical depth of the CMB. The solid black vertical line corresponds to the local $L_X$/SFR relation from Mineo, Gilfanov, and Sunyaev (2012), while the dot-dashed line is the $L_X$/SFR prediction taken from Fragos et al. (2013b). As obvious, the low-metallicity $L_X$/SFR result from (HERA Collaboration et al., 2021b) is consistent with expectations that the first sources were more X-ray efficient due to their lower metallicities, and disfavoring the local $L_X$/SFR relation by $> 1\sigma$.

In the following sections, we will study the imprint of metallicity-dependent $L_X$/SFR relations in the 21-cm signal from the Cosmic Dawn[1]. Assuming a mass-metallicity relation, we compute the evolution of the 21-cm signal corresponding to

[1]The 21-cm signal depends on metallicity also through its impact on the stellar population (e.g. Magg et al. 2021; Muñoz et al. 2022), as well as dust attenuation of UV photons (e.g. Mirocha and Furlanetto 2019). Here the focus is on its role in setting the X-ray luminosity to SFR relation, deferring more focused studies to future work.

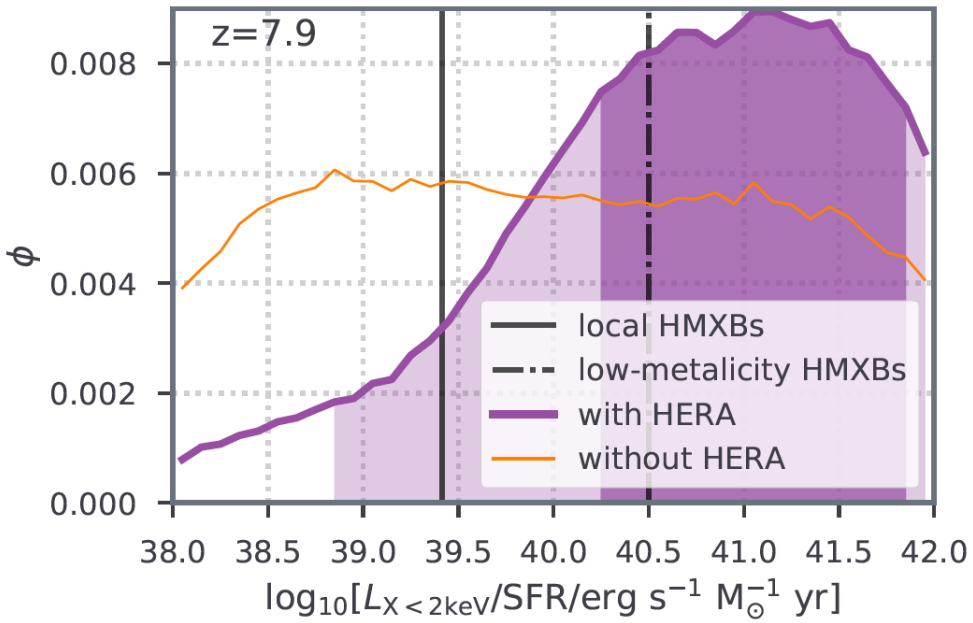


**Figure 5.4:** Marginalized PDFs of $L_X$/SFR posteriors constrained with HERA Phase-I (HERA Collaboration et al. 2021a). The shaded (light) region represents 65%(95%) confidence interval. The constraints including HERA Collaboration et al. (2021a) (vertical black dot dashed line) disfavor the local $L_X$/SFR relation (vertical black solid line) by $> 1\sigma$. Figure taken from HERA Collaboration et al. (2021b).

two different scalings of $L_x$/SFR with metallicity[2]. We quantify the impact of these relations on the X-ray emissivity and IGM temperature evolution, and also make forecasts for the corresponding 21-cm signal.

## 5.2 X-ray background

In this section, we present our model for computing the inhomogeneous X-ray background during the Cosmic Dawn. We begin with a discussion of empirical and theoretical $L_X$/SFR $-$ Z relations used in §5.2.1. The simulations are 500 comoving Mpc per side, computed using a $256^3$ grid smoothed down from $1024^3$ initial conditions. These volumes are large enough to accurately sample cosmic variance during the EoH (as concluded in Chapter §4; Kaur, Gillet, and Mesinger 2020).

### 5.2.1 Lx-sfr-Z

We assume that early galaxy populations can be characterized by an average $L_X$/SFR relation.

[2]Throughout "metallicity" is used to refer to the gas-phase metallicity, $12 + \log_{10}(O/H)$. Solar gas-phase metallicity $(12 + \log_{10}(O/H)_\odot)$ is taken to be 8.69 (Asplund et al. 2004). Absolute metallicity, $Z_\odot$ is taken to be 0.02.

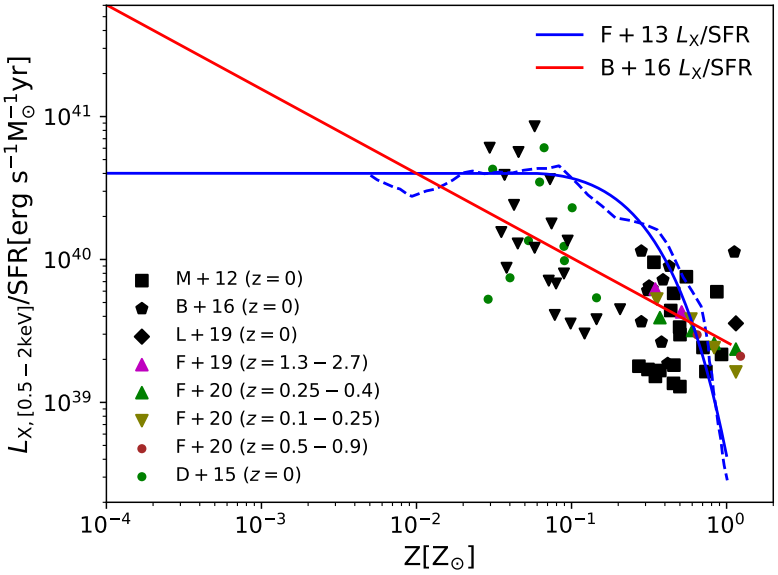


**Figure 5.5:** Soft-band $L_X$/SFR vs $Z$. The F+13a curve (solid blue) is constructed by fitting the XRB synthesis model 265 (dashed blue) of Fragos et al. (2013b). The red line is the empirical fit of observation data of local Lyman break analogs (black pentagons) from Brorby et al. (2016). To compare these models with observations, some observational estimates from the literature are also marked. Black squares are $L_X$/SFR estimates of $z = 0$ HMXB dominant star-forming galaxies from Mineo, Gilfanov, and Sunyaev (2012), constructed using X-ray, infrared and UV data from Chandra, SPITZER, GALEX, and 2MASS archives. Their corresponding metallicities were taken from Douna et al. (2015). Black diamonds are resolved samples of galaxies observed in both infrared (SINGS survey) and Chandra X-ray from Lehmer et al. (2019b). Green circles correspond are from Douna et al. (2015), estimated primarily from blue compact dwarf galaxies, with upper limits denoted by upside-down triangles in black. Stacked Chandra data from the COSMOS Legacy survey (Fornasini et al. 2019; Fornasini, Civano, and Suh 2020) in the redshift range $z = 0.1 - 2.7$ is shown with corresponding triangles. All data points are converted into the soft-band.

The first scaling relation is taken from B+16, as discussed earlier, with the following best-fit:

$$\log_{10}\left(\frac{L_{X,[0.5-8\ \mathrm{keV}]}}{\mathrm{erg\ s^{-1}}}\right) = a\log_{10}\left(\frac{\mathrm{SFR}}{\mathrm{M_\odot\ yr^{-1}}}\right) + b\ \log_{10}\left(\frac{(\mathrm{O/H})}{(\mathrm{O/H})_\odot}\right) + c, \tag{5.1}$$

where $L_{X,[0.5-8\ \mathrm{keV}]}$ is the X-ray luminosity in $0.5 - 8$ keV range, $\mathrm{a} = 1.03 \pm 0.06, \mathrm{b} = -0.64 \pm 0.17, \mathrm{c} = 39.46 \pm 0.11$.

The second $L_X$/SFR – $Z$ relation is taken from stellar evolution models of HMXBs provided in F+13a, as discussed earlier. Specifically, we use model 265 which is also the maximum likelihood model employed in Madau and Fragos (2017). We find that

the following Schechter function provides a good fit for its $L_X$/SFR – $Z$ relation:

$$\log_{10}\left(\frac{L_{\rm bol}/{\rm SFR}}{\rm erg\ s^{-1}\ M_\odot^{-1}\ yr}\right) = A + \alpha \log_{10}\left(Z/Z_{\rm turn}\right) - Z/Z_{\rm turn}\ . \tag{5.2}$$

Here, $L_{\rm bol}$/SFR is the bolometric X-ray luminosity per star formation rate in erg s$^{-1}$ M$_\odot^{-1}$ yr, $A = 41.3$, $\alpha = 0.3$, and $Z_{\rm turn} = 8 \times 10^{-3}$. We also set the X-ray luminosity to constant below the peak value at $Z/Z_{\rm turn} \leq \alpha/\ln 10$, to prevent the empirical fit from decreasing towards the lowest metallicities, in agreement with the constant $L_X$/SFR predicted by the F+13a model at these metallicities. This is due to sparse sampling of the relatively broad luminosity functions (LFs) of X-ray binaries, which require $\sim$ tens of galaxies to get unbiased estimates of the population-average values of $L_X$/SFR (e.g. Lehmer et al. 2021).

From the Fig. 5.5, we see that both B+16 and F+13a $L_X$/SFR – $Z$ relations pass through the observational data; however, they show dramatically different trends towards very low metallicities. As we shall see further below, galaxies with $Z \lesssim 10^{-2}$Z$_\odot$ likely dominate the X-ray background during the EoH. In this regime, the model from F+13a asymptotes to a much lower value of $L_X$/SFR than the empirical relation from B+16. The theoretical explanation for this is that once metallicity goes below a certain value (roughly 0.05 Z$_\odot$), stellar winds become inefficient and only have a marginal impact on the stellar evolution (e.g. Fragos et al. 2013b). However, these models do not vary the IMF, which could have an additional impact on the HMXB luminosity at very low metallicities (c.f. Fig. 7 in F+13a). Moreover, we note that the B+16 $L_X$/SFR–$Z$ relation is derived empirically, and was not intended to be extrapolated to the lowest metallicities we show in the figure.

Therefore, the $L_X$/SFR–$Z$ relation is highly uncertain at the lowest metallicities. It is important to note however that here we are not arguing for the validity of any specific $L_X$/SFR – $Z$ relation. Instead, we are exploring the observational impact of $L_X$/SFR – $Z$ relations during the Cosmic Dawn. Therefore the B+16 and F+13a scalings are useful in that they assign very different properties to the first generations of HMXBs. Indeed, we would want to eventually *infer these relations directly from future 21-cm data.*

### 5.2.2 Mass-metallicity relation

In the previous section, we presented the two different $L_X$/SFR–$Z$ relations we use in this study. We now discuss our adopted prescription for assigning $Z$ to high-redshift

galaxies.

The metallicity of galaxies is determined by a complex interplay of the inflow of the pristine gas, SFR, and the outflow of the metal-enriched gas. An important scaling relation for estimating the metal-enrichment of galaxies is the correlation between the galaxy-averaged gas-phase metallicity and the stellar mass of the galaxy ($M_*$), commonly referred to as the mass-metallicity relation (MZR; Lequeux et al. 1979; Mannucci et al. 2010; Lara-López et al. 2010; Yates, Kauffmann, and Guo 2012; Zahid et al. 2014; Cresci, Mannucci, and Curti 2019; Curti et al. 2020)[3]. This universal relation was first noticed in the observational studies of a small number of nearby galaxies by Lequeux et al. (1979). Tremonti et al. (2004) further studied $\sim 50,000$ local galaxies observed with SDSS, and found tight constraints on their MZR, for stellar masses varying from $10^{8.5}$ $M_\odot$ to $10^{11.5}$ $M_\odot$. The relation has been observed at redshifts as high as $z = 3.5$ (e.g., Tremonti et al. 2004; Erb et al. 2006; Maiolino et al. 2008; Ellison et al. 2008; Mannucci et al. 2010; Zahid et al. 2014; Sanders et al. 2018; Curti et al. 2020; Sanders et al. 2021), and has also been found in theoretical works (e.g., Yates, Kauffmann, and Guo 2012; Ucci et al. 2021).

Here we adopt the empirical MZR from Zahid et al. (2014):

$$Z = Z_0 + \log_{10}(1 - e^{-(M_*/M_0)^\gamma}) \,, \tag{5.3}$$

where $Z_0$ is the saturation metallicity, $M_0$ is a characteristic stellar mass scale above which the metallicity asymptotically approaches $Z_0$. The relation reduces to a power-law with index $\gamma$ at $M_* < M_0$, and flattens at higher masses. The redshift dependence is incorporated in $M_0$ as: $M_0 \equiv 10^b$. By fitting to data from SDSS, the Deep Extragalactic Evolutionary Probe 2 (DEEP2), FMOS-COSMOS, and Smithsonian Hectospec Lensing Survey (SHELS), that span a redshift range up to 1.6, Zahid et al. (2014) found a set of best-fit parameters as follows: $Z_0 = 9.100$, $b = 9.135 + 2.64\log_{10}(1+z)$ and $\gamma = 0.522$. We illustrate this relation in Figure 5.6 at $z = 4$–$9$ using solid curves. For reference, we also show data from the cosmological, hydrodynamic simulations of Pallottini et al. (2014), in which they follow ISM and IGM metal enrichment, with simulation boxes of 10 $h^{-1}$ Mpc per side, using a customized version of the public code, RAMSES (Teyssier (2002)). We plot their

[3]The mass-metallicity relation can also be understood as the 2D projection of the more general 3D fundamental metallicity relation (FMR), relating metallicity to the stellar mass and SFR (e.g. Mannucci et al. 2010; Hunt et al. 2012). In our analytic model, the stellar mass and SFR are themselves related deterministically (i.e. through the main sequence of star-forming galaxies), thus it suffices to only specify one or the other.

mean gas metallicity as a function of stellar mass at three redshifts (4, 6 and 9), along with scatter around metallicities of individual galaxies at $z \sim 5$ (cyan '+' markers). Y+15 curves are from Yue et al. (2015) where they use the stellar mass to UV magnitude relation from Duncan et al. (2014), combined with the FMR from Mannucci et al. (2010). We also show $Z$–$M_*$ predictions from semi-analytical GAEA models of Fontanot et al. (2021), tested using the VANDELS survey (McLure et al. 2018; Pentericci et al. 2018). Additionally, we show the empirical MZR from Curti et al. (2020), which depends on both stellar mass and SFR. This relation is more similar to the FMR (Mannucci et al. 2010), which is usually regarded as redshift-independent:

$$Z = Z_0 - (\gamma/\beta)\log_{10}(1.0 + (M_*/M_0)^{-\beta}) \,, \tag{5.4}$$

where,

$$\log_{10}(M_0) = m_0 + m_1 \log_{10}(\mathrm{SFR}) \,. \tag{5.5}$$

Here the parameter $\beta$ quantifies how fast the relation saturates, and $\gamma$ is the low-mass end slope. The best-fit parameters are: $Z_0 = 8.779$, $\gamma = 0.31$, $\beta = 2.1$, $m_0 = 10.11$, $m_1 = 0.56$. $\mathrm{M}_0$ and SFR have units of $\mathrm{M}_\odot\ \mathrm{yr}^{-1}$.

In making Fig. 5.6, we used the stellar – halo mass and the SFR – stellar mass relations from Park et al. (2019) when required; these were calibrated to reproduce high-redshift UV LFs and other EoR data (see details in §4.3 of Chapter 4).

From Figure 5.6 we see that the high-redshift simulations and semi-analytic models are in reasonable agreement with the MZR from Zahid et al. (2014), though the evolution towards the highest redshifts and smallest masses is highly uncertain. Therefore the 21-cm forecasts we present in §5.4 should be taken with caution.

### 5.2.3 X-ray emissivity during the Cosmic Dawn

The $L_X$/SFR–$Z$ relations and MZR discussed in the previous sections allow us to compute an average X-ray luminosity for a galaxy, given its SFR and stellar mass. To compute the X-ray background we then need to relate the SFR and stellar mass to the typical mass of the host halo, since then we can integrate over well-established HMFs.

For this, we use the simple and flexible power law scaling relations from Park et al. (2019) for stellar to halo mass relation and compute SFR as described in §4.3 of

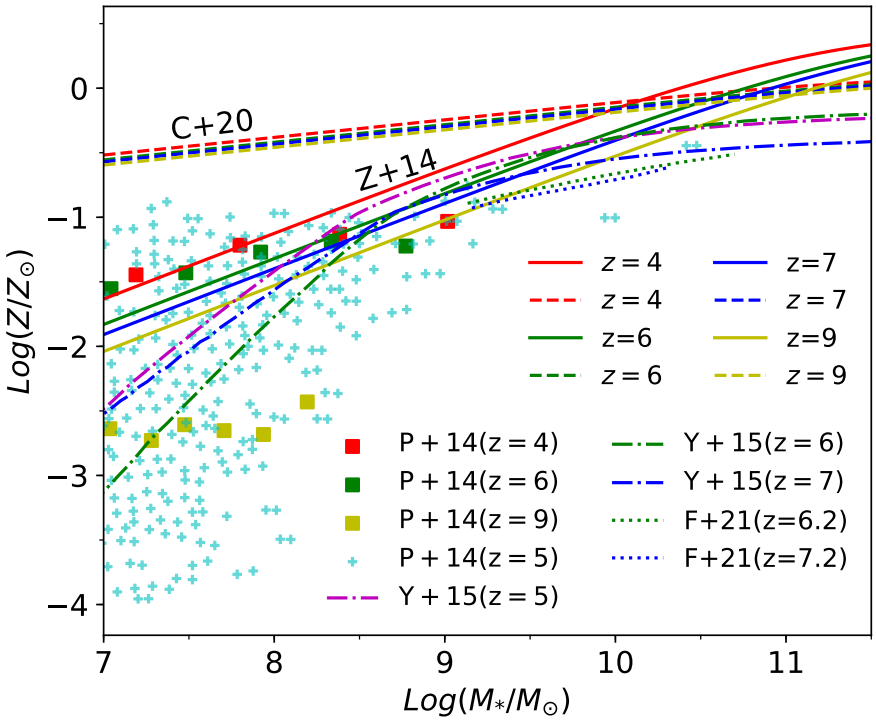


**Figure 5.6:** Gas-phase metallicity vs stellar mass relation (MZR) from Zahid et al. (2014) (see eq. 5.3) is shown with solid curves (Z+14) and from Curti et al. (2020) with dashed curves (C+20). The curves are color-coded according to redshift. We also plot mean relations from the hydrodynamic simulations of Pallottini et al. (2014) (P+14, squares), Yue et al. (2015) (Y+15, dot-dashed curves), and semi-analytic models of Fontanot et al. (2021) (F+21, dotted curves). Cyan crosses denote values from individual galaxies in Pallottini et al. (2014) at $z = 5$, illustrating the galaxy-to-galaxy scatter.

Chapter 4. These simple scaling relations seem sufficient to characterize the population-averaged properties of high-$z$ galaxies[4].

With the above, we can express the comoving, soft-band X-ray emissivity (in erg s$^{-1}$ Mpc$^{-3}$) at position $\mathbf{x}$ and redshift $z$ as:

$$\epsilon_{0.5-2\mathrm{keV}}(\mathbf{x}, z) = \int_0^\infty \mathrm{d}M_\mathrm{h} \frac{\mathrm{d}n}{\mathrm{d}M_\mathrm{h}} e^{-\left(\frac{M_\mathrm{turn}}{M_\mathrm{h}}\right)} \dot{M}_* \frac{L_\mathrm{X}}{\mathrm{SFR}}(Z, M_*, z) \,. \tag{5.6}$$

Here $\mathrm{d}n/\mathrm{d}M_\mathrm{h}$ is the local (conditional) halo mass function, $e^{-(M_\mathrm{turn}/M_\mathrm{h})}$ is the duty cycle as described in Chapter 4, and $L_\mathrm{X}/\mathrm{SFR}(Z, M_*, z)$ is related to the halo mass through equations (1) – (5). When computing mock observations below, we use these fiducial values: $f_{*,10}$ = 0.05, $\alpha_*$ = 0.5, $f_{\mathrm{esc},10}$ = 0.1, $\alpha_\mathrm{esc}$ = -0.5, $M_\mathrm{turn}$ = 5 × 10$^8$ M$_\odot$ and $t_*$ = 0.5. These values are the same as used in Chapter 4.

In the top panel of Figure 5.7 we show our fiducial star-formation rate density (SFRD) evolution, with the corresponding X-ray emissivity shown in the second panel (for both B+16 and F+13a $L_\mathrm{X}$/SFR–$Z$ relations). Because structure formation is hierarchical, the mass and metallicity of the typical galaxy population increase with time. At early times, most galaxies were extremely metal-poor and so the B+16 $L_\mathrm{X}$/SFR–$Z$ relation implies an X-ray emissivity that is a factor of ∼5 larger than the one from F+13a at $z \sim 20$. When the characteristic metallicity of star-forming galaxies surpasses $Z \gtrsim 0.01 Z_\odot$, the F+13a relation implies higher X-ray luminosities than B+16 (see Figure 5.5). From the second panel of Figure 5.7, we see this transition happening at $z \sim 10$, with F+13a implying a higher emissivity over the range $6 < z < 10$. As can be seen from Figure 5.5, we expect this trend to reverse again, with B+16 having higher luminosities at $Z \gtrsim Z_\odot$. However, such highly metal-enriched galaxies are too massive and rare to be relevant during the Cosmic Dawn.

We further quantify the properties of the relevant galaxies in Fig. 5.8, where we plot the fractional contribution to the X-ray emissivity of galaxies within a given logarithmic metallicity bin. The PDFs shift to higher metallicities and become wider with decreasing redshift. This is driven by the evolution of the HMF which shifts to larger masses and flattens with time. We see explicitly that the transition when the F+13a emissivity surpasses that of B+16 at $z \lesssim 10$ corresponds to when the mean of the PDFs goes above $Z \sim 0.01\ Z_\odot$. As we discuss further below, the EoH for

[4]Here we are only interested in the faint-end galaxies that dominate the photon budget (e.g Qin et al. 2021). We therefore do not include a separate power law at the bright end, typically associated with AGN feedback (e.g. Furlanetto, Peng Oh, and Briggs 2006; Behroozi and Silk 2015; Mirocha, Furlanetto, and Sun 2017; Sabti, Muñoz, and Blas 2021; Rudakovskyi et al. 2021). Such bright galaxies sit on the exponential tail of the HMF, and are thus too rare to be important for determining cosmic radiation fields.

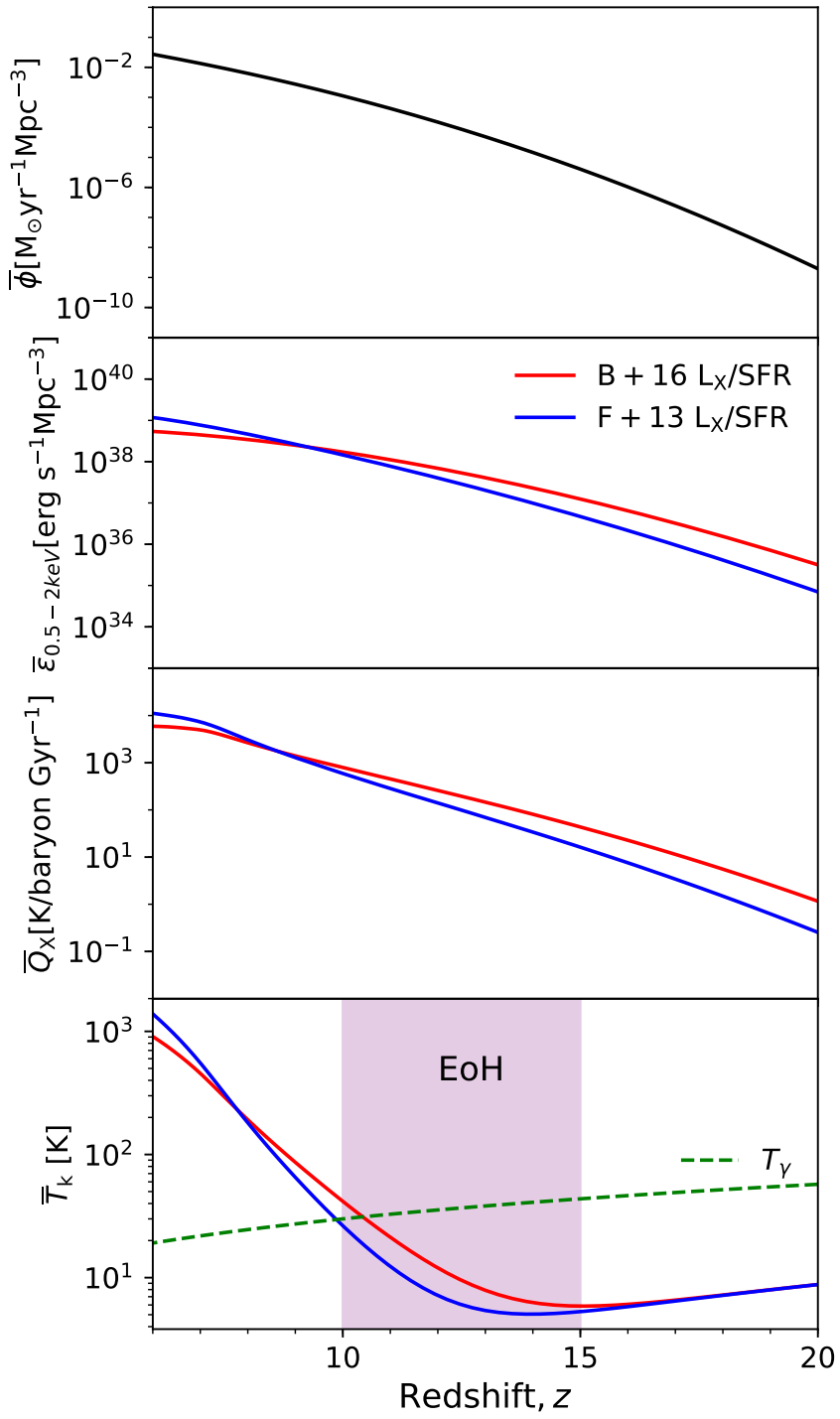


**Figure 5.7:** *From top to bottom*: redshift evolution of the (volume-averaged) star formation rate density (SFRD), soft-band X-ray emissivity (eq. 5.6), X-ray heating rate per baryon, $\overline{Q}_X$ (eq. 4.11), and kinetic temperature of the neutral IGM, $\overline{T}_k$ (eq. 4.10) computed using `21cmFAST`. Red and blue curves correspond to the $L_X$/SFR–$Z$ relations from B+16 and F+13a, respectively. In the bottom panel we also show the cosmic microwave background (CMB) temperature ($T_\gamma$) evolution with the dashed line, and approximately demarcate the epoch of heating (EoH).

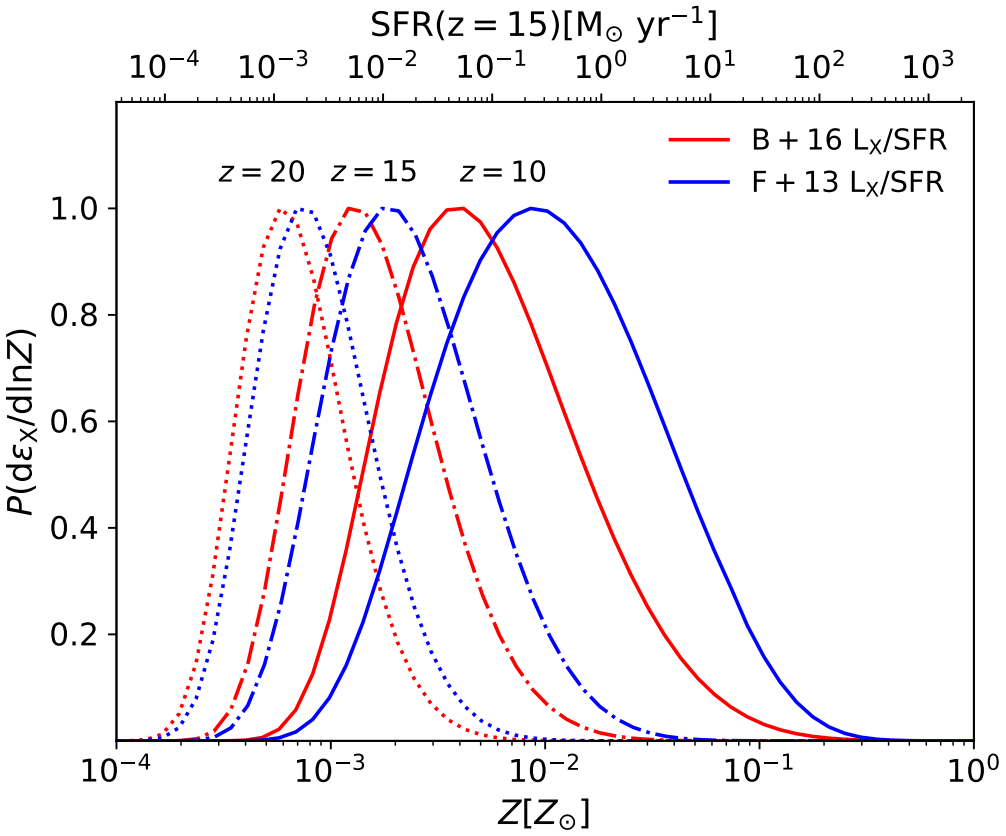


**Figure 5.8:** Fractional contribution to the total X-ray emissivity sourced by galaxies per logarithmic metallicity bin. B+16 and F+13a $L_X$/SFR–$Z$ relations are shown with red and blue curves respectively. Here different line styles represent different redshifts. On the top x-axis, we denote the corresponding SFR at $z = 15$. For viewing purposes, we normalize all PDFs to peak at unity.

these models corresponds to $10 \lesssim z \lesssim 15$. As a result, the EoH is driven by galaxies with metallicities $10^{-3} \lesssim Z/Z_{\odot} \lesssim 10^{-2}$ and SFRs roughly in the range $10^{-3} \lesssim \dot{M}_*/M_{\odot}\ \mathrm{yr}^{-1} \lesssim 10^{-1}$ (c.f. the top axis shows the corresponding SFRs implied by our model at $z = 15$).

## 5.3 Evolution of IGM properties

### 5.3.1 Temperature

We now compute the global evolution of the thermal and ionization state of the IGM, for the two X-ray emissivities shown in the previous section. We calculate the X-ray heating and ionization rates $Q_X$, $\Gamma_X$ respectively, and the redshift evolution of kinetic temperature $T_k$ in a similar manner as explained in Chapter 4 with the help of equations 4.9, 2.17, 4.11, 4.6 and 4.12.

In the bottom two panels of Figure 5.7, we show the volume-averaged $Q_X$ and $T_k$ corresponding to our two fiducial $L_X$/SFR–$Z$ relations. In the temperature panel, we also show the evolution of the CMB temperature, that provides the radio background in standard 21-cm models. We roughly demarcate the EoH as shown in the figure. The heating rate and kinetic temperature follow the same qualitative trend seen in the emissivity panel, with B+16 resulting in a higher temperature at redshifts $z \gtrsim 8$. The transition redshift at which F+13a surpasses B+16 is somewhat lower for temperature (bottom panel) compared to the emissivity (second panel). This is because the temperature depends on the light-cone integral over the emissivity, and not just its instantaneous value. The flattening of the heating rate seen at $z \lesssim 8$ is due to reionization by UV photons, which decreases the neutral fractions of hydrogen and helium.

### 5.3.2 21-cm signal

As mentioned in the introduction, we use the cosmic 21-cm signal as our fiducial observational data set, as it has the largest potential of constraining the thermal state of the gas in those early epochs.

In the top panel of Figure 5.9 we plot the redshift evolution of the global 21-cm signal, $\overline{\delta T}_b$, corresponding to the B+16 and F+13a $L_X$/SFR–$Z$ relations with solid red and blue lines respectively. Since the B+16 scaling implies stronger X-ray heating during the EoH, its $\overline{\delta T}_b$ has an earlier and shallower absorption trough as compared with F+13a. The differences between the global signal evolution implied by the two

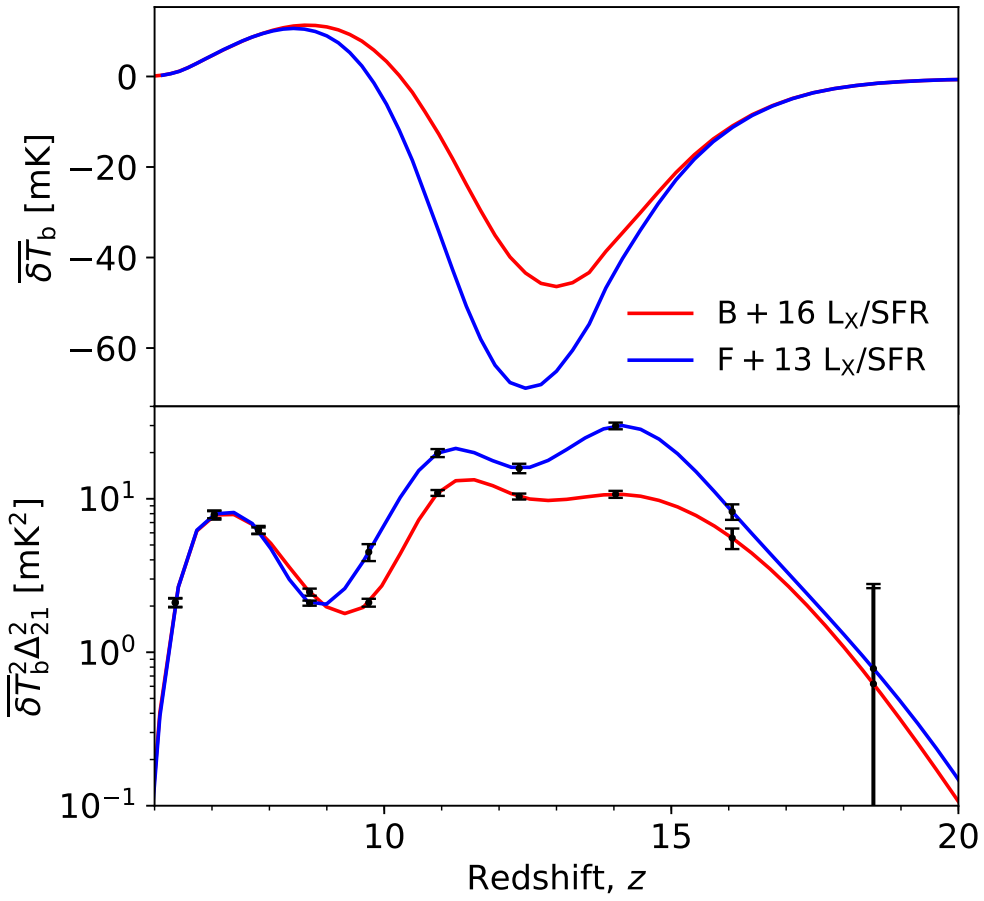


**Figure 5.9:** *Top panel*: redshift evolution of the global signal, $\overline{\delta T}_b$ for B+16 and F+13a $L_X$/SFR–$Z$ relations shown as red and blue curves, respectively. *Bottom panel:* corresponding redshift evolution of the 21-cm PS evaluated at $k = 0.1$ Mpc$^{-1}$. Error bars denote the $1\sigma$ uncertainty expected from a 1000h observation assuming optimistic foregrounds with the Square Kilometer Array (see Sect. 5.4 for details).

$L_X$/SFR–$Z$ relations peak during the epoch of heating with a 25 mK difference in the depths of the absorption troughs.

In the bottom panel of Figure 5.9 we plot the redshift evolution of the 21-cm power spectrum (PS) amplitude, evaluated at $k = 0.1$ Mpc$^{-1}$. We focus on this wavemode as it corresponds to a "sweet spot" for 21-cm interferometers: large enough to mitigate foreground contamination yet small enough to have low thermal noise (e.g. Mertens et al. 2020; Trott et al. 2020; HERA Collaboration et al. 2021a). The redshift evolution of the large-scale 21-cm power shows the characteristic three peaks, corresponding to the major astrophysical epochs: WF coupling, EoH, and EoR. We also show the expected thermal and cosmic variance noise for a 1000h observation, assuming optimistic foregrounds from Pober et al. (2014), with SKA (see §4.4 of Chapter 5 for details on how these uncertainties are calculated).

Comparing the two solid curves, we see that the B+16 scaling results in an earlier EoH. This increases the overlap between the EoH and the epoch of WF coupling: IGM in regions with an under-abundance of galaxies still has different spin and kinetic temperatures at the same time that the IGM in regions with an over-abundance of galaxies becomes hot (e.g. Mesinger, Ferrara, and Spiegel 2013). This decreases the temperature contrast during CD, resulting in lower PS amplitudes by up to a factor of $\sim 3$ for the B+16 scaling, compared with F+13a. We note that these two scenarios can be distinguished with a 1000h observation with SKA1-low.

## 5.4 Can constant X-ray luminosity – SFR models reproduce the metallicity-dependent signal?

Upcoming 21-cm observations will provide a physics-rich data set, allowing us to *infer* galaxy properties from the data directly. In particular, the signal is very sensitive to the X-ray properties of the first galaxies (e.g. Kern et al. 2017; Park et al. 2019), suggesting that the data could tell us the correct $L_X$/SFR–$Z$ and MZR scalings.

However, performing inference requires parametrizing these relations and adopting physically-motivated priors on the corresponding parameters. This is challenging, as our current understanding of stellar evolution and IMFs is insufficient to motivate such parameterizations and priors. In principle, these difficulties can be mitigated with Bayesian model selection (e.g., Binnie and Pritchard 2019a; Qin et al. 2020), which we will explore in a follow-up work. Nevertheless, having simpler models of $L_X$/SFR would make inference easier and quicker.

Indeed, most current models of the X-ray background during the Cosmic Dawn assume a constant $L_X$/SFR (e.g. Ghara et al. 2020; Mondal et al. 2020; Greig et al. 2021a; Greig et al. 2021b; HERA Collaboration et al. 2021b; though see Madau and Fragos 2017; Eide et al. 2018), motivated by the theoretical argument that the impact of metallicity-driven winds becomes negligible below $Z \lesssim 0.05\ Z_\odot$ (e.g. Fragos et al. 2013b). In this section, we quantify whether this simplification can recover the evolution of IGM properties of our metallicity-dependent models presented in the previous section. We make mock 21-cm PS observations using both B+16 and F+13a $L_X$/SFR–$Z$ relations, and then perform inference assuming a constant $L_X$/SFR. As the figure of merit, we compare the recovered 21-cm power spectra and the X-ray heating rates to the "truth" from the mock observations.

Our two mock observations correspond to the fiducial B+16 and F+13a models discussed in the previous section. To compute the thermal noise, we use the python module `21cmSENSE`[5] (Pober et al., 2013b; Pober et al., 2014) and assume a 1000h integration (6h per night) with the SKA1-low (as explained in details in §4.4 of chapter 4). In order to tightly constrain X-ray parameters and *maximize the importance of the metallicity dependence*, we use the "Optimistic foreground" flag in `21cmSENSE`. This setting assumes that the foreground wedge extends only up to the full-width half-max of the primary beam ; modes outside of this contaminated wedge are assumed to be free of systematics. Our mock observations span the redshift range $z = 5.8$ – 21.6 and wavemode range $k$= 0.1 – 1 Mpc$^{-1}$.

For performing inference using these mock observations, we use the public `21cmMC` module[6] (Greig and Mesinger, 2015; Greig and Mesinger, 2017a; Greig and Mesinger, 2018). `21cmMC` is a Bayesian sampler of `21cmFAST`, which forward-models 21-cm light-cones computed with `21cmFAST`, to calculate parameter inference. It provides two options for sampling the light-cones: the default option relies on a Monte Carlo Markov Chain (MCMC)-based tool, EMCEE (Goodman and Weare 2010; Akeret et al. 2013) and the other option is a nestled sampler called Multinest [7] ((Feroz and Hobson, 2008; Feroz, Hobson, and Bridges, 2009)), which was included in `21cmMC` by Qin et al. (2020). At each step, it compares the likelihood of its sampled model w.r.t. the mock observation using $\chi^2$ analysis. It utilizes the relationship between likelihood and prior and gives posterior distribution as a by-product of evidence calculation. Besides being a computationally less expensive option, it is consistent with parameter recovery of `21cmFAST` models with MCMC-based sampling of `21cmMC` (e.g. Binnie and Pritchard (2019b)). For sampled runs, we use box size of 250 Mpc while keeping resolution same as mock. The light-cones are then compressed to obtain the 3D PS, using the method outlined in Greig and Mesinger (2018).

In addition to the mock 21-cm signal, we also use the following current observations in the likelihood: (i) $z \geq 6$ UV luminosity functions (Finkelstein 2016; Ishigaki et al. 2018a; Bouwens et al. 2021, etc.), (ii) the electron scattering optical depth to CMB ( Planck Collaboration et al. (2016b)), and (iii) the dark fraction in the spectra of high-z quasars (e.g. McGreer, Mesinger, and D'Odorico (2015a)). We sample the following astrophysical parameters, adopting flat priors over the quoted ranges: $\log_{10} f_{*,10} \in [-3, 0]$, $\log_{10} f_{\rm esc,10} \in [-3, 0]$, $\alpha_* \in [-0.5, 1]$, $\alpha_{\rm esc} \in [-1, 0.5]$,

[5] https://github.com/jpober/21cmSense
[6] https://github.com/21cmfast/21CMMC
[7] https://github.com/rjw57/MultiNest

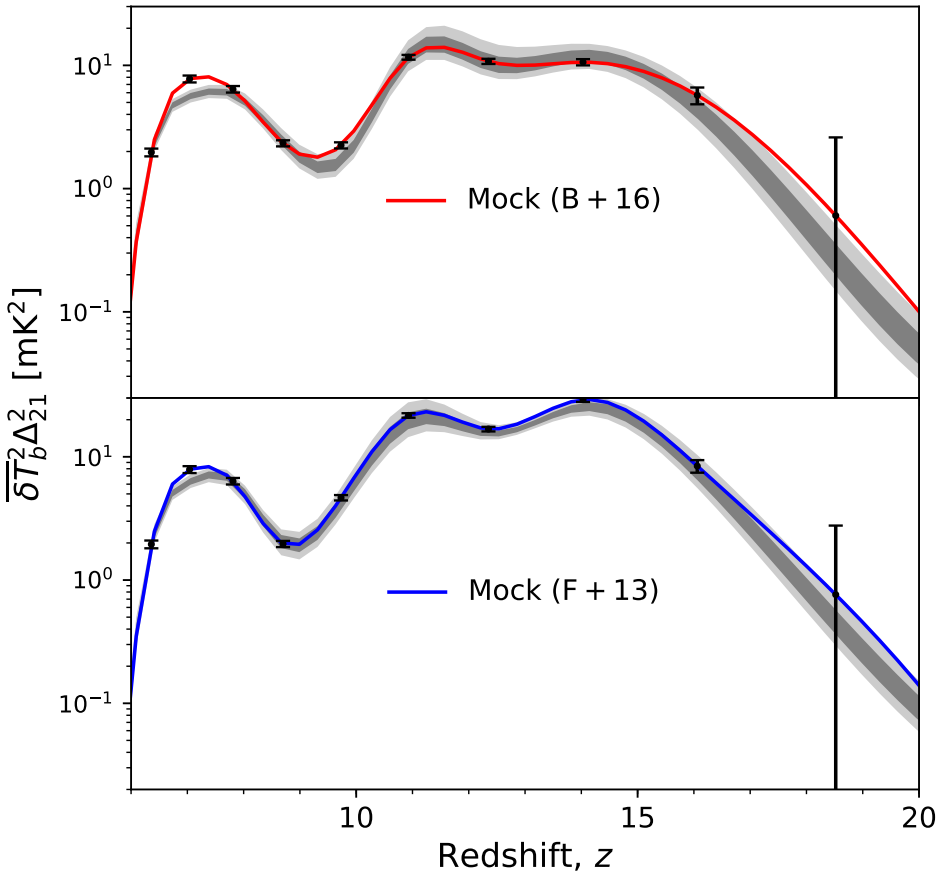


**Figure 5.10:** Redshift evolution of 21-cm power spectra evaluated at $k = 0.1\text{Mpc}^{-1}$. The two mock observations are shown in red (top panel; B+16) and blue (bottom panel; F+13a), with $1\sigma$ noise (thermal + cosmic variance) denoted with error bars (see text for details. The dark and light shaded regions correspond to $16-84\%$ and $2-98\%$ credible intervals (C.I.), respectively, obtained assuming a model with a constant (i.e. metallicity independent) $L_X$/SFR.

$\log_{10}(M_{\text{turn}}/\text{M}_\odot) \in [8, 10]$, $\log_{10}(L_X/\text{SFR}/\text{erg s}^{-1}\ \text{M}_\odot^{-1}\ \text{yr}) \in [38, 44]$ and $E_0 \in [0.1 - 1.5]$ keV.

In Figure 5.10, we show the recovered posteriors on the evolution of large-scale ($k = 0.1$ Mpc$^{-1}$) 21-cm PS. Points with error bars correspond to the mock observations assuming B+16 (top) and F+13a (bottom) scalings, while the shaded regions denote the posteriors obtained assuming a constant $L_X$/SFR. In Appendix B, we also show the PS posteriors as functions of wavemodes for all of the redshift samples we use in the mock observations.

The simple, constant $L_X$/SFR models are able to recover the PS evolution of the more sophisticated B+16 and F+13a models quite well. The posteriors are consistent

with the mock data at $1\sigma$ throughout the EoH.[8]

Interestingly, the largest discrepancies are found during the EoR, where the constant $L_X$/SFR models underestimate the B+16 21-cm PS by up to tens of percent. This is because most of the $L_X$/SFR constraining power comes from the EoH. Since the $L_X$/SFR–$Z$ scaling is very steep, the EoH galaxies at $10 \lesssim z \lesssim 15$ are considerably more efficient at emitting X-rays compared to EoR galaxies at $5 \lesssim z \lesssim 10$. By fitting to the EoH, the constant $L_X$/SFR models thus end up overpredicting the X-ray background during the EoR. In the case of B+16, this results in the neutral IGM patches being partially ionized by X-rays with long mean free paths. This decreases the 21-cm contrast between ionized and neutral regions during the patchy EoR, resulting in a smaller PS amplitude.

This is further illustrated in Figure 5.11, where we plot the analogous recovery of the X-ray heating rate (*left panels*) and the EoR history (*right panels*). Constant $L_X$/SFR models have a steeper redshift evolution of the heating rate. The inferred value of $L_X$/SFR corresponds to that of galaxies during the EoH at $10 \lesssim z \lesssim 15$, when the 21-cm signal is most sensitive to the X-ray background. However, towards the end of the EoR at $z \sim 6$, the inferred heating rate from constant $L_X$/SFR models can overestimate that from the mock observations by a factors of $\sim$ few – 10.

This overestimate of the X-ray background also means that the EoR begins earlier in constant $L_X$/SFR models (see right panels of Fig. 5.11), driven by a larger contribution of X-rays to reionization. The earlier onset of the EoR in constant $L_X$/SFR models can be partially compensated by increasing the UV ionizing emission of smaller halos. In our model this is mostly achieved through the $\alpha_{\rm esc}$ parameter, which we find is indeed the only UV parameter whose marginal PDFs are not consistent with the value of the mock observation at more than $2\sigma$ (see Appendix A). We will further quantify the recovery of galaxy properties using different parametric relations for both $L_X$/SFR and MZR in future work.

Our results imply that constant $L_X$/SFR models provide a reasonable simplification for modeling the 21-cm signal during the EoH. However, they overpredict the X-ray background at lower redshifts ($z < 10$). Tying observations over large redshift intervals without properly accounting for population-evolution (e.g. metallicity) could thus introduce significant errors.

[8] We remind the reader that our choice of "Optimistic Foregrounds" results in the small noise errors seen in this figure and in Appendix B. As a result the recovered posteriors are very narrow. We used the 'Optimistic Foregrounds' setting of `21cmSENSE` precisely to show the maximum expected bias from ignoring the metallicity dependence of $L_X$/SFR.

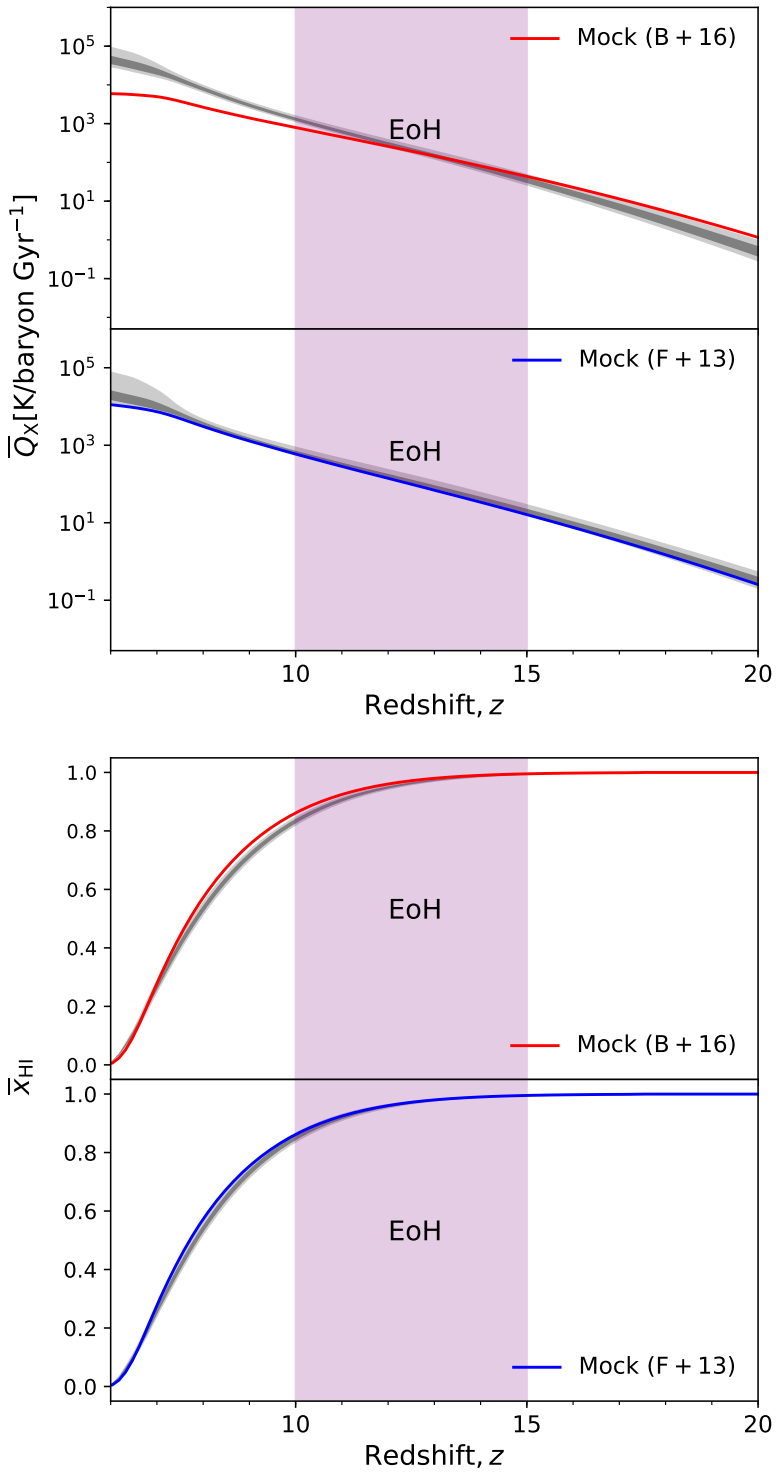


**Figure 5.11:** Same as Figure 5.10, but here showing the volume-weighted X-ray heating rate per baryon (*left panels*) and neutral hydrogen fraction (*right panels*).

## 5.5 Conclusions

The redshifted 21-cm signal is a promising probe of heating and ionization processes in the early Universe. In particular, we expect the heating of the IGM prior to reionization to be dominated by HMXBs, hosted by galaxies too faint to be observed directly. We expect these early galaxies to be metal poor, likely implying a more X-ray luminous HMXB population than observed in local galaxies (e.g. Linden et al. 2010; Fragos et al. 2013b; Basu-Zych et al. 2012; Brorby et al. 2016; Lehmer et al. 2021).

We adopt two very different $L_X$/SFR–$Z$ relations: (i) an empirical power law from Brorby et al. (2016); and (ii) a theoretical stellar evolution model from Fragos et al. (2013b). For the same galaxy evolution model, (i) and (ii) result in differences of up to a factor of $\sim$2–3 in the IGM temperature and 21-cm signal during the Cosmic Dawn.

HMXBs hosted by galaxies with SFRs of order $10^{-3}$ – $10^{-1}$ $M_\odot$ $yr^{-1}$ and metallicities of order 0.001 – 0.01 $Z_\odot$ dominate the IGM heating. The assumed $L_X$/SFR–$Z$ relation can shift these ranges by factors of $\sim$ few.

We also use the two $L_X$/SFR–$Z$ relations to compute mock 21-cm PS observations, assuming optimistic foreground removal and 1000h integration with SKA. We performed inference using the common simplification of a constant $L_X$/SFR. The constant $L_X$/SFR models reproduce the IGM properties from the metallicity-dependent $L_X$/SFR simulations quite well. However, since the inferred value of $L_X$/SFR corresponds to the dominant population during the EoH ($z \sim 10$–$15$; when the 21-cm signal is most sensitive to the IGM temperature), they overpredict the XRB at lower redshifts ($z \lesssim 10$). Thus, accurate inference over a broad range of redshifts should account for metallicity evolution and the $L_X$/SFR–$Z$ relation.

# Chapter 6

# Inferring the properties of HMXBs

In this chapter, we perform Bayesian inference to constrain the properties of the early HMXBs during the EoH. By employing a Schechter-like parameterization for the $L_X$/SFR–$Z$ relation and allowing the MZR to vary (see Chapter 5), we infer the parameters governing the EoH from mock 21-cm observations.

The structure of this chapter is as follows. In §6.1, we explain the motivation behind this work. We discuss our methodology in §6.2, showing some preliminary results in §6.3. We end the chapter with a discussion on future plans in §6.4. This is work in progress, expected to be submitted in 2023 (Qin et al, in prep.). Here we just briefly mention the current status.

## 6.1 Motivation

As discussed earlier, the 21-cm signal has the potential to probe the properties of HMXB and their host galaxies, including their $L_X$/SFR–$Z$ and MZR scalings. In our previous work discussed in Chapter 5, we saw how our simple metal-independent $L_X$/SFR models were able to recover the mock 21-cm observations and various IGM properties generated with metal-dependent $L_X$/SFR scalings of F+13a and B+16 models, during most of the EoH. However, the constant-metallicity models introduced biases at lower redshifts, including the EoR. Would a joint inference from EoR and EoH 21-cm observations bias the inferred properties of HXMBs, if metallicity dependence and the mass-metallicity relation are not properly included? How well could we constrain these properties of HMXBs and the host galaxy ISM? In a follow-up work (Qin et al., in prep), we employ a flexible parametrization of $L_X$/SFR–$Z$ and the MZR relations, and quantify how well they can be recovered from upcoming 21-cm observations.

## 6.2 Inference Methodology

### 6.2.1 Free parameters of the model

Our galaxy model consists of 13 free parameters which are summarized below. These include various UV and X-ray parameters based on the astrophysical model of Park et al. (2020) discussed in Chapter 4 (see §4.3), as well as those related to $L_X$/SFR–$Z$ and MZR relations introduced in Chapter 5 (in §5.2.1 and §5.2.2 respectively).

(i) $f_{*,10}$: The normalization of stellar fraction $f_*$ evaluated for halo mass of $10^{10}$ $M_\odot$. For generating mock observations we take its fiducial value as 0.05. We assume a prior over the following range: $f_{*,10} \in [-3, 0]$ in logarithmic space.

(ii) $\alpha_*$: The power-law index of $f_*$–$M_h$ scaling. We take its fiducial value as 0.5 and assume a flat prior over the range: $\alpha_* \in [-0.5, 1]$.

(iii) $f_{esc,10}$: The normalization of UV-escape fraction $f_{esc}$ evaluated for halo mass of $10^{10}$ $M_\odot$. For generating mock observations we take its fiducial value as 0.1, and for performing inference we take a prior over the range: $f_{esc,10} \in [-3, 0]$ in logarithmic space.

(iv) $\alpha_{esc}$: The power-law index of $f_{esc}$–$M_h$ scaling. Its fiducial value for mock is taken as -0.5. For inference, we assume a flat prior over the range: $\alpha_{esc} \in [-1, 0.5]$.

(v) $M_{turn}$: The fiducial value of the turnover halo mass for generating mock is taken as be $5 \times 10^8$ $M_\odot$, while the prior is varies over the range: $M_{turn}/M_\odot \in [8, 10]$ in logarithmic space.

(vi) $t_*$: The fiducial value of the star-formation time scale is taken as 0.5, while the flat prior is varied over (0, 1].

(vii) $E_0$: The fiducial value of minimum energy of X-ray photons escaping into the IGM is taken as 0.5 keV, and the flat prior on the parameter is varied between [0.1, 1.5].

(viii) $\alpha_X$: The power-law index of X-ray SED. Its fiducial value is taken as 1 while the allowed range for the flat prior is: [-1, 3].

(ix) $L_{X<2keV}$/SFR: The soft-band X-ray luminosity to SFR. We choose the prior over the following range: $L_{X<2keV}/SFR) \in [38, 45]$ in logarithmic space.

(xi) $Z_{turn}$: the turnover metallicity above which the $L_X$/SFR falls exponentially with $Z$ in our $L_X$/SFR–$Z$ model (see Fig. 5.5 of Chapter 5). We assume a flat prior over the range: $Z_{turn} \in [-1.5, 0]$.

(xi)$\alpha_Z$: The power-law slope of our $L_X$/SFR–$Z$ model at low metallicity. We assume a flat prior over the range: $\alpha_Z \in [-0.5, 1.0]$.

(xii)$M_{\rm turn,\,Z}$: a redshift dependent characteristic mass scale above which metallicity saturates, as explained in eq. 5.3 of Chapter 5. We choose a prior over the range: $M_{\rm turn,\,Z}/{\rm M}_\odot \in [8, 10]$ in logarithmic space.

(xiii) $\gamma_Z$: The power law index of MZR for stellar mass less than turnover mass. Its fiducial value is taken to be 0.522. We take a flat prior over the range: $\gamma_Z \in [-0.5, 1.5]$.

## 6.3 Preliminary results

We quantify how various parameters of our model are constrained by the observed UV LFs, $L_X$/SFR–$Z$ observations and mock observations of the 21-cm power spectra obtained with F+13a and B+16 models of the previous work. In Fig. 6.1 we show a corner plot of the posterior distribution over the model parameter discussed in the previous section (*blue curves*). The solid curves denote values used for the mock 21-cm observation. For comparison, in red we also show the posteriors recovered assuming a constant $L_X$/SFR, for those parameters that exist in that model (see previous chapter). The parameter recovery is very good, with the notable exception of $\alpha_{\rm esc}$, which is highly biased. This bias is a result of our underestimation of non Gaussian cosmic variance (discussed in the next section).

The top panels of the figure contain the recovered posteriors on $L_X$/SFR–$Z$ (*middle panel*) as well as MZR at different redshifts (*right panel*). The $L_X$/SFR–$Z$ observations (shown previously in Fig. 5.5) are marked as black circles along with their error bars. It can be seen that both relations are recovered by our inference within 1 $\sigma$. Note that we assume the power law $L_X$/SFR–$Z$ relation from B+16 (*top middle panel*), which we recover using our Schecter form that is a good match of the model from F+13a. Despite the mismatch of functional shapes, the $L_X$/SFR–$Z$ relation is reasonably recovered.

## 6.4 Future plans

Unfortunately, our constraints shown in Fig. 6.1 are limited by cosmic variance. Our choice of "optimistic" foregrounds meant that the instrument error bars were so small as to be sensitive to non-Gaussianity in the error covariance (e.g Iliev et al. 2006; Watkinson and Pritchard 2015; Majumdar et al. 2018). Because we did not covary the cosmic initial random seed, our predictions assuming Gaussian errors are somewhat biased and overly optimistic. We are currently re-running our inferences

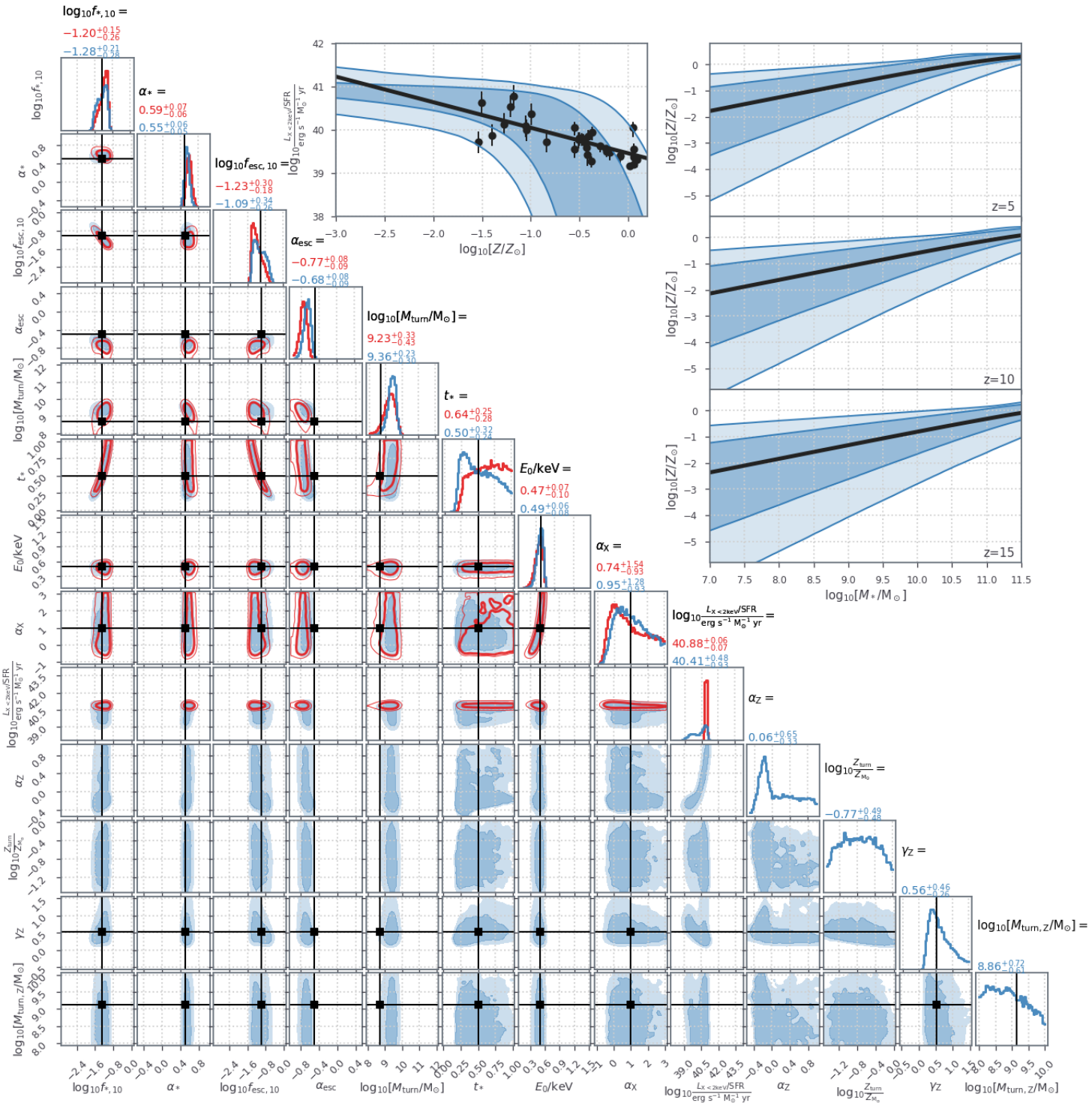


**Figure 6.1:** Recovered posteriors of our fiducial model with parametrized $L_X$/SFR–$Z$ and MZR scalings (blue), together with the recovery of a simplified, constant $L_X$/SFR–$Z$ model (*red*). 2D and 1D posteriors of the model parameters are shown in the bottom left, while the $L_X$/SFR–$Z$ and MZR posteriors are shown in the top. Data points in the $L_X$/SFR–$Z$ panel correspond to local observations (see Fig. 5.5 for references), and are used to motivate the prior for the high metallicity turnover for our $L_X$/SFR–$Z$ relation. Solid curves and vertical lines denote values used to generate the 21-cm mock observation, but using different cosmic seeds than used for inference.

assuming the more realistic "moderate foreground model" (for details of the model, see §4.4 of Chapter 4) for computing noise and using larger boxes for accounting for cosmic variance. This will allow us to more accurately quantify what constraints can be expected on these properties from upcoming observations, as well as the level of bias introduced by neglecting the metallicity evolution of the Xray emissivity.

Furthermore, the unresolved cosmic X-ray background (CXB) can be used to place upper limits on the X-ray emissivity of high-redshift galaxies (e.g. Furlanetto, Peng Oh, and Briggs 2006; McQuinn 2012; Dijkstra et al. 2012; Fialkov et al. 2016). Because of redshifting, the CXB from the EoH sources is sourced by photons with energies of $\sim$ 10–20 keV. This is in contrast with the photons that are responsible for heating the IGM, with energies below 1–2 keV (see previous chapter). Therefore, using the unresolved CXB to place upper limits on the X-ray luminosity of the first galaxies is highly dependent on the assumed SED between 1 and 20 keV. We will explore double power-law SED models, motivated by recent NuSTAR observations of HXMB-dominated nearby galaxies (e.g. Lehmer et al. 2015).

# Chapter 7

# Conclusions and future prospects

The 21-cm signal is set to revolutionize our understanding of the high-redshift Universe covering the epoch of reionization, Cosmic Dawn, and possibly the later stages of the dark ages. It will soon be detectable by various ongoing or upcoming interferometric experiments such as HERA and SKA. The X-rays emitted by high-mass X-ray binaries are expected to be the dominant sources of heating of the IGM during the epoch of heating, leaving its imprint in the 21-cm signal. Therefore, in this Thesis, we have employed the 21-cm signal to infer the X-ray properties of the early galaxies.

As the signal depends on the thermal and ionization state of the intergalactic medium, a correct interpretation of its observations calls for accurate modeling of the early galaxies and their cosmic radiation fields which drive the signal. Since the early sources of radiation were hosted by rare and biased halos, the additional power of 21-cm fluctuations on large scales is not properly captured by cosmological simulations of small box sizes. This problem becomes all the more relevant for modeling the X-ray radiation which can have mean free paths of hundreds of megaparsecs at high redshifts. We have addressed this problem of underestimation and bias of the 21-cm power in cosmological simulations of small box sizes. Using the three-dimensional 21-cm power spectrum as the observable, we have quantified the minimum size of a simulation box required to achieve reliable results on the 21-cm signal from the Cosmic Dawn up to the epoch of reionization. By taking a reference box of length 1.1 Gpc per side, we performed a convergence study by running simulations of varying box sizes as well as initial conditions of the Gaussian random field. The telescope noise associated with the signal was also taken into account, for which we computed thermal noise for 1000h integration with SKA-1 Low. Besides thermal noise and sample variance, we also factored in Poisson uncertainty associated with the power spectrum. Our study indicates that simulation boxes of size 200-300 Mpc underestimate the 21-cm power by $\sim$7–9 percent during the Cosmic

Dawn. This bias is however not particularly noticeable in boxes of length less than 200 Mpc during the EoR. We also observed a notable scatter in the power spectra of different realizations of the same box length. Both the bias and scatter decrease with increasing box size. The average of the absolute differences in the power spectra of smaller boxes with respect to our reference over different realizations reached up to $\sim 7$ mK$^2$ for the smallest box of length 188 Mpc. The quantity in terms of total noise reached values of $\sim 4\sigma$ for the smallest boxes of lengths 188 and 281 Mpc. For the summary statistic, we marginalized these differences in terms of noise over the entire wavemode-redshift space and weighted them with the corresponding signal-to-noise ratios. We came to the conclusion that we need simulations of box length of at least 250 Mpc per size in order for the signal to converge at the level of $\lesssim 1\sigma$ of total noise. We tested our results for a different astrophysical model in which the turnover halo mass was increased by a factor of 10. The variance in the smallest simulation box increases while the punchline results remain roughly the same. We conclude that simulation boxes of length $\gtrsim 250$ Mpc are required for this model too.

After working out the minimum simulation box size for modeling the X-rays, we moved on to our next work, which involved modelling the X-ray radiation emitted by high-mass X-ray binaries during the EoH. Both low-redshift and theoretical models imply that the galaxy-integrated X-ray luminosity to star-formation rate scaling of HMXBs should increase in metal-poor environments, typical of early galaxies. In our work, we studied the imprint of metallicity ($Z$) dependence of $L_X$/SFR relations in the 21-cm signal from the Cosmic Dawn. Assuming a mass-metallicity relation, we computed how the 21-cm signal evolves corresponding to two different scalings of $L_X$/SFR with $Z$. We quantified the impact of $L_X$/SFR–$Z$ relations on X-ray emissivity and temperature evolution of the IGM and made forecasts for the associated 21-cm signal. For our fiducial models, galaxies with star-formation rates of the order $10^{-3}$ M$_\odot$ yr$^{-1}$–$10^{-1}$ M$_\odot$ yr$^{-1}$ and metallicities between $10^{-3}$ Z$_\odot$ and $10^{-2}$ Z$_\odot$ are the dominant contributors of the X-ray background during the EoH. Different $L_X$/SFR–$Z$ relations result in factors of $\sim 3$ differences in these ranges, as well as in the mean IGM temperature and the large-scale 21-cm power, at a given redshift. We computed mock 21-cm observations adopting as a baseline a 1000h integration with SKA, for the two $L_X$/SFR–$Z$ relations. We performed inference on these mock observations using the common simplification of a constant $L_X$/SFR, finding that constant $L_X$/SFR models can recover the IGM evolution of the more complicated $L_X$/SFR–$Z$ simulations only during the EoH. At $z < 10$, where the typical galaxies

are more polluted, constant $L_X$/SFR models over-predict the XRB and its relative contribution to the early stages of reionization. We are further working in the same direction, aiming to probe the nature of high-redshift HMXBs through the 21-cm signal. With the help of a single parameterization for $L_X$/SFR relations, we perform Bayesian inference to constrain the X-ray properties of the early galaxies during the EoH.

These are exciting times for studying the high-redshift HMXBs with the help of the 21-cm hydrogen line as interferometers have already started to provide constraints on Cosmic Dawn and epoch of heating.

# Appendix A

# Dependence on astrophysics

This Appendix contains the work of Kaur, Gillet, and Mesinger (2020), performed with a different astrophysical model, therefore serving as an extension to Chapter 4.

In order to test the dependence of the conclusions obtained in Chapter 4 on the astrophysical parameters, we perform another convergence test, by increasing $M_{\rm turn}$ by a factor of 10 i.e. $M_{\rm turn} = 5 \times 10^9$ M$_\odot$, while keeping the other parameters the same. Increasing $M_{\rm turn}$ corresponds to increasing the bias of star-forming galaxies. This will result in a delay in all astrophysical epochs as the relevant radiation fields are affected. The bias will also enhance spatial fluctuations and therefore increase the amplitude of the power spectrum (e.g. Greig and Mesinger 2017a). With the mentioned astrophysical model, simulations were run for different box sizes, i.e. $N_{\rm real} = 20, 20, 15, 10, 10$ realizations of $L = 188, 281, 375, 469, 563$ Mpc respectively, comparing them to a 1125 Mpc mock observation generated with the same astrophysics. The right panel of Figure A.1 shows the power spectrum of the reference run with box size 1125 Mpc. As compared to the previous astrophysical model, this model has a large scale PS with delay in WF coupling, EoH and EoR peaks shifted to $z \sim 12$, 9, and 6 respectively. The left panel shows the slice-plot through the corresponding to the brightness temperature at $z \sim 12$ and the bottom panel shows the corresponding signal-to-noise plot. Noise PS corresponding to this astrophysical has more amplitude than the that of the previous model at large scales (compare with 4.11). This is because sample variance is higher in case of larger power spectrum.

The absolute differences in the power spectra of smaller boxes w.r.t. the reference box, averaged over realizations (c.f. 4.25), are plotted in Fig. A.2, and the differences in terms of noise are shown in Fig. A.3. As expected, the relative differences decrease with increase in box size.

The punchline plot of S/N-weighted average (e.q. 4.26) is shown Fig. A.4, which is analogous to Fig. 4.15 for our fiducial astrophysics. It can be seen that the variance in the smallest box sizes has increased for this model. Overall, the trends are roughly

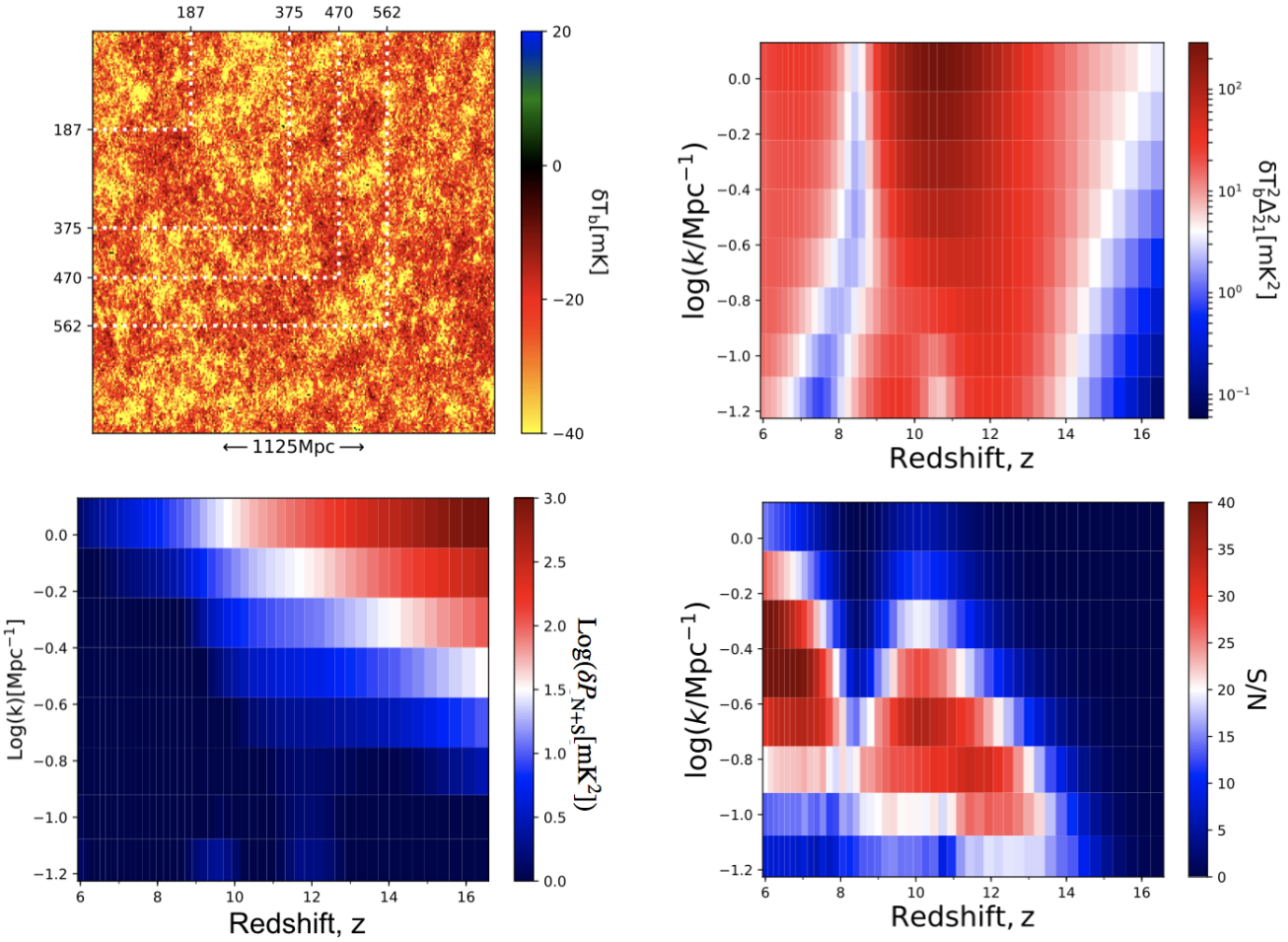


**Figure A.1:** *Top left panel* contains a slice through the brightness temperature at $z = 12$ in a simulation box of length 1125 Mpc per side. The white dotted lines mark different simulation sizes. *Top right* and *Bottom left panels* display the redshift evolution of the 21-cm PS and noise, respectively, *Bottom right panel* shows the corresponding signal-to-noise ratio.

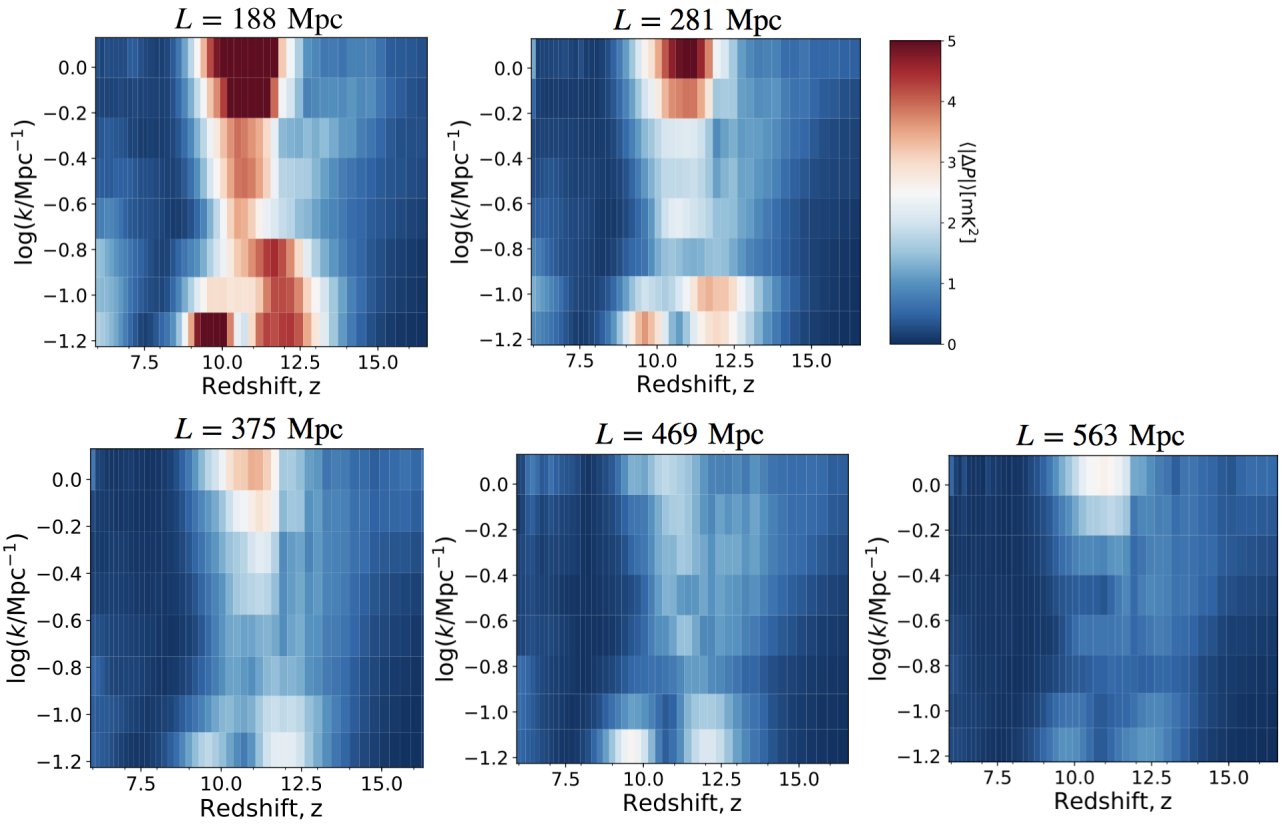


**Figure A.2:** Absolute difference in the PS of $L$=188, 281, 375, 469 and 563 Mpc boxes, with respect to the reference 1125 Mpc box, averaged over different realizations.

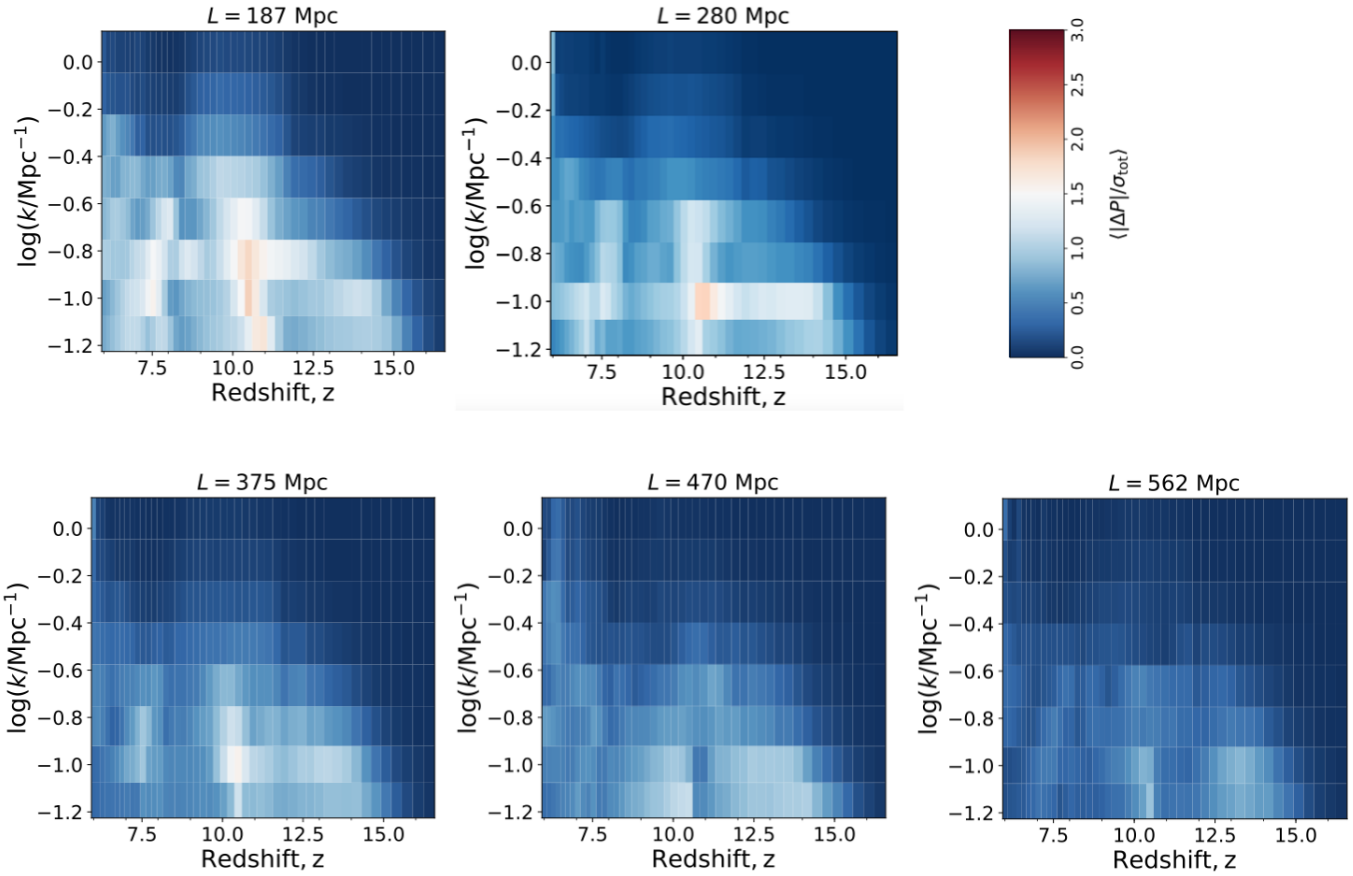


**Figure A.3:** Same as Fig. A.2, but dividing by the total noise (thermal and sample variance) in each (k; z) bin.

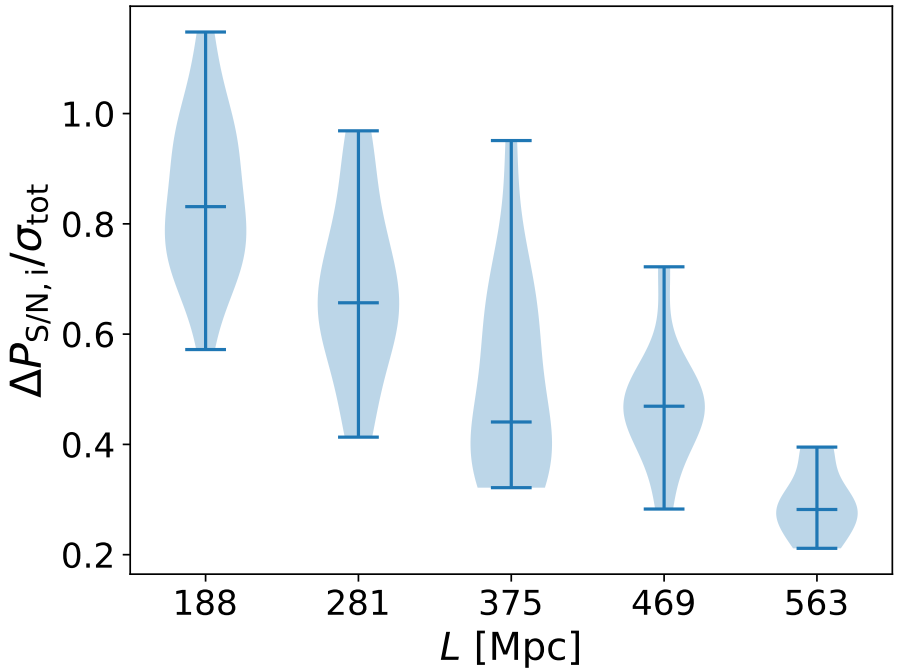


**Figure A.4:** Violin plots of the S/N-weighted average over (k; z) of the absolute difference in PS amplitude, in units of the total noise (see equation). The middle horizontal lines denote the median of the distributions over realizations, *i*, while the bars enclose the full extent. Both the median and the spread of the S/N-weighted PS error decrease with increasing box size.

the same as those noted for the fiducial model. Specifically, it can be concluded that box sizes of $\gtrsim$ 250 Mpc are required for the PS to converge to within 1 $\sigma$ of the total noise. This is mostly because although the large-scale 21-cm PS of the $M_{\rm turn} = 5 \times 10^9$ M$_\odot$ model is larger, so is the corresponding sample variance component of the noise. Therefore the convergence criteria expressed in terms of the total noise are comparable.

# Appendix B

# 21-cm power spectra

In this Appendix, we include the supplementary material related to the work of Kaur et al. (2022) in which we studied the effect of the correlation of $L_X$/SFR from HMXBs with metallicity on the 21-cm signal.

Here we show the 21-cm power spectra used in the two inferences from Chapter 5. In Figure A1, the black curves correspond to the B+16 $L_X$/SFR–$Z$ relation, with error bars marking $1\sigma$ noise. The recovered posterior assuming a metallicity-independent $L_X$/SFR is shown in red. Figure Fig. A2 is analogous to Fig. A1, but using the F+13a relation for the mock observation. We see that the constant $L_X$/SFR models reproduce the 21-cm PS quite well over the EoH. However, the steeper redshift evolution implied by the constant $L_X$/SFR models over-estimates the contribution of X-rays to the early stages of the EoR (see Fig. 5.11), which translates to a $\sim$ tens of percent underprediction of large scale 21-cm power (c.f. Fig. 5.10) and a biased recovery of the ionizing escape fraction scaling with halo mass, $\alpha_{\rm esc}$, shown in Fig. A3. We explore the recovery of galaxy parameters using different parametric relations for $L_X$/SFR and MZR in a follow-up work discussed in Chapter 6.

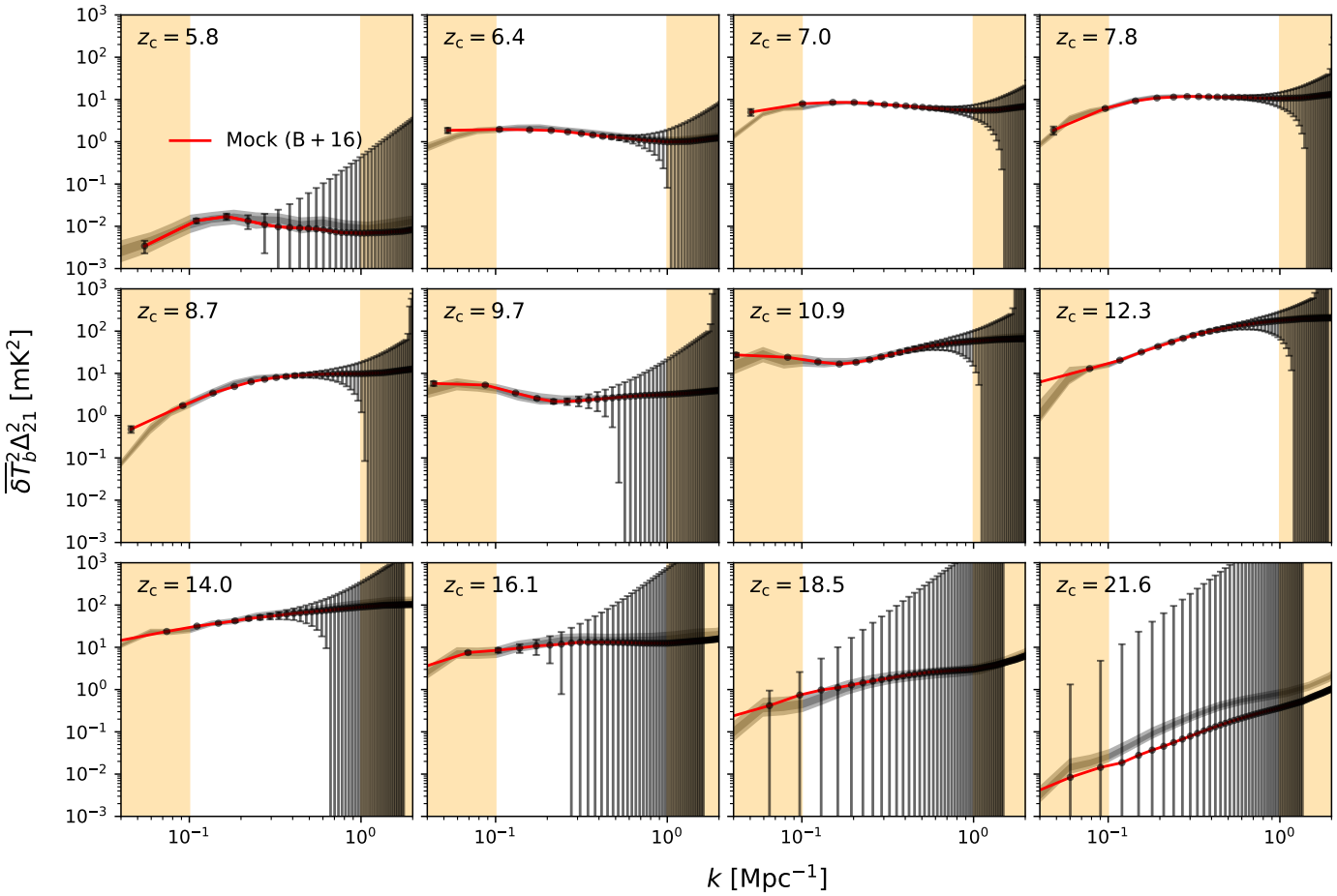


**Figure A1:** 21-cm power spectra. The mock observation corresponding to the B+16 $L_X$/SFR–$Z$ scaling is shown in red with error bars representing $1\sigma$ noise assuming a 1000 hr observation with SKA1-low. The dark and light shaded regions denote 16-84% and 2-98% confidence intervals, respectively, obtained assuming a constant $L_X$/SFR. $z_c$ denotes the central redshift of the light-cone chunk used to compute the power spectra. We demarcate with yellow stripes the $k$ modes outside of the $k$ = 0.1 – 1 Mpc$^{-1}$ range used to compute the likelihood.

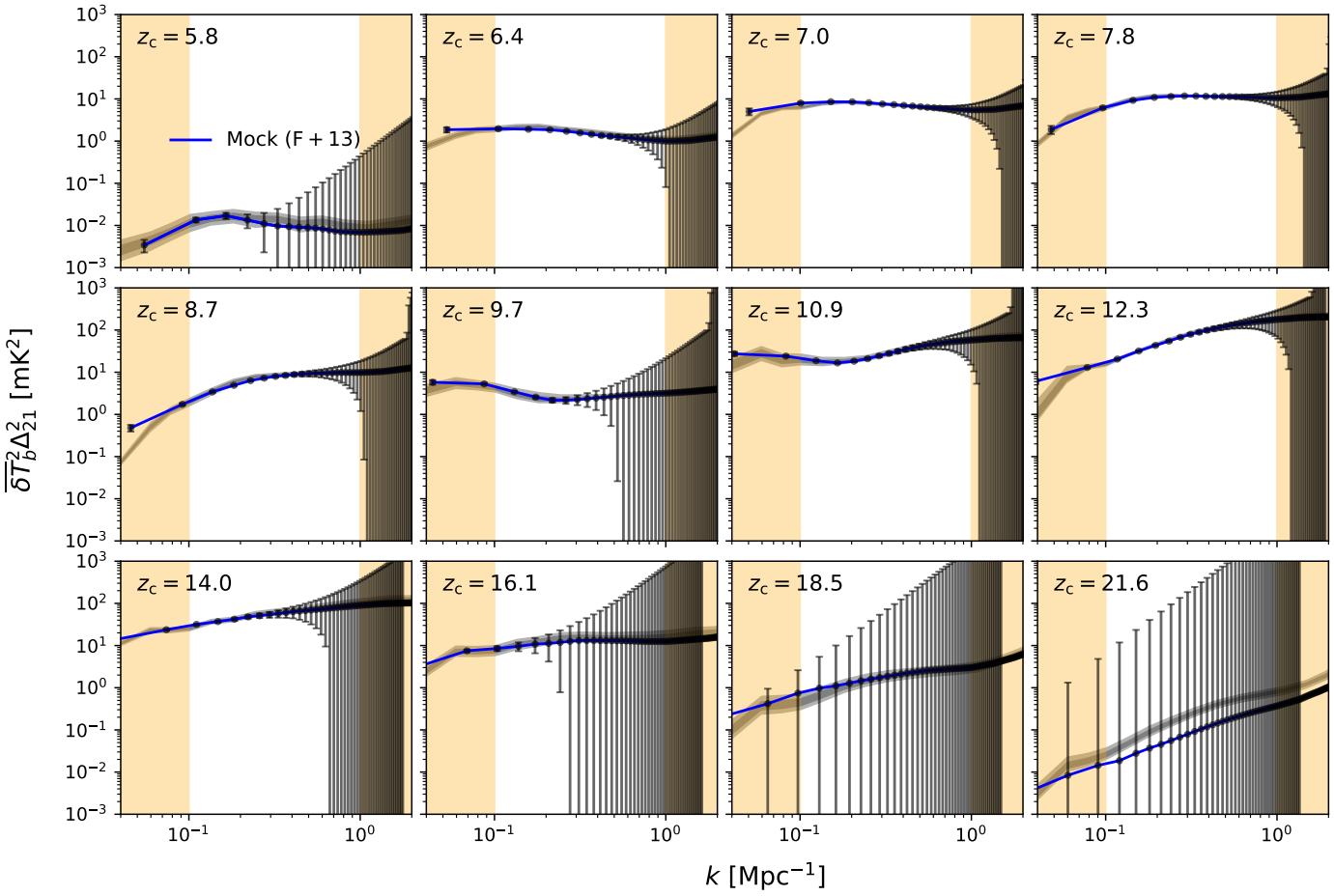


**Figure A2:** Same as Figure A1 but using F+13a $L_X$/SFR–$Z$ scaling as our mock observation (blue curve).

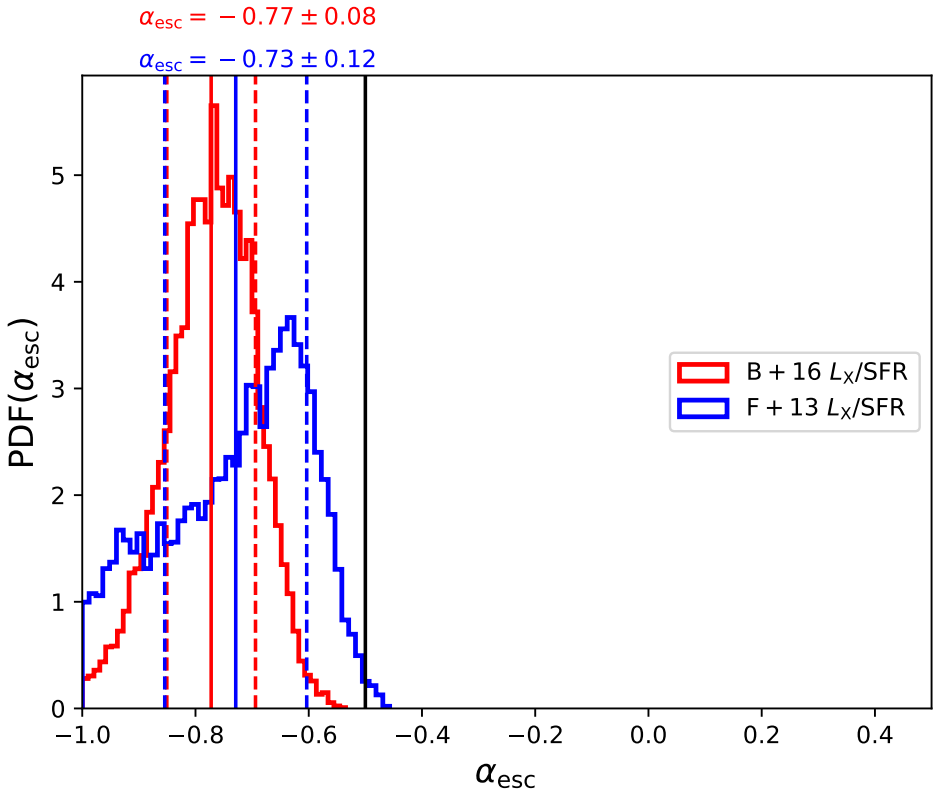


**Figure A3:** Marginalized 1D PDFs of the power law scaling index of the ionizing escape fraction with halo mass, $\alpha_{esc}$, for constant $L_X$/SFR models. The PDFs inferred from mock data created using B+16 / F+13a relations are denoted in red / blue. The mean and 1 $\sigma$ r.m.s. width are denoted with solid and dashed vertical lines, respectively. The vertical black denotes the "true" value used in making the mock simulations. The horizontal range shows the extent of our flat prior on $\alpha_{esc}$. Due to our choice of "Optimistic foregrounds", $\alpha_{esc}$ is very tightly constrained from the mock data. However, the recovered values for the constant $L_X$/SFR models are biased, in order to compensate for the their implied additional contribution of X-rays to the very early stages of reionization, as discussed in the text. We will return to the recovery of galaxy properties in a follow-up work, including parametric models for the X-ray properties of the first galaxies.

# List of Figures

# List of Tables

# List of acronyms

| | |
|---|---|
| **EoR** | **E**poch **o**f **R**eionization |
| **IGM** | **I**nter **G**alactic **M**edium |
| **CMB** | **C**osmic **M**icrowave **B**ackground |
| **JWST** | **J**ames **W**ebb **S**pace **T**elescope |
| **ALMA** | **A**tacama **L**arge **M**illimeter/submillimeter **A**rray |
| **HMXB** | **H**igh **M**ass **X**ray **B**inary |
| **CDM** | **C**old **D**ark **M**atter |
| **CD** | **C**osmic **D**awn |
| **EoH** | **E**poch **o**f **H**eating |
| **COBE** | **CO**smic **B**ackground **E**xplorer |
| **WMAP** | **W**ilkinson **M**icrowave **A**nisotropy **P**robe |
| **EoH** | **E**poch **o**f **H**eating |
| **BAO** | **B**aryonic **A**coustic **O**scillations |
| **SDSS** | **S**loan **D**igital **S**ky **S**urvey |
| **FRW** | **F**riedmann **R**obertson **W**alker |
| **HMF** | **H**alo **M**ass **F**unction |
| **QSO** | **Q**uasi- **S**tellar **O**bject |
| **IMF** | **I**nitial **M**ass **F**unction |
| **LAE** | **L**yman **A**alpha **E**mitters |
| **AGN** | **A**ctive **G**alactic **N**uclei |
| **ISM** | **I**nter **S**tellar **M**edium |
| **CDF-S** | **C**handra **D**eep **F**ield **S**outh |
| **LMXB** | **L**ow **M**ass **X**ray **B**inary |
| **PS** | **P**ower **S**pectrum |
| **SED** | **S**pectral **E**nergy **D**istribution |
| **PAPER** | **P**recision **A**rray to **P**robe the **E**poch of **R**eionization |
| **MWA** | **M**urchison **W**idefield **A**rray |
| **GMRT** | **G**iant **M**etrewave **R**adio **T**elescope |
| **HERA** | **H**ydrogen **E**och of **R**eionization **A**rray |
| **SKA** | **S**quare **K**ilometer **A**rray |
| **SARAS** | **S**haped **A**ntennas to measure the background **RA**dio **S**pectrum |
| **EDGES** | **E**xperiment to **D**etect the **G**lobal **E**oR **S**ignature |
| **RT** | **R**adiative **T**ransfer |
| **LF** | **L**uminosity **F**unction |
| **FWHM** | **F**ull **W**idth **H**alf **M**aximum |
| **ULX** | **U**ltra **L**luminous **X**ray Sources |
| **LBA** | **L**yman **B**reak **A**nalog |
| **GALEX** | **GAL**axy evolution **EX**plorer |
| **CANDELS** | **C**osmic **A**ssembly **N**ear-infrared **D**eep **E**xtragalactic **L**egacy **S**urvey |
| **MOSDEF** | **MOS**FIRE **D**eep **E**volution **F**ield |
| **2MASS** | **2M**icron **A**ll **S**ky **S**urvey |
| **DEEP2** | **D**eep **E**xtragalactic **E**volutionary **P**robe2 |

| | |
|---|---|
| **SHELS** | **S**mithsonian **H**ectospec **L**ensing **S**urvey |
| **SFRD** | **S**tar **F**ormation **R**ate **D**ensity |
| **MCMC** | **M**onte **C**arlo **M**arkov **C**hain |
| **NuSTAR** | **Nu**clear **S**pectroscopic **T**elescope **AR**ray |

# Bibliography


Abel, Tom, Greg L. Bryan, and Michael L. Norman (Jan. 2002). "The Formation of the First Star in the Universe". In: *Science* 295.5552, pp. 93–98. DOI: 10.1126/science.295.5552.93. arXiv: astro-ph/0112088 [astro-ph].

Aird, J., A. L. Coil, and A. Georgakakis (Mar. 2017). "X-rays across the galaxy population - I. Tracing the main sequence of star formation". In: MNRAS 465.3, pp. 3390–3415. DOI: 10.1093/mnras/stw2932. arXiv: 1611.03508 [astro-ph.GA].

Aird, J. et al. (Aug. 2015). "The evolution of the X-ray luminosity functions of unabsorbed and absorbed AGNs out to z$\sim$ 5". In: MNRAS 451.2, pp. 1892–1927. DOI: 10.1093/mnras/stv1062. arXiv: 1503.01120 [astro-ph.HE].

Akeret, Joël et al. (Aug. 2013). "CosmoHammer: Cosmological parameter estimation with the MCMC Hammer". In: *Astronomy and Computing* 2, pp. 27–39. DOI: 10.1016/j.ascom.2013.06.003.

Asplund, M. et al. (Apr. 2004). "Line formation in solar granulation. IV. [O I], O I and OH lines and the photospheric O abundance". In: A&A 417, pp. 751–768. DOI: 10.1051/0004-6361:20034328. arXiv: astro-ph/0312290 [astro-ph].

Atek, Hakim et al. (Oct. 2018). "The extreme faint end of the UV luminosity function at z $\sim$ 6 through gravitational telescopes: a comprehensive assessment of strong lensing uncertainties". In: MNRAS 479.4, pp. 5184–5195. DOI: 10.1093/mnras/sty1820. arXiv: 1803.09747 [astro-ph.GA].

Baek, S. et al. (Nov. 2010). "Reionization by UV or X-ray sources". In: A&A 523, A4, A4. DOI: 10.1051/0004-6361/201014347. arXiv: 1003.0834 [astro-ph.CO].

Bardeen, J. M. et al. (May 1986). "The Statistics of Peaks of Gaussian Random Fields". In: ApJ 304, p. 15. DOI: 10.1086/164143.

Barkana, Rennan (Mar. 2018). "Possible interaction between baryons and dark-matter particles revealed by the first stars". In: Nature 555.7694, pp. 71–74. DOI: 10.1038/nature25791. arXiv: 1803.06698 [astro-ph.CO].

Barkana, Rennan and Abraham Loeb (July 2001). "In the beginning: the first sources of light and the reionization of the universe". In: *Physics Reports* 349.2, 125–238. ISSN: 0370-1573. DOI: 10.1016/s0370-1573(01)00019-9. URL: http://dx.doi.org/10.1016/S0370-1573(01)00019-9.

Barkana, Rennan and Abraham Loeb (July 2004). "Unusually Large Fluctuations in the Statistics of Galaxy Formation at High Redshift". In: *The Astrophysical Journal* 609.2, pp. 474–481. DOI: 10.1086/421079. URL: https://doi.org/10.1086/421079.

Barkana, Rennan and Abraham Loeb (May 2005). "A Method for Separating the Physics from the Astrophysics of High-Redshift 21 Centimeter Fluctuations". In: ApJ 624.2, pp. L65–L68. DOI: 10.1086/430599. arXiv: astro-ph/0409572 [astro-ph].

Basu-Zych, Antara R. et al. (Dec. 2012). "THE X-RAY STAR FORMATION STORY AS TOLD BY LYMAN BREAK GALAXIES IN THE 4 Ms CDF-S". In: *The Astrophysical Journal* 762.1, p. 45. ISSN: 1538-4357. DOI: 10.1088/0004-637x/762/1/45. URL: http://dx.doi.org/10.1088/0004-637X/762/1/45.

Baumann, Daniel (July 2009). "TASI Lectures on Inflation". In: *arXiv e-prints*, arXiv:0907.5424, arXiv:0907.5424. arXiv: 0907.5424 [hep-th].

Beardsley, A. P. et al. (Dec. 2016). "First Season MWA EoR Power spectrum Results at Redshift 7". In: ApJ 833.1, 102, p. 102. DOI: 10.3847/1538-4357/833/1/102. arXiv: 1608.06281 [astro-ph.IM].

Becker, Robert H. et al. (Dec. 2001). "Evidence for Reionization at z∼6: Detection of a Gunn-Peterson Trough in a z=6.28 Quasar". In: AJ 122.6, pp. 2850–2857. DOI: 10.1086/324231. arXiv: astro-ph/0108097 [astro-ph].

Behroozi, Peter et al. (May 2019). "UniverseMachine: The correlation between galaxy growth and dark matter halo assembly from $z = 0$–10". In: *Monthly Notices of the Royal Astronomical Society* 488.3, 3143–3194. ISSN: 1365-2966. DOI: 10.1093/mnras/stz1182. URL: http://dx.doi.org/10.1093/mnras/stz1182.

Behroozi, Peter S. and Joseph Silk (Jan. 2015). "A SIMPLE TECHNIQUE FOR PREDICTING HIGH-REDSHIFT GALAXY EVOLUTION". In: *The Astrophysical Journal* 799.1, p. 32. ISSN: 1538-4357. DOI: 10.1088/0004-637x/799/1/32. URL: http://dx.doi.org/10.1088/0004-637X/799/1/32.

Belczynski, Krzysztof, Vassiliki Kalogera, and Tomasz Bulik (June 2002). "A Comprehensive Study of Binary Compact Objects as Gravitational Wave Sources: Evolutionary Channels, Rates, and Physical Properties". In: ApJ 572.1, pp. 407–431. DOI: 10.1086/340304. arXiv: astro-ph/0111452 [astro-ph].

Belczynski, Krzysztof et al. (Jan. 2008). "Compact Object Modeling with the StarTrack Population Synthesis Code". In: *The Astrophysical Journal Supplement Series* 174.1, pp. 223–260. DOI: 10.1086/521026. URL: https://doi.org/10.1086/521026.

Binnie, T. and J. R. Pritchard (July 2019a). "Bayesian model selection with future 21cm observations of the epoch of reionization". In: MNRAS 487.1, pp. 1160–1177. DOI: 10.1093/mnras/stz1297. arXiv: 1903.09064 [astro-ph.IM].

— (July 2019b). "Bayesian model selection with future 21cm observations of the epoch of reionization". In: MNRAS 487.1, pp. 1160–1177. DOI: 10.1093/mnras/stz1297. arXiv: 1903.09064 [astro-ph.IM].

Bond, J. R. and S. T. Myers (Mar. 1996). "The Peak-Patch Picture of Cosmic Catalogs. I. Algorithms". In: ApJS 103, p. 1. DOI: 10.1086/192267.

Bond, J. R. et al. (Oct. 1991). "Excursion Set Mass Functions for Hierarchical Gaussian Fluctuations". In: ApJ 379, p. 440. DOI: 10.1086/170520.

Boroson, Bram, Dong-Woo Kim, and Giuseppina Fabbiano (Feb. 2011). In: *The Astrophysical Journal* 729.1, p. 12. DOI: 10.1088/0004-637x/729/1/12. URL: https://doi.org/10.1088/0004-637x/729/1/12.

Bouwens, R. J. et al. (Oct. 2014). "UV-continuum Slopes of >4000 z ∼4-8 Galaxies from the HUDF/XDF, HUDF09, ERS, CANDELS-South, and CANDELS-North Fields". In: ApJ 793.2, 115, p. 115. DOI: 10.1088/0004-637X/793/2/115. arXiv: 1306.2950 [astro-ph.CO].

Bouwens, R. J. et al. (Apr. 2015). "UV Luminosity Functions at Redshifts $z \sim 4$ to $z \sim 10$ : 10,000 Galaxies from HST Legacy Fields". In: ApJ 803.1, 34, p. 34. DOI: 10.1088/0004-637X/803/1/34. arXiv: 1403.4295 [astro-ph.CO].

Bouwens, R. J. et al. (Nov. 2021). "Low-luminosity Galaxies in the Early Universe Have Observed Sizes Similar to Star Cluster Complexes". In: *The Astronomical Journal* 162.6, p. 255. ISSN: 1538-3881. DOI: 10.3847/1538-3881/abfda6. URL: http://dx.doi.org/10.3847/1538-3881/abfda6.

Bouwens, Rychard J. et al. (Dec. 2016a). "ALMA Spectroscopic Survey in the Hubble Ultra Deep Field: The Infrared Excess of UV-Selected z = 2-10 Galaxies as a

Function of UV-Continuum Slope and Stellar Mass". In: ApJ 833.1, 72, p. 72. DOI: 10.3847/1538-4357/833/1/72. arXiv: 1606.05280 [astro-ph.GA].

Bouwens, Rychard J. et al. (Dec. 2016b). "ALMA Spectroscopic Survey in the Hubble Ultra Deep Field: The Infrared Excess of UV-Selected z = 2-10 Galaxies as a Function of UV-Continuum Slope and Stellar Mass". In: ApJ 833.1, 72, p. 72. DOI: 10.3847/1538-4357/833/1/72. arXiv: 1606.05280 [astro-ph.GA].

Bowman, Judd D. et al. (Mar. 2018). "An absorption profile centred at 78 megahertz in the sky-averaged spectrum". In: Nature 555.7694, pp. 67–70. DOI: 10.1038/nature25792. arXiv: 1810.05912 [astro-ph.CO].

Bromm, Volker, Paolo S. Coppi, and Richard B. Larson (Jan. 2002). "The Formation of the First Stars. I. The Primordial Star-forming Cloud". In: ApJ 564.1, pp. 23–51. DOI: 10.1086/323947. arXiv: astro-ph/0102503 [astro-ph].

Brorby, M., P. Kaaret, and A. Prestwich (July 2014). "X-ray binary formation in low-metallicity blue compact dwarf galaxies". In: MNRAS 441.3, pp. 2346–2353. DOI: 10.1093/mnras/stu736. arXiv: 1404.3132 [astro-ph.GA].

Brorby, M. et al. (Feb. 2016). "Enhanced X-ray emission from Lyman break analogues and a possibleLX–SFR–metallicity plane". In: *Monthly Notices of the Royal Astronomical Society* 457.4, 4081–4088. ISSN: 1365-2966. DOI: 10.1093/mnras/stw284. URL: http://dx.doi.org/10.1093/mnras/stw284.

Chen, Xuelei and Jordi Miralda-Escudé (Feb. 2004). "The Spin-Kinetic Temperature Coupling and the Heating Rate due to Ly$\alpha$ Scattering before Reionization: Predictions for 21 Centimeter Emission and Absorption". In: ApJ 602.1, pp. 1–11. DOI: 10.1086/380829. arXiv: astro-ph/0303395 [astro-ph].

Chevalier, R. A. and A. W. Clegg (Sept. 1985). "Wind from a starburst galaxy nucleus". In: Nature 317.6032, pp. 44–45. DOI: 10.1038/317044a0.

Ciardi, B. et al. (Feb. 2006). "The effect of minihaloes on cosmic reionization". In: MNRAS 366.2, pp. 689–696. DOI: 10.1111/j.1365-2966.2005.09908.x. arXiv: astro-ph/0511623 [astro-ph].

Ciardi, Benedetta and Andrea Ferrara (Feb. 2005). "The First Cosmic Structures and Their Effects". In: Space Sci. Rev. 116.3-4, pp. 625–705. DOI: 10.1007/s11214-005-3592-0. arXiv: astro-ph/0409018 [astro-ph].

Clark, B. G. (Jan. 1999). "Coherence in Radio Astronomy". In: *Synthesis Imaging in Radio Astronomy II*. Ed. by G. B. Taylor, C. L. Carilli, and R. A. Perley. Vol. 180. Astronomical Society of the Pacific Conference Series, p. 1.

Cohn, J. D. and Martin White (Apr. 2008). "Dark matter halo abundances, clustering and assembly histories at high redshift". In: MNRAS 385.4, pp. 2025–2033. DOI: 10.1111/j.1365-2966.2008.12972.x. arXiv: 0706.0208 [astro-ph].

Cole, Shaun et al. (Sept. 2005). "The 2dF Galaxy Redshift Survey: power-spectrum analysis of the final data set and cosmological implications". In: MNRAS 362.2, pp. 505–534. DOI: 10.1111/j.1365-2966.2005.09318.x. arXiv: astro-ph/0501174 [astro-ph].

Cresci, G., F. Mannucci, and M. Curti (July 2019). "Fundamental metallicity relation in CALIFA, SDSS-IV MaNGA, and high-z galaxies". In: A&A 627, A42, A42. DOI: 10.1051/0004-6361/201834637. arXiv: 1811.06015 [astro-ph.GA].

Curti, Mirko et al. (Jan. 2020). "The mass-metallicity and the fundamental metallicity relation revisited on a fully $T_e$-based abundance scale for galaxies". In: MNRAS 491.1, pp. 944–964. DOI: 10.1093/mnras/stz2910. arXiv: 1910.00597 [astro-ph.GA].

Das, Arpan et al. (July 2017). "High-mass X-ray binaries and the cosmic 21-cm signal: impact of host galaxy absorption". In: MNRAS 469.1, pp. 1166–1174. DOI: 10.1093/mnras/stx943. arXiv: 1702.00409 [astro-ph.CO].

Datta, A., J. D. Bowman, and C. L. Carilli (Nov. 2010). "Bright Source Subtraction Requirements for Redshifted 21 cm Measurements". In: ApJ 724.1, pp. 526–538. DOI: 10.1088/0004-637X/724/1/526. arXiv: 1005.4071 [astro-ph.CO].

DeBoer, David R. et al. (Apr. 2017). "Hydrogen Epoch of Reionization Array (HERA)". In: PASP 129.974, p. 045001. DOI: 10.1088/1538-3873/129/974/045001. arXiv: 1606.07473 [astro-ph.IM].

Di Matteo, Tiziana et al. (Jan. 2002). "Radio Foregrounds for the 21 Centimeter Tomography of the Neutral Intergalactic Medium at High Redshifts". In: ApJ 564.2, pp. 576–580. DOI: 10.1086/324293. arXiv: astro-ph/0109241 [astro-ph].

Dijkstra, Mark et al. (Mar. 2012). "Constraints on the redshift evolution of the $L_X$-SFR relation from the cosmic X-ray backgrounds". In: MNRAS 421.1, pp. 213–223. DOI: 10.1111/j.1365-2966.2011.20292.x. arXiv: 1108.4420 [astro-ph.CO].

Dixon, Keri L. et al. (Mar. 2016). "The large-scale observational signatures of low-mass galaxies during reionization". In: MNRAS 456.3, pp. 3011–3029. DOI: 10.1093/mnras/stv2887. arXiv: 1512.03836 [astro-ph.CO].

Douna, V. M. et al. (July 2015). "Metallicity dependence of high-mass X-ray binary populations". In: A&A 579, A44, A44. DOI: 10.1051/0004-6361/201525617. arXiv: 1505.05483 [astro-ph.GA].

Doussot, Aristide, Hy Trac, and Renyue Cen (Jan. 2019). "SCORCH. II. Radiation-hydrodynamic Simulations of Reionization with Varying Radiation Escape Fractions". In: ApJ 870.1, 18, p. 18. DOI: 10.3847/1538-4357/aaef75. arXiv: 1712.04464 [astro-ph.CO].

Duncan, K. et al. (Nov. 2014). "The mass evolution of the first galaxies: stellar mass functions and star formation rates at $4 < z < 7$ in the CANDELS GOODS-South field". In: MNRAS 444.3, pp. 2960–2984. DOI: 10.1093/mnras/stu1622. arXiv: 1408.2527 [astro-ph.GA].

Efstathiou, G. and M. J. Rees (Feb. 1988). "High-redshift quasars in the Cold Dark Matter cosmogony". In: MNRAS 230, 5p–11p. DOI: 10.1093/mnras/230.1.5P.

Eide, Marius B. et al. (May 2018). "The epoch of cosmic heating by early sources of X-rays". In: MNRAS 476.1, pp. 1174–1190. DOI: 10.1093/mnras/sty272. arXiv: 1801.09719 [astro-ph.CO].

Eisenstein, Daniel J. and Wayne Hu (Jan. 1999). "Power Spectra for Cold Dark Matter and Its Variants". In: ApJ 511.1, pp. 5–15. DOI: 10.1086/306640. arXiv: astro-ph/9710252 [astro-ph].

Eisenstein, Daniel J. et al. (Nov. 2005). "Detection of the Baryon Acoustic Peak in the Large-Scale Correlation Function of SDSS Luminous Red Galaxies". In: ApJ 633.2, pp. 560–574. DOI: 10.1086/466512. arXiv: astro-ph/0501171 [astro-ph].

Ellison, Sara L. et al. (Jan. 2008). "Clues to the Origin of the Mass-Metallicity Relation: Dependence on Star Formation Rate and Galaxy Size". In: ApJ 672.2, p. L107. DOI: 10.1086/527296. arXiv: 0711.4833 [astro-ph].

Erb, Dawn K. et al. (July 2006). "The Stellar, Gas, and Dynamical Masses of Star-forming Galaxies at $z \sim 2$". In: *The Astrophysical Journal* 646.1, 107–132. ISSN: 1538-4357. DOI: 10.1086/504891. URL: http://dx.doi.org/10.1086/504891.

Ewall-Wice, A. et al. (Nov. 2018). "Modeling the Radio Background from the First Black Holes at Cosmic Dawn: Implications for the 21 cm Absorption Amplitude". In: ApJ 868.1, 63, p. 63. DOI: 10.3847/1538-4357/aae51d. arXiv: 1803.01815 [astro-ph.CO].

Fabbiano, G. (Jan. 1989). "X-rays from normal galaxies." In: ARA&A 27, pp. 87–138. DOI: 10.1146/annurev.aa.27.090189.000511.

Fan, Xiaohui et al. (July 2006). "Constraining the Evolution of the Ionizing Background and the Epoch of Reionization with z$_\sim$6 Quasars. II. A Sample of 19

Quasars". In: AJ 132.1, pp. 117–136. DOI: 10.1086/504836. arXiv: astro-ph/0512082 [astro-ph].

Feroz, F. and M. P. Hobson (Jan. 2008). "Multimodal nested sampling: an efficient and robust alternative to Markov Chain Monte Carlo methods for astronomical data analyses". In: *Monthly Notices of the Royal Astronomical Society* 384.2, pp. 449–463. ISSN: 1365-2966. DOI: 10.1111/j.1365-2966.2007.12353.x. URL: http://dx.doi.org/10.1111/j.1365-2966.2007.12353.x.

Feroz, F., M. P. Hobson, and M. Bridges (Oct. 2009). "MULTINEST: an efficient and robust Bayesian inference tool for cosmology and particle physics". In: MNRAS 398.4, pp. 1601–1614. DOI: 10.1111/j.1365-2966.2009.14548.x. arXiv: 0809.3437 [astro-ph].

Ferrarese, Laura and Holland Ford (Feb. 2005). "Supermassive Black Holes in Galactic Nuclei: Past, Present and Future Research". In: Space Sci. Rev. 116.3-4, pp. 523–624. DOI: 10.1007/s11214-005-3947-6. arXiv: astro-ph/0411247 [astro-ph].

Fialkov, Anastasia, Rennan Barkana, and Eli Visbal (Feb. 2014). "The observable signature of late heating of the Universe during cosmic reionization". In: Nature 506.7487, pp. 197–199. DOI: 10.1038/nature12999. arXiv: 1402.0940 [astro-ph.CO].

Fialkov, Anastasia et al. (Oct. 2016). "Constraining the redshifted 21-cm signal with the unresolved soft X-ray background". In: *Monthly Notices of the Royal Astronomical Society* 464.3, pp. 3498–3508. ISSN: 0035-8711. DOI: 10.1093/mnras/stw2540. eprint: https://academic.oup.com/mnras/article-pdf/464/3/3498/18519053/stw2540.pdf. URL: https://doi.org/10.1093/mnras/stw2540.

Field, George B. (Jan. 1958). "Excitation of the Hydrogen 21-CM Line". In: *Proceedings of the IRE* 46, pp. 240–250. DOI: 10.1109/JRPROC.1958.286741.

Finkelstein, Steven L. (Aug. 2016). "Observational Searches for Star-Forming Galaxies at z > 6". In: PASA 33, e037, e037. DOI: 10.1017/pasa.2016.26. arXiv: 1511.05558 [astro-ph.GA].

Fontanot, Fabio et al. (July 2021). "The evolution of the mass-metallicity relations from the VANDELS survey and the GAEA semi-analytic model". In: MNRAS 504.3, pp. 4481–4492. DOI: 10.1093/mnras/stab1213. arXiv: 2104.08295 [astro-ph.GA].

Fornasini, Francesca M., Francesca Civano, and Hyewon Suh (June 2020). "Connecting the metallicity dependence and redshift evolution of high-mass X-ray binaries". In: MNRAS 495.1, pp. 771–783. DOI: 10.1093/mnras/staa1211. arXiv: 2004.13033 [astro-ph.HE].

Fornasini, Francesca M. et al. (Nov. 2019). "The MOSDEF Survey: The Metallicity Dependence of X-Ray Binary Populations at z $\sim$ 2". In: ApJ 885.1, 65, p. 65. DOI: 10.3847/1538-4357/ab4653. arXiv: 1909.08635 [astro-ph.HE].

Fragos, T. et al. (Oct. 2013a). "Energy Feedback from X-Ray Binaries in the Early Universe". In: ApJ 776.2, L31, p. L31. DOI: 10.1088/2041-8205/776/2/L31. arXiv: 1306.1405 [astro-ph.CO].

Fragos, T. et al. (Feb. 2013b). "X-Ray Binary Evolution Across Cosmic Time". In: ApJ 764.1, 41, p. 41. DOI: 10.1088/0004-637X/764/1/41. arXiv: 1206.2395 [astro-ph.HE].

Furlanetto, Steven R. and Abraham Loeb (Aug. 2004). "Large-Scale Structure Shocks at Low and High Redshifts". In: *The Astrophysical Journal* 611.2, pp. 642–654. DOI: 10.1086/422242. URL: https://doi.org/10.1086/422242.

Furlanetto, Steven R., S. Peng Oh, and Frank H. Briggs (Oct. 2006). "Cosmology at low frequencies: The 21cm transition and the high-redshift Universe". In: *Physics Reports* 433.4-6, 181–301. ISSN: 0370-1573. DOI: 10.1016/j.physrep.2006.08.002. URL: http://dx.doi.org/10.1016/j.physrep.2006.08.002.

Furlanetto, Steven R. and Samuel Johnson Stoever (June 2010). "Secondary ionization and heating by fast electrons". In: MNRAS 404.4, pp. 1869–1878. DOI: 10.1111/j.1365-2966.2010.16401.x. arXiv: 0910.4410 [astro-ph.CO].

Furlanetto, Steven R., Matias Zaldarriaga, and Lars Hernquist (Sept. 2004). "Statistical Probes of Reionization with 21 Centimeter Tomography". In: *The Astrophysical Journal* 613.1, 16–22. ISSN: 1538-4357. DOI: 10.1086/423028. URL: http://dx.doi.org/10.1086/423028.

Gehlot, B. K. et al. (Sept. 2019). "The first power spectrum limit on the 21-cm signal of neutral hydrogen during the Cosmic Dawn at z = 20-25 from LOFAR". In: MNRAS 488.3, pp. 4271–4287. DOI: 10.1093/mnras/stz1937. arXiv: 1809.06661 [astro-ph.IM].

George, E. M. et al. (Jan. 2015). "A MEASUREMENT OF SECONDARY COSMIC MICROWAVE BACKGROUND ANISOTROPIES FROM THE 2500 SQUARE-DEGREE SPT-SZ SURVEY". In: *The Astrophysical Journal* 799.2, p. 177. DOI: 10.1088/0004-637x/799/2/177. URL: https://doi.org/10.1088/0004-637x/799/2/177.

Ghara, R. et al. (Feb. 2020). "Constraining the intergalactic medium at z $\approx$ 9.1 using LOFAR Epoch of Reionization observations". In: MNRAS 493.4, pp. 4728–4747. DOI: 10.1093/mnras/staa487. arXiv: 2002.07195 [astro-ph.CO].

Ghosh, Pranab and Nicholas E. White (Oct. 2001). "X-Ray Probes of Cosmic Star Formation History". In: *The Astrophysical Journal* 559.2, pp. L97–L100. DOI: 10.1086/323641. URL: https://doi.org/10.1086/323641.

Giacconi, R. et al. (July 1971). "Discovery of Periodic X-Ray Pulsations in Centaurus X-3 from UHURU". In: ApJ 167, p. L67. DOI: 10.1086/180762.

Gilfanov, M. (Mar. 2004). "Low-mass X-ray binaries as a stellar mass indicator for the host galaxy". In: *Monthly Notices of the Royal Astronomical Society* 349.1, pp. 146–168. ISSN: 0035-8711. DOI: 10.1111/j.1365-2966.2004.07473.x. eprint: https://academic.oup.com/mnras/article-pdf/349/1/146/11180080/349-1-146.pdf. URL: https://doi.org/10.1111/j.1365-2966.2004.07473.x.

Gilfanov, M., H. J. Grimm, and R. Sunyaev (Jan. 2004a). "$L_X$-SFR relation in star-forming galaxies". In: MNRAS 347.3, pp. L57–L60. DOI: 10.1111/j.1365-2966.2004.07450.x. arXiv: astro-ph/0301331 [astro-ph].

— (July 2004b). "Statistical properties of the combined emission of a population of discrete sources: astrophysical implications". In: MNRAS 351.4, pp. 1365–1378. DOI: 10.1111/j.1365-2966.2004.07874.x. arXiv: astro-ph/0312540 [astro-ph].

Gillet, Nicolas J. F., Andrei Mesinger, and Jaehong Park (Jan. 2020). "Combining high-z galaxy luminosity functions with Bayesian evidence". In: MNRAS 491.2, pp. 1980–1997. DOI: 10.1093/mnras/stz2988. arXiv: 1906.06296 [astro-ph.GA].

Ginzburg, V. L. and S. I. Syrovatsk (1969). "Developments in the Theory of Synchrotron Radiation and its Reabsorption". In: *Annual Review of Astronomy and Astrophysics* 7.1, pp. 375–420. DOI: 10.1146/annurev.aa.07.090169.002111. eprint: https://doi.org/10.1146/annurev.aa.07.090169.002111. URL: https://doi.org/10.1146/annurev.aa.07.090169.002111.

Glover, S. C. O. and P. W. J. L. Brand (Mar. 2001). "On the photodissociation of $H_2$ by the first stars". In: MNRAS 321.3, pp. 385–397. DOI: 10.1046/j.1365-8711.2001.03993.x. arXiv: astro-ph/0005576 [astro-ph].

Gnedin, Nickolay Y. and Peter A. Shaver (June 2004). "Redshifted 21 Centimeter Emission from the Pre-Reionization Era. I. Mean Signal and Linear Fluctuations". In: ApJ 608.2, pp. 611–621. DOI: 10.1086/420735. arXiv: astro-ph/0312005 [astro-ph].

Goodman, Jonathan and Jonathan Weare (Jan. 2010). "Ensemble samplers with affine invariance". In: *Communications in Applied Mathematics and Computational Science* 5.1, pp. 65–80. DOI: 10.2140/camcos.2010.5.65.

Greig, Bradley and Andrei Mesinger (June 2015). "21CMMC: an MCMC analysis tool enabling astrophysical parameter studies of the cosmic 21 cm signal". In: MNRAS 449.4, pp. 4246–4263. DOI: 10.1093/mnras/stv571. arXiv: 1501.06576 [astro-ph.CO].

— (Dec. 2017a). "Simultaneously constraining the astrophysics of reionization and the epoch of heating with 21CMMC". In: MNRAS 472.3, pp. 2651–2669. DOI: 10.1093/mnras/stx2118.

— (Mar. 2017b). "The global history of reionization". In: MNRAS 465.4, pp. 4838–4852. DOI: 10.1093/mnras/stw3026. arXiv: 1605.05374 [astro-ph.CO].

— (July 2018). "21CMMC with a 3D light-cone: the impact of the co-evolution approximation on the astrophysics of reionization and cosmic dawn". In: MNRAS 477.3, pp. 3217–3229. DOI: 10.1093/mnras/sty796. arXiv: 1801.01592 [astro-ph.CO].

Greig, Bradley, Andrei Mesinger, and Léon V. E. Koopmans (Jan. 2020). "Reionization and cosmic dawn astrophysics from the Square Kilometre Array: impact of observing strategies". In: MNRAS 491.1, pp. 1398–1407. DOI: 10.1093/mnras/stz3138. arXiv: 1906.07910 [astro-ph.CO].

Greig, Bradley et al. (Apr. 2017a). "Are we witnessing the epoch of reionisation at z = 7.1 from the spectrum of J1120+0641?" In: MNRAS 466.4, pp. 4239–4249. DOI: 10.1093/mnras/stw3351. arXiv: 1606.00441 [astro-ph.CO].

Greig, Bradley et al. (Apr. 2017b). "Ly$\alpha$ emission-line reconstruction for high-z QSOs". In: MNRAS 466.2, pp. 1814–1838. DOI: 10.1093/mnras/stw3210. arXiv: 1605.09388 [astro-ph.GA].

Greig, Bradley et al. (Jan. 2021a). "Exploring reionization and high-z galaxy observables with recent multiredshift MWA upper limits on the 21-cm signal". In: MNRAS 500.4, pp. 5322–5335. DOI: 10.1093/mnras/staa3494. arXiv: 2008.02639 [astro-ph.CO].

Greig, Bradley et al. (Jan. 2021b). "Interpreting LOFAR 21-cm signal upper limits at z $\approx$ 9.1 in the context of high-z galaxy and reionization observations". In: MNRAS 501.1, pp. 1–13. DOI: 10.1093/mnras/staa3593. arXiv: 2006.03203 [astro-ph.CO].

Grimes, J. P. et al. (July 2005). "A Chandra X-Ray Investigation of the Violent Interstellar Medium: From Dwarf Starbursts to Ultraluminous Infrared Galaxies". In: ApJ 628.1, pp. 187–204. DOI: 10.1086/430692. arXiv: astro-ph/0503685 [astro-ph].

Grimm, H. J., M. Gilfanov, and R. Sunyaev (Sept. 2002). "The Milky Way in X-rays for an outside observer. Log(N)-Log(S) and luminosity function of X-ray binaries from RXTE/ASM data". In: A&A 391, pp. 923–944. DOI: 10.1051/0004-6361:20020826. arXiv: astro-ph/0109239 [astro-ph].

— (Mar. 2003). "High-mass X-ray binaries as a star formation rate indicator in distant galaxies". In: MNRAS 339.3, pp. 793–809. DOI: 10.1046/j.1365-8711.2003.06224.x. arXiv: astro-ph/0205371 [astro-ph].

Gunn, James E. and Bruce A. Peterson (Nov. 1965). "On the Density of Neutral Hydrogen in Intergalactic Space." In: ApJ 142, pp. 1633–1636. DOI: 10.1086/148444.

Guo, Qi et al. (May 2011). "From dwarf spheroidals to cD galaxies: simulating the galaxy population in a $\Lambda$CDM cosmology". In: MNRAS 413.1, pp. 101–131. DOI: 10.1111/j.1365-2966.2010.18114.x. arXiv: 1006.0106 [astro-ph.CO].

Guth, A. H. and S. Y. Pi (Oct. 1982). "Fluctuations in the New Inflationary Universe". In: Phys. Rev. Lett. 49.15, pp. 1110–1113. DOI: 10.1103/PhysRevLett.49.1110.

Guth, Alan H. (Jan. 1981). "Inflationary universe: A possible solution to the horizon and flatness problems". In: Phys. Rev. D 23.2, pp. 347–356. DOI: 10.1103/PhysRevD.23.347.

Haiman, Zoltán, Tom Abel, and Martin J. Rees (May 2000). "The Radiative Feedback of the First Cosmological Objects". In: ApJ 534.1, pp. 11–24. DOI: 10.1086/308723. arXiv: astro-ph/9903336 [astro-ph].

Harrison, E. R. (May 1970). "Fluctuations at the Threshold of Classical Cosmology". In: *Phys. Rev. D* 1 (10), pp. 2726–2730. DOI: 10.1103/PhysRevD.1.2726. URL: https://link.aps.org/doi/10.1103/PhysRevD.1.2726.

HERA Collaboration et al. (Aug. 2021a). "First Results from HERA Phase I: Upper Limits on the Epoch of Reionization 21 cm Power Spectrum". In: *arXiv e-prints*, arXiv:2108.02263, arXiv:2108.02263. arXiv: 2108.02263 [astro-ph.CO].

HERA Collaboration et al. (Aug. 2021b). "HERA Phase I Limits on the Cosmic 21-cm Signal: Constraints on Astrophysics and Cosmology During the Epoch of Reionization". In: *arXiv e-prints*, arXiv:2108.07282, arXiv:2108.07282. arXiv: 2108.07282 [astro-ph.CO].

Hui, Lam and Nickolay Y. Gnedin (Nov. 1997). "Equation of state of the photoionized intergalactic medium". In: MNRAS 292.1, pp. 27–42. DOI: 10.1093/mnras/292.1.27. arXiv: astro-ph/9612232 [astro-ph].

Hunt, Leslie et al. (Nov. 2012). "Scaling relations of metallicity, stellar mass and star formation rate in metal-poor starbursts – I. A Fundamental Plane". In: *Monthly Notices of the Royal Astronomical Society* 427.2, 906–918. ISSN: 1365-2966. DOI: 10.1111/j.1365-2966.2012.21761.x. URL: http://dx.doi.org/10.1111/j.1365-2966.2012.21761.x.

Iliev, I. T. et al. (July 2006). "Simulating cosmic reionization at large scales - I. The geometry of reionization". In: MNRAS 369.4, pp. 1625–1638. DOI: 10.1111/j.1365-2966.2006.10502.x. arXiv: astro-ph/0512187 [astro-ph].

Iliev, Ilian T. et al. (Mar. 2014). "Simulating cosmic reionization: how large a volume is large enough?" In: MNRAS 439.1, pp. 725–743. DOI: 10.1093/mnras/stt2497. arXiv: 1310.7463 [astro-ph.CO].

Ishigaki, Masafumi et al. (Feb. 2018a). "Full-data Results of Hubble Frontier Fields: UV Luminosity Functions at z $\sim$ 6-10 and a Consistent Picture of Cosmic Reionization". In: ApJ 854.1, 73, p. 73. DOI: 10.3847/1538-4357/aaa544. arXiv: 1702.04867 [astro-ph.GA].

— (Feb. 2018b). "Full-data Results of Hubble Frontier Fields: UV Luminosity Functions at $z \sim 6-10$ and a Consistent Picture of Cosmic Reionization". In: ApJ 854.1, 73, p. 73. DOI: 10.3847/1538-4357/aaa544. arXiv: 1702.04867 [astro-ph.GA].

Jaacks, Jason, Steven L. Finkelstein, and Volker Bromm (Sept. 2019). "Legacy of star formation in the pre-reionization universe". In: MNRAS 488.2, pp. 2202–2221. DOI: 10.1093/mnras/stz1529. arXiv: 1804.07372 [astro-ph.GA].

Jaacks, Jason et al. (Jan. 2018). "Baseline metal enrichment from Population III star formation in cosmological volume simulations". In: *Monthly Notices of the Royal Astronomical Society* 475.4, pp. 4396–4410. ISSN: 0035-8711. DOI: 10.1093/mnras/sty062. eprint: https://academic.oup.com/mnras/article-pdf/475/4/4396/23957767/sty062.pdf. URL: https://doi.org/10.1093/mnras/sty062.

Jenkins, A. et al. (Feb. 2001). "The mass function of dark matter haloes". In: MNRAS 321.2, pp. 372–384. DOI: 10.1046/j.1365-8711.2001.04029.x. arXiv: astro-ph/0005260 [astro-ph].

Kaaret, Philip, Joseph Schmitt, and Mark Gorski (Oct. 2011). "X-RAYS FROM BLUE COMPACT DWARF GALAXIES". In: *The Astrophysical Journal* 741.1, p. 10. ISSN:

1538-4357. DOI: 10.1088/0004-637x/741/1/10. URL: http://dx.doi.org/10.1088/0004-637X/741/1/10.

Kaiser, N. (Sept. 1984). "On the spatial correlations of Abell clusters." In: ApJ 284, pp. L9–L12. DOI: 10.1086/184341.

Kaur, Harman Deep, Nicolas Gillet, and Andrei Mesinger (June 2020). "Minimum size of 21-cm simulations". In: MNRAS 495.2, pp. 2354–2362. DOI: 10.1093/mnras/staa1323. arXiv: 2004.06709 [astro-ph.CO].

Kaur, Harman Deep et al. (July 2022). "The 21-cm signal from the cosmic dawn: metallicity dependence of high-mass X-ray binaries". In: MNRAS 513.4, pp. 5097–5108. DOI: 10.1093/mnras/stac1226. arXiv: 2203.10851 [astro-ph.GA].

Kaurov, Alexander A. and Nickolay Y. Gnedin (June 2014). "Recombination Clumping Factor during Cosmic Reionization". In: ApJ 787.2, 146, p. 146. DOI: 10.1088/0004-637X/787/2/146. arXiv: 1311.2594 [astro-ph.CO].

Kern, Nicholas S. et al. (Oct. 2017). "Emulating Simulations of Cosmic Dawn for 21 cm Power Spectrum Constraints on Cosmology, Reionization, and X-Ray Heating". In: ApJ 848.1, 23, p. 23. DOI: 10.3847/1538-4357/aa8bb4. arXiv: 1705.04688 [astro-ph.CO].

Komatsu, E. et al. (Sept. 2003). "First-Year Wilkinson Microwave Anisotropy Probe (WMAP) Observations: Tests of Gaussianity". In: ApJS 148.1, pp. 119–134. DOI: 10.1086/377220. arXiv: astro-ph/0302223 [astro-ph].

Komatsu, E. et al. (Feb. 2009). "Five-Year Wilkinson Microwave Anisotropy Probe Observations: Cosmological Interpretation". In: ApJS 180.2, pp. 330–376. DOI: 10.1088/0067-0049/180/2/330. arXiv: 0803.0547 [astro-ph].

Komatsu, E. et al. (Feb. 2011). "Seven-year Wilkinson Microwave Anisotropy Probe (WMAP) Observations: Cosmological Interpretation". In: ApJS 192.2, 18, p. 18. DOI: 10.1088/0067-0049/192/2/18. arXiv: 1001.4538 [astro-ph.CO].

Koopmans, Leon et al. (Aug. 2019). "Peering into the Dark (Ages) with Low-Frequency Space Interferometers". In: *arXiv e-prints*, arXiv:1908.04296, arXiv:1908.04296. arXiv: 1908.04296 [astro-ph.IM].

Lacey, Cedric and Shaun Cole (June 1993). "Merger rates in hierarchical models of galaxy formation". In: MNRAS 262.3, pp. 627–649. DOI: 10.1093/mnras/262.3.627.

Lara-López, M. A. et al. (Oct. 2010). "A fundamental plane for field star-forming galaxies". In: A&A 521, L53, p. L53. DOI: 10.1051/0004-6361/201014803. arXiv: 1005.0509 [astro-ph.CO].

Lehmer, B. D. et al. (Mar. 2007). In: *The Astrophysical Journal* 657.2, pp. 681–699. DOI: 10.1086/511297. URL: https://doi.org/10.1086/511297.

Lehmer, B. D. et al. (July 2008). In: *The Astrophysical Journal* 681.2, pp. 1163–1182. DOI: 10.1086/588459. URL: https://doi.org/10.1086/588459.

Lehmer, B. D. et al. (Nov. 2010). "A Chandra Perspective on Galaxy-wide X-ray Binary Emission and its Correlation with Star Formation Rate and Stellar Mass: New Results from Luminous Infrared Galaxies". In: ApJ 724.1, pp. 559–571. DOI: 10.1088/0004-637X/724/1/559. arXiv: 1009.3943 [astro-ph.CO].

Lehmer, B. D. et al. (June 2012). "The 4 Ms Chandra Deep Field-South Number Counts Apportioned by Source Class: Pervasive Active Galactic Nuclei and the Ascent of Normal Galaxies". In: ApJ 752.1, 46, p. 46. DOI: 10.1088/0004-637X/752/1/46. arXiv: 1204.1977 [astro-ph.CO].

Lehmer, B. D. et al. (June 2015). "The 0.3-30 keV Spectra of Powerful Starburst Galaxies: NuSTAR and Chandra Observations of NGC 3256 and NGC 3310". In: ApJ 806.1, 126, p. 126. DOI: 10.1088/0004-637X/806/1/126. arXiv: 1505.00789 [astro-ph.GA].

Lehmer, B. D. et al. (July 2016). "The Evolution of Normal Galaxy X-Ray Emission through Cosmic History: Constraints from the 6 MS Chandra Deep Field-South". In: ApJ 825.1, 7, p. 7. DOI: 10.3847/0004-637X/825/1/7. arXiv: 1604.06461 [astro-ph.GA].

Lehmer, Bret D. et al. (July 2019a). "X-Ray Binary Luminosity Function Scaling Relations for Local Galaxies Based on Subgalactic Modeling". In: ApJS 243.1, 3, p. 3. DOI: 10.3847/1538-4365/ab22a8. arXiv: 1905.05197 [astro-ph.GA].

— (July 2019b). "X-Ray Binary Luminosity Function Scaling Relations for Local Galaxies Based on Subgalactic Modeling". In: ApJS 243.1, 3, p. 3. DOI: 10.3847/1538-4365/ab22a8. arXiv: 1905.05197 [astro-ph.GA].

Lehmer, Bret D. et al. (Jan. 2021). "The Metallicity Dependence of the High-mass X-Ray Binary Luminosity Function". In: *The Astrophysical Journal* 907.1, p. 17. ISSN: 1538-4357. DOI: 10.3847/1538-4357/abcec1. URL: http://dx.doi.org/10.3847/1538-4357/abcec1.

Lequeux, J. et al. (Dec. 1979). "Chemical Composition and Evolution of Irregular and Blue Compact Galaxies". In: A&A 80, p. 155.

Lewis, Antony (Oct. 2011). "The real shape of non-Gaussianities". In: J. Cosmology Astropart. Phys. 2011.10, 026, p. 026. DOI: 10.1088/1475-7516/2011/10/026. arXiv: 1107.5431 [astro-ph.CO].

Linden, T. et al. (Dec. 2010). "The Effect of Starburst Metallicity on Bright X-ray Binary Formation Pathways". In: ApJ 725.2, pp. 1984–1994. DOI: 10.1088/0004-637X/725/2/1984. arXiv: 1005.1639 [astro-ph.CO].

Liu, Adrian and Max Tegmark (May 2011). "A method for 21 cm power spectrum estimation in the presence of foregrounds". In: *Phys. Rev. D* 83 (10), p. 103006. DOI: 10.1103/PhysRevD.83.103006. URL: https://link.aps.org/doi/10.1103/PhysRevD.83.103006.

Livermore, R. C., S. L. Finkelstein, and J. M. Lotz (Feb. 2017). "Directly Observing the Galaxies Likely Responsible for Reionization". In: ApJ 835.2, 113, p. 113. DOI: 10.3847/1538-4357/835/2/113. arXiv: 1604.06799 [astro-ph.GA].

Livermore, Rachael C. (Jan. 2016). "Pushing the Frontiers: uncovering the earliest galaxies in the Hubble Frontier Fields". In: *IAU Focus Meeting* 29B, pp. 812–815. DOI: 10.1017/S1743921316006918.

Ma, Xiangcheng et al. (Oct. 2020). "No missing photons for reionization: moderate ionizing photon escape fractions from the FIRE-2 simulations". In: MNRAS 498.2, pp. 2001–2017. DOI: 10.1093/mnras/staa2404. arXiv: 2003.05945 [astro-ph.GA].

Madau, Piero and Mark Dickinson (2014). "Cosmic Star-Formation History". In: *Annual Review of Astronomy and Astrophysics* 52.1, pp. 415–486. DOI: 10.1146/annurev-astro-081811-125615. eprint: https://doi.org/10.1146/annurev-astro-081811-125615. URL: https://doi.org/10.1146/annurev-astro-081811-125615.

Madau, Piero and Tassos Fragos (May 2017). "Radiation Backgrounds at Cosmic Dawn: X-Rays from Compact Binaries". In: *The Astrophysical Journal* 840.1, p. 39. ISSN: 1538-4357. DOI: 10.3847/1538-4357/aa6af9. URL: http://dx.doi.org/10.3847/1538-4357/aa6af9.

Madau, Piero and Francesco Haardt (Nov. 2015). "Cosmic Reionization after Planck: Could Quasars Do It All?" In: ApJ 813.1, L8, p. L8. DOI: 10.1088/2041-8205/813/1/L8. arXiv: 1507.07678 [astro-ph.CO].

Madau, Piero, Avery Meiksin, and Martin J. Rees (Feb. 1997). "21 Centimeter Tomography of the Intergalactic Medium at High Redshift". In: ApJ 475.2, pp. 429–444. DOI: 10.1086/303549. arXiv: astro-ph/9608010 [astro-ph].

Magg, Mattis et al. (Oct. 2021). "Effect of the cosmological transition to metal-enriched star-formation on the hydrogen 21-cm signal". In: *arXiv e-prints*, arXiv:2110.15948, arXiv:2110.15948. arXiv: 2110.15948 [astro-ph.CO].

Maiolino, R. et al. (Sept. 2008). "AMAZE. I. The evolution of the mass-metallicity relation at z > 3". In: A&A 488.2, pp. 463–479. DOI: 10.1051/0004-6361:200809678. arXiv: 0806.2410 [astro-ph].

Majumdar, Suman et al. (May 2018). "Quantifying the non-Gaussianity in the EoR 21-cm signal through bispectrum". In: MNRAS 476.3, pp. 4007–4024. DOI: 10.1093/mnras/sty535. arXiv: 1708.08458 [astro-ph.CO].

Mannucci, F. et al. (Sept. 2010). "A fundamental relation between mass, star formation rate and metallicity in local and high-redshift galaxies". In: *Monthly Notices of the Royal Astronomical Society* 408.4, 2115–2127. ISSN: 0035-8711. DOI: 10.1111/j.1365-2966.2010.17291.x. URL: http://dx.doi.org/10.1111/j.1365-2966.2010.17291.x.

Mapelli, M. et al. (Oct. 2010). "Ultra-luminous X-ray sources and remnants of massive metal-poor stars". In: MNRAS 408.1, pp. 234–253. DOI: 10.1111/j.1365-2966.2010.17048.x. arXiv: 1005.3548 [astro-ph.CO].

McGreer, Ian D., Andrei Mesinger, and Valentina D'Odorico (Feb. 2015a). "Model-independent evidence in favour of an end to reionization by z ≈ 6". In: MNRAS 447.1, pp. 499–505. DOI: 10.1093/mnras/stu2449. arXiv: 1411.5375 [astro-ph.CO].

— (Feb. 2015b). "Model-independent evidence in favour of an end to reionization by z ≈ 6". In: MNRAS 447.1, pp. 499–505. DOI: 10.1093/mnras/stu2449. arXiv: 1411.5375 [astro-ph.CO].

McLeod, D. J., R. J. McLure, and J. S. Dunlop (July 2016). "The z = 9-10 galaxy population in the Hubble Frontier Fields and CLASH surveys: the z = 9 luminosity function and further evidence for a smooth decline in ultraviolet luminosity density at z≥ 8". In: MNRAS 459.4, pp. 3812–3824. DOI: 10.1093/mnras/stw904. arXiv: 1602.05199 [astro-ph.GA].

McLure, R. J. et al. (Sept. 2018). "The VANDELS ESO public spectroscopic survey". In: MNRAS 479.1, pp. 25–42. DOI: 10.1093/mnras/sty1213. arXiv: 1803.07414 [astro-ph.GA].

McQuinn, Matthew (Oct. 2012). "Constraints on X-ray emissions from the reionization era". In: MNRAS 426.2, pp. 1349–1360. DOI: 10.1111/j.1365-2966.2012.21792.x. arXiv: 1206.1335 [astro-ph.CO].

— (Sept. 2016). "The Evolution of the Intergalactic Medium". In: ARA&A 54, pp. 313–362. DOI: 10.1146/annurev-astro-082214-122355. arXiv: 1512.00086 [astro-ph.CO].

McQuinn, Matthew et al. (Dec. 2006). "Cosmological Parameter Estimation Using 21 cm Radiation from the Epoch of Reionization". In: ApJ 653.2, pp. 815–834. DOI: 10.1086/505167. arXiv: astro-ph/0512263 [astro-ph].

McQuinn, Matthew et al. (Oct. 2007). "Studying reionization with Ly$\alpha$ emitters". In: MNRAS 381.1, pp. 75–96. DOI: 10.1111/j.1365-2966.2007.12085.x. arXiv: 0704.2239 [astro-ph].

Mellema, Garrelt et al. (Oct. 2006). "Simulating cosmic reionization at large scales - II. The 21-cm emission features and statistical signals". In: MNRAS 372.2, pp. 679–692. DOI: 10.1111/j.1365-2966.2006.10919.x. arXiv: astro-ph/0603518 [astro-ph].

Mertens, F. G. et al. (Apr. 2020). "Improved upper limits on the 21 cm signal power spectrum of neutral hydrogen at z ≈ 9.1 from LOFAR". In: MNRAS 493.2, pp. 1662–1685. DOI: 10.1093/mnras/staa327. arXiv: 2002.07196 [astro-ph.CO].

Mesinger, Andrei (2019). *The Cosmic 21-cm Revolution; Charting the first billion years of our universe*. IOP Publishing. DOI: 10.1088/2514-3433/ab4a73.

Mesinger, Andrei and Mark Dijkstra (Nov. 2008). "Ultraviolet radiative feedback during the advanced stages of reionization". In: MNRAS 390.3, pp. 1071–1080. DOI: 10.1111/j.1365-2966.2008.13776.x. arXiv: 0806.3090 [astro-ph].

Mesinger, Andrei, Andrea Ferrara, and David S. Spiegel (May 2013). "Signatures of X-rays in the early Universe". In: MNRAS 431.1, pp. 621–637. DOI: 10.1093/mnras/stt198. arXiv: 1210.7319 [astro-ph.CO].

Mesinger, Andrei and Steven Furlanetto (Nov. 2007). "Efficient Simulations of Early Structure Formation and Reionization". In: ApJ 669.2, pp. 663–675. DOI: 10.1086/521806. arXiv: 0704.0946 [astro-ph].

Mesinger, Andrei, Steven Furlanetto, and Renyue Cen (Feb. 2011). "21CMFAST: a fast, seminumerical simulation of the high-redshift 21-cm signal". In: MNRAS 411.2, pp. 955–972. DOI: 10.1111/j.1365-2966.2010.17731.x. arXiv: 1003.3878 [astro-ph.CO].

Mesinger, Andrei and Steven R. Furlanetto (June 2008). "Ly$\alpha$ emitters during the early stages of reionization". In: MNRAS 386.4, pp. 1990–2002. DOI: 10.1111/j.1365-2966.2008.13039.x. arXiv: 0708.0006 [astro-ph].

Mesinger, Andrei et al. (Jan. 2015). "Can the intergalactic medium cause a rapid drop in Ly$\alpha$ emission at z > 6?" In: MNRAS 446.1, pp. 566–577. DOI: 10.1093/mnras/stu2089. arXiv: 1406.6373 [astro-ph.CO].

Mineo, S., M. Gilfanov, and R. Sunyaev (May 2011). "The collective X-ray luminosity of HMXB as a SFR indicator". In: *Astronomische Nachrichten* 332.4, p. 349. DOI: 10.1002/asna.201011497. arXiv: 1009.4873 [astro-ph.HE].

— (Jan. 2012). "X-ray emission from star-forming galaxies - I. High-mass X-ray binaries". In: MNRAS 419.3, pp. 2095–2115. DOI: 10.1111/j.1365-2966.2011.19862.x. arXiv: 1105.4610 [astro-ph.HE].

Mineo, S., M. Gilfanov, and R. Sunyaev (Oct. 2012). "X-ray emission from star-forming galaxies - II. Hot interstellar medium". In: *Monthly Notices of the Royal Astronomical Society* 426.3, 1870–1883. ISSN: 0035-8711. DOI: 10.1111/j.1365-2966.2012.21831.x. URL: http://dx.doi.org/10.1111/j.1365-2966.2012.21831.x.

Miralda-Escudé, Jordi, Martin Haehnelt, and Martin J. Rees (Feb. 2000). "Reionization of the Inhomogeneous Universe". In: ApJ 530.1, pp. 1–16. DOI: 10.1086/308330. arXiv: astro-ph/9812306 [astro-ph].

Mirocha, Jordan and Steven R. Furlanetto (Feb. 2019). "What does the first highly redshifted 21-cm detection tell us about early galaxies?" In: MNRAS 483.2, pp. 1980–1992. DOI: 10.1093/mnras/sty3260. arXiv: 1803.03272 [astro-ph.GA].

Mirocha, Jordan, Steven R. Furlanetto, and Guochao Sun (Jan. 2017). "The global 21-cm signal in the context of the high- z galaxy luminosity function". In: MNRAS 464.2, pp. 1365–1379. DOI: 10.1093/mnras/stw2412. arXiv: 1607.00386 [astro-ph.GA].

Mitra, Sourav, T. Roy Choudhury, and Andrea Ferrara (Jan. 2018). "Cosmic reionization after Planck II: contribution from quasars". In: MNRAS 473.1, pp. 1416–1425. DOI: 10.1093/mnras/stx2443. arXiv: 1606.02719 [astro-ph.CO].

Mondal, R. et al. (Apr. 2015). "The effect of non-Gaussianity on error predictions for the Epoch of Reionization (EoR) 21-cm power spectrum." In: MNRAS 449, pp. L41–L45. DOI: 10.1093/mnrasl/slv015. arXiv: 1409.4420 [astro-ph.CO].

Mondal, R. et al. (Nov. 2020). "Tight constraints on the excess radio background at z = 9.1 from LOFAR". In: MNRAS 498.3, pp. 4178–4191. DOI: 10.1093/mnras/staa2422. arXiv: 2004.00678 [astro-ph.CO].

Morales, Miguel F. (Feb. 2005). "Power Spectrum Sensitivity and the Design of Epoch of Reionization Observatories". In: ApJ 619.2, pp. 678–683. DOI: 10.1086/426730. arXiv: astro-ph/0406662 [astro-ph].

Morales, Miguel F. and Jacqueline Hewitt (Nov. 2004). "Toward Epoch of Reionization Measurements with Wide-Field Radio Observations". In: ApJ 615.1, pp. 7–18. DOI: 10.1086/424437. arXiv: astro-ph/0312437 [astro-ph].

Morales, Miguel F. et al. (June 2012). "Four Fundamental Foreground Power Spectrum Shapes for 21 cm Cosmology Observations". In: ApJ 752.2, 137, p. 137. DOI: 10.1088/0004-637X/752/2/137. arXiv: 1202.3830 [astro-ph.IM].

Muñoz, Julian B. et al. (Apr. 2022). "The impact of the first galaxies on cosmic dawn and reionization". In: MNRAS 511.3, pp. 3657–3681. DOI: 10.1093/mnras/stac185. arXiv: 2110.13919 [astro-ph.CO].

Munoz, Julian B. et al. (Apr. 2022). "The impact of the first galaxies on cosmic dawn and reionization". In: MNRAS 511.3, pp. 3657–3681. DOI: 10.1093/mnras/stac185. arXiv: 2110.13919 [astro-ph.CO].

Mutch, Simon J. et al. (Sept. 2016). "Dark-ages reionization and galaxy-formation simulation– VI. The origins and fate of the highest known redshift galaxy". In: *Monthly Notices of the Royal Astronomical Society* 463.4, 3556–3562. ISSN: 1365-2966. DOI: 10.1093/mnras/stw2187. URL: http://dx.doi.org/10.1093/mnras/stw2187.

Naoz, S. and R. Barkana (Sept. 2005). "Growth of linear perturbations before the era of the first galaxies". In: *Monthly Notices of the Royal Astronomical Society* 362.3, 1047–1053. ISSN: 1365-2966. DOI: 10.1111/j.1365-2966.2005.09385.x. URL: http://dx.doi.org/10.1111/j.1365-2966.2005.09385.x.

Ocvirk, Pierre et al. (Aug. 2020). "Cosmic Dawn II (CoDa II): a new radiation-hydrodynamics simulation of the self-consistent coupling of galaxy formation and reionization". In: MNRAS 496.4, pp. 4087–4107. DOI: 10.1093/mnras/staa1266. arXiv: 1811.11192 [astro-ph.GA].

Oesch, P. A. et al. (Mar. 2018). "The Dearth of z $\sim$ 10 Galaxies in All HST Legacy Fields—The Rapid Evolution of the Galaxy Population in the First 500 Myr". In: ApJ 855.2, 105, p. 105. DOI: 10.3847/1538-4357/aab03f. arXiv: 1710.11131 [astro-ph.GA].

Oh, S. Peng (June 2001). "Reionization by Hard Photons. I. X-Rays from the First Star Clusters". In: *The Astrophysical Journal* 553.2, pp. 499–512. DOI: 10.1086/320957. URL: https://doi.org/10.1086/320957.

Oh, S. Peng and Katherine J. Mack (Dec. 2003). "Foregrounds for 21-cm observations of neutral gas at high redshift". In: MNRAS 346.3, pp. 871–877. DOI: 10.1111/j.1365-2966.2003.07133.x. arXiv: astro-ph/0302099 [astro-ph].

Ouchi, Masami et al. (Nov. 2010). "Statistics of 207 Ly$\alpha$ Emitters at a Redshift Near 7: Constraints on Reionization and Galaxy Formation Models". In: ApJ 723.1, pp. 869–894. DOI: 10.1088/0004-637X/723/1/869. arXiv: 1007.2961 [astro-ph.CO].

Pacucci, Fabio et al. (Sept. 2014). "The X-ray spectra of the first galaxies: 21 cm signatures". In: MNRAS 443.1, pp. 678–686. DOI: 10.1093/mnras/stu1240. arXiv: 1403.6125 [astro-ph.CO].

Page, L. et al. (Sept. 2003). "First-Year Wilkinson Microwave Anisotropy Probe (WMAP) Observations: Interpretation of the TT and TE Angular Power Spectrum Peaks". In: ApJS 148.1, pp. 233–241. DOI: 10.1086/377224. arXiv: astro-ph/0302220 [astro-ph].

Pallottini, A. et al. (May 2014). "Simulating cosmic metal enrichment by the first galaxies". In: MNRAS 440.3, pp. 2498–2518. DOI: 10.1093/mnras/stu451. arXiv: 1403.1261 [astro-ph.CO].

Park, Jaehong et al. (Mar. 2019). "Inferring the astrophysics of reionization and cosmic dawn from galaxy luminosity functions and the 21-cm signal". In: MNRAS 484.1, pp. 933–949. DOI: 10.1093/mnras/stz032. arXiv: 1809.08995 [astro-ph.GA].

Park, Jaehong et al. (Jan. 2020). "Properties of reionization-era galaxies from JWST luminosity functions and 21-cm interferometry". In: MNRAS 491.3, pp. 3891–3899. DOI: 10.1093/mnras/stz3278. arXiv: 1909.01348 [astro-ph.CO].

Parsons, Aaron et al. (July 2012). "A Sensitivity and Array-configuration Study for Measuring the Power Spectrum of 21 cm Emission from Reionization". In: ApJ 753.1, 81, p. 81. DOI: 10.1088/0004-637X/753/1/81. arXiv: 1103.2135 [astro-ph.IM].

Parsons, Aaron R. et al. (Apr. 2010). "The Precision Array for Probing the Epoch of Re-ionization: Eight Station Results". In: AJ 139.4, pp. 1468–1480. DOI: 10.1088/0004-6256/139/4/1468. arXiv: 0904.2334 [astro-ph.CO].

Parsons, Aaron R. et al. (June 2014). "New Limits on 21 cm Epoch of Reionization from PAPER-32 Consistent with an X-Ray Heated Intergalactic Medium at z = 7.7". In: ApJ 788.2, 106, p. 106. DOI: 10.1088/0004-637X/788/2/106. arXiv: 1304.4991 [astro-ph.CO].

Patil, A. H. et al. (Mar. 2017). "Upper Limits on the 21 cm Epoch of Reionization Power Spectrum from One Night with LOFAR". In: ApJ 838.1, 65, p. 65. DOI: 10.3847/1538-4357/aa63e7. arXiv: 1702.08679 [astro-ph.CO].

Pentericci, L. et al. (Sept. 2018). "The VANDELS ESO public spectroscopic survey: Observations and first data release". In: A&A 616, A174, A174. DOI: 10.1051/0004-6361/201833047. arXiv: 1803.07373 [astro-ph.GA].

Perlmutter, S. et al. (June 1999). "Measurements of Ω and Λ from 42 High-Redshift Supernovae". In: ApJ 517.2, pp. 565–586. DOI: 10.1086/307221. arXiv: astro-ph/9812133 [astro-ph].

Persic, M. and Y. Rephaeli (Feb. 2007). "Galactic star formation rates gauged by stellar end-products". In: A&A 463.2, pp. 481–492. DOI: 10.1051/0004-6361:20054146. arXiv: astro-ph/0610321 [astro-ph].

Planck Collaboration et al. (Sept. 2016a). "Planck 2015 results. XIII. Cosmological parameters". In: A&A 594, A13, A13. DOI: 10.1051/0004-6361/201525830. arXiv: 1502.01589 [astro-ph.CO].

Planck Collaboration et al. (Dec. 2016b). "Planck intermediate results. XLVII. Planck constraints on reionization history". In: A&A 596, A108, A108. DOI: 10.1051/0004-6361/201628897. arXiv: 1605.03507 [astro-ph.CO].

Pober, Jonathan C. et al. (May 2013a). "Opening the 21 cm Epoch of Reionization Window: Measurements of Foreground Isolation with PAPER". In: ApJ 768.2, L36, p. L36. DOI: 10.1088/2041-8205/768/2/L36. arXiv: 1301.7099 [astro-ph.CO].

Pober, Jonathan C. et al. (Mar. 2013b). "The Baryon Acoustic Oscillation Broadband and Broad-beam Array: Design Overview and Sensitivity Forecasts". In: AJ 145.3, 65, p. 65. DOI: 10.1088/0004-6256/145/3/65. arXiv: 1210.2413 [astro-ph.CO].

— (Feb. 2014). "What Next-generation 21 cm Power Spectrum Measurements can Teach us About the Epoch of Reionization". In: ApJ 782.2, 66, p. 66. DOI: 10.1088/0004-637X/782/2/66. arXiv: 1310.7031 [astro-ph.CO].

Ponnada, S., M. Brorby, and P. Kaaret (Jan. 2020). "Effects of metallicity on high-mass X-ray binary formation". In: MNRAS 491.3, pp. 3606–3612. DOI: 10.1093/mnras/stz2929. arXiv: 1910.06925 [astro-ph.GA].

Press, William H. and Paul Schechter (Feb. 1974). "Formation of Galaxies and Clusters of Galaxies by Self-Similar Gravitational Condensation". In: ApJ 187, pp. 425–438. DOI: 10.1086/152650.

Prestwich, A. H. et al. (May 2013). "ULTRA-LUMINOUS X-RAY SOURCES IN THE MOST METAL POOR GALAXIES". In: *The Astrophysical Journal* 769.2, p. 92. ISSN: 1538-4357. DOI: 10.1088/0004-637x/769/2/92. URL: http://dx.doi.org/10.1088/0004-637X/769/2/92.

Pritchard, Jonathan R. and Steven R. Furlanetto (Apr. 2007). "21-cm fluctuations from inhomogeneous X-ray heating before reionization". In: MNRAS 376.4, pp. 1680–1694. DOI: 10.1111/j.1365-2966.2007.11519.x. arXiv: astro-ph/0607234 [astro-ph].

Qin, Yuxiang et al. (June 2020). "A tale of two sites - I. Inferring the properties of minihalo-hosted galaxies from current observations". In: MNRAS 495.1, pp. 123–140. DOI: 10.1093/mnras/staa1131. arXiv: 2003.04442 [astro-ph.CO].

Qin, Yuxiang et al. (Nov. 2020). "A tale of two sites – II. Inferring the properties of minihalo-hosted galaxies with upcoming 21-cm interferometers". In: *Monthly Notices of the Royal Astronomical Society* 501.4, 4748–4758. ISSN: 1365-2966. DOI: 10.1093/mnras/staa3408. URL: http://dx.doi.org/10.1093/mnras/staa3408.

Qin, Yuxiang et al. (Sept. 2021). "Reionization and galaxy inference from the high-redshift Ly $\alpha$ forest". In: MNRAS 506.2, pp. 2390–2407. DOI: 10.1093/mnras/stab1833. arXiv: 2101.09033 [astro-ph.CO].

Rafelski, Marc et al. (Aug. 2012). "Metallicity Evolution of Damped Ly$\alpha$ Systems Out to z $\sim$5". In: ApJ 755.2, 89, p. 89. DOI: 10.1088/0004-637X/755/2/89. arXiv: 1205.5047 [astro-ph.CO].

Rahmati, Alireza et al. (Apr. 2013). "On the evolution of the H I column density distribution in cosmological simulations". In: MNRAS 430.3, pp. 2427–2445. DOI: 10.1093/mnras/stt066. arXiv: 1210.7808 [astro-ph.CO].

Ranalli, P., A. Comastri, and G. Setti (Feb. 2003). "The 2-10 keV luminosity as a Star Formation Rate indicator". In: A&A 399, pp. 39–50. DOI: 10.1051/0004-6361:20021600. arXiv: astro-ph/0211304 [astro-ph].

Rauch, Michael (Jan. 1998). "The Lyman Alpha Forest in the Spectra of QSOs". In: ARA&A 36, pp. 267–316. DOI: 10.1146/annurev.astro.36.1.267. arXiv: astro-ph/9806286 [astro-ph].

Ricotti, Massimo and Jeremiah P. Ostriker (Aug. 2004). "X-ray pre-ionization powered by accretion on the first black holes – I. A model for the WMAP polarization measurement". In: *Monthly Notices of the Royal Astronomical Society* 352.2, pp. 547–562. DOI: 10.1111/j.1365-2966.2004.07942.x. eprint: https://academic.oup.com/mnras/article-pdf/352/2/547/18651610/352-2-547.pdf. URL: https://doi.org/10.1111/j.1365-2966.2004.07942.x.

Riess, Adam G. et al. (Sept. 1998). "Observational Evidence from Supernovae for an Accelerating Universe and a Cosmological Constant". In: AJ 116.3, pp. 1009–1038. DOI: 10.1086/300499. arXiv: astro-ph/9805201 [astro-ph].

Rogers, Alan E. E. and Judd D. Bowman (Aug. 2008). "Spectral Index of the Diffuse Radio Background Measured from 100 to 200 MHz". In: AJ 136.2, pp. 641–648. DOI: 10.1088/0004-6256/136/2/641. arXiv: 0806.2868 [astro-ph].

Ross, Hannah E. et al. (July 2017). "Simulating the impact of X-ray heating during the cosmic dawn". In: MNRAS 468.4, pp. 3785–3797. DOI: 10.1093/mnras/stx649. arXiv: 1607.06282 [astro-ph.CO].

Ross, Hannah E. et al. (July 2019). "Evaluating the QSO contribution to the 21-cm signal from the Cosmic Dawn". In: MNRAS 487.1, pp. 1101–1119. DOI: 10.1093/mnras/stz1220. arXiv: 1808.03287 [astro-ph.CO].

Rudakovskyi, Anton et al. (Oct. 2021). "Constraints on warm dark matter from UV luminosity functions of high-z galaxies with Bayesian model comparison". In: MNRAS 507.2, pp. 3046–3056. DOI: 10.1093/mnras/stab2333. arXiv: 2104.04481 [astro-ph.CO].

Sabti, Nashwan, Julian B. Muñoz, and Diego Blas (Oct. 2021). "GALLUMI: A Galaxy Luminosity Function Pipeline for Cosmology and Astrophysics". In: *arXiv e-prints*, arXiv:2110.13168, arXiv:2110.13168. arXiv: 2110.13168 [astro-ph.CO].

Sanders, Ryan L. et al. (May 2018). "The MOSDEF Survey: A Stellar Mass-SFR-Metallicity Relation Exists at z $\sim$ 2.3". In: ApJ 858.2, 99, p. 99. DOI: 10.3847/1538-4357/aabcbd. arXiv: 1711.00224 [astro-ph.GA].

Sanders, Ryan L. et al. (June 2021). "The MOSDEF Survey: The Evolution of the Mass–Metallicity Relation from z = 0 to $z \sim 3.3$". In: *The Astrophysical Journal* 914.1, p. 19. ISSN: 1538-4357. DOI: 10.3847/1538-4357/abf4c1. URL: http://dx.doi.org/10.3847/1538-4357/abf4c1.

Santos, M. G. et al. (Aug. 2010). "Fast large volume simulations of the 21-cm signal from the reionization and pre-reionization epochs". In: MNRAS 406, pp. 2421–2432. DOI: 10.1111/j.1365-2966.2010.16898.x. arXiv: 0911.2219.

Santos, Mário G., Asantha Cooray, and Lloyd Knox (June 2005). "Multifrequency Analysis of 21 Centimeter Fluctuations from the Era of Reionization". In: ApJ 625.2, pp. 575–587. DOI: 10.1086/429857. arXiv: astro-ph/0408515 [astro-ph].

Schaye, Joop (Oct. 2001). "Model-independent Insights into the Nature of the Ly$\alpha$ Forest and the Distribution of Matter in the Universe". In: ApJ 559.2, pp. 507–515. DOI: 10.1086/322421. arXiv: astro-ph/0104272 [astro-ph].

Schenker, Matthew A. et al. (Nov. 2014). In: ApJ 795.1, 20, p. 20. DOI: 10.1088/0004-637X/795/1/20. arXiv: 1404.4632 [astro-ph.CO].

Schreier, E. et al. (Mar. 1972). "Evidence for the Binary Nature of Centaurus X-3 from UHURU X-Ray Observations." In: ApJ 172, p. L79. DOI: 10.1086/180896.

Scoccimarro, Román (Oct. 1998). "Transients from initial conditions: a perturbative analysis". In: *Monthly Notices of the Royal Astronomical Society* 299.4, pp. 1097–1118. ISSN: 0035-8711. DOI: 10.1046/j.1365-8711.1998.01845.x. eprint: https://academic.oup.com/mnras/article-pdf/299/4/1097/3869550/299-4-1097.pdf. URL: https://doi.org/10.1046/j.1365-8711.1998.01845.x.

Shakura, N. I. and R. A. Sunyaev (Jan. 1973). "Black holes in binary systems. Observational appearance." In: A&A 24, pp. 337–355.

Shaver, P. A. et al. (May 1999). "Can the reionization epoch be detected as a global signature in the cosmic background?" In: A&A 345, pp. 380–390. arXiv: astro-ph/9901320 [astro-ph].

Sheth, Ravi K. and Giuseppe Tormen (Sept. 1999). "Large-scale bias and the peak background split". In: MNRAS 308.1, pp. 119–126. DOI: 10.1046/j.1365-8711.1999.02692.x. arXiv: astro-ph/9901122 [astro-ph].

Simcoe, Robert A. et al. (Dec. 2012). "Extremely metal-poor gas at a redshift of 7". In: Nature 492.7427, pp. 79–82. DOI: 10.1038/nature11612. arXiv: 1212.0548 [astro-ph.CO].

Singh, Saurabh et al. (Feb. 2022). "On the detection of a cosmic dawn signal in the radio background". In: *Nature Astronomy* 6, pp. 607–617. DOI: 10.1038/s41550-022-01610-5. arXiv: 2112.06778 [astro-ph.CO].

Smoot, G. F. et al. (Sept. 1992). "Structure in the COBE Differential Microwave Radiometer First-Year Maps". In: ApJ 396, p. L1. DOI: 10.1086/186504.

Sobacchi, Emanuele and Andrei Mesinger (Mar. 2014). "Inhomogeneous recombinations during cosmic reionization". In: *Monthly Notices of the Royal Astronomical Society* 440.2, pp. 1662–1673. ISSN: 0035-8711. DOI: 10.1093/mnras/stu377. eprint: https://academic.oup.com/mnras/article-pdf/440/2/1662/18502076/stu377.pdf. URL: https://doi.org/10.1093/mnras/stu377.

Springel, Volker and Lars Hernquist (Feb. 2003). "The history of star formation in a $\Lambda$ cold dark matter universe". In: MNRAS 339.2, pp. 312–334. DOI: 10.1046/j.1365-8711.2003.06207.x. arXiv: astro-ph/0206395 [astro-ph].

Stark, Daniel P. et al. (Oct. 2010). "Keck spectroscopy of faint 3 < z < 7 Lyman break galaxies – I. New constraints on cosmic reionization from the luminosity and

redshift-dependent fraction of Lyman $\alpha$ emission". In: *Monthly Notices of the Royal Astronomical Society* 408.3, pp. 1628–1648. DOI: 10.1111/j.1365-2966.2010.17227.x. eprint: https://academic.oup.com/mnras/article-pdf/408/3/1628/18582186/mnras0408-1628.pdf. URL: https://doi.org/10.1111/j.1365-2966.2010.17227.x.

Sun, G. and S. R. Furlanetto (July 2016). "Constraints on the star formation efficiency of galaxies during the epoch of reionization". In: MNRAS 460.1, pp. 417–433. DOI: 10.1093/mnras/stw980. arXiv: 1512.06219 [astro-ph.GA].

Sunyaev, R. A., B. M. Tinsley, and D. L. Meier (Jan. 1978). "Observable properties of primeval giant elliptical galaxies or ten million Orions at high redshift." In: *Comments on Astrophysics* 7.6, pp. 183–195.

Taam, Ronald E. and Bruce A. Fryxell (1989). "The Hydrodynamics of Accretion from Stellar Winds". In: *American Scientist* 77.6, pp. 539–545. ISSN: 00030996. URL: http://www.jstor.org/stable/27856004 (visited on 05/14/2022).

Tegmark, Max et al. (Jan. 1997). "How Small Were the First Cosmological Objects?" In: ApJ 474, p. 1. DOI: 10.1086/303434. arXiv: astro-ph/9603007 [astro-ph].

Tegmark, Max et al. (May 2004). "The Three-Dimensional Power Spectrum of Galaxies from the Sloan Digital Sky Survey". In: ApJ 606.2, pp. 702–740. DOI: 10.1086/382125. arXiv: astro-ph/0310725 [astro-ph].

Teyssier, R. (Apr. 2002). "Cosmological hydrodynamics with adaptive mesh refinement. A new high resolution code called RAMSES". In: A&A 385, pp. 337–364. DOI: 10.1051/0004-6361:20011817. arXiv: astro-ph/0111367 [astro-ph].

Tingay, S. J. et al. (Jan. 2013). "The Murchison Widefield Array: The Square Kilometre Array Precursor at Low Radio Frequencies". In: PASA 30, e007, e007. DOI: 10.1017/pasa.2012.007. arXiv: 1206.6945 [astro-ph.IM].

Tinker, Jeremy et al. (Dec. 2008). "Toward a Halo Mass Function for Precision Cosmology: The Limits of Universality". In: ApJ 688.2, pp. 709–728. DOI: 10.1086/591439. arXiv: 0803.2706 [astro-ph].

Trac, H. Y. and N. Y. Gnedin (Feb. 2011). "Computer Simulations of Cosmic Reionization". In: *Advanced Science Letters* 4, pp. 228–243. DOI: 10.1166/asl.2011.1214. arXiv: 0906.4348 [astro-ph.CO].

Tremonti, Christy A. et al. (Oct. 2004). "The Origin of the Mass-Metallicity Relation: Insights from 53,000 Star-forming Galaxies in the Sloan Digital Sky Survey". In: ApJ 613.2, pp. 898–913. DOI: 10.1086/423264. arXiv: astro-ph/0405537 [astro-ph].

Trott, Cathryn M. et al. (Apr. 2020). "Deep multiredshift limits on Epoch of Reionization 21 cm power spectra from four seasons of Murchison Widefield Array observations". In: MNRAS 493.4, pp. 4711–4727. DOI: 10.1093/mnras/staa414. arXiv: 2002.02575 [astro-ph.CO].

Tumlinson, Jason and J. Michael Shull (Jan. 2000). "Zero-Metallicity Stars and the Effects of the First Stars on Reionization". In: ApJ 528.2, pp. L65–L68. DOI: 10.1086/312432. arXiv: astro-ph/9911339 [astro-ph].

Tzanavaris, P. and I. Georgantopoulos (Mar. 2008). In: A&A 480.3, pp. 663–670. DOI: 10.1051/0004-6361:20078193. arXiv: 0801.4381 [astro-ph].

Ucci, Graziano et al. (Dec. 2021). "Astraeus V: The emergence and evolution of metallicity scaling relations during the Epoch of Reionization". In: *arXiv e-prints:2112.02115*, arXiv:2112.02115, arXiv:2112.02115. arXiv: 2112.02115 [astro-ph.GA].

*Understanding the Epoch of Cosmic Reionization* (Jan. 2016). Vol. 423. Astrophysics and Space Science Library. DOI: 10.1007/978-3-319-21957-8.

van Haarlem, M. P. et al. (Aug. 2013). "LOFAR: The LOw-Frequency ARray". In: A&A 556, A2, A2. DOI: 10.1051/0004-6361/201220873. arXiv: 1305.3550 [astro-ph.IM].

Vedantham, Harish, N. Udaya Shankar, and Ravi Subrahmanyan (Feb. 2012). "Imaging the Epoch of Reionization: Limitations from Foreground Confusion and Imaging Algorithms". In: ApJ 745.2, 176, p. 176. DOI: 10.1088/0004-637X/745/2/176. arXiv: 1106.1297 [astro-ph.IM].

Visbal, Eli et al. (July 2012). "The signature of the first stars in atomic hydrogen at redshift 20". In: Nature 487.7405, pp. 70–73. DOI: 10.1038/nature11177. arXiv: 1201.1005 [astro-ph.CO].

Warren, Michael S. et al. (Aug. 2006). "Precision Determination of the Mass Function of Dark Matter Halos". In: ApJ 646.2, pp. 881–885. DOI: 10.1086/504962. arXiv: astro-ph/0506395 [astro-ph].

Watkinson, C. A. and J. R. Pritchard (Dec. 2015). "The impact of spin-temperature fluctuations on the 21–cm moments". In: MNRAS 454.2, pp. 1416–1431. DOI: 10.1093/mnras/stv2010. arXiv: 1505.07108 [astro-ph.CO].

Watkinson, Catherine A. et al. (Jan. 2019). "The 21-cm bispectrum as a probe of non-Gaussianities due to X-ray heating". In: MNRAS 482.2, pp. 2653–2669. DOI: 10.1093/mnras/sty2740. arXiv: 1808.02372 [astro-ph.CO].

Wise, John H. et al. (Jan. 2012). "The Birth of a Galaxy: Primordial Metal Enrichment and Stellar Populations". In: ApJ 745.1, 50, p. 50. DOI: 10.1088/0004-637X/745/1/50. arXiv: 1011.2632 [astro-ph.CO].

Wouthuysen, S. A. (Jan. 1952). "On the excitation mechanism of the 21-cm (radio-frequency) interstellar hydrogen emission line." In: AJ 57, pp. 31–32. DOI: 10.1086/106661.

Xu, Hao, John H. Wise, and Michael L. Norman (July 2013). "POPULATION III STARS AND REMNANTS IN HIGH–REDSHIFT GALAXIES". In: *The Astrophysical Journal* 773.2, p. 83. ISSN: 1538-4357. DOI: 10.1088/0004-637x/773/2/83. URL: http://dx.doi.org/10.1088/0004-637X/773/2/83.

Xu, Hao et al. (Dec. 2016). "Galaxy Properties and UV Escape Fractions during the Epoch of Reionization: Results from the Renaissance Simulations". In: ApJ 833.1, 84, p. 84. DOI: 10.3847/1538-4357/833/1/84. arXiv: 1604.07842 [astro-ph.GA].

Yates, Robert M., Guinevere Kauffmann, and Qi Guo (May 2012). "The relation between metallicity, stellar mass and star formation in galaxies: an analysis of observational and model data". In: MNRAS 422.1, pp. 215–231. DOI: 10.1111/j.1365-2966.2012.20595.x. arXiv: 1107.3145 [astro-ph.CO].

Yue, B. et al. (May 2015). "Intensity mapping of [C ii] emission from early galaxies". In: *Monthly Notices of the Royal Astronomical Society* 450.4, 3829–3839. ISSN: 0035-8711. DOI: 10.1093/mnras/stv933. URL: http://dx.doi.org/10.1093/mnras/stv933.

Zahid, H. Jabran et al. (Aug. 2014). "THE UNIVERSAL RELATION OF GALACTIC CHEMICAL EVOLUTION: THE ORIGIN OF THE MASS-METALLICITY RELATION". In: *The Astrophysical Journal* 791.2, p. 130. ISSN: 1538-4357. DOI: 10.1088/0004-637x/791/2/130. URL: http://dx.doi.org/10.1088/0004-637X/791/2/130.

Zahn, Oliver et al. (June 2011). "Comparison of reionization models: radiative transfer simulations and approximate, seminumeric models". In: MNRAS 414.1, pp. 727–738. DOI: 10.1111/j.1365-2966.2011.18439.x. arXiv: 1003.3455 [astro-ph.CO].

Zaldarriaga, Matias, Steven R. Furlanetto, and Lars Hernquist (June 2004). "21 Centimeter Fluctuations from Cosmic Gas at High Redshifts". In: ApJ 608.2, pp. 622–635. DOI: 10.1086/386327. arXiv: astro-ph/0311514 [astro-ph].

Zel'Dovich, Y. B. (Mar. 1970). "Reprint of 1970A&A.....5...84Z. Gravitational instability: an approximate theory for large density perturbations." In: A&A 500, pp. 13–18.

Zeldovich, Yaa B. (Jan. 1972). "A hypothesis, unifying the structure and the entropy of the Universe". In: MNRAS 160, 1P. DOI: 10.1093/mnras/160.1.1P.